2014

Nonlinear Dispersive Partial Differential Equations of Physical Relevance with Applications to Vortex Dynamics

Robert VanGorder
University of Central Florida

NONLINEAR DISPERSIVE PARTIAL DIFFERENTIAL EQUATIONS OF PHYSICAL RELEVANCE WITH APPLICATIONS TO VORTEX DYNAMICS

by

ROBERT ASHTON VAN GORDER
B.S. University of Central Florida, 2009
M.S. University of Central Florida, 2013

A dissertation submitted in partial fulfillment of the requirements
for the degree of Doctor of Philosophy
in the Department of Mathematics
in the College of Sciences
at the University of Central Florida
Orlando, Florida

Spring Term
2014

Major Professors:
D. J. Kaup and K. Vajravelu (Co-chairs)

ABSTRACT

Nonlinear dispersive partial differential equations occur in a variety of areas within mathematical physics and engineering. We study several classes of such equations, including scalar complex partial differential equations, vector partial differential equations, and finally non-local integro-differential equations. For physically interesting families of these equations, we demonstrate the existence (and, when possible, stability) of specific solutions which are relevant for applications. While multiple application areas are considered, the primary application that runs through the work would be the nonlinear dynamics of vortex filaments under a variety of physical models. For instance, we are able to determine the structure and time evolution of several physical solutions, including the planar, helical, self-similar and soliton vortex filament solutions in a quantum fluid. Properties of such solutions are determined analytically and numerically through a variety of approaches. Starting with complex scalar equations (often useful for studying two-dimensional motion), we progress through more complicated models involving vector partial differential equations and non-local equations (which permit motion in three dimensions). In many of the examples considered, the qualitative analytical results are used to verify behaviors previously observed only numerically or experimentally.

ACKNOWLEDGMENTS

TABLE OF CONTENTS

xxviii

CHAPTER 1

INTRODUCTION

We shall be concerned with a few particular families of nonlinear dispersive partial differential equations. By dispersive, one means that waves of different wavelengths travel at different phase velocities. Fairly common examples of such partial differential equations would be the nonlinear Schrödinger (NLS) equation and the Korteweg-de Vries (KdV) equation. For our purposes, the types of equations we consider often deal with curvature, so that the time evolution of a solution curve is determined by structure of the curve. Such partial differential equations naturally appear in studies of vortex dynamics, particularly vortex filaments, and this will be the primary application we consider. While other applications will be discussed when they fit the theme of a particular chapter, the motion of a vortex filament under a variety of conditions will be an application common to all chapters.

The types of equations we shall be interested in will often take one of a few forms, consisting of either a single scalar equation, vector equations, or non-local equation, and the order of this investigation shall proceed in this general direction, with Chapters 2,3,4,5 considering scalar partial differential equations, Chapter 6 considering a vector partial differential equation, and Chapter 7 dealing with a specific nonlocal equation.

In Chapter 2, we shall explore a class of periodic solutions to four specific equations which are useful in mathematical physics. The first of these is the partial differential equation governing the motion of a planar vortex filament under the local induction approximation (LIA) in the Cartesian coordinate frame, which takes the form [98]

$$iu_t = -\frac{u_{xx}}{[1 + |u_x|^2]^{3/2}} \, . \tag{1.1}$$

For more general rotating filaments (those that happen too be strongly non-planar), it is more appropriate to apply the partial differential equation [17]

$$iu_t = -\frac{u_{xx}}{[1 + |u_x|^2]^{3/2}} - \frac{1}{2} \frac{u_x(u_x^* u_{xx} - u_x u_{xx}^*)}{[1 + |u_x|^2]^{3/2}} \, , \tag{1.2}$$

where * denotes complex conjugation. For both models, planar filaments have been shown to exist [99, 109] and correspond to one type of stationary solution. For the latter model, helical stationary solutions also exist. The most interesting solutions are those which are neither planar nor helical, yet are still essentially stationary states of the model. We find that solutions of this equation can exhibit a wide variety of behaviors. If one considers the arclength - tangent vector frame (which is derived treating the tangent vector to the filament as the unknown quantity which must be solved for), one obtains an equation of the form [95]

$$iu_t = -u_{xx} + \frac{2u^* u_x^2}{1 + |u|^2} \, . \tag{1.3}$$

This equation has the property that its planar solutions can be obtained in closed form, in terms of an elliptic function. In contrast, planar solutions to the equations corresponding to the Cartesian frame can, at best, be solved for implicitly. We end the chapter with a

2

discussion of periodic solutions to the Wadati-Konno-Ichikawa-Shimizu (WKIS) equation, which is a type of integrable evolution equation inspired by the derivative NLS which has been shown to have application in high energy physics [64]. The WKIS equation [101] takes the form

$$iu_t = -\left(\frac{u}{\sqrt{1+|u|^2}}\right)_{xx}. \tag{1.4}$$

In Chapter 3, we consider the oribital stability of some of the periodic solutions to models considered in Chapter 2. To do so, we invoke the Vakhitov-Kolokolov (VK) stability criterion, which relates the orbital stability of a solution to the change in the integral of motion

$$P(u_\omega(x,t)) = \int |u_\omega(x,t)|^2 dx \tag{1.5}$$

with respect to a spectral parameter, ω. Doing so, we are able to determine when the planar filaments in both the Cartesian and arclength - tangent vector models are orbitally stable. Similarly, we are able to determine when the space-periodic solutions to the WKIS model are orbitally stable. The stability criterion is typically applied to situations where the solution is a soliton which decays as $x \to \pm\infty$. However, the solutions studied here are periodic in space, so we modify the method and define the quantity P over a single period, as opposed to the real-line. In the limit where the period is taken to infinity, one may recover the standard VK criterion. As a matter of fact, it is possible to apply the criterion to other types of waves, and we demonstrate this by considering the orbital stability properties of a family of Peregrine solitons (which are one possible model of rogue waves [73]). Provided the change in P with respect to the spectral parameter is of constant sign and finite, we can consider

such situations where the modulus u is not time-constant. Our findings seem to suggest that it will be possible to consider the orbital stability of a more broad class of nonlinear dispersive equations, and this is commented on in the conclusions given in Chapter 8.

In Chapter 4, we take the local vortex filament models to the maximal extent of their applicability in order to determine the structure of the vortex filaments upon self-intersection, which allows us to form vortex loops. We first consider a type of scaling for the planar vortex filaments. With this scaling, we are able to define piecewise continuous solutions to the LIA, which we then use to construct self-intersecting vortex filaments. We do this using planar filaments (corresponding to steady state solutions) and self-similar filaments (which give unsteady vortex filament solutions). These types of solutions allow us to study situations where there are sharp kinks in the vortex filaments. Self intersections and sharp kinks are two vortex filament configurations which would physically destroy vortex filaments in standard fluids, so these types of solutions give us insight into cases where vortexes may break apart.

Regarding the vortex models, the first three chapters essentially address the motion of a vortex filament in a standard fluid, or the limit where superfluid effects become negligible. In a superfluid, however, the requisite models will be more complicated. In Chapter 5, we consider the motion of vortex filaments in a superfluid under the quantum form of the LIA. This formulation accounts for superfluid friction and a normal fluid velocity impinging on the vortex filament. The focus of Chapter 5 will be on potential forms of the quantum LIA. By potential, we mean that these models involve an unknown complex potential field which must be solved for, and hence these models are essentially two-dimensional. (The potential

function will often be written $u(x,t) = y(x,t) + iz(x,t)$, where y and z denote coordinates orthogonal to x.) Since one dimension is neglected, these models are best when the motion of filaments is primarily rotational. In Cartesian coordinates, the potential approximation to the LIA takes the form [102]

$$iu_t = aF(|u_x|^2)u_x x + bG(|u_x|)u_x \,, \tag{1.6}$$

where a and b are complex coefficients which shall depend on physical parameters. Under a number of assumptions or reductions, we study a variety of solutions to this equation. Planar solutions and their generalizations are first studied. We next consider a family of helical solutions. The helical vortex filament solutions correspond to Kelvin waves [89] which ride along the vortex filaments. While the potential models can accurately approximate the rotational properties of these waves, they fail to account for the transverse velocity. We address this point later when the vector equations are studied. As an example of the unsteady types of solutions possible, we consider self-similar solutions for the potential form of the Cartesian formulation of the quantum LIA.

Regarding Chapter 6, in this chapter we turn our attention to the exact vector form of the quantum LIA. While the potential equations studied in Chapter 5 approximate the full vector equations, the potential equations discussed in previous chapters essentially confine the motion of the filament solutions (and any waves along the filament) to two spatial dimensions. By considering the vector equations, we can study the full three-dimensional motion of the filaments. We consider the quantum LIA, as opposed to the standard fluid LIA, which omits certain parameters, since the standard LIA is simply the limit where all

superfluid parameters are taken to zero. We first study the decay of helical Kelvin waves on a quantum vortex filament. We start with waves of constant amplitude, and show that these correspond to a critical wave number. These solutions can be described in exact form. When we consider other wave numbers, we find that the helical Kelvin waves either amplify (and diverge at $t \to \infty$) or they decay (which is the physically reasonable case). The situation where the helical filaments decay to line filaments, we are able to give a nice analytical description of the problem. By assuming a helical filament solution with amplitude, phase, and transverse velocity, all dependent on time, we reduce the vector form of the quantum LIA into a system of three time-dependent ordinary differential equations. The analysis of these equations then lends insight into the behavior of helical Kelvin waves on a quantum vortex filament.

We are also able to study the planar filaments in the context of a quantum fluid. There are two possibilities. First, in order for the planar filament to maintain its form, the normal fluid velocity must take on a very specific (and space-variable) form. While this gives a nice mathematical solution, due to the restriction on the type of normal fluid velocity allowed, this case is not particularly interesting in terms of physical application. In the more physically appealing case, where the normal fluid velocity is not confined, we show that a filament which is planar in the standard fluid LIA should become deformed when superfluid parameters are included. Interestingly, the deformed planar filaments demonstrate an interesting amplification/de-amplification property when the normal fluid velocity is aligned along the filament. The role of superfluid friction is to introduce torsional effects as the

6

filaments rotate. This has the effect of giving the deformed planar filaments a structure which appears to be a hybrid of planar and helical shapes.

Our final investigation in Chapter 6 involves a generalization of the Hasimoto transformation (which takes the standard fluid LIA and maps it into a cubic NLS equation [42]) whereby we take the quantum form of the LIA and map it into a type of complex Ginzburg-Landau equation (a natural complex-coefficient generalization of NLS), [114]

$$iu_t = au_{xx} + b|u|^2u + c(u^2 - u^{*2})u + A(t)u\,, \tag{1.7}$$

where a, b, and c are complex-valued constants depending on the physical parameters and $A(t)$ is an arbitrary differentiable time-dependent function. To simplify the mathematics, we take $c = 0$, without loss of qualitative information in the cases we consider. From here, we are able to consider Stokes waves and even solitons on a quantum vortex filament. We also study a class of traveling wave solutions. The most important solutions here would be the solitons, and the results here generalize the Hasimoto solitons found over forty years ago for the standard fluid LIA to solitons under the quantum LIA for the first time.

Finally, in Chapter 7, we turn our attention to non-local equations governing the motion of vortex filaments. The LIA itself is a local approximation to the non-local Biot-Savart dynamics, so these results are a more general form of those considered in earlier chapters. Hence, although it appears concise and rather elegant, this equation is quite complicated to solve. In Chapter 7, we present two solutions to this model. First, we consider planar filaments. The integro-differential equation is too hard to solve exactly, but we are able

to use the method of multiple scales in order to obtain an accurate analytical approximation for the problem. The second class of solutions studied are the helical filaments. For these solutions, we are able to exactly determine the rotational and translational velocities in terms of the other model parameters. Therefore, we are able to determine the form and motion of both planar and helical vortex filaments in a qualitative sense, under the non-local Biot-Savart model.

Each of the chapters consists of material published or submitted for publication by the author. The material has been organized in such as way that permits each chapter to be more or less self contained. Therefore, one should be able to read the chapters independently. Some of the studied equations will feature in more than one chapter, and are cross referenced where needed. The actual analytical methods and approaches are self contained for each chapter, so it will not be necessary to read one chapter in order to understand the mathematics of another. Still, redundancies are kept to a minimum whenever possible. Chapters 2 through 4 constitute a study of potential forms for the simpler dispersion relations considered here. Chapter 5 constitutes a generalization of some of these results to the more complicated case where superfluid effects are added to the vortex filament dynamics, and this chapter is completely self contained. Chapter 6 contains some results on the full three-dimensional vortex dynamics under the quantum form of the LIA. Finally, Chapter 7 brings us back to the study of the self-induced motion of a vortex filament in a standard fluid. Two specific solution types are considered under this case, and each is compared to the corresponding

results under the LIA. There is a common reference list for all chapters, given in alphabetical order, at the end of this document.

CHAPTER 2

PERIODIC SOLUTIONS OF SOME NONLINEAR

DISPERSIVE PDES

2.1 Integrable stationary solution for the fully nonlinear local induction equation describing the motion of a vortex filament

We demonstrate an implicit exact stationary solution to the fully nonlinear local induction equation describing the motion of a vortex filament. The solution, which is periodic in the spatial variable, is governed by a second order nonlinear equation which has two exact first integrals. These results were considered in Van Gorder [99].

2.1.1 Background

Recently Shivamoggi and van Heijst [84] reformulated the Da Rios-Betchov equations in the extrinsic vortex filament coordinate space, and were able to find an exact solutions to an approximate equation governing a localized stationary solution. The approximation in the governing equation was due to the Shivamoggi and van Heijst's consideration of a

first order approximation of $\frac{dx}{ds} = 1/\sqrt{1 + y_x^2 + z_x^2}$. Previously, an order zero approximation to this equation was considered by Dmitriyev [26]. Such approximations result in exact solutions, but these solutions may break down outside of specific parameter regimes; namely, for all but very small value of the amplitude parameter. Herein, we avoid making the simplifying assumption on $\frac{dx}{ds}$. Although this results in a far more representative governing equations for large amplitudes, the governing equations are far more complicated. Such governing equations were then solved with a perturbation technique (in Van Gorder [98]) which suggested oscillating solutions in the large amplitude regime.

We begin with a review of some of the derivations in [98], as these shall be essential in both motivating the solutions as well as providing needed components with which to actually perform the computations. The self-induced velocity of a vortex filament in the LIA is given by (Da Rios [24], Arms and Hama [8]) $\mathbf{v} = \gamma\kappa\mathbf{t} \times \mathbf{n}$, where $\mathbf{t}$ and $\mathbf{n}$ are unit tangent and unit normal vectors to the vortex filament, respectively, κ is the curvature and γ is the strength of the vortex filament. Consider the vortex filament essentially aligned along the x-axis and assume the deviations from the x-axis to be small (Dmitriyev [26]): $\mathbf{r} = x\mathbf{i}_x + y(x,t)\mathbf{i}_y + z(x,t)\mathbf{i}_z$. We then have that

$$\mathbf{t} = \frac{d\mathbf{r}}{ds} = \frac{d\mathbf{r}}{dx}\frac{dx}{ds} = (\mathbf{i}_x + y_x\mathbf{i}_y + z_x\mathbf{i}_z)\frac{dx}{ds} \quad \text{and} \quad \mathbf{v} = y_t\mathbf{i}_y + z_t\mathbf{i}_z\,, \tag{2.1}$$

where

$$\frac{dx}{ds} = \frac{1}{\sqrt{1 + y_x^2 + z_x^2}}\,. \tag{2.2}$$

We compute

$$\kappa \mathbf{n} = \frac{d\mathbf{t}}{ds} = \frac{d\mathbf{t}}{dx}\frac{dx}{ds} = \frac{d^2\mathbf{r}}{dx^2}\left(\frac{dx}{ds}\right)^2 + \frac{d\mathbf{r}}{dx}\left(\frac{d}{dx}\frac{dx}{ds}\right)\frac{dx}{ds}$$

$$= -\left(y_x y_{xx} + z_x z_{xx}\right)\left(\frac{dx}{ds}\right)^4 \mathbf{i}_x + \left(y_x x + z_x^2 y_{xx} - y_x z_x z_{xx}\right)\left(\frac{dx}{ds}\right)^4 \mathbf{i}_y \qquad (2.3)$$

$$+ \left(z_x x + y_x^2 z_{xx} - y_x z_x y_{xx}\right)\left(\frac{dx}{ds}\right)^4 \mathbf{i}_z \,.$$

Placing (2.1) and (2.3) into $\mathbf{v} = \gamma \kappa \mathbf{t} \times \mathbf{n}$, we obtain

$$\mathbf{v} = \gamma \left(y_x z_{xx} - z_x y_{xx}\right)\left(\frac{dx}{ds}\right)^3 \mathbf{i}_x - \gamma z_{xx}\left(\frac{dx}{ds}\right)^3 \mathbf{i}_y + \gamma y_{xx}\left(\frac{dx}{ds}\right)^3 \mathbf{i}_z \,, \qquad (2.4)$$

so

$$y_t = -\gamma z_{xx}\left(\frac{dx}{ds}\right)^3 = -\gamma z_{xx}\left(1 + y_x^2 + z_x^2\right)^{-3/2} \qquad (2.5)$$

and

$$z_t = \gamma y_{xx}\left(\frac{dx}{ds}\right)^3 = \gamma y_{xx}\left(1 + y_x^2 + z_x^2\right)^{-3/2} \qquad (2.6)$$

must hold. Defining $\Phi = -(y + iz)$, (2.5) reduces to

$$i\Phi_t + \gamma \left(1 + |\Phi_x|^2\right)^{-3/2} \Phi_{xx} = 0 \,. \qquad (2.7)$$

In order to recover y and z once a solution Φ to (2.7) is known, note that $y = -\mathcal{R}e\,\Phi$ and $z = -\mathcal{I}m\,\Phi$. A first order approximation of the factor raised to the power $-3/2$ results in Eq. (9) of Shivamoggi and van Heijst [84] after an appropriate transformation (since an approximation was taken early in [84], the transformation $\Phi \to i\Phi$ is needed to bring a first order approximation of (2.7) into the form given in [84]). A zeroth order approximation was considered earlier by Dmitriyev [26]. Note that equation (2.7) is very similar to the equation $iv_t + v_{ss} - 2v^*v_s^2/(1 + |v|^2) = 0$ obtained by Umeki [95], where v denotes directly

the tangential vector of the filament. While both are obtained through different derivations, both are equivalent to the localized induction approximation (LIA).

2.1.2 Stationary solution governed by an integrable equation

Observe that (2.7) is similar in form to the Schrödinger equation for a free particle, only with a function of $|\Phi_x|$ replacing the constant coefficient. Let us assume a solution of the form $\Phi(x,t) = e^{-i\gamma t}\psi(x)$ where $\psi \in \mathbb{R}$. Then (2.7) is reduced to

$$\psi + \left(1 + (\psi')^2\right)^{-3/2}\psi'' = 0\,. \tag{2.8}$$

Multiplying by $2\psi'$ and integrating, we obtain the first integral

$$\psi^2 - \frac{2}{\sqrt{1 + (\psi')^2}} = C\,, \tag{2.9}$$

where C is a constant of motion determined by any specified boundary or initial data. In the case where $\psi(0) = 0$ and $\psi'(0) = 1$ (as in [84]; locally near $|x| << 0$), $C = -\sqrt{2}$. Algebraic manipulation of (2.9) leads to $(\psi^2 - C)^2\psi'^2 = 4 - (\psi^2 - C)$. Separating variables ψ and x, we obtain the implicit relation

$$\pm x + C_2 = \int^{\psi} \frac{(q^2 - C)dq}{\sqrt{4 - (q^2 - C)^2}} = \frac{1}{2}\int^{\psi^2 - C} \frac{\xi d\xi}{\sqrt{(C + \xi)(2 + \xi)(2 - \xi)}}\,. \tag{2.10}$$

If we perform the integration on (2.10), we obtain

$$\pm x + C_2 = \begin{cases} -\frac{2}{C-2}F\left(\frac{\psi}{\sqrt{2+C}}, \frac{\sqrt{2+C}}{\sqrt{C-2}}\right) - E\left(\frac{\psi}{\sqrt{2+C}}, \frac{\sqrt{2+C}}{\sqrt{C-2}}\right) & \text{if } C \neq 2, \\ \text{sgn}(\psi)\left\{\tanh^{-1}\left(\frac{2}{\sqrt{4-\psi^2}}\right) - \sqrt{4 - \psi^2}\right\} & \text{if } C = 2, \end{cases} \tag{2.11}$$

13

where F and E denote elliptic integrals of the first and second kind, respectively. In this sense, ψ is akin to a composite Jacobi amplitude. We remark that a similar solution was obtained by Hasimoto [41], through a different derivation. Hasimoto's derivation started with $\mathbf{v} = Y\mathbf{i}_y$, as opposed to $\mathbf{v} = y_t\mathbf{i}_y + z_t\mathbf{i}_z$. Assuming a stationary solution, Hasimoto's assumption leads to $Y_{xx} + \frac{\Omega}{\gamma}\left(1 + Y_x^2\right)^{3/2}Y = 0$ (in our notation, as the coordinate system of Hasimoto differs from ours). While similar in form to (2.8), there is some information loss going from the solution ϕ (which, implicitly, contains $y(x)$ and $z(x)$) to the solution $Y(x)$ of Hasimoto's equation. Hasimoto presents a solution $Y = A\mathrm{cn}(\xi, k)$ (where $x = x(\xi)$, ξ is a parametrization linking Y and x implicitly), which has initial conditions $Y(0, k) = A$ and $Y'(0) = 0$. Mapping these conditions into our solution for ϕ, which obeys the same type of ODE, we find these conditions imply $C = -2$ (which can be obtained from (2.11) in the limiting case $C \to -2$). Observe that we cannot, with the transformation given in Hasimoto [41], recover the solutions satisfying initial data given in [84] ($\psi(0) = 0$ and $\psi'(0) = 1$). Hence, our solution can be seen as a generalization of the implicit solution of Hasimoto, which is equivalent to our solution in the $C = -2$ case.

Exact inversion of relation (2.11) to obtain ψ is not possible given the appearance of two distinct elliptic functions; however, we can numerically invert the relation to recover ψ for given initial data, which would determine C and C_2 exactly. Note that we can just as easily attempt to solve (2.8) numerically for such initial data, and we obtain the types of solutions one would expect from the inversion of (2.11). Numerical integration yields the expected periodic solutions for ψ (see Fig. 2.1). The fact that the relation (2.11) depends

on C (and thus, on the initial data) is shown in Fig. 2.2, where we see that the amplitude and period are dependent on initial data. Note that the intercepts on the phase portraits (Fig. 2.1) can be calculated exactly from (2.9): For instance, when $\psi'(0) = 1$, the $\psi = 0$ intercepts are $\psi' = \pm\sqrt{\frac{4-\sqrt{2}+(\psi(0))^2}{((\psi(0))^2-\sqrt{2})^2}}$ and the $\psi' = 0$ intercepts are $\psi = \pm\sqrt{(\psi(0)^2 + 2 - \sqrt{2})}$.

The oscillatory solutions should not be surprising, as (2.8) essentially defines a nonlinear oscillator. Suppose we were to define a solution $\Phi(x,t) = e^{+i\gamma t}\chi(x)$ where $\chi(x) \in \mathbb{R}$ (this differs from the above solution, as we have taken $+\gamma$ as opposed to $-\gamma$ in the exponential). The resulting stationary equation then reads $\chi'' = \left(1 + (\chi')^2\right)^{3/2}\chi$. For non-negative initial data, near $x = 0$ we have $\chi'' > \chi$ which suggests that, locally, χ is bounded below by a function $\tilde{\chi}$ satisfying $\tilde{\chi}'' = \tilde{\chi}$. Using initial data $\chi(0) = 0$, $\chi'(0) = 1$, $\tilde{\chi}(x) = \sinh(x)$. So, $\chi(x)$ grows at least as fast as $\sinh(x)$, suggesting that the $\Phi(x,t) = e^{+i\gamma t}\chi(x)$ solution is not reasonable.
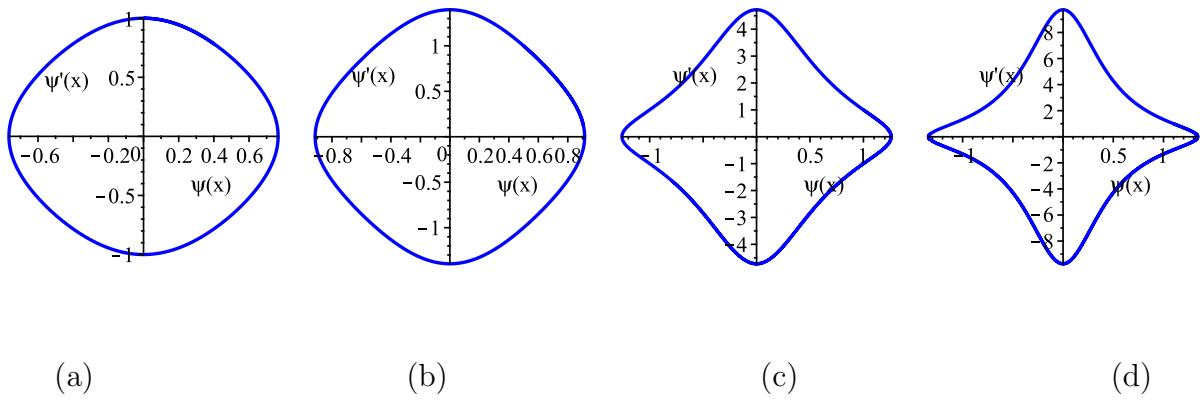
Figure 2.1: Phase portraits for $\psi(x)$ when $\psi(0) = 0$ (a), 0.5 (b), 1 (c), 1.1 (d) while $\psi'(0) = 1$.
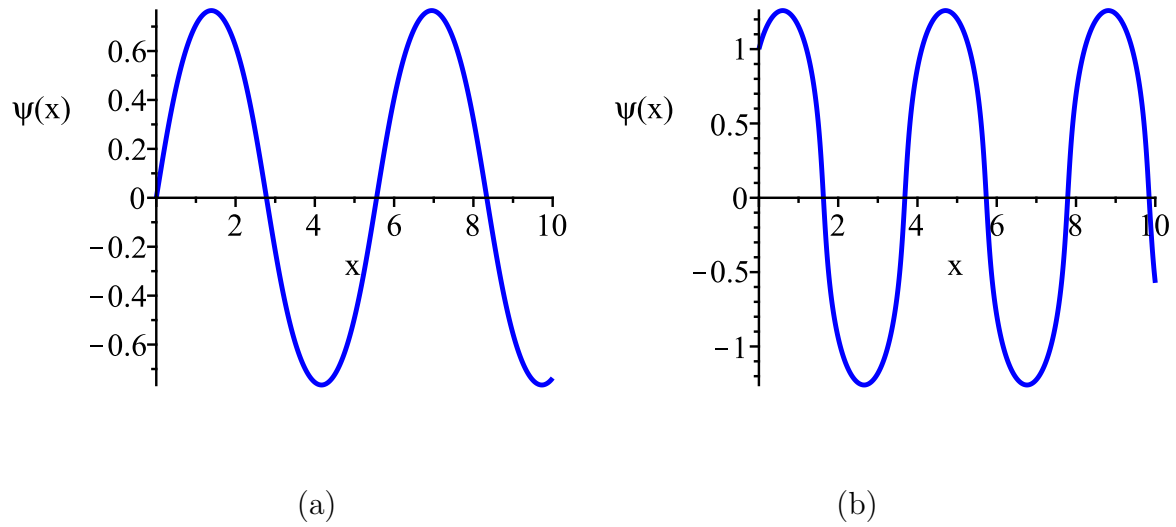
Figure 2.2: Plots of $\psi(x)$ when $\psi(0) = 0$ (a), 1 (b), while $\psi'(0) = 1$.

16

2.2 General rotating quantum vortex filaments under the 2D local induction approximation (LIA)

In his study of superfluid turbulence in the low-temperature limit, Svistunov [92] derived a Hamiltonian equation for the self-induced motion of a vortex filament. Under the local induction approximation (LIA), the Svistunov formulation is equivalent to a nonlinear dispersive partial differential equation. In this section, we consider a family of rotating vortex filament solutions for the LIA reduction of the Svistunov formulation, which we refer to as the 2D LIA (since it permits a potential formulation in terms of two of the three Cartesian coordinates). This class of solutions contains the well-known Hasimoto-type planar vortex filament as one reduction and helical solutions as another. More generally, we obtain solutions which are periodic in the space variable. A systematic analytical study of the behavior of such solutions is carried out. In the case where vortex filaments have small deviations from the axis of rotation, closed analytical forms of the filament solutions are given. A variety of numerical simulations are provided to demonstrate the wide range of rotating filament behaviors possible. Doing so, we are able to determine a number of vortex filament structures not previously studied. We find that the solution structure progresses from planar to helical, and then to more intricate and complex filament structures, possibly indicating the onset of superfluid turbulence. These results were presented in Van Gorder [109].

2.2.1 Background

The self-induced velocity of the vortex in the reference frame moving with the superfluid according to the local induction approximation (LIA) was given by Hall and Vinen [39, 40]. (This model is also referred to as the HVBK model, or Hall-Vinen-Bekarevich-Khalatnikov model. See Bekarevich and Khalatnikov [13].) Under a local induction approximation (LIA), the Biot-Savart law inherent in such models can be approximated, and Schwarz [81] obtained a type of quantum LIA

$$\mathbf{v} = \gamma\kappa\mathbf{t} \times \mathbf{n} + \alpha\mathbf{t} \times (\mathbf{U} - \gamma\kappa\mathbf{t} \times \mathbf{n}) - \alpha'\mathbf{t} \times (\mathbf{t} \times (\mathbf{U} - \gamma\kappa\mathbf{t} \times \mathbf{n})). \qquad (2.12)$$

Here $\mathbf{U}$ is the dimensionless normal fluid velocity, $\mathbf{t}$ and $\mathbf{n}$ are the unit tangent and unit normal vectors to the vortex filament, κ is the dimensionless average curvature, $\gamma = \Gamma \ln(c/\kappa a_0)$ is a dimensionless composite parameter (Γ is the dimensionless quantum of circulation, c is a scaling factor of order unity, $a_0 \approx 1.3 \times 10^{-8}$cm is the effective core radius of the vortex), α and α' are dimensionless friction coefficients which are small (except near the λ-point; for reference, the λ-point is the temperature (which at atmospheric pressure is ≈ 2.17K) below which normal fluid Helium transitions to superfluid Helium[51]). Regarding reasonable values of α and α', Table 1 of Schwarz[81] shows that at temperature $T = 1$K we have $\alpha = 0.005$ and $\alpha' = 0.003$, while at temperature $T = 1.5$K we have $\alpha = 0.073$ and $\alpha' = 0.018$. Thus, it makes sense to consider these friction terms as small parameters.

In the $\alpha, \alpha' \to 0$ limit (the zero-temperature limit), the motion of vortex lines is described by the standard Biot-Savart law

$$\frac{d\mathbf{r}}{dt} = \frac{\kappa}{4\pi} \int \frac{(\mathbf{r}_0 - \mathbf{r}) \times d\mathbf{r}_0}{|\mathbf{r}_0 - \mathbf{r}|} \,. \tag{2.13}$$

Often the Biot-Savart law (2.13) is replaced by the LIA. In this case, self-induced velocity of a vortex filament is approximated by [8, 24]

$$\mathbf{v} = \gamma \kappa \mathbf{t} \times \mathbf{n} \,, \tag{2.14}$$

where κ is the quantized curvature and γ is the strength of the vortex filament. Hasimoto [42] obtained a 1-soliton solution of the LIA in the curvature-torsion frame. Exact stationary solutions to the LIA in extrinsic coordinate space have been discussed by Kida [49] in the case of torus knots, planar solutions, and helices; some of these solutions are given by elliptic integrals.

Hasimoto [41] considered a planar vortex filament in the curvature-torsion frame of reference. This influential and often cited paper demonstrates the relation between the curvature of a vortex filament and elastica. Such a solution was also considered by Kida [49], who obtained results in terms of elliptic integrals in the moving (time-dependent) arc length coordinate frame, with stability results for some filaments in this framework provided later [50]. Fukumoto [33] considered the influence of background flows on such stationary states. For the Cartesian frame, some preliminary results were determined in Van Gorder [99], though only some special solutions were given. There is an alternate formulation, given by Umeki [95, 96], which provides the LIA in an arc-length coordinate frame. The Hasimoto

filament can be determined exactly in this frame (as is also true of the curvature-torsion frame), and the results were worked out by Van Gorder [100]. However, the conversion between the arc-length and Cartesian solutions is not simple, so it is worthwhile to consider the Cartesian case directly. Small amplitude space-periodic solutions of planar type were obtained through a multiple scales analysis by Van Gorder [105]. Such solutions are valid in the small-amplitude regime when the nonlinearity becomes sufficiently weak, though solutions break down after that.

In the present section, we shall be interested in generalized rotating vortex filaments. In order to describe such vortex filaments, we will employ the form of the LIA described in Boffetta et al. [17] (which we refer to as the 2D LIA, for reasons outlined later) and derived from the Svistunov model [92]. We show that the model contains both planar and helical filaments (those most often studied in the literature), and that these are really two narrow special cases of rotating planar vortex filaments. In particular, when the solutions have constant amplitude and space-variable phase, they correspond to the helical filaments of Sonin [89]. Meanwhile, when the phase is constant in space, and the amplitude varies, we recover the planar vortex filaments of Hasimoto type. Each of these solutions is rather narrow, and in general we will have solutions in between these two extremes.

We shall first provide a formulation of the 2D LIA of Boffetta et al. [17]. We demonstrate why this model is useful for studying non-planar filaments (such as filaments which may exhibit large spatial changes). The remainder of the section constitutes an analytical and numerical study of the generalized rotating filaments. First, we determine the

20

system of nonlinear differential equations governing the structure of such a vortex filament. We show that, in general, the phase and amplitude of such a filament are strongly coupled. The change in the phase can be given strictly in terms of the amplitude, which allows us to write one equation for the amplitude which itself depends on two parameters. Studying this equation, we demonstrate the existence of space-periodic filament solutions (in particular, filaments that are periodic in the y and z components, $y(x+T,t) = y(x,t)$ and $z(x+T,t) = z(x,t)$). We show that the period T can be calculated in terms of the model parameters. While the complexity of the differential equation governing the amplitude prevents exact solutions, we can obtain approximate solutions which are perturbative in nature. One of these types of solutions is like the planar filament, whereas the other is quite distinct. Finally, numerical solutions are provided for a variety of cases, in order to demonstrate the range of solutions possible.

The results indicate a wide variety of behaviors not previously demonstrated mathematically, which hold both helical and planar solutions are rather narrow special cases. In some of the more exotic solutions, we expect degeneracy into turbulence to occur. Hence, some of the solutions discussed here may be useful in the study of the onset of superfluid turbulence. So, these solutions are not a minor generalization of the exact planar or helical filament solutions already known. Rather, consideration of this more general formulation shows us that there are a wide variety of behaviors possible for rotating filaments in the Svistunov model under the LIA.

2.2.2 Formulation

First we consider the LIA (2.14) directly. Let us assume $\mathbf{r}(x,t) = (r_1(x,t), r_2(x,t), r_3(x,t))$, where the r_k's are functions to be determined by the LIA. Calculating $\mathbf{t}$ and $\kappa\mathbf{n}$ and taking the cross product, we obtain the PDE system

$$(r_1)_t = \gamma(r_2)_x^2 \left(\frac{(r_3)_x}{(r_2)_x} \right)_x \left((r_1)_x^2 + (r_2)_x^2 + (r_3)_x^2 \right)^{-3/2}, \tag{2.15}$$

$$(r_2)_t = \gamma(r_3)_x^2 \left(\frac{(r_1)_x}{(r_3)_x} \right)_x \left((r_1)_x^2 + (r_2)_x^2 + (r_3)_x^2 \right)^{-3/2}, \tag{2.16}$$

$$(r_3)_t = \gamma(r_1)_x^2 \left(\frac{(r_2)_x}{(r_1)_x} \right)_x \left((r_1)_x^2 + (r_2)_x^2 + (r_3)_x^2 \right)^{-3/2}. \tag{2.17}$$

If the filament is aligned along the x-axis and includes a translational velocity term (which means that the waves along a vortex filament are permitted to move along the reference axis, in addition to the rotational motion), we take $r_1(x,t) = x + \beta t$. In this case, we identify r_2 and r_3 with the y and z axes, as $r_2(x,t) = y(x,t)$ and $r_3(x,t) = z(x,t)$, respectively. As a result, the system (2.15)-(2.17) becomes

$$\beta = \gamma \frac{y_x z_{xx} - z_x y_{xx}}{(1 + y_x^2 + z_x^2)^{3/2}}, \tag{2.18}$$

$$y_t = -\frac{\gamma z_{xx}}{(1 + y_x^2 + z_x^2)^{3/2}}, \quad z_t = \frac{\gamma y_{xx}}{(1 + y_x^2 + z_x^2)^{3/2}}. \tag{2.19}$$

From (2.19), it makes sense to consider a potential function $\Phi(x,t) = y(x,t) + iz(x,t)$, which would put (2.18)-(2.19) into the form

$$\beta = \frac{\gamma}{2i} \frac{\Phi_x^* \Phi_{xx} - \Phi_x \Phi_{xx}^*}{(1 + |\Phi_x|^2)^{3/2}}, \tag{2.20}$$

$$i\Phi_t + \gamma \frac{\Phi_{xx}}{(1 + |\Phi_x|^2)^{3/2}} = 0. \tag{2.21}$$

The best way to understand these conditions would be that (2.21) gives a potential formulation of the LIA provided that the consistency condition (2.20) is satisfied. When $\beta = 0$, there is no drift. In certain situations, it may suffice to find a solution Φ to (2.21) such that the right hand side of (2.20) is very small (though not zero), which results in an approximate solution to the LIA.

The derivation outlined above has been used in many studies, as it is useful when either the amplitude or wave-number are small. Shivamoggi and van Heijst [84] reformulated the Da Rios-Betchov equations in the extrinsic vortex filament coordinate space and were able to find an exact solutions to an approximate equation governing a localized stationary solution. In doing so, they re-derived the Cartesian form of the LIA (refereed to as the extrinsic form of the LIA), and obtained a truncated approximation - assuming a very small amplitude. Van Gorder [98, 99] employed this formulation to study a number of special case solutions. Limitations and benefits to this type of formulation can be seen in [106], where (for the helical case) the direct approach using (2.21) (and extensions to the quantum case, where $\alpha, \alpha' \neq 0$) is most useful when perturbations along filaments are of sufficient bounded variation. Of course, if $\Phi_x^* \Phi_{xx} - \Phi_x \Phi_{xx}^*$ is a constant, then we can calculate a parameter β which takes care of the translation. For more complicated scenarios, when $\Phi_x^* \Phi_{xx} - \Phi_x \Phi_{xx}^*$ is not a constant in x, the solution of (2.21) will be an approximation to the LIA, rather than an exact solution.

In the case of a purely planar vortex filament, $\Phi(x,t) = e^{-it}\phi(x)$, where $\phi(x)$ is real-valued. In this case, $\Phi_x^* \Phi_{xx} - \Phi_x \Phi_{xx}^* \equiv 0$, so there is no drift, hence a (2.21) is exactly

equivalent to the LIA. In the case where $\Phi_x^* \Phi_{xx} - \Phi_x \Phi_{xx}^*$ is small, though not identically zero, (2.21) is still a reasonably good approximation to the LIA (which itself is an approximation to the fully non-local vortex filament dynamics). However, in the case where $\Phi_x^* \Phi_{xx} - \Phi_x \Phi_{xx}^*$ is not small, we evidently need a different formulation, as a solution to (2.21) will not adequately approximate a solution of the LIA. This formulation should somehow involve a term of the form $\Phi_x^* \Phi_{xx} - \Phi_x \Phi_{xx}^*$, and should collapse down to (2.21) when the term $\Phi_x^* \Phi_{xx} - \Phi_x \Phi_{xx}^*$ vanishes. When this term does vanish, there is no translation of the waves along the filament, and the only motion is rotation.

As it turns out, the formulation of Boffetta et al. [17], derived in a completely different fashion, shall be of use to us here. In the context of superfluids in the low-temperature limit (i.e., in the absence of superfluid friction parameters), the Cartesian form of the LIA was previously derived by Svistunov in 1995 [92], where the Cartesian representation of the LIA dynamics are represented as a Hamiltonian system for a single periodic vortex line along one axis. Introducing potential $\Psi(x,t) = y(x,t) + iz(x,t)$, Svistunov showed that the Biot-Savart law (2.13) could be written in Hamiltonian form

$$i\Psi_t = \frac{\delta}{\delta \Psi^*} H[w] \,, \tag{2.22}$$

where

$$H[\Psi] = \frac{\kappa}{4\pi} \int \int \frac{1 + Re[\Psi_x^*(x_1)\Psi_x(x_2)]}{\sqrt{(x_1 - x_2)^2 + |\Psi(x_1) - \Psi(x_2)|^2}} dx_1 dx_2 \,. \tag{2.23}$$

24

This is a type of 2D Biot-Savart law. Introducing a cutoff at the vortex filament radius $a < |\mathbf{r} - \mathbf{r}_0|$, the Hamiltonian reduces to the LIA

$$\hat{H}[\Psi] = 2\frac{\kappa}{4\pi}\ln(\ell/a)\int\sqrt{1 + |\Psi_x(x_1)|^2}dx_1 = \kappa\gamma L[w]\,, \qquad (2.24)$$

where $\gamma = \frac{1}{2\pi}\ln(\ell/a)$ is the filament strength, ℓ is a characteristic length scale, and $L[w]$ is the total vortex line length. So, under the LIA, the Hamiltonian is just a scaling of the total vortex length. In equation (4) of Boffetta et al. [17], it was shown that the equation of motion for this Hamiltonian becomes

$$i\Psi_t + \left(\frac{\Psi_x}{\sqrt{1 + |\Psi_x|^2}}\right)_x = 0\,, \qquad (2.25)$$

where here we have used a different scaling of t to remove a factor of two from (2.25). It shall be this equation that we are interested in. Symmetry properties of this model have been discussed by Sonin [90]. Helical waves from the Cartesian form of the LIA (2.25) were considered by Sonin [89]. For more on such Hamiltonian formulations, see Goldstein and Petrich [37], Langer and Singer [52] and references therein. Fukumoto and Miyajima [34] construct an integrable hierarchy for the localized induction equation, and determine Kida-type solutions. One area of interest is vortex line reconnections. While a simplification of the full Biot-Savart law which neglects global behavior in favor of local behavior, the LIA has been shown to admit solutions which do permit self-crossings [81, 92, 105], so it can qualitatively describe vortex line reconnection events in strong turbulence. In contrast, the LIA is not very useful for the study of weak Kelvin wave turbulence, since resonant wave interactions are not present in the simplified LIA model [17].

Performing the differentiation in x on the second term in (2.25), we obtain exactly the type of formulation needed:

$$i\Psi_t + \gamma \frac{\Psi_{xx}}{(1 + |\Psi_x|^2)^{3/2}} + \frac{\gamma}{2} \frac{\Psi_x \left(\Psi_x^* \Psi_{xx} - \Psi_x \Psi_{xx}^*\right)}{(1 + |\Psi_x|^2)^{3/2}} = 0 \,. \tag{2.26}$$

Note that when $\Psi_x^* \Psi_{xx} - \Psi_x \Psi_{xx}^* \to 0$, (2.26) reduces to (2.21) as required (so it accounts for the planar case perfectly). On the other hand, (2.26) also accounts for situations where $\Psi_x^* \Psi_{xx} - \Psi_x \Psi_{xx}^*$ is large. Therefore, this equation is ideal for studying non-planar rotating vortex filaments.

2.2.3 Analytical and numerical properties of the rotating filament solutions

We first outline properties of a general rotating filament under (2.25). Later, we shall examine more explicit properties of such filaments, in order to construct analytical or numerical solutions. To model a rotating filament, we assume a solution of the form

$$\Psi(x,t) = e^{-\gamma i t}\psi(x) \,. \tag{2.27}$$

In general, ψ must be complex-valued (in order to capture all possible physical behaviors). This class of solution can describe a planar vortex filament when ψ is real-valued; however, when ψ is permitted to be complex-valued, a far wider range of solutions are possible. The Hasimoto-type solutions derived previously move without change in form [49]. This is in direct analogy to the solutions originally obtained by Hasimoto [41]. However, if we relax

one condition, namely that ψ be a real-valued function, we can obtain a more general class of solutions. Such solutions will correspond to bending or twisting of the Hasimoto solutions.

Writing ψ in polar form will be more useful, so we consider functions real-valued $R(x)$ and $\Theta(x)$ such that $\psi(x) = R(x)\exp(i\Theta(x))$. Once such a solution is known, then by the definition of $\Psi(x,t)$ we shall have the vortex filament

$$
\begin{aligned}
\mathbf{r}(x,t) &= (x, y(x,t), z(x,t)) = (x, \mathrm{Re}[e^{-i\gamma t}\psi(x)], \mathrm{Im}[e^{-i\gamma t}\psi(x)]) \\
&= (x, R(x)\cos(i\{\Theta(x) - \gamma t\}), R(x)\sin(i\{\Theta(x) - \gamma t\})).
\end{aligned}
\tag{2.28}
$$

Equation (2.26) then gives

$$
R + \frac{R'' - R\Theta'^2 + i(2R'\Theta' + R\Theta'')}{\left(1 + R'^2 + R^2\Theta'^2\right)^{3/2}} = 0.
\tag{2.29}
$$

Since R and Θ are real-valued functions, we can separate real and imaginary parts. We obtain the real-valued system

$$
R + \frac{R'' - R\Theta'^2}{\left(1 + R'^2 + R^2\Theta'^2\right)^{3/2}} = 0 \quad \text{and} \quad 2R'\Theta' + R\Theta'' = 0.
\tag{2.30}
$$

Solving the latter for Θ', we find $\Theta'(x) = \Theta_1 R^{-2}(x)$ where Θ_1 is a constant of integration. If $\Theta_1 = 0$, we effectively have a reduction to the real-valued case considered when studying a planar vortex filament moving without change in form. In such a case, one has

$$
R + \frac{R''}{\left(1 + R'^2\right)^{3/2}} = 0,
\tag{2.31}
$$

which is exactly what one gets from (2.21) in the case of a planar filament. This directly gives the Hasimoto planar filament in the Cartesian frame of reference. Various properties of these planar filaments have been discussed previously [99, 105]. On the other hand, when

27

$R(x)$ is constant, say $R(x) = R_0$, we obtain a complex exponential solution corresponding to a solution of the form $\Theta(x) = \Theta_1 x + \Theta_0$: $\Psi(x,t) = R_0 \exp(i[\Theta_1 x + \Theta_0 - t])$. When placed back into (2.28), this gives a helical solution. Hence, we may recover the helical solutions of [89] in the constant $R(x)$ case. We remark that in the case of the full Hall-Vinen model (2.12) with non-zero friction parameters $\alpha > 0$ and $\alpha' > 0$, the motion of purely helical vortex filaments have been described recently by Van Gorder [106], although the model considered there used the form of the LIA corresponding to (2.21) in the case where Ak is sufficiently small - and thus neglected any translational effects.

Both the planar and helical filaments are narrow special cases. For the more general case where $\Theta_1 \neq 0$ and R is not constant, the first equation in (2.30) becomes

$$R + \frac{R'' - \Theta_1^2 R^{-3}}{\left(1 + R'^2 + \Theta_1^2 R^{-2}\right)^{3/2}} = 0 \,. \tag{2.32}$$

Note that (2.32) is equivalent to

$$\frac{d}{dx}\left\{ R^2 - \frac{1}{\sqrt{1 + R'^2 + \Theta_1^2 R^{-2}}} \right\} = 0 \,, \tag{2.33}$$

so a first integral for (2.32) is given by

$$R^2 - \frac{1}{\sqrt{1 + R'^2 + \Theta_1^2 R^{-2}}} = I \,, \tag{2.34}$$

where I is an integration constant. The dynamics of (2.34) will therefore depend on two explicit parameters, Θ_1 and I, as well as on the amplitude of the filament at the origin, $R(0)$. It is possible to find bounded periodic solutions $R(x)$ to (2.34). In order for such solutions to exist, we should restrict $I_*(\Theta_1) < I < I^*(\Theta_1)$, where $I_*(\Theta_1)$ and $I^*(\Theta_1)$ are constants that

depends on the value of Θ_1 taken. From the form of (2.34), we should have $I_*(\Theta_1) > -1$. On the other hand, assume that we have a bounded periodic solution satisfying $R_* \leq R(x) \leq R^*$, so that $R' = 0$ when either $R = R_*$ or $R = R^*$. Then, we must have

$$R_*^2 - \frac{1}{\sqrt{1 + \Theta_1^2 R_*^{-2}}} = I \,, \tag{2.35}$$

therefore $I^*(\Theta_1) < R_*^2$.

It is perhaps easiest to view the dependence of a solution $R(x)$ on the constants Θ_1 and I by way of phase portraits, since these are useful for displaying periodic solutions. The cases for $\Theta_1 = 0$ and $\Theta_1 \neq 0$ are qualitatively distinct. In particular, when $\Theta_1 = 0$, we obtain planar filaments which correspond to periodic $R(x)$ with $R_{\min} = -R_{\max}$, therefore $R(x)$ takes both positive and negative values - as seen in Fig. 2.3(a). In contrast, when $\Theta_1 \neq 0$, we cannot have $R(x) = 0$ for any x, else we have a division by zero. The result is that $R(x)$ remains positive for all x, and profiles for this case are demonstrated in Fig. 2.3(b). Note that there exists a single point at which $R'(x) \equiv 0$ for all x and $R(x) = R_0$, a constant. This point in the phase space corresponds directly to a helical filament with amplitude R_0.

(a)   (b)
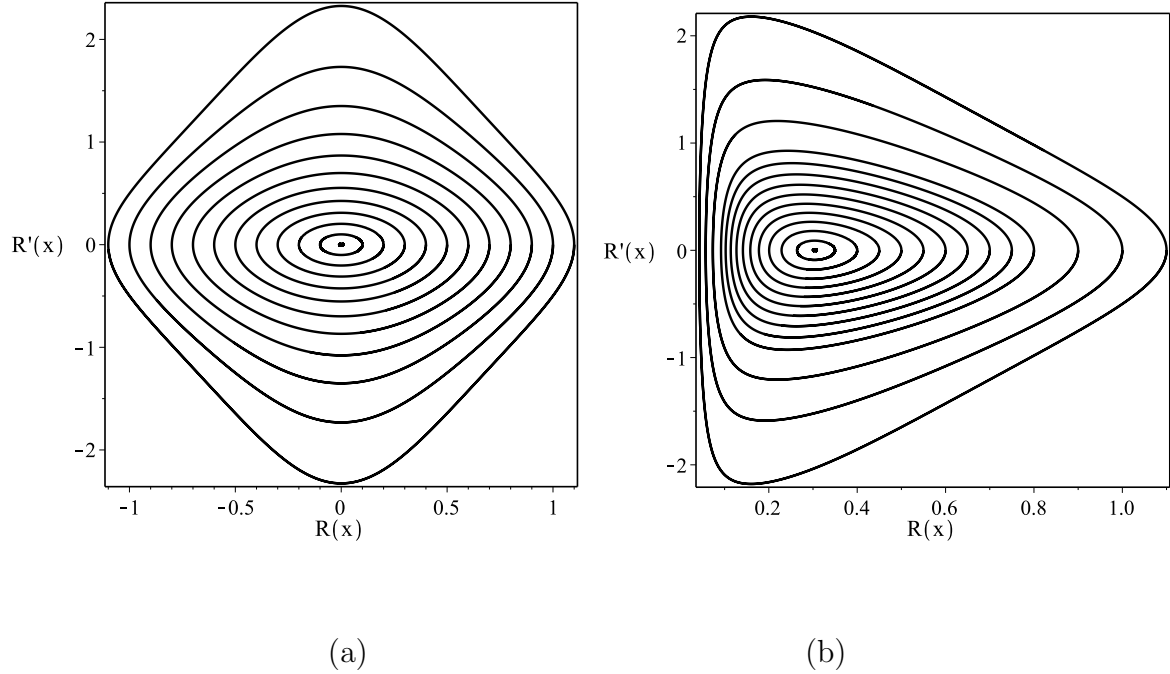
Figure 2.3: Plots of the solutions $R(x)$ to (2.34) in the phase space (R, R') when (a) $\Theta_1 = 0$, (b) $\Theta_1 = 0.1$. The helical filament corresponds to $(R, R') = (0.2517, 0)$ and gives the minimal possible values of J, namely $J = -0.8660$. The functions $R(x)$ corresponding to planar filaments are found in (a), while the functions $R(x)$ which are always positive are found in (b). This latter class of solutions corresponds to neither planar nor helical filaments; rather, such solutions correspond to generalized rotating filaments.

We should remark that it is possible to solve (2.34) implicitly by separating variables. After appropriate manipulations, such a solution can be put into the implicit form

$$x = \pm \frac{1}{2} \int_{R_*^2 - I}^{R(x)^2 - I} \frac{\xi d\xi}{\sqrt{(4 - \xi^2)(\xi + I) - \Theta_1^2 \xi^2}}. \tag{2.36}$$

This solution is not particularly enlightening, so numerical results shall be considered later for many different values of Θ_1 and I. However, this formula does give one a way to calculate the period of such a solution, assuming the upper and lower bounds on $R(x)$ are known. A period T occurs when the solution trajectory goes from R_* to R^* and then back to R_*. Since the equation (2.34) depends only on R^2 and not on R explicitly, the solution should be symmetric in the sense that exactly half of the period occurs when the trajectory goes from R_* to R^*. Therefore, we obtain the following formula for the period T of the function $R(x)$:

$$T = \int_{R_*^2 - I}^{R^{*2} - I} \frac{\xi d\xi}{\sqrt{(4 - \xi^2)(\xi + I) - \Theta_1^2 \xi^2}}. \tag{2.37}$$

We make one final interesting point before moving on to some specific cases. Recall that $\Theta'(x) = \Theta_1 R(x)^{-2}$. If $R(x)$ is periodic with period T, then so is $\Theta'(x)$. Further, one may show that the integral of a periodic function is periodic (and the period is preserved), therefore $\Theta(x)$ is periodic with period T. We then have that $\psi(x)$ is periodic whenever its amplitude $|\psi(x)|$ is periodic. This in turn implies that the filament is periodic in the space variable with respect to the y and z components, that is to say, $y(x + T, t) = y(x, t)$ and $z(x + T, t) = z(x, t)$ for all x and all t. This makes sense, as the manner of motion is rotational.

2.2.4   Small amplitude perturbations along a filament

Let us introduce the functions $\zeta = R'/R$, $\xi = \Theta'$. We obtain the coupled system

$$1 + \frac{\zeta' + \zeta^2 - \xi^2}{1 + R^2(\zeta^2 + \xi^2)} = 0\,,$$
$$\xi' + 2\zeta\xi = 0\,. \tag{2.38}$$

Assuming a small amplitude solution $|\psi| = |R| << 1$, say $|R| \approx \epsilon$ for a small parameter $\epsilon > 0$, and noting that such an assumption does not imply that ζ is small, we obtain the simpler system

$$\zeta' + \zeta^2 - \xi^2 = -1\,,$$
$$\xi' + 2\zeta\xi = 0\,. \tag{2.39}$$

We find two classes of solutions to this transformed equation. The first family of solutions is parametrized by an arbitrary constant $a \in \mathbb{R}$ and reads

$$\xi(x) = 0 \quad \text{and} \quad \zeta(x) = -\tan(x + a)\,. \tag{2.40}$$

Writing these in terms of R and Θ gives

$$R(x) = \frac{\epsilon}{\sqrt{1 + \tan^2(x + a)}} \quad \text{and} \quad \Theta(x) = \Theta_0\,. \tag{2.41}$$

The profile for the vortex filament is then

$$\mathbf{r}(x, t) = \left(x, \frac{\epsilon\cos(t - \Theta_0)}{\sqrt{1 + \tan^2(x + a)}}, -\frac{\epsilon\sin(t - \Theta_0)}{\sqrt{1 + \tan^2(x + a)}} \right)\,. \tag{2.42}$$

Note that this solution depends on three parameters: a, ϵ and Θ_0.

The second class of solutions is also parametrized by an arbitrary constant $a \in \mathbb{R}$ and is given by

$$\xi(x) = -\frac{8}{\sqrt{a^2 + 64} + a\cos(2x)} \quad \text{and} \quad \zeta(x) = -\frac{1}{2}\frac{\xi'(x)}{\xi(x)} = -\frac{a\sin(2x)}{\sqrt{a^2 + 64} + a\cos(2x)}. \quad (2.43)$$

We find

$$R(x) = \epsilon\sqrt{\sqrt{a^2 + 64} + a\cos(2x)} \quad \text{and} \quad \Theta(x) = \Theta_0 + \tan^{-1}\left(\frac{\sqrt{a^2 + 64} - a}{8}\tan(x)\right). \quad (2.44)$$

The vortex filament is then described in the asymptotic limit by the formula

$$\mathbf{r}(x,t) = \left(x, \epsilon\sqrt{\sqrt{a^2 + 64} + a\cos(2x)}\cos\left(\Theta_0 - t + \tan^{-1}\left(\frac{\sqrt{a^2 + 64} - a}{8}\tan(x)\right)\right),\right.$$
$$\left.\epsilon\sqrt{\sqrt{a^2 + 64} + a\cos(2x)}\sin\left(\Theta_0 - t + \tan^{-1}\left(\frac{\sqrt{a^2 + 64} - a}{8}\tan(x)\right)\right)\right). \quad (2.45)$$

Again, this is a three-parameter family of vortex filament solutions.

The analytical solution in the small amplitude regime given here are in good agreement with numerical solutions, which shall be discussed in the next part of the section. The first solution presented here corresponds to a rotation of the planar filament, due to the parameter Θ_0. The second solution, however, is quite distinct from this. In fact, the solution (2.45) is a hybrid of the planar and helical solutions. The amplitude effectively behaves likes a planar filament, but the phase is space-variable. This is in contrast to the planar filament, which corresponds to space-independent phase. Meanwhile, the true helical filament has a constant amplitude and a linear dependence of the phase on the space variable x. So, the solution (2.45) is distinct from each of the two simpler cases. In terms of the phase portraits

in Fig. 2.3, the family of solutions (2.41) behave like the solutions shown in Fig. 2.3(a), whereas the family of solutions (2.45) behave like those shown in Fig. 2.3(b).

2.2.5 Numerical solutions and comparison with the analytical results

In order to capture the behavior of the filaments corresponding to $w(x, t)$ with unconstrained amplitude and phase, we resort to numerical simulations of the coupled system of ordinary differential equations (2.29), obtaining numerical solutions for $R(x)$ and $\Theta(x)$. Taking the initial conditions $R(0) = R_0$, $R'(0) = 0$ gives a periodic solution for R. Note that using $R'(0) \neq 0$ does not change this fact: it simply translates the graph of R along the x-axis. Likewise, we set $\Theta(0) = \Theta_0$, $\Theta'(0) = \Theta_1$. The choice of Θ_0 is not particularly interesting; however, by varying Θ_1, we can obtain qualitatively different solutions. For $\Theta_1 = 0$, we obtain planar vortex filaments. However, as Θ_1 increases, these solutions give way to more complex solution forms which become irregular in shape. As Θ_1 increases further, the solutions become more like the regular helical solution. So, it seems that the planar vortex filaments and the helical vortex filaments are on two ends of a spectrum of solutions parametrized by Θ_1.

In Fig. 2.4, we plot the filament solutions in the Cartesian reference frame for distinct model parameters. Note that (a) and (b) depict planar filaments, while (f) depicts a perturbed helical filament. The filaments intermediate to these two are given in (c),(d) and (e). In particular, (c) demonstrates the bending of a planar filament when torsion increases.

In (d) and (e), this planar filament gradually is deformed (through appropriate choice of parameters) into a helical filament, though (d) and (e) exhibit less regularity than either a planar or a helical filament. Finally, (g),(h) and (i) demonstrate more exotic behaviors which occur at larger amplitudes. These larger-amplitude filaments likely give way to superfluid turbulence. In Fig. 2.5, we provide a cross-section in the $y - z$-plane (directed along the x-axis), so as to more clearly depict the structures present in Fig. 2.4.
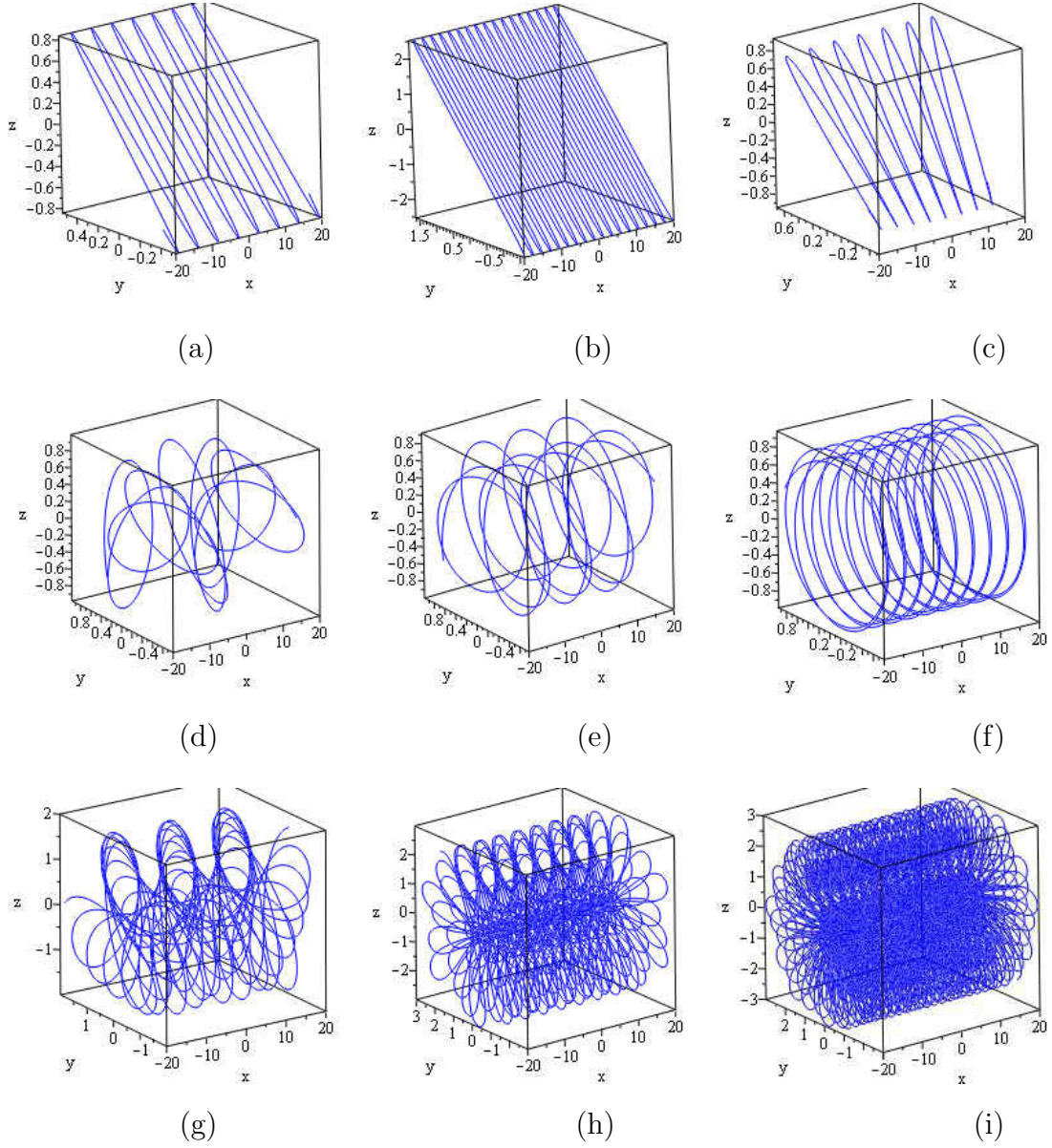
Figure 2.4: Plots of the vortex filament solutions (2.27), when $R'(0) = 0$, $\Theta(0) = 1$, and (a) $R(0) = 1$, $\Theta'(0) = 0$, (b) $R(0) = 3$, $\Theta'(0) = 0$, (c) $R(0) = 1$, $\Theta'(0) = 0.05$, (d) $R(0) = 1$, $\Theta'(0) = 0.5$, (e) $R(0) = 1$, $\Theta'(0) = 1$, (f) $R(0) = 1$, $\Theta'(0) = 2.5$, (g) $R(0) = 2$, $\Theta'(0) = 1.5$, (h) $R(0) = 3$, $\Theta'(0) = 1.5$, (i) $R(0) = 3$, $\Theta'(0) = 5$.
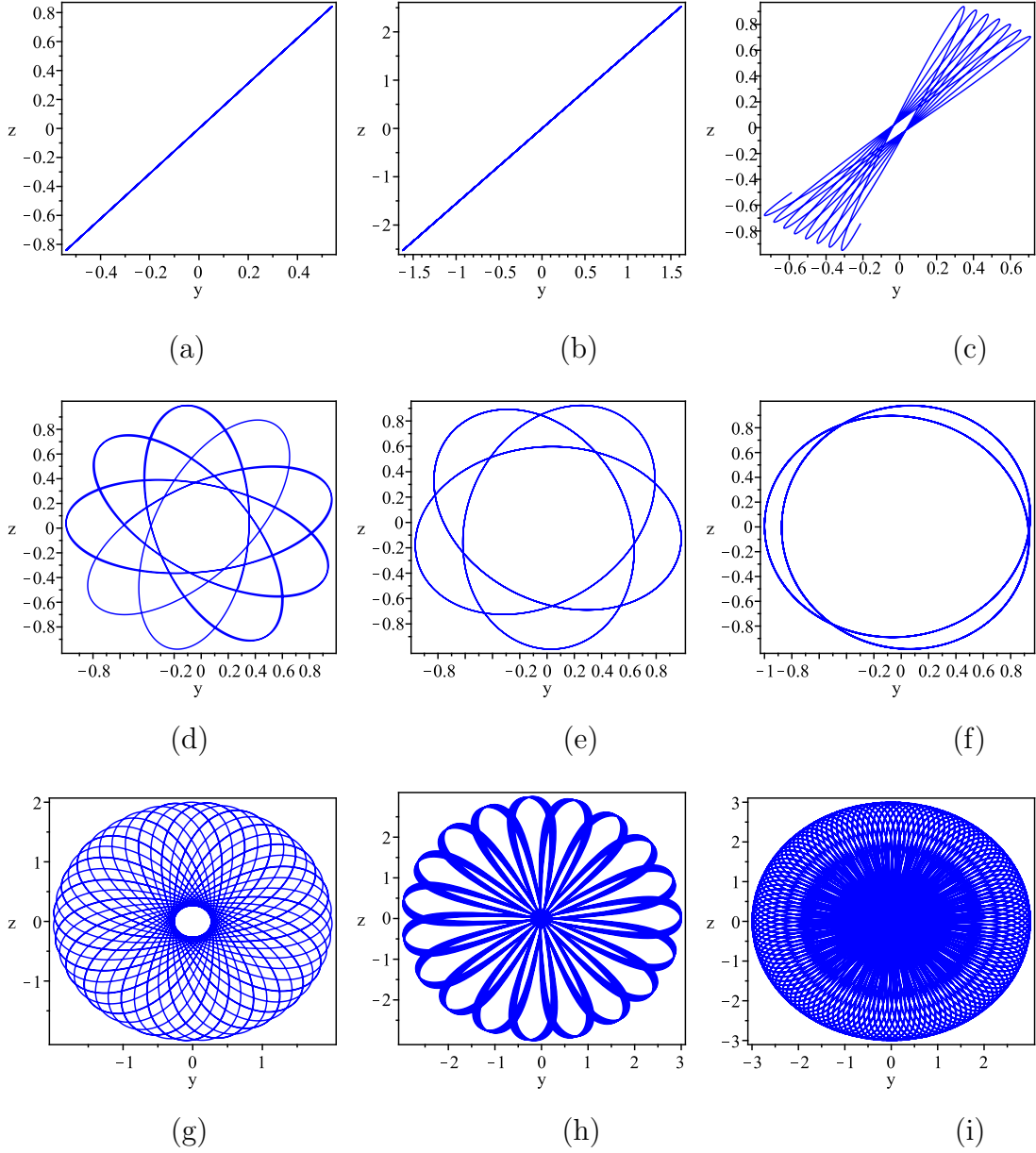
Figure 2.5: Cross sections of the vortex filament solutions (2.27) in the y-z plane, when $R'(0) = 0$, $\Theta(0) = 1$, and (a) $R(0) = 1$, $\Theta'(0) = 0$, (b) $R(0) = 3$, $\Theta'(0) = 0$, (c) $R(0) = 1$, $\Theta'(0) = 0.05$, (d) $R(0) = 1$, $\Theta'(0) = 0.5$, (e) $R(0) = 1$, $\Theta'(0) = 1$, (f) $R(0) = 1$, $\Theta'(0) = 2.5$, (g) $R(0) = 2$, $\Theta'(0) = 1.5$, (h) $R(0) = 3$, $\Theta'(0) = 1.5$, (i) $R(0) = 3$, $\Theta'(0) = 5$. Though the three-dimensional plots of the filaments in Fig. 2.4 may appear unstructured in some cases, this view directed along the x-axis shows that all solutions exhibit at least some symmetry.

The numerical solution in the first panel is a planar vortex filament, with ψ real-valued. Increasing Θ_1, we find that the phase $\Theta(x)$ becomes increasingly linear, although periodic oscillations appear added to this linear trend. These oscillations are smoothed as Θ_1 increases further. As Θ_1 increases, and $\Theta(x)$ exhibits more of a linear trend, the solutions take on the form of helical filaments. For the pure helical filament, $R(x) = R_0$ for all x, i.e. the amplitude is constant. As both amplitude and phase increase in value, the pure helical structure gives way to a filament which creates more intricate shapes. While the structures appear nearly chaotic, they actually are ordered, and exhibit certain symmetries.

The numerical results shown in panels (c) and (d) of 2.4, corresponding to those solutions which lie in between the planar and helical filaments, show clear agreement with the small amplitude results of the previous subsection, namely the small amplitude solution (2.45). For this solution, the modulus of the potential function, $|R(x)|$, is strictly positive yet periodic, while the phase, $\Theta(x)$, is increasing yet exhibits an oscillatory behavior about a linear trend. Indeed, from the small amplitude solution (2.45), it is clear that the amplitude satisfies

$$0 < \epsilon\sqrt{\sqrt{a^2 + 64} - a} \leq R(x) \leq \epsilon\sqrt{\sqrt{a^2 + 64} + a}\,. \tag{2.46}$$

This is in contrast to the planar filament, which changes signs on each period. Regarding the phase, from (2.45) we have that

$$\Theta_1 = \frac{\sqrt{a^2 + 64} - a}{8} \quad \text{or} \quad a = \frac{4(1 - \Theta_1^2)}{\Theta_1}\,. \tag{2.47}$$

Hence, the arbitrary constant a in (2.45) is determined uniquely by the value of the parameter Θ_1. If we expand $\Theta(x)$ found in (2.45) in a Taylor series in x, and make use of (2.47), we find

$$\Theta(x) = \Theta_0 + \Theta_1 x + \Theta_1(1 - \Theta_1^2)\left\{\frac{x^3}{3} + \frac{2 - 3\Theta_1^2}{15}x^5 + O(x^7)\right\}. \qquad (2.48)$$

So, in the small amplitude case, $\Theta_1 = 0$ corresponds exactly to the planar filament ($\Theta(x) = \Theta_0$), while $\Theta_1 = 1$ corresponds to a helical case ($\Theta(x) = \Theta_0 + x$). For $0 < \Theta_1 < 1$, we obtain the intermediate solutions shown numerically in parts (c)-(d) of Figs. 2.4-2.5.

When ψ takes the form of an amplitude function with constant phase, $\psi(x) = R(x)e^{-i\kappa}$, we obtain the planar vortex filament, along the lines studied by Hasimoto and others [41, 49, 50, 105]. If the initial conditions for this type of solution are varied, we see that the filaments will twist with increasing x (this is best seen in Fig. 2.4(c) and Fig. 2.5(c)). We begin to see the emergence of solutions which are intermediate to the purely planar filaments (which rotate along the reference axis, yet remain on a plane) and the helical filaments (which form a rotating helical structure about the reference axis). Hence, the solution shown in Fig. 2.4(c) is a deformation of the Hasimoto solution to the LIA. This twisted planar filament is deformed further due to additional variations in the initial data, and it eventually becomes more helical in appearance.

When ψ is a simple complex exponential ($\psi(x) = Ae^{-i\kappa x}$), we obtain filaments that form a helix about the reference axis. This helix rotates in a cork-screw manner as time increases. Such solutions were previously considered in the low temperature limit by Sonin [89]. If such a ψ is perturbed, we obtain a nearly helical filament which has been deformed

in a manner which changes the periodicity of the filament in space. Such filaments are seen in the cross-section provided in Fig. 2.5 (d), (e) and (f). In particular, Fig. 2.4(f) represents a helical filament under a slight perturbation. In contrast, Figs. 2.5(e) and (d) demonstrate progressively greater deviations from the helical filament.

For larger amplitudes or sufficiently large initial change in in the phase of ψ, we obtain solutions that become far more complicated in form. While many of these types of solutions, as shown in Fig. 2.4(g), (h), and (i), appear almost chaotic in form, the corresponding cross-sections in Fig. 2.5 demonstrate that these solutions do exhibit order. Of course, unlike the planar or helical filaments, which have the possibility of being robust and maintaining their form in the face of structural perturbations, it is not likely that some of these more complicated structures would persist. More likely, vortex filaments with initial profiles matching some of these more complicated forms would likely give way to more complicated turbulence and reconnection events, due to excessive bending of the thin vortex. In this regime, non-local effects from the full Biot-Savart law (2.13) are likely to be needed.

2.2.6 Discussion

Physically, our results correspond to rotating vortex filaments which are open (the filaments do not cross) and remain within a finite distance from the reference axis. By varying two parameters, we have shown that there are essentially four classes of solutions. The most tame are planar and helical vortex filaments, and which can be exactly described analytically. Note

that the planar filament is the unique filament with space-variable curvature and zero torsion, while the pure helical filament has constant curvature and variable torsion. Intermediate to these two types of filaments are a class of solutions which merge properties of both types of filaments, and are essentially irregular helical filaments. These irregular helical filaments have variable curvature and torsion, which makes them much more complicated to solve analytically. In the small-amplitude regime, such filaments are approximated by the expression (2.45). Overall, these filaments are rather well-behaved and appear likely to persist.

Meanwhile, the fourth class of solutions occur at larger amplitudes or for more sharp increases of the phase of the stationary solutions. These solutions are more complicated and must be obtained numerically, since perturbation results are not useful in the intermediate amplitude regime. Some of these solutions are highlighted in Fig. 2.4 (g),(h),(i). While the solutions may appear disordered or chaotic, they actually do exhibit a form of regularity, as see by inspecting Fig. 2.5. Such solutions give us insight into the transition to strong turbulence in the Svistunov model we have considered here. Since the LIA approximates such turbulence, the cost is that such solutions exhibit far more regularity than might be expected. That said, these structures appear too intricate to persist in the case of superfluid friction (such as that included in the Hall-Vinen model), and these filaments would likely give way to turbulence in experiments. These filaments would also be likely candidates for single-filament reconnection events. This would occur when the vortex filament curves sharply, breaks, and the reconnects elsewhere along the filament. Of course, in terms of mathematics, such a

41

solution would not be well-defined (it would be multivalued). To overcome this, one can introduce an alternate scaling $\mathbf{r}(x, t) = (f(x), y(x, t), z(x, t))$. Picking f appropriately, one could obtain solutions along a curve as opposed to a straight line, which would permit a description of the intersecting filament solutions. This was considered for planar filaments perturbatively in [105].

In addition to being useful for the study of the zero temperature limit of superfluid turbulence, the solutions to the 2D LIA (both analytical and numerical) are useful as a baseline of comparison for more complicated models. One such model is the full Biot-Savart law (2.13), which is complicated enough to mandate numerical solutions alone. Of course, the full Biot-Savart model of self-induced motion is non-local, whereas the LIA is a local model. As has previously been discussed, the LIA is most useful (and, in most agreement with the Biot-Savart law) in the case of strong turbulence. For weak turbulence [17], the LIA is much less useful, and other models may be considered, such as a truncated LIA that permits resonant wave interactions which are not present in the simplified LIA model [17]. Understanding the time evolution of a vortex filament solution to the 2D LIA is also useful in that such a solution serves as a baseline of comparison for solution to the more complicated models which include superfluid friction parameters. Indeed, for $1 >> \alpha > \alpha' > 0$, the solutions can be viewed as perturbations to the solutions presented here (at least in the rotating filament case).

Regarding other reference fames, since the motion of a self-induced vortex filament is often described in terms of curvature and torsion, we shall note how to recover these quan-

tities from the Cartesian representation here. Using the Cartesian representation $\mathbf{r}(x,t) = (x, R(x)\cos(\Theta(x) - t), R(x)\sin(\Theta(x) - t))$, one can obtain the curvature at a point $\mathcal{C}(x,t)$ and the torsion at a point $\mathcal{T}(x,t)$ using the standard formulas

$$\mathcal{C}(x,t) = \frac{|\mathbf{r}_x \times \mathbf{r}_{xx}|}{|\mathbf{r}_x|^3} \quad \text{and} \quad \mathcal{T}(x,t) = \frac{(\mathbf{r}_x \times \mathbf{r}_{xx}) \cdot \mathbf{r}_{xxx}}{|\mathbf{r}_x \times \mathbf{r}_{xx}|^2}. \tag{2.49}$$

While these expressions are rather complicated for arbitrary R and Θ, let us consider the special cases of planar and helical filaments. For the planar filament, $\Theta(x) = \Theta_0$, a constant, so we find

$$\mathcal{C}(x,t) = \frac{|R''(x)|}{(1 + R'^2)^{3/2}} \quad \text{and} \quad \mathcal{T}(x,t) = 0. \tag{2.50}$$

This is in agreement with what we know of the planar filament, in that it has zero torsion. As mentioned above, the deformation of the planar filament (obtained by perturbing the condition $\Theta(x) = \Theta_0$ so that $\Theta(x)$ has a small x-dependent contribution) twists the filament, resulting in non-zero torsion. On the other hand, if instead we assume $R(x) = R_0$, the constant amplitude solution results in

$$\mathcal{C}(x,t) = \frac{\sqrt{R_0^4\Theta'^6 + R_0^2\Theta'^4 + R_0^2\Theta''^2}}{\left(1 + R_0^2\Theta'^2\right)^{3/2}}, \tag{2.51}$$

$$\mathcal{T}(x,t) = \frac{\Theta'^5 + 3\Theta'\Theta''^2 - \Theta'^2\Theta'''}{R_0^2\Theta'^6 + \Theta'^4 + \Theta''^2}\cos(\Theta(x) - t) - \frac{\Theta''(2\Theta'^3 + \Theta''')}{R_0^2\Theta'^6 + \Theta'^4 + \Theta''^2}\sin(\Theta(x) - t). \tag{2.52}$$

In the case of a purely helical filament, $\Theta(x) = \kappa x$, and we have

$$\mathcal{C}(x,t) = \frac{R_0 k^2}{1 + R_0^2 k^2} \quad \text{and} \quad \mathcal{T}(x,t) = \frac{k}{1 + R_0^2 k^2}\cos(kx - t). \tag{2.53}$$

We see that the purely helical filament has positive constant curvature. Torsion varies depending on both x and t in a manner consistent with a helical curve.

It has been suggested [57] that chaos is possible in some parameter regimes for the full HVBK model (including superfluid friction parameters). While this was for self-similar solutions, the same comment could of course be made for the HVBK model without the self-similarity restriction. Then, once the superfluid friction parameters are included (in the "warmer" temperature regime of about 1K), it is possible that the larger amplitude solutions here would give way to chaos. In principle, for small α and α', the full HVBK model is a perturbation of the low-temperature LIA considered here. It would make sense, then, to consider a perturbation to the larger amplitude solutions, to account for α and α', to first order. Such an analysis would cast light onto the stability of such solutions under small perturbations. Such small perturbations would likely either:

(i) cause instabilities that would grow into turbulence, or

(ii) case decay of the filament due to the drag terms.

In other words, we might expect the rotating filaments discussed here to either degenerate into a turbulent regime (non-integrable turbulence, more precisely) or to slowly decay into a line filament (so that small perturbations along the filament die off as time grows). This is a promising area of future work.

2.3 Exact solution for the self-induced motion of a vortex filament in the arclength representation of the LIA

We review two formulations of the fully nonlinear local induction equation approximating the self-induced motion of the vortex filament (in the local induction approximation), corresponding to the Cartesian and arclength coordinate systems, respectively. The arclength representation, put forth by Umeki, results in a type of $1+1$ derivative nonlinear Schrödinger (NLS) equation describing the motion of such a vortex filament. We obtain exact stationary solutions to this derivative NLS equation; such exact solutions are a rarity. These solutions are periodic in space and we determine the nonlinear dependence of the period on the amplitude. The results here were obtained in the reference Van Gorder [100].

2.3.1 Background

While solutions under various approximations to the LIA are indeed useful for certain applications, the study of the fully nonlinear equations governing the self-induced motion of a vortex filament in the LIA is itself with merit. The fully nonlinear equation governing the self-induced motion of a vortex filament in the LIA was previously derived in Van Gorder [98, 99] in the Cartesian coordinate space. To this end, consider the vortex filament essentially aligned along the x-axis: $\mathbf{r} = x\mathbf{i}_x + y(x,t)\mathbf{i}_y + z(x,t)\mathbf{i}_z$. We then have that

$$\mathbf{t} = \frac{d\mathbf{r}}{ds} = \frac{d\mathbf{r}}{dx}\frac{dx}{ds} = (\mathbf{i}_x + y_x\mathbf{i}_y + z_x\mathbf{i}_z)\frac{dx}{ds} \qquad (2.54)$$

and $\mathbf{v} = y_t \mathbf{i}_y + z_t \mathbf{i}_z$, where $\frac{dx}{ds} = 1/\sqrt{1 + y_x^2 + z_x^2}$. From the governing equation $\mathbf{v} = \gamma \kappa \mathbf{t} \times \mathbf{n}$, we compute the quantities

$$
\begin{aligned}
y_t &= -\gamma z_{xx} \left(\frac{dx}{ds} \right)^3 = -\gamma z_{xx} \left(1 + y_x^2 + z_x^2 \right)^{-3/2} , \\
z_t &= \gamma y_{xx} \left(\frac{dx}{ds} \right)^3 = \gamma y_{xx} \left(1 + y_x^2 + z_x^2 \right)^{-3/2} ,
\end{aligned}
\tag{2.55}
$$

and, upon defining $\Phi(x,t) = y(x,t) + iz(x,t)$, it was shown in Van Gorder [99] that the coupled system of real partial differential equations (2.55) reduces to the single complex partial differential equation

$$
i\Phi_t + \gamma \left(1 + |\Phi_x|^2 \right)^{-3/2} \Phi_{xx} = 0 .
\tag{2.56}
$$

Dmitriyev [26] considered the approximation $i\Phi + \gamma \Phi_{xx} = 0$, while Shivamoggi and van Heijst [84] considered a quadratic approximation to the nonlinearity in (2.56). The full nonlinear equation was obtained in [98]. In order to recover y and z once a solution Φ to (2.56) is known, note that $y = \mathcal{R}e\ \Phi$ and $z = \mathcal{I}m\ \Phi$. Some mathematical properties of equation (2.56) were discussed in Van Gorder [99] in the case where periodic stationary solutions are possible, though a systematic study of all such stationary solutions was not considered. Spatially-periodic solutions (2.56) were shown to be governed by an implicit relation involving the sum of elliptic integrals of differing kinds. The amplitude of such periodic solutions was shown to obey $|\psi| < \sqrt{2}$.

The formulation (2.56), corresponding to the Cartesian coordinate system, is one possible way to describe the fully nonlinear self-induced motion of a vortex filament in the LIA. Umeki [95] obtained an alternate formulation, applying an arclength-based coordinate

46

system as opposed to a Cartesian coordinate system. Umeki defines $\mathbf{r} = \mathbf{t} \times \mathbf{t}_s$, where s is the arclength element. Now, $\mathbf{t}_t = \mathbf{t} \times \mathbf{t}_{ss}$. Let us write $\mathbf{t} = (\tau_x, \tau_y, \tau_z)$. Then Umeki defines the complex field v by

$$\tau_x + i\tau_y = \frac{2v}{1 + |v|^2}, \qquad \tau_z = \frac{1 - |v|^2}{1 + |v|^2}. \tag{2.57}$$

The relation $\mathbf{t}_t = \mathbf{t} \times \mathbf{t}_{ss}$ then implies

$$(\tau_x + i\tau_y)_t = i\left((\tau_x + i\tau_y)_{ss}\tau_z - (\tau_x + i\tau_y)\tau_{zss}\right), \tag{2.58}$$

$$2\tau_{zt} = i\left((\tau_x^* + i\tau_y^*)_{ss}(\tau_x + i\tau_y) - (\tau_x^* + i\tau_y^*)(\tau_x + i\tau_y)_{ss}\right). \tag{2.59}$$

From here, Umeki [95] then found

$$iv_t + v_{ss} - 2v^* v_s^2/(1 + |v|^2) = 0, \tag{2.60}$$

where v denotes directly the tangential vector of the filament. While the Cartesian and arc-length formulations are obtained through different derivations, both formulations are equivalent to the localized induction equation (LIE). Umeki [96] showed that there exists a transformation between solutions to (2.56) and solutions to (2.60). A plane wave solution to (2.60) exists [96], and Umeki [96] was also able to show that the famous 1-soliton solution of Hasimoto [42] is given by

$$v(s, t) = \frac{\nu \operatorname{sech}(k(s - ct))}{\nu \operatorname{sech}^2(k(s - ct)) - 2}\left(\tanh(k(s - ct)) - \frac{ic}{2k}\right), \tag{2.61}$$

$\nu = 2k^2/(4k^2 + c^2)$, $0 < \nu < 1/2$ in the arclength representation.

2.3.2 Stationary solutions

We now turn our attention to obtaining stationary solutions, which has not been done for the local induction equation in the arclength representation. Let us consider the ansatz

$$v(s,t) = e^{-i\alpha^2 t} q(\alpha s) \,, \tag{2.62}$$

where q is assumed to be a real-valued function, which puts (2.60) into the form

$$q + q_{ss} - \frac{2qq_s^2}{1+q^2} = 0 \,. \tag{2.63}$$

Hence, the solution (2.62) is invariant under $\alpha \in \mathbb{R}$, so without loss of generality we shall consider $\alpha = 1$ henceforth. We should remark that a factor of $e^{+i\alpha^2 t}$ in (2.62) results in unstable solutions, so the '$-$' case in the exponent is what we limit our attention to. Also note that (2.63) is essentially a nonlinear oscillator provided $2q_s^2 < 1 + q^2$.

Our goal is to obtain an exact solution for (2.63), and defining a conserved quantity will greatly help in constructing a second integral. To this end, let us define the quantity

$$E = -\frac{q_s^2 - q^2 - 1}{(1+q^2)^2} \,, \tag{2.64}$$

$E \in (0,1)$. Observe that the quantity is conserved:

$$\frac{dE}{ds} = -\frac{2q_s}{(1+q^2)} \left(q + q_{ss} - \frac{2qq_s^2}{1+q^2} \right) = 0 \,. \tag{2.65}$$

For a fixed value of E, we find that

$$q_s^2 = (1+q^2) \left(1 - (1+q^2)E \right) \,, \tag{2.66}$$

48

and, upon separating variables,

$$\int_{q_0}^{q} \frac{d\xi}{\sqrt{(1+\xi^2)\,(1-(1+\xi^2)E)}} = \pm(s - s_0)\,, \tag{2.67}$$

where $q_0 = q(s_0)$ is a second arbitrary constant. Performing the required integration, we obtain the expression

$$\frac{1}{\sqrt{E}} F\left(\frac{\sqrt{E}}{\sqrt{1-E}}q, \frac{\sqrt{1-E}}{\sqrt{E}}i\right) = \pm(s - \hat{s})\,, \tag{2.68}$$

where $\hat{s}$ is a constant involving s_0 and q_0. Here, F is the elliptic integral of the first kind.

Inverting (2.68) to obtain $q(s)$, we find that

$$q(s) = \frac{\sqrt{1-E}}{\sqrt{E}} \operatorname{sn}\left(\pm\sqrt{E}(s - \hat{s}), \frac{\sqrt{1-E}}{\sqrt{E}}i\right)\,, \tag{2.69}$$

where $\operatorname{sn}(a,b)$ denotes the Jacobi elliptic function. While (2.69) is a closed form expression, it involves the conserved quantity E, which is perhaps not so satisfying. Note that the amplitude of q may be found from (2.66); setting $q_s = 0$, we find that the amplitude $A = A(E)$ is given by

$$A = \max_s |q(s)| = \frac{\sqrt{1-E}}{\sqrt{E}}\,. \tag{2.70}$$

It follows that $E = 1/(1 + A^2)$, hence (2.69) becomes

$$q(s) = A \operatorname{sn}\left(\pm\frac{1}{\sqrt{1+A^2}}(s - \hat{s}), Ai\right)\,. \tag{2.71}$$

With this we have obtained an exact stationary solution $q(s)$ in terms of amplitude A. In Fig. 2.6 we plot the phase portrait for q versus q_s, which demonstrates the exact periodic solutions. In Fig. 2.7, we display solution profiles for various values of the amplitude A.

49
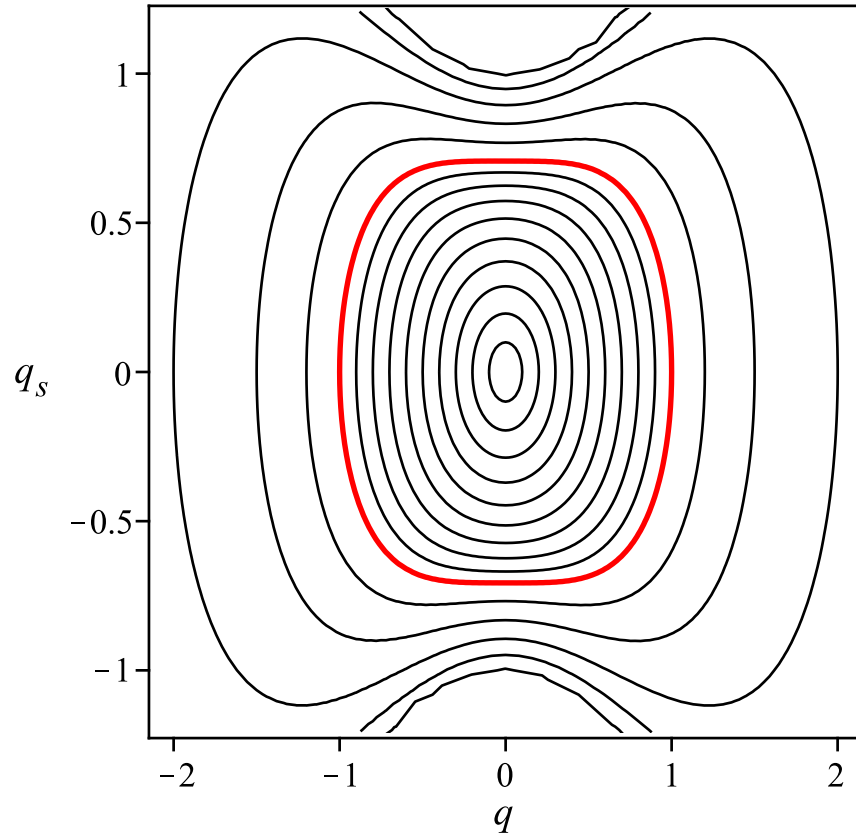
Figure 2.6: Phase portrait in (q, q_s) for the solution to the fully nonlinear oscillator equation modelling the local induction equation under the arclength representation.
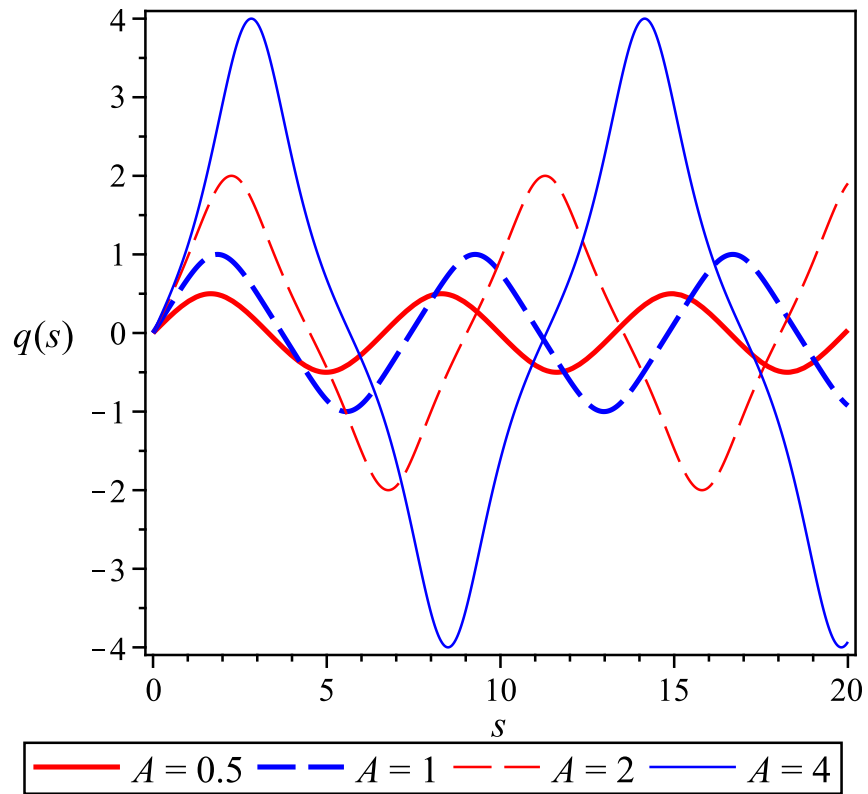
Figure 2.7: Plots of the solution $q(s)$ given in (2.71) for various values of the amplitude A. Note that the period of the solutions is strongly influenced by the amplitude. The nonlinear dependence of the period T with the amplitude A is shown graphically in Fig. 2.8.

We should remark that in the Cartesian case, solutions to models which are low-order approximations to the fully nonlinear model agree well for small amplitudes, and we expect the same will hold here (though we omit the details of any approximating models here).

A similar exact solution was obtained by Hasimoto [41], through a different derivation, for a two-dimensional model (recall that our model is three-dimensions). Hasimoto's derivation started with $\mathbf{v} = Y\mathbf{i}_y$, as opposed to $\mathbf{v} = y_t\mathbf{i}_y + z_t\mathbf{i}_z$. Assuming a stationary solution, Hasimoto's assumption leads to an equation $Y_{xx} + \frac{\Omega}{\gamma}\left(1 + Y_x^2\right)^{3/2} Y = 0$. Hasimoto finds a solution $Y = A\mathrm{cn}(\xi, k)$ (where $x = x(\xi)$, ξ is a parametrization linking Y and x implicitly), which has initial conditions $Y(0, k) = A$ and $Y'(0) = 0$. Hence, Hasimoto's solution for the two-dimensional problem is a direct analogy to the solution for the three-dimensional problem we've found here under the arclength representation.

Observe the nonlinear dependence of the period on the amplitude. From this exact relation, we see that the period $T = T(A)$ obeys the relation

$$
\begin{aligned}
T(A) &= 4\sqrt{1 + A^2} \int_0^{\frac{\pi}{2}} \frac{d\theta}{\sqrt{1 + A^2\sin^2\theta}} \\
&= 4K\left(\frac{A}{\sqrt{1 + A^2}}\right),
\end{aligned}
\tag{2.72}
$$

where K is the elliptic quarter period. Recalling the asymptotic expansion

$$
K(m) \approx \frac{\pi}{2} + \frac{\pi}{8}\frac{m^2}{1 - m^2} - \frac{\pi}{16}\frac{m^4}{1 - m^2}
\tag{2.73}
$$

which is a good approximation for $m < 1/2$, we have

$$
T(A) \approx 2\pi + \frac{\pi}{2}A^2 - \frac{\pi}{4}\frac{A^4}{1 + A^2},
\tag{2.74}
$$

52

which in turn is a good approximation for the small-amplitude regime $A < 1/\sqrt{3}$. The large amplitude asymptotics are slightly less standard. For $m > 2$, there exists an accurate asymptotic expansion

$$4K\left(1 - \frac{1}{m}\right) \approx J(m), \tag{2.75}$$

where

$$\begin{aligned} J(m) =& 4\left(1 + \frac{1}{m} + \frac{5}{16m^2} + \frac{7}{32m^3}\right)\ln\left(2\sqrt{2m}\right) \\ & - \left(\frac{1}{m} + \frac{7}{8m^2} + \frac{17}{24m^3}\right). \end{aligned} \tag{2.76}$$

When $m > 2$, the argument of K is less than or equal to $1/2$. Thus,

$$T(A) \approx J\left(\frac{\sqrt{1 + A^2}}{\sqrt{1 + A^2} - A}\right) \tag{2.77}$$

is a good approximation for $A > 1/\sqrt{3}$.

In Fig. 2.8, we plot the the period $T(A)$ of the solution (2.71) versus the amplitude A. The approximate asymptotic solutions are also included in their valid regions. Then, in Fig. 2.9, we plot the relative error in these approximations, showing the agreement between the exact and asymptotic solutions. For the $A > 1/\sqrt{3}$ asymptotics, only retaining the logarithmic term (as a lowest order approximation) is not completely sufficient, as demonstrated in Fig. 2.9.
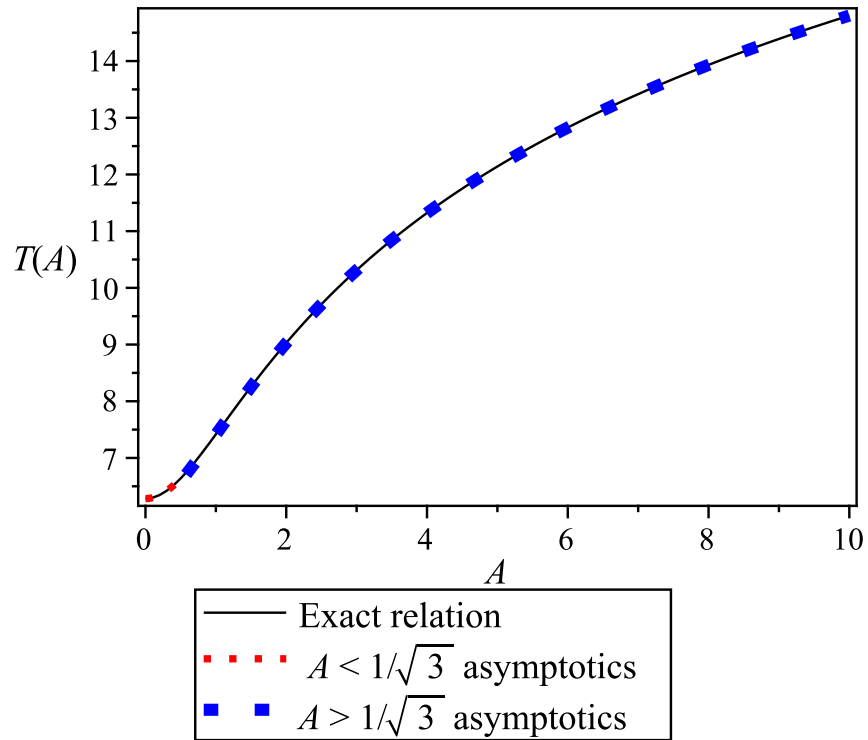
Figure 2.8: Plot of the period $T(A)$ of the solution (2.71) versus the amplitude A. The exact relation is found by numerically plotting (2.72). Note that both the $A < 1/\sqrt{3}$ and $A > 1/\sqrt{3}$ asymptotic expansions are excellent fits to the exact relation.
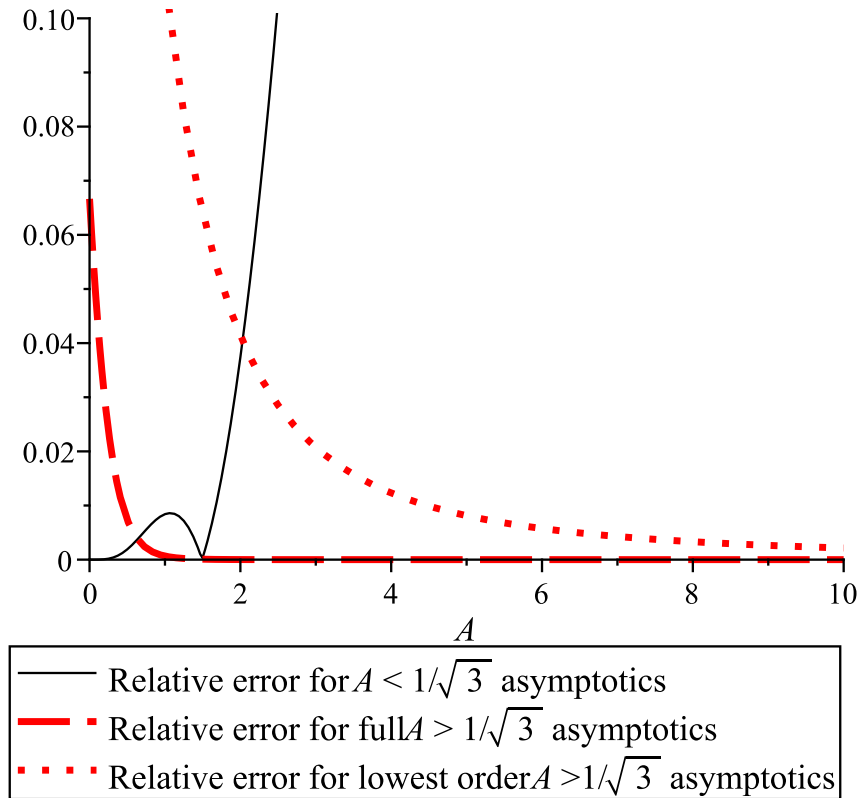
Figure 2.9: Relative error $|T(A) - T_{\text{approx}}|/|T(A)|$ of the approximations to $T(A)$. We also include the lowest order approximation $T(A) \approx 4\ln(2\sqrt{2m})$ for the $A > 1/\sqrt{3}$ case. We see the good agreement with the $A < 1/\sqrt{3}$ asymptotics and $A > 1/\sqrt{3}$ asymptotics where needed.

55

2.3.3 Discussion

We have found an exact stationary solution for the self-induced motion of a vortex filament in the arclength representation of the LIA. Such a formula is interesting in both its simplicity and its potential applications. Note that this representation is simpler than that found in the Cartesian representation; in particular, the integral representation permits a clean inversion so that we may obtain solutions in the form (2.71). In the Cartesian case, however, the solutions were defined implicitly by a linear combination of elliptic integrals, which was then inverted numerically. Umeki [96] gives a relation between the arclength and Cartesian representations which can be used to map the arclength formula into a formula for the Cartesian representation. This involves complicated mathematical expressions and we omit the details of this inversion here.

2.4   Exact stationary solution method for the Wadati-Konno-Ichikawa-Shimizu (WKIS) equation

We consider a method of obtaining exact implicit relations governing stationary solutions to the Wadati-Konno-Ichikawa-Shimizu (WKIS) equation. After a suitable transform, we put the WKIS equation into the form of a nonlinear ordinary differential equation. This equation has exact first and second integrals of motion. From this second integral, the exact equation governing the stationary solution to the WKIS equation is obtained. This relation

may easily be inverted and plotted, to give the exact solution profiles. Furthermore, an exact formula for the period of oscillation in terms of the model parameters is obtained. The results presented in this section were considered in Van Gorder [101].

2.4.1 Background

The Wadati-Konno-Ichikawa-Shimizu (WKIS) equation [35]-[20] reads

$$iu_t + \left(\frac{u}{\sqrt{1 + |u|^2}} \right)_{xx} = 0. \tag{2.78}$$

Wadati, et al. [118] proposed a new scheme of the inverse scattering method, and applied it, for example, to a type of derivative NSL. Shimizu and Wadati [82] extended this and proposed a new integrable nonlinear evolution equation.

While the WKIS equation is an interesting integrable equation with desireable properties, it has not been frequently studied in the literature. Lakshmanan and Ganesan [53] showed that a generalized version of Hirota's equation with linear inhomogeneities is equivalent to a generalized continuum Heisenberg ferromagnetic spin chain equation as well as to a generalized WKIS-type equation. They showed this using both geometrical and gauge methods. Then, Lakshmanan and Ganesan [54] considered the equivalence of generalized versions of these equations through a moving helical space curve formalism and stereographic representation. The scattering problem was considered and it was shown that an infinite number of constants of motion can exist for these systems. Boiti, et al. [19] also consid-

ered the spectral problem of the WKIS equation and certain nonlinear evolution equations related to it. The Bäcklund transformations (BTs) together with the completeness relations of the eigenfunctions of the relevant generating operators were found. The elementary BTs were found and it was shown that they can be cast into a form similar to that found by Darboux for the Schrödinger spectral problem. The nonlinear superposition formulae are also explicitly written. Ying, et al. [122] studied the nonlinearization of spectral problems of the WKIS equation and presented its integrable decomposition.

In the present section, we shall study stationary solutions to the WKIS equation. First, we derive a first integral governing the spatial part of the stationary solution. Then, for certain parametric values, we show that the WKIS equation admits a closed-form implicit representation for the stationary solution. In a subset of this parameter regime, we are able to demonstrate the existence of periodic solutions in the space variable of the form $u(x,t) = e^{-ikt}\psi(x)$. It is worthwhile to note that this was done recently for two equations arising in vortex dynamics [99, 100] to which the WKIS equation is similar. Finally, we provide an alternate formulation of the first integral of the WKIS equation, which nicely demonstrates the oscillatory nature of these periodic solutions. The period, which depends nonlinearly on the model parameters, may be computed in an exact manner.

2.4.2 Stationary solutions

Let us assume a stationary solution of the form

$$u(x,t) = e^{-ikt}\psi(x),\tag{2.79}$$

where $\psi(x)$ is a real field. We shall assume $k \neq 0$. When $k = 0$, we obtain the trivial solution

$$\psi(x) = \frac{Ax + b}{\sqrt{1 - (Ax + b)^2}}.\tag{2.80}$$

When $k \neq 0$, we obtain the ordinary differential equation

$$k\psi + \left(\frac{\psi}{\sqrt{1 + \psi^2}}\right)'' = 0.\tag{2.81}$$

Equation (2.81) is integrable, though it may be hard to see from this form. Let us define a new dependent variable ϕ by

$$\phi(x) = \frac{\psi(x)}{\sqrt{1 + \psi(x)^2}}.\tag{2.82}$$

Note that $-1 < \phi(x) < 1$ for all x. Then, (2.81) is put into the form

$$\phi'' + \frac{k\phi}{\sqrt{1 - \phi^2}} = 0.\tag{2.83}$$

Multiplying by $2\phi'$ and performing one integration, we find that (2.83) becomes

$$\phi'^2 - 2k\sqrt{1 - \phi^2} = 2kI,\tag{2.84}$$

where $I \in \mathbb{R}$ is a constant. We have taken the arbitrary constant of integration to take the form $2kI$ as it will lead to later simplifications in the solution form. Solving for ϕ', we find that

$$\phi' = \pm\sqrt{2k\sqrt{1 - \phi^2} + 2kI}.\tag{2.85}$$

Then, separating variables, we obtain the implicit integral relation

$$\int_{\phi_0}^{\phi} \frac{d\xi}{\sqrt{2k\sqrt{1-\xi^2}+2kI}} = \pm(x-x_0)\,, \tag{2.86}$$

which fixes ϕ. Here, $\phi_0 = \phi(x_0)$ is a second arbitrary constant. Let us make the change of variable $\nu = \sqrt{1-\xi^2}$. Then,

$$\pm(x-x_0) = -\int_{\sqrt{1-\phi_0^2}}^{\sqrt{1-\phi^2}} \frac{\nu d\nu}{\sqrt{(1-\nu^2)(2k\nu+2kI)}} = \chi(\phi)\,. \tag{2.87}$$

Note that (2.83) is a dynamical problem

$$\phi'' = -\frac{d}{d\phi}U(\phi)\,, \tag{2.88}$$

with potential $U(\phi) = -k\sqrt{1-\phi^2}$. Then, under the assumption of an oscillating solution ϕ, we require the kinetic energy kI to satisfy $\min\{U\} < kI < 0$, i.e., $-k < kI < 0$. With $k > 0$, the constant of motion I satisfies $-1 < I < 0$.

From (2.87), we have (for $-1 < I < 0$)

$$\begin{aligned}
\chi(\phi) =& i\sqrt{\frac{2(I+1)}{k}}E\left(\frac{\sqrt{I+\sqrt{1-\phi^2}}}{I-1}, \frac{\sqrt{I^2-1}}{I+1}\right) \\
& - i\sqrt{\frac{2}{k(I+1)}}F\left(\frac{\sqrt{I+\sqrt{1-\phi^2}}}{I-1}, \frac{\sqrt{I^2-1}}{I+1}\right)\,,
\end{aligned} \tag{2.89}$$

where F and E are elliptic integrals of the first and second kind, respectively. The solution $\phi(x)$ is then governed by the implicit relation

$$\begin{aligned}
\pm i\sqrt{\frac{k}{2}}(x-\hat{x}) =& \sqrt{I+1}E\left(\frac{\sqrt{I+\sqrt{1-\phi^2}}}{I-1}, \frac{\sqrt{I^2-1}}{I+1}\right) \\
& - \frac{1}{\sqrt{I+1}}F\left(\frac{\sqrt{I+\sqrt{1-\phi^2}}}{I-1}, \frac{\sqrt{I^2-1}}{I+1}\right)\,.
\end{aligned} \tag{2.90}$$

We may convert the explicit relation (2.90) back into a relation for ψ. Note that

$$\sqrt{I + \sqrt{1 - \phi^2}} = \sqrt{I + \frac{1}{\sqrt{1 + \psi^2}}} = \sqrt{\frac{\sqrt{1 + \psi^2} + I}{\sqrt{1 + \psi^2}}} \,. \tag{2.91}$$

We then obtain

$$\pm i \sqrt{\frac{k}{2}}(x - \hat{x}) = \sqrt{I + 1} E\left(\frac{\sqrt{\frac{\sqrt{1 + \psi^2} + I}{\sqrt{1 + \psi^2}}}}{I - 1}, \frac{\sqrt{I^2 - 1}}{I + 1} \right)$$

$$- \frac{1}{\sqrt{I + 1}} F\left(\frac{\sqrt{\frac{\sqrt{1 + \psi^2} + I}{\sqrt{1 + \psi^2}}}}{I - 1}, \frac{\sqrt{I^2 - 1}}{I + 1} \right) \,. \tag{2.92}$$

In Fig. 2.10, we provide a phase portrait describing solutions to (2.81). In Fig. 2.11, we display several of these solutions as functions of x. As expected, the system is unstable for $k < 0$, while oscillatory solutions are obtained for $k > 0$.
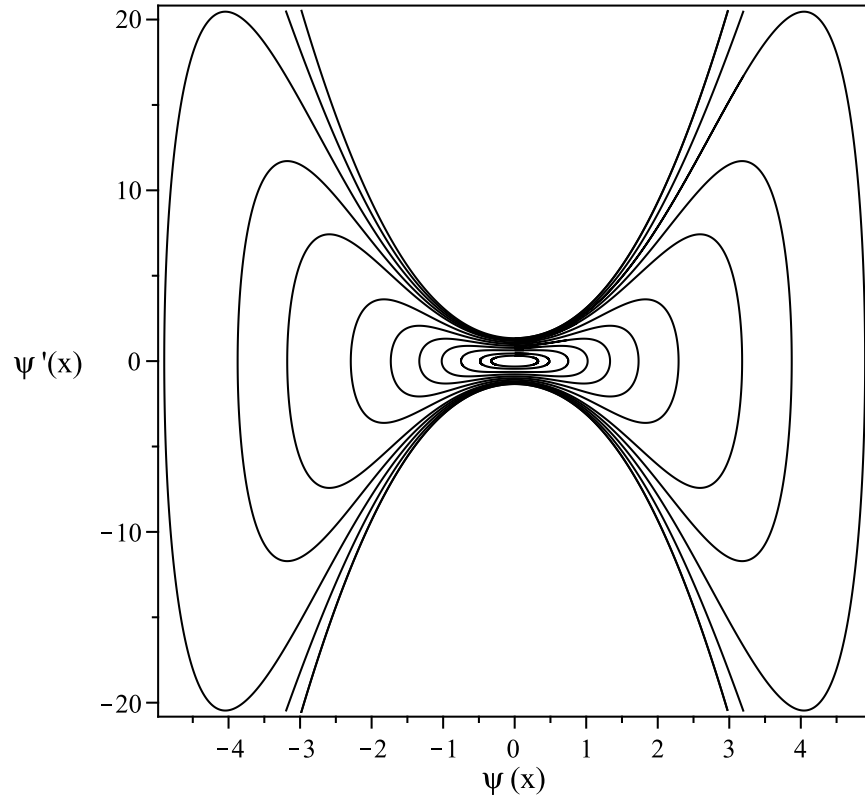
Figure 2.10: Phase portraits for the space-periodic solutions $\psi(x)$ to the WKIS equations, which exist for $-1 < I < 0$. We fix $k = 1$.
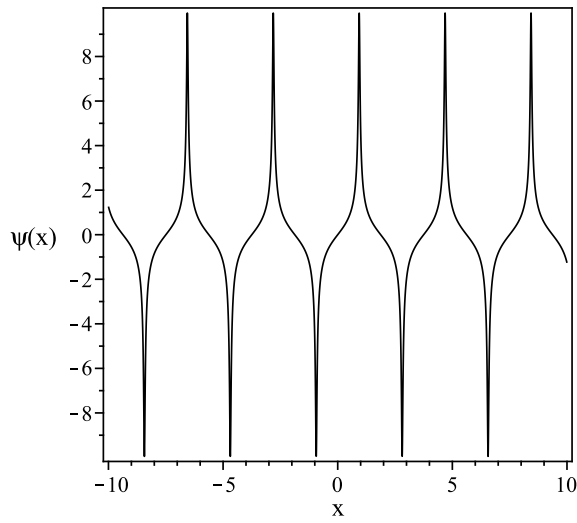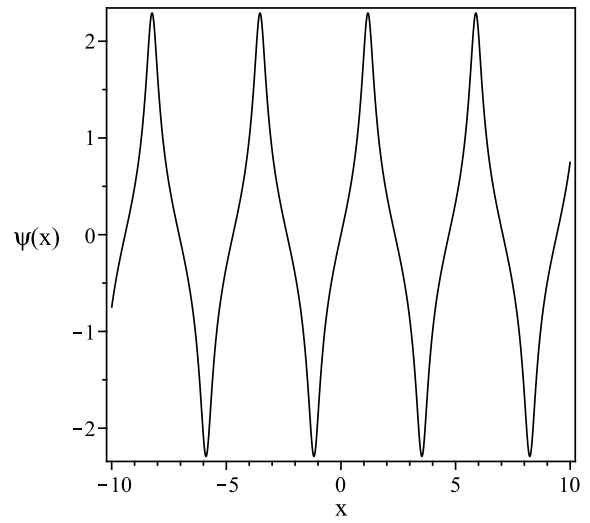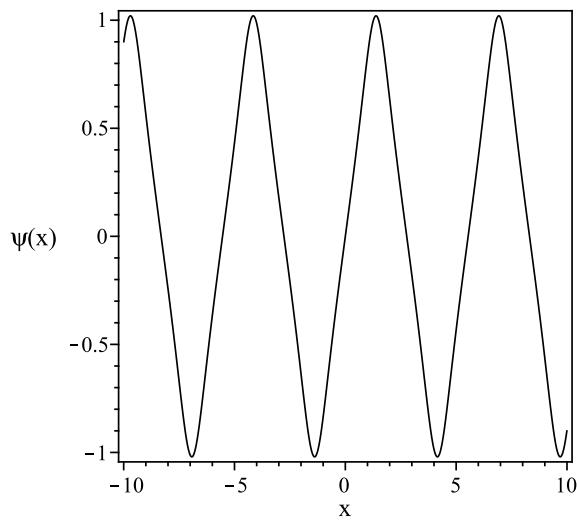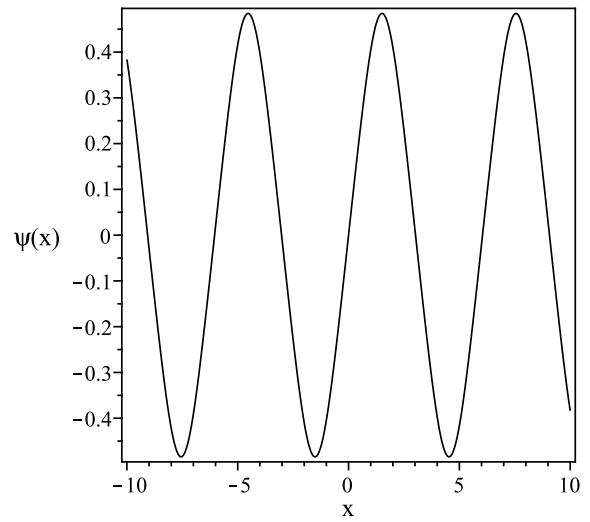
Figure 2.11: Plots of the space-periodic solutions $\psi(x)$ to the WKIS equation, which exist

for (a) $I = -0.1$, (b) $I = -0.4$, (c) $I = -0.7$, and (d) $I = -0.9$. Here, $k = 1$.

2.4.3 Alternate formulation

The formulation in §2 is one possibility. Here, we present an alternate formulation, which gives us an equivalent yet different form for the first integrals. Let us define $\theta(x)$ by $\phi(x) = \sin\theta(x)$. Without any loss of generality, we take $-\frac{\pi}{2} \leq \theta \leq \frac{\pi}{2}$. This way, $\cos\theta(x) \geq 0$. Then (2.83) becomes

$$\theta'' + \tan(\theta)\left(k\sec(\theta) - \theta'^2\right) = 0. \tag{2.93}$$

There exists a constant J such that

$$\frac{\cos(\theta)\theta'}{\sqrt{2k\cos(\theta) + J}} = 1 \tag{2.94}$$

for all x. Integrating this relation, it is clear that $\theta(x)$ satisfies the implicit relation

$$\int_{\theta_0}^{\theta(x)} \frac{\cos\xi d\xi}{\sqrt{2k\cos\xi + J}} = \pm(x - x_0), \tag{2.95}$$

where $\theta_0 = \theta(x_0)$ and x_0 is a constant.

From this formulation, it is clear to see that the period T of any periodic solution is given by

$$T = 4\int_0^{\frac{\pi}{2}} \frac{\cos\xi d\xi}{\sqrt{2k\cos\xi + J}}. \tag{2.96}$$

If we desire the period in terms of the representation given with I as opposed to J, note that the maximal value of ϕ is given by $\phi_{\max} = \sqrt{1 - I^2}$. Then, from (2.87) we have

$$T = \frac{4}{\sqrt{2k}}\int_0^{\sqrt{1-I^2}} \frac{d\xi}{\sqrt{I + \sqrt{1 - \xi^2}}} = \frac{1}{4\sqrt{2k}}\int_{|I|}^1 \frac{\nu d\nu}{\sqrt{(1 - \nu^2)(\nu - |I|)}}. \tag{2.97}$$

Evaluation of the latter integral yields the exact formula

$$T = \frac{8}{\sqrt{k}} K\left(\frac{\sqrt{2}(1-|I|)}{2}\right) - \frac{4}{\sqrt{k}} E\left(\frac{\sqrt{2}(1-|I|)}{2}\right),\qquad(2.98)$$

where E and K denote elliptic integrals of the second and third kind, respectively.

In Fig. 2.12, we plot the period T as a function of the integration constant I. The period is bounded and increasing in I and decreasing in k, and we find that the extreme values are given by

$$T = \frac{2\pi}{\sqrt{k}} \qquad \text{at} \qquad I = -1 \qquad (2.99)$$

and

$$T = \frac{1}{\sqrt{k}} \left(8K\left(\frac{\sqrt{2}}{2}\right) - 4E\left(\frac{\sqrt{2}}{2}\right)\right) \approx \frac{9.4306}{\sqrt{k}} \qquad \text{at} \qquad I = 0\,. \qquad (2.100)$$
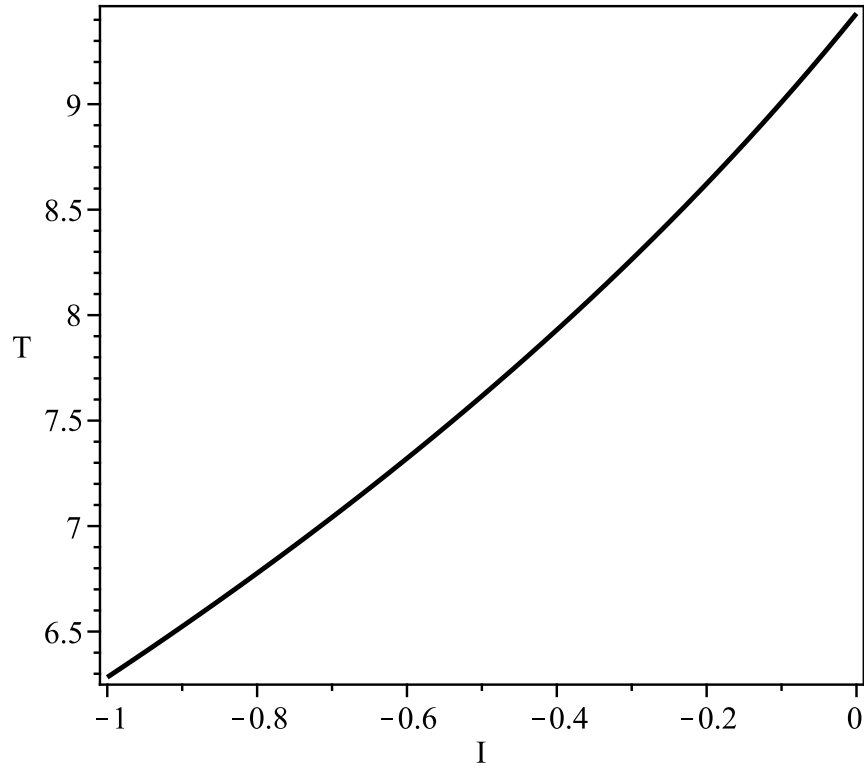
Figure 2.12: Plot of the period T of the space-periodic solutions $\psi(x)$ to the WKIS equation for various values of the constant of motion I. Here, $k = 1$.

2.4.4 Discussion

What we have done here is reformulate the WKIS equation as a nonlinear ordinary differential equation. The governing equation has two integrals of motion, and the latter results in an exact implicit relation connecting the solution to the space variable, x. From these implicit relations, we may recover the exact solution. These solutions connect two steady states, resulting in the observed oscillatory (space-periodic) stationary solutions. An alternate, yet equivalent, formulation is provided as well. With these, we are able to construct an exact nonlinear relation between the model parameters and the period of oscillation in space.

We see that when the integral of motion has a constant of motion $-1 < I < 0$, there will always exist a space-periodic solution of finite period, and the dependence of the period on the model parameters is given in (2.98). As $I \to -1^+$, the amplitude of the solutions tends to zero. Meanwhile, when $I \to 0^-$, the solutions become singular on a finite domain. This behavior is demonstrated in Figs. 2.10 and 2.11. We also find that solutions exist for other regions ($I < -1$ and $I > 0$). However, these solutions are either singular at infinitely many points or non-periodic.

67

CHAPTER 3

STABILITY RESULTS FOR CERTAIN PERIODIC OR

LOCALIZED SOLUTIONS

3.1   Orbital stability for rotating planar vortex filaments in the Cartesian and arclength forms of the local induction approximation

The local induction approximation (LIA) is commonly used to study the motion of a vortex filament in a fluid. The fully nonlinear form of the LIA is equivalent to a type of derivative nonlinear Schrödinger (NLS) equation, and stationary solutions of this equation correspond to rotating planar vortex filaments. Such solutions were first discussed in the plane by Hasimoto [41], and have been described both in Cartesian three-space and in the arclength formulation in subsequent works. Despite their interest, fully analytical stability results have been elusive. In the present section, we present elegant and simple proofs of the orbital stability for the stationary solutions to the derivative nonlinear Schrödinger equations governing the self-induced motion of a vortex filament under the LIA, in both the extrinsic (Cartesian) and intrinsic (arclength) coordinate representations. Such results constitute an

exact criterion for the orbital stability of rotating planar vortex filament solutions for the vortex filament problem under the LIA. The results presented in this section were originally obtained in Van Gorder [103].

3.1.1 Introduction to the problem

We now consider orbital stability results for the solutions obtained in Sections 2.1 and 2.3. While there have been some studies on the stability of a vortex filament in various physical situations, these studies often are numerical or approximate. Widnall [119] studied the stability of helical vortex filaments; in particular, the stability of helical vortex filaments of small pitch were considered using the so-called "cut-off approximation" and numerical integration. Tsai and Widnall [93] then studied the stability of short waves on a vortex filament embedded in a strain field; see also Moore and Saffman [67] and Aref and E.P. Flinchem [7]. Regarding the stability of multiple helical vortex filaments, Okulov [68] considered the problem of N helical vortex arrays. There have been a number of simulations and numerical analyses for stability of vortex dynamics in a variety of situations. For instance, Fenton and Karma [30] discussed vortex filament stability in the context of a three-dimensional continuous myocardium with fiber rotation. This illustrates the fact that, while vortex problems are quite old and have been well-represented in the literature, there is still active interest in the stability of vortex solutions to a variety of flows.

Planar vortex filaments correspond to space-periodic stationary solutions of the LIA, so it makes sense to apply the Vakhitov-Kolokolov (VK) stability criterion to determine the orbital stability of such solutions. The governing equations are strongly nonlinear, so we apply the method discussed in Van Gorder [104] for the integrable WKIS model, in order to determine the orbital stability of these stationary solutions in an exact analytical manner. That is to say, our results are completely analytical, and involve no numerical approximations. In this way, the results are rather elegant and we show that the sign of the spectral parameter of the filament solution completely determines the orbital stability of the solutions. We remark that linear stability for related filaments (solitary waves and traveling waves) were considered by Kida [50] through numerical approximations.

While there are multiple formulations of the LIA, corresponding to different reference frames, in the present section we shall consider two coordinate frames, namely the Cartesian and arclength frames. The Cartesian frame allows us to visualize the vortex filaments directly, and we shall be able to more easily determine the meaning of the stability results in terms of the types of vortex motion. The arclength frame is also useful, since it permits us to determine the vortex filament as an exact closed-form function of the single arclength variable along which the filament resides in terms of the spectral parameter (in a generalization of the exact solution given previously[100]). We do not consider the intrinsic curvature-torsion frame here, although this analysis can be carried out along the same lines.

3.1.2 Stability methods

In order to discuss the orbital stability of such a stationary solution, a useful tool is the Vakhitov-Kolokolov (VK) stability criterion [97], which has been applied to discuss the stability of stationary solutions in one or many spectral parameters; see [61, 87, 58, 66] for some applications. The criterion has been applied to a variety of nonlinear Schrödinger (NLS)-type equations such as those governing optical solitons [72, 46], perturbed cubic NLS equations [65], NLS quations governing solitons in self-induced transparent media [18], two-dimensional NLS equations [79], and two-component lattice NLS equations [63], to name a few areas of application. Therefore, it is reasonable to consider the criterion for the desired stationary solutions to the type of derivative NLS equation which results from the fully nonlinear LIA governing a planar vortex filament.

Consider the Vakhitov-Kolokolov (VK) stability criterion governing orbital stability of a solution $\Phi(x,t) = e^{-i\omega t}\psi_\omega(x)$ to a derivative NLS equation such that $\psi_\omega(x+T) = \psi_\omega(x)$. Defining the integral of motion

$$P(\Phi(x,t)) = \int_0^T |\Phi(x,t)|^2\,dx = \int_0^T |\psi_\omega(x)|^2 dx\,, \tag{3.1}$$

the VK criterion state that the stationary solution is orbitally stable at some $\omega = \omega_0$ provided that

$$\frac{d}{d\omega}P(\psi_\omega(x)) < 0 \tag{3.2}$$

for $\omega = \omega_0$. Here we take the periodic form of the criterion, since we shall be interested in spatially periodic solutions. As such, we define P over a single period T. (If we were con-

cerned with solitary wave solutions ψ, we would define P with an integration over the real line.) For periodic ψ, this criterion is in analogue to Lyapunov stability. This criteria was originally applied to the standard NLS equation, in the case of solitary wave solutions. Since then, the criterion has been applied to a number of Hamiltonian systems (many exhibiting $\mathbf{U}(1)$-invariance, or even more general symmetries). Generalizations to non-integrable situations are possible in some cases; see Yang [121].

3.1.3 The Cartesian problem

Van Gorder [98, 99] considered the Cartesian coordinate space $\mathbf{r} = (x, y, z)$ and transformed the LIA $\mathbf{v} = \gamma \kappa \mathbf{t} \times \mathbf{n}$ into the potential form

$$i\Phi_t + \gamma \left(1 + |\Phi_x|^2\right)^{-3/2} \Phi_{xx} = 0 \,, \tag{3.3}$$

where $\Phi = y + iz$. This is a non-standard derivative nonlinear Schrödinger (NLS) equation. Note that (3.3) is $\mathbf{U}(1)$-invariant. Once a solution to (3.3) is known, the position of the vortex filament is given by $\mathbf{r}(x, t) = (x, \text{Re}\Phi(x, t), \text{Im}\Phi(x, t))$. A stationary solution to the LIA takes the form $\Phi(x, t) = e^{-i\omega\gamma t}\psi(x)$ (where ω is the spectral parameter), and this puts equation (3.3) into the form

$$\omega\psi + (1 + \psi'^2)^{-3/2}\psi'' = 0 \,. \tag{3.4}$$

Here we assume real-valued ψ, since this is consistent with planar vortex filaments. Space-periodic solutions of this type were explored in [99]. This equation has periodic solutions for

$\omega > 0$ corresponding to planar vortex filaments, which are therefore given by the formula $\mathbf{r}(x,t) = (x, \cos(\omega\gamma t)\psi(x), -\sin(\omega\gamma t)\psi(x))$. The period of such solutions depends strongly on ω. When $\omega \leq 0$, this equation has only $\psi \equiv 0$ as a periodic solution. Equation (3.4) admits the first integral [98] $\omega\psi^2 - 2(1 + \psi'^2)^{-1/2} = -E$, where E is a constant. We find that $E \in (0, 2)$ for $\omega > 0$ and $E > 2$ when $\omega < 0$. It may be shown that any real-valued space-periodic function ψ is bounded like $-\sqrt{(2-E)/\omega} \leq \psi \leq \sqrt{(2-E)/\omega}$. In Fig. 3.1 we show a schematic diagram of the coordinate geometry with a sample planar vortex filament imposed. In Fig. 3.2, we show the influence of the spectral parameter ω on the shape. Clearly, small values of the spectral parameter permit large amplitude solutions. The spectral parameter ω also strongly influences the period of the solutions.
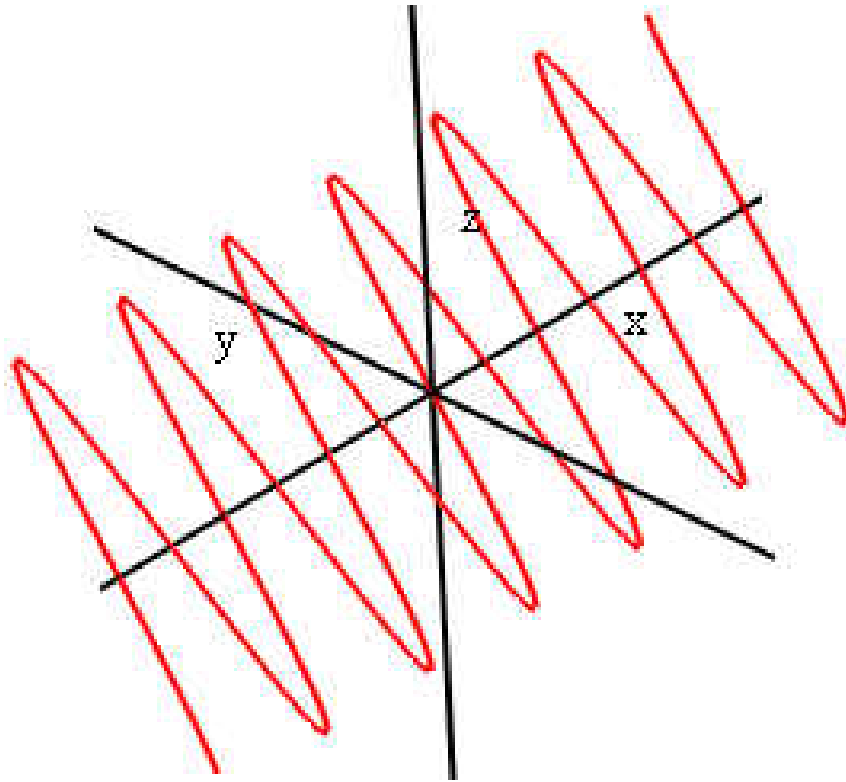
Figure 3.1: Plot of the problem geometry for $\omega > 0$ in the Cartesian reference frame. The curve represents the planar vortex filament. As time increases, the structure rotates about the x-axis.
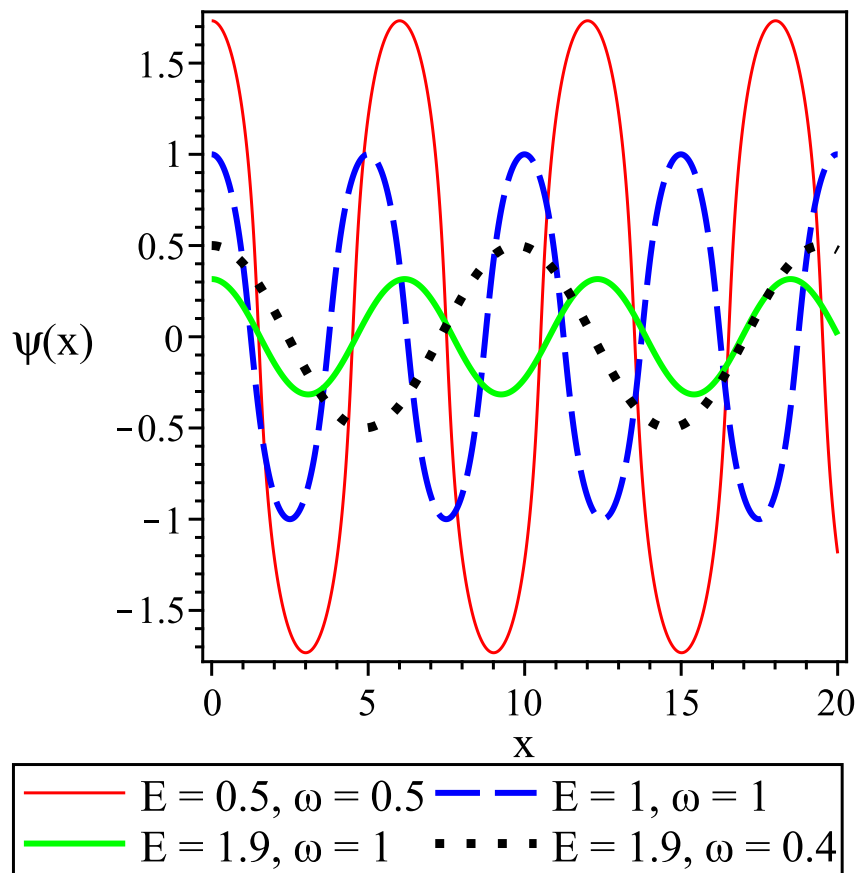
Figure 3.2: Plot of the solution profiles $\psi(x)$ with spectral parameter ω and constant of motion E. Clearly, both parameters strongly influence the amplitude and space-period of the stationary solutions. Each stationary solution $\psi(x)$ corresponds to a planar vortex filament as shown in Fig. 3.1.

First, consider the case of $\omega > 0$. We have the period

$$T(E, \omega) = 4 \int_0^{\sqrt{(2-E)/\omega}} \frac{(E + \omega\eta^2)d\eta}{\sqrt{(2 - E - \omega\eta^2)(2 + E + \omega\eta^2)}} \,. \tag{3.5}$$

In order to determine the orbital stability of such periodic solutions, we shall look at the influence of the spectrum on the quantity (3.2). We define $P(E, \omega)$ over one closed orbit, so for any fixed E we define (in accordance with the definition (3.1))

$$\begin{aligned}
P(E, \omega) &= \int_0^T \psi^2(x)dx \\
&= 2 \int_{\psi_{\min}}^{\psi_{\max}} \eta^2 \frac{(E + \omega\eta^2)d\eta}{\sqrt{(2 - E - \omega\eta^2)(2 + E + \omega\eta^2)}} \\
&= \int_0^{\sqrt{(2-E)/\omega}} \frac{4(E + \omega\eta^2)\eta^2 d\eta}{\sqrt{(2 - E - \omega\eta^2)(2 + E + \omega\eta^2)}} \,.
\end{aligned} \tag{3.6}$$

We have $P(E, \omega) = \omega^{-3/2}\mu_+(E)$, where we define

$$\mu_+(E) = 2 \int_E^2 \frac{\rho\sqrt{\rho - E}}{\sqrt{(2 - \rho)(2 + \rho)}} d\rho \,. \tag{3.7}$$

We find that $\mu_+(0) = \frac{8}{3}K\left(\frac{\sqrt{2}}{2}\right) = 4.9443$ (where K denotes the elliptic integral of the third kind), $\mu_+(2) = 0$, and $\mu_+(E)$ is monotone decreasing on $E \in (0, 2)$. Then, for fixed $E \in (0, 2)$, we have

$$\frac{\partial P}{\partial \omega} = -\frac{3}{2\omega^{5/2}}\mu_+(E) < 0 \tag{3.8}$$

for any fixed orbit corresponding to an $E \in (0, 2)$. By the VK stability criterion, the solutions $\psi_\omega(x)$ are orbitally stable.

For $\omega < 0$, a standard perturbation analysis shows that an unbounded solution $\psi_\omega(x)$ where $\lim_{|x| \to \infty} |\psi_\omega(x)| = \infty$ is unstable. We omit the details. We have established the following result:

76

Theorem 1: A non-zero stationary solution $e^{-i\omega t}\psi(x)$ for the fully nonlinear partial differential equation (3.3) governing the self-induced motion of a vortex filament in the LIA is stable if its spectrum is positive definite (it has no negative energy excited states, $\omega > 0$) and it is unstable if its spectrum contains negative energy excitations ($\omega < 0$). Since $\omega > 0$ corresponds to space-periodic solutions, the space-periodic stationary solutions (corresponding to the planar vortex filaments) are stable in the Cartesian frame of reference.

3.1.4 The arclength problem

Umeki [95] obtained an alternate formulation of the LIA, using the intrinsic arclength based coordinate system as opposed to the extrinsic Cartesian coordinate system. Umeki defines $\mathbf{r} = \mathbf{t} \times \mathbf{t}_s$, where s is the arclength element. The LIA then takes the form $\mathbf{t}_t = \mathbf{t} \times \mathbf{t}_{ss}$. Writing $\mathbf{t} = (\tau_x, \tau_y, \tau_z)$, Umeki [95] defines the complex field v by

$$\tau_x + i\tau_y = 2v\left(1 + |v|^2\right)^{-1}, \quad \tau_z = \left(1 - |v|^2\right)\left(1 + |v|^2\right)^{-1}. \tag{3.9}$$

The relation $\mathbf{t}_t = \mathbf{t} \times \mathbf{t}_{ss}$ then implies

$$iv_t + v_{ss} - 2v^*v_s^2\left(1 + |v|^2\right)^{-1} = 0. \tag{3.10}$$

Note that (3.10) is $\mathbf{U}(1)$-invariant. A mapping between the intrinsic and extrinsic LIA formulations was provided recently by Umeki [96]. Regarding planar vortex filaments, an exact form for the stationary solution was given in the arclength representation in [100]. Due to the difference in structure between the arclength and Cartesian systems, the amplitude

77

of the exact stationary solutions was not bounded like was the case in the Cartesian frame [100].

Under the assumption of a stationary solution $e^{-i\omega t}q(s)$, $\omega \neq 0$ (corresponding to a planar vortex filament [100]), (3.10) reduces to

$$\omega q + q_{ss} - 2qq_s^2\left(1 + q^2\right)^{-1} = 0.\tag{3.11}$$

When $\omega = 0$, (3.10) reduces to $q_{ss} - 2qq_s^2(1 + q^2)^{-1} = 0$. Constructing the first integral we have $q_s/(1 + q^2) = I_0$, which admits the singular solution $q(s) = \tan(I_0 s + I_1)$ for $I_0 \neq 0$, or a constant solution if $I_0 = 0$. We shall therefore restrict our attention to $\omega \neq 0$.

For $\omega \neq 0$, we introduce the quantity $I = (\omega(1 + q^2) - q_s^2)(1 + q^2)^{-2}$. This quantity is conserved:

$$\frac{dI}{ds} = -\frac{2q_s}{(1 + q^2)^2}\left\{\omega q + q_{ss} - \frac{2qq_s^2}{1 + q^2}\right\} = 0.\tag{3.12}$$

First consider the $\omega > 0$ case. If $q_s = 0$, then $\omega = (1 + q^2)I$, hence the maximal value of q is given by $q_{\max} = \sqrt{\frac{\omega - I}{I}}$, where $0 < I < \omega$ if $\omega > 0$, while $q_{\min}$ takes the negative of this value. Taking $q_{\max} = A$, it will be more useful to express I in terms of A. We have $I = \frac{\omega}{\sqrt{1+A^2}}$. So,

$$q_s^2 = \omega(1 + q^2)\left(1 - (1 + q^2)(1 + A^2)^{-1}\right).\tag{3.13}$$

The period $T(A, \omega)$ is then given by

$$T(A, \omega) = \frac{4}{\sqrt{\omega}}\int_0^A \frac{d\xi}{\sqrt{(1 + \xi^2)\left(1 - \frac{1+\xi^2}{1+A^2}\right)}}.\tag{3.14}$$

From (3.14), it is apparent that

$$P(A, \omega) = \int_0^T |v(s,t)|^2\,dx = \frac{4}{\sqrt{\omega}}\int_0^A \frac{\xi^2 d\xi}{\sqrt{(1 + \xi^2)\left(1 - \frac{1+\xi^2}{1+A^2}\right)}}.\tag{3.15}$$

78

We then have $P(A, \omega) = \nu(A)/\sqrt{\omega}$, where

$$\nu(A) = 4 \left\{ (1 + A^2)\mathcal{E}\left(\frac{A}{\sqrt{1 + A^2}}\right) - \mathcal{K}\left(\frac{A}{\sqrt{1 + A^2}}\right) \right\}. \tag{3.16}$$

Here again $\mathcal{K}$ is the complete elliptic integral of the first kind, while $\mathcal{E}$ is the complete elliptic integral of the second kind. We find that $\nu'(A) > 0$ for all $A > 0$, while $\nu(0) = 0$, hence $\nu(A) > 0$ for all positive A. Then,

$$\frac{dP}{d\omega} = -\frac{\nu(A)}{2\omega^{3/2}} < 0, \tag{3.17}$$

for all $\omega > 0$ and all $A > 0$. By the VK stability criterion outlined, the solutions $q(x)$ are orbitally stable when $\omega > 0$.

Consider next the case where $\omega \leq 0$. To get real and bounded solutions, if $q_{\max}$ is a local maximum, we have $q_{\max} = \sqrt{\frac{|\omega| - |I|}{|I|}}$, where $\omega < I < 0$. Then, $|I| = \frac{|\omega|}{1 + q_{\max}^2}$, and

$$q_s^2 = -|\omega|(1 + q^2)\left(1 - \frac{1 + q^2}{1 + q_{\max}^2}\right) \leq 0, \tag{3.18}$$

with equality holding only when $\omega = 0$. Since we assume q to be real, the only possibility is $q_s \equiv 0$ and $\omega = 0$. Hence, bounded real-valued solutions do not exist for $\omega < 0$. Consider the solution $q(s) \equiv q_{\max}$, which is constant and satisfies (3.18). As we see from (3.11), the only possible constant solution is the zero solution $q(s) \equiv 0$. We have demonstrated the following result:

Theorem 2: A bounded stationary solution $e^{-i\omega t}q(s)$ for the derivative nonlinear Schrödinger equation (3.10) governing the self-induced motion of a vortex filament in the arclength representation of the LIA exists and is stable if its spectrum is positive definite ($\omega > 0$). Bounded

solutions do not exist for negative spectral parameters ($\omega < 0$). As $\omega > 0$ corresponds to space-periodic solutions, the space-periodic stationary solutions (corresponding to the planar vortex filaments) are stable in the arclength frame of reference.

In the case $\omega = 1$, the exact solution to (3.11) was given in equation (14) of Van Gorder [100]. Modifying this solution to account for arbitrary $\omega > 0$, we obtain the new exact solution

$$v(s,t) = e^{-i\omega t}q(s) = Ae^{-i\omega t} \text{ sn} \left(\sqrt{\frac{\omega}{1 + A^2}}(s - s_0), Ai \right) , \qquad (3.19)$$

where sn denotes the appropriate Jacobi elliptic function, A is the amplitude, and s_0 is an arbitrary constant.

3.1.5 Discussion

We have determined the orbital stability of stationary solutions for the self-induced motion of a vortex filament under the LIA under both the Cartesian and arclength formulations. While these formulations describe the same physical scenario, they result in structurally distinct types of nonlinear dispersion equations. For both models, the stationary solutions are orbitally stable provided that the spectrum is positive definite. This agreement should be expected from the physics, since both models are describing the same phenomenon in different frameworks. What this means is that the planar vortex filaments (described by the space-periodic stationary solutions) in a standard fluid are stable under small perturbations

or disturbances, when modeled under the LIA. Mathematically, the results are interesting from the standpoint of their simplicity: The power integral P may be determined in an exact analytical form for the spectral parameter ω. Hence, we determine the orbital stability exactly, without resorting to numerical simulations or even analytical approximations or perturbations.

The Cartesian results are likely the most physically telling. Here the sign of ω indicates the direction of motion of the filament (i.e., the manner in which the planar filament rotates), so the way in which the planar filament rotates influences the orbital stability of the stationary state corresponding the the planar filament. As such, the manner of rotation directly influences the persistence of a planar filament. The planar filament corresponding to $\omega > 0$ persists, whereas for $\omega < 0$ the planar filament does not develop.

As mentioned before, the method employed here was applied to the integrable WKIS model in [104] to determine the orbital stability of space-periodic stationary solutions arising in that model. Compared to the nonlinear dispersion relations (3.3) and (3.10) considered, we see that the WKIS model is also a member of such a family of equations. This highlights the fact that for some families of dispersion relations we may apply the analytical method discussed here to deduce the orbital stability of space-periodic stationary solutions. Indeed, the method is concise and can be applied to a number of other derivative nonlinear Schrödinger (NLS) type equations admitting space-periodic stationary solutions.

On a final note, the orbital stability presented here is one type of stability. One could also consider transverse stability of the space-periodic solutions. Due to the form of the

stationary solution, we know that $|\Phi(x, t)|$ is $U(1)$-invariant, which means that the modulus $|\Phi(x, t)|$ is time-independent. For other types of solution, this is not the case, so a different analysis would be called for. Such considerations are needed when we consider only locally stationary states, such as traveling waves on the vortex filament, since these are not true stationary states.

3.2 Orbital stability for stationary solutions of the Wadati-Konno-Ichikawa-Schimizu (WKIS) equation

We determine the orbital stability properties of the space-periodic stationary solutions to the Wadati-Konno-Ichikawa-Shimizu (WKIS) equation previously obtained in Section 2.4. The stability result is completely analytic, whereas most results for similar equations are numerical. The method is concise and can be applied to a number of other derivative nonlinear Schrödinger (NLS) type equations admitting space-periodic stationary solutions. The method presented here was published in Van Gorder [104].

3.2.1 Introduction to the problem

Very recently, the present author studied stationary solutions to the WKIS equation [101], and these results were highlighted in Section 2.4. It was shown that there exist space-periodic

solutions of the form $u(x,t) = e^{-ikt}\psi(x)$. Such space-periodic stationary solutions have been found in related derivative NLS models of the form $iu_t = F(|u_x|, |u|)u_{xx}$; for example, such solutions describe the Hasimoto [41] planar vortex filament in variety of geometries [98, 99, 100]. The period T of such solutions, which depends nonlinearly on the model parameters, may be computed in an exact manner in terms of elliptic functions.

The space-periodic solutions for the integrable WKIS demonstrate the variety of solutions possible for various types of derivative NLS equations. However, it is natural to wonder if such solutions are orbitally stable or unstable. In the present section, we determine the orbital stability of the space-periodic stationary solutions for the WKIS model. The results are completely analytical, in contrast to mainly numerical results in the literature for many types of derivative NLS equations.

3.2.2 Properties of the stationary solutions

Let us assume a stationary solution of the form

$$u(x,t) = e^{-ikt}\psi(x)\,, \tag{3.20}$$

where $\psi(x)$ is a real field. We shall assume the spectral parameter k satisfies $k \neq 0$. When $k = 0$, we showed that the only finite solution is constant [101]. Using (3.20) in the WKIS equation, it is clear that $\psi(x)$ satisfies

$$k\psi + \left(\frac{\psi}{\sqrt{1+\psi^2}}\right)'' = 0\,. \tag{3.21}$$

Equation (3.21) is integrable, though it may be hard to see from this form. Let us define a new function $\phi(x)$ by

$$\phi(x) = \frac{\psi(x)}{\sqrt{1 + \psi(x)^2}} \,. \tag{3.22}$$

Note that $-1 < \phi(x) < 1$ for all x. Then, (3.21) is put into the form

$$\phi'' + \frac{k\phi}{\sqrt{1 - \phi^2}} = 0 \,. \tag{3.23}$$

Now, (3.23) is a dynamical problem

$$\phi'' = -\frac{\mathrm{d}}{\mathrm{d}\phi} U(\phi) \,, \tag{3.24}$$

with potential $U(\phi) = -k\sqrt{1 - \phi^2}$. Assuming a space-periodic solution $\phi(x)$, the kinetic energy kI satisfies $\min\{U\} < kI < 0$, i.e., $-k < kI < 0$. So, the spectral parameter satisfies $k > 0$ and the constant of motion satisfies $-1 < I < 0$.

A first and second integral for (3.23) was constructed [101], and it was found that

$$\pm (x - x_0) = \int_{\phi_0}^{\phi} \frac{d\xi}{\sqrt{2k\sqrt{1 - \xi^2} + 2kI}} \,, \tag{3.25}$$

where ϕ_0 is another constant of motion. The solution $\phi(x)$ is then governed by the implicit relation in terms of elliptic integrals F and E:

$$\pm i\sqrt{\frac{k}{2}}(x - \hat{x}) = \sqrt{I + 1}\, E\left(\frac{\sqrt{I + \sqrt{1 - \phi^2}}}{I - 1}, \frac{\sqrt{I^2 - 1}}{I + 1}\right)$$
$$- \frac{1}{\sqrt{I + 1}} F\left(\frac{\sqrt{I + \sqrt{1 - \phi^2}}}{I - 1}, \frac{\sqrt{I^2 - 1}}{I + 1}\right) \,. \tag{3.26}$$

Inverting the relation (3.22), an implicit relation for $\psi(x)$ reads

$$\pm i \sqrt{\frac{k}{2}}(x-\hat{x}) = \sqrt{I+1}\, E\left(\frac{\sqrt{\frac{\sqrt{1+\psi^2}+I}{\sqrt{1+\psi^2}}}}{I-1}, \frac{\sqrt{I^2-1}}{I+1}\right)$$
$$-\frac{1}{\sqrt{I+1}}F\left(\frac{\sqrt{\frac{\sqrt{1+\psi^2}+I}{\sqrt{1+\psi^2}}}}{I-1}, \frac{\sqrt{I^2-1}}{I+1}\right). \tag{3.27}$$

Since $\phi(x)$ is periodic, then so is $\psi(x)$. Furthermore, by (3.22), both must share the same period. Let $T(k,I)$ denote this period. Then from (3.25), we have

$$\begin{aligned} T(k,I) &= 2\int_{\phi_{\min}}^{\phi_{\max}} \frac{d\xi}{\sqrt{2k\sqrt{1-\xi^2}+2kI}} \\ &= \frac{2\sqrt{2}}{\sqrt{k}}\int_0^{\sqrt{1-I^2}} \frac{d\xi}{\sqrt{\sqrt{1-\xi^2}+I}} \\ &= \frac{4\sqrt{2}}{\sqrt{k}}\int_{|I|}^1 \frac{\zeta\, d\zeta}{\sqrt{(1-\zeta^2)(\zeta-|I|)}}. \end{aligned} \tag{3.28}$$

Integrating, we have

$$T(k,I) = \frac{8}{\sqrt{k}}E\left(\frac{\sqrt{2(1-|I|)}}{2}\right) - \frac{4}{\sqrt{k}}K\left(\frac{\sqrt{2(1-|I|)}}{2}\right), \tag{3.29}$$

where we correct a couple typos (note, for instance, that the square roots need to include $1-|I|$ in equation (21) of Van Gorder [101]. Here E and K denote elliptic integrals of the second and third kind, respectively.

From these formulas, it may still be hard to visualize the behavior of the solutions $\psi(x)$. In Fig. 3.3, we plot solutions $\psi(x)$ for various amplitudes. In Fig. 3.4, we plot the period $T(k,I)$ as a function of the spectral parameter k, for various values of I. The solutions

show the space periodicity of $\psi(x)$. As k increases, the period of solutions decreases rapidly.

So, for large k, the solutions oscillate rapidly.
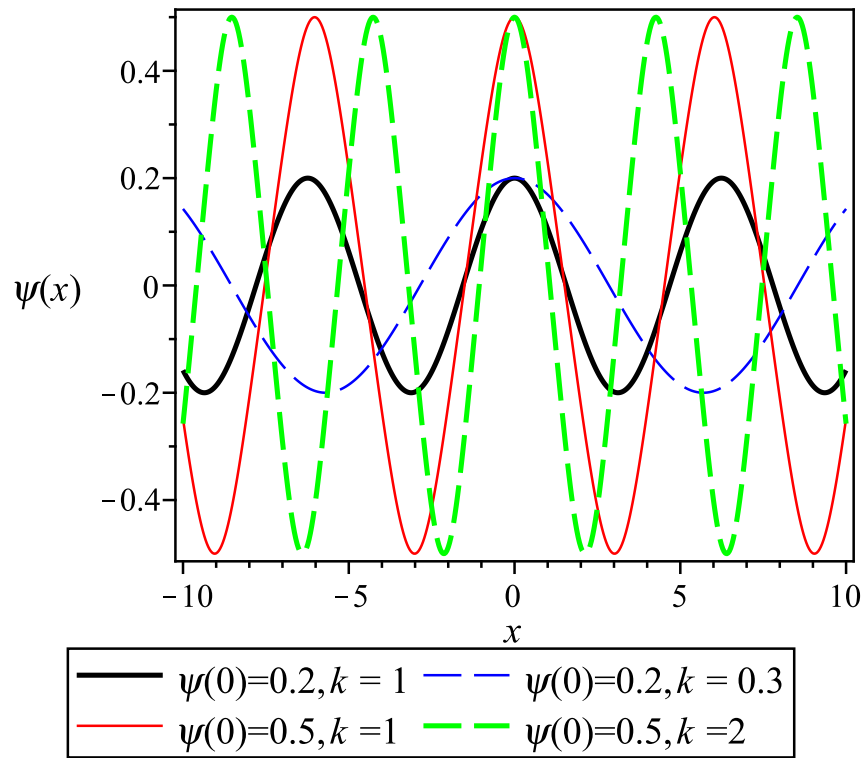
Figure 3.3: Plots of the solutions $\psi(x)$ for various values of k and various amplitudes $\psi(0)$.
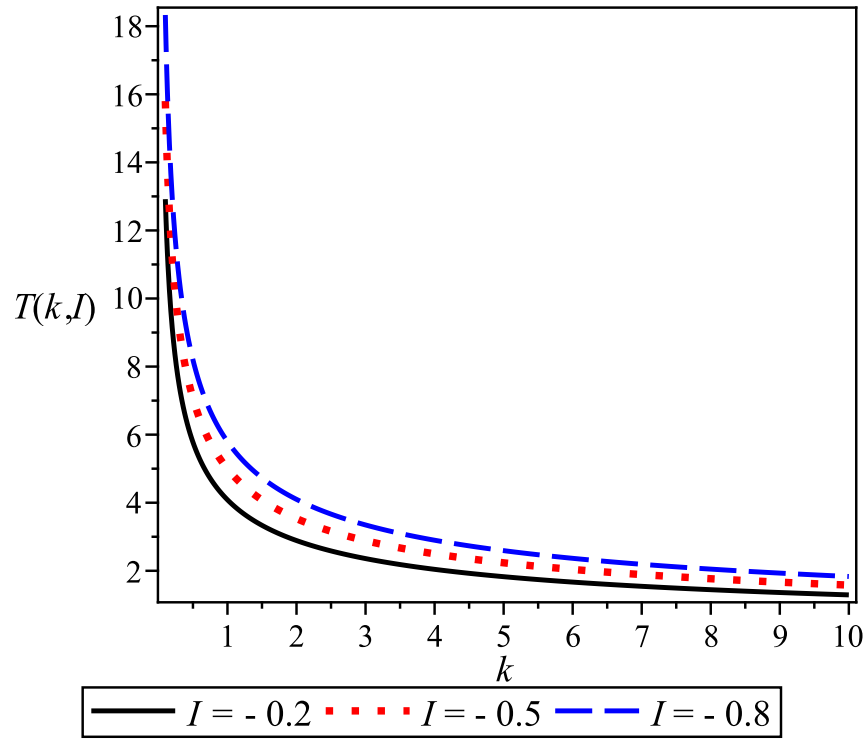
Figure 3.4: Plot of the period $T(k, I)$ given in formula (3.29) as a function of k for various values of $I \in (-1, 0)$.

3.2.3 Stability result

In order to discuss the orbital stability of such a stationary solution, a useful tool is the Vakhitov-Kolokolov (VK) stability criterion [97], which has been applied to discuss the stability of stationary solutions in one or many spectral parameters; see [61, 87, 58, 66] for some applications.

Consider the Vakhitov-Kolokolov (VK) stability criterion governing orbital stability of a solution $\Phi(x,t) = e^{-i\omega t}\psi_\omega(x)$ to a derivative NLS equation such that $\psi_\omega(x+T) = \psi_\omega(x)$. We apply the method as outlined in the previous section. Returning to the present problem, for a stationary solution (3.20), the power integral is defined by

$$P(k,I) = \frac{1}{2}\int_0^T |u(x,t)|^2 dx = \frac{1}{2}\int_0^{T(k,I)} \psi(x)^2 dx\,. \tag{3.30}$$

The implicit form of the integral will be far more useful, since we do not have an explicit formula for ψ in terms of x. An integral in ψ is more complicated, so in keeping with the notation of the previous section, we develop a formulation in terms of ϕ. Note that $\psi^2 = \phi^2/(1-\phi^2)$. We then use the power integral given by

$$\begin{aligned}
P(k,I) &= \int_{\phi_{\min}}^{\phi_{\max}} \frac{\xi^2}{(1-\xi^2)} \frac{d\xi}{\sqrt{2k\sqrt{1-\xi^2}+2kI}} \\
&= \frac{\sqrt{2}}{\sqrt{k}}\int_0^{\sqrt{1-I^2}} \frac{\xi^2 d\xi}{(1-\xi^2)\sqrt{\sqrt{1-\xi^2}+I}} \\
&= \frac{\sqrt{2}}{\sqrt{k}}\int_{|I|}^1 \frac{1-\zeta^2}{\zeta\sqrt{(1-\zeta^2)(\zeta-|I|)}}d\zeta\,.
\end{aligned} \tag{3.31}$$

Evaluating the integral, we find

$$P(k,I) = \frac{\mu(I)}{\sqrt{k}}\,, \tag{3.32}$$

89

where we define the function $\mu(I)$ by

$$\mu(I) = 2\left(\frac{1+|I|}{|I|}\right)\Pi\left(-\frac{1-|I|}{2|I|},\frac{\sqrt{2(1-|I|)}}{2}\right) - 4E\left(\frac{\sqrt{2(1-|I|)}}{2}\right) \tag{3.33}$$

where Π denotes the incomplete elliptic integral of the third kind. We find that $\mu(-1) = 0$, $\lim_{I\to 0^-}\mu(I) = +\infty$, and $\mu(I)$ is monotone increasing on $I \in (-1,0)$. Hence, $\mu(I)$ is positive on $I \in (-1,0)$. Now,

$$\frac{\partial P}{\partial k} = -\frac{\mu(I)}{2k^{3/2}} < 0 \tag{3.34}$$

for all $k > 0$ and all $I \in (-1,0)$. Space-periodic solutions $\psi(x)$ exist if and only if $k > 0$ and $I \in (-1,0)$. Therefore, by the VK stability criterion, the stationary solution (3.20) with space-periodic $\psi(x)$ is orbitally stable provided it exists. We have therefore show the following stability result:

Theorem 3: A non-zero stationary solution $e^{-i\omega t}\psi(x)$ with space-periodic $\psi(x)$ (meaning $-1 < I < 0$) to the WKIS equation is orbitally stable if its spectrum is positive definite (it has no negative energy excited states, i.e. $k > 0$).

3.2.4 Discussion

Previously, it was shown that space-periodic stationary solutions exist for the WKIS equation [101]. However, the stability of such solutions was unknown. Given a periodic solution $\psi(x)$ to (3.21) (which exists for $-1 < I < 0$), we have been able to prove that a non-zero stationary solution $e^{-i\omega t}\psi(x)$ for the WKIS equation is orbitally stable if its spectrum is positive definite

(it has no negative energy excited states, i.e. $k > 0$). Hence, the class of stationary solutions with space-periodic behavior, such as those displayed in Fig. 3.3, are indeed orbitally stable.

Of interest, note that the stability result was completely analytic, as opposed to numerical. Hence, we can view this as an exact as opposed to approximate result. The method can likely be applied to a number of other types of derivative NLS equations, in order to deduce orbital stability of space-periodic stationary solutions. Like in the present case, we would expect many cases to exhibit exact results, likely in terms of elliptic functions and integrals.

3.3   Stability for a localized soliton

The Peregrine soliton is one possible model of a rogue wave. Importantly, this type of soliton corresponds nicely to rogue waves recently observed experimentally in a water tank [21] and in an optical fiber [48]. Starting with a family of Peregrine solitons indexed by their spectral parameter, we analytically demonstrate a type of instability in the Peregrine soliton through a concise orbital stability analysis. This analysis is completely analytical, and to verify the approach we also discuss a numerical linear instability analysis. We give the growth/decay rate for these solitons as a function of the initial amplitude, which for each soliton shall depend on the spectral parameter. The procedure outlined here follows that of Van Gorder [110].

3.3.1 Background

The generation of rogue waves has been a topic of much research and debate [70]. The interaction of solitons with background waves or currents has been considered [69], and generation of such waves through instabilities has been analytically modeled through the use of Akhmediev breathers [27]. In the absence of wave-current interaction the Benjamin-Feir (BF) or modulational instability [14] and an essentially linear space-time focusing [47] have been considered as possible candidates for rogue wave formation. Physically, these rogue wave have traditionally been considered in studies of freak ocean waves [28]. Recently, rogue waves were observed experimentally in a water tank [21]. However, attention has also been directed toward the role of rogue waves in optics [88].

The Peregrine soliton [73] is one type of rational solitary wave solution to the cubic NLS $i\psi_t + \frac{1}{2}\psi_{xx} + |\psi|^2\psi = 0$. This type of soliton occurs as a degenerate limit of both Kuznetsov-Ma and Akhmediev breathers [91]. The soliton is localized in both space and time, and therefore it reproduces the transient nature of rogue waves in a qualitative manner. Importantly, the Peregrine soliton corresponds nicely to rogue waves recently observed experimentally in a water tank [21]. The Peregrine soliton has also been found experimentally in optical fiber [48], and such solitons can also occur in superfluids and Bose-Einstein condensates [16], as well as plasmas [9]. Mathematical properties of Peregrine solitons were considered in [91]. A vector Peregrine solition is possible [12], as are so-called higher order Peregrine solitons [43]. The structural stability under generalized forms of the standard NLS

have been considered [4, 10]; such studies involve studying the effect of adding small terms to the NLS has on the resulting rogue wave solitons. A linear modulation stability analysis was recently considered for a class of rogue waves in the presence of an unstable condensate [123]. Modulational instability of the $\mathcal{PT}$-symmetric and anti-symmetric rogue waves have also been considered [15]. Note that one may consider a Peregrine soliton on a fluctuating background [83].

In this section, we shall study the orbital instability of a family of Peregrine solitons. Members of this family are rational solitons which are parameterized by the spectral parameter ω. After demonstrating the existence of this family for all $\omega < 0$, we demonstrate the orbital instability of these Peregrine solitons through a concise analytical stability analysis. This stability analysis is completely analytical and relatively straightforward. Still, to verify the analytical method we shall also consider a numerical linear instability analysis, which is shown to agree with the analytical results. Physically, we are able to provide the growth or decay rate for these solitons as a function of the initial amplitude at $t = 0$. It is noteworthy that the amplitude of these solitons depends fundamentally on the spectral parameter, hence the phase and amplitude of the solitons are closely related.

3.3.2 Parameterized family of rational solitons

We shall be interested in a family of such rational solitons, indexed by their spectral parameters. This type of scaling follows from symmetry properties of the NLS equation, and

a special case was considered in [2] (see equation (7) of that paper). Assuming a rational soliton $\psi_\omega(x,t) = \rho_\omega(x,t)e^{-i\omega t}$, where $\omega < 0$ is the spectral parameter, we find (after calculations we omit here)

$$\psi_\omega(x,t) = \sqrt{|\omega|}\left(1 - \frac{4(1 + 2|\omega|it)}{1 + 4[|\omega|x^2 + \omega^2 t^2]}\right)e^{-i\omega t}. \tag{3.35}$$

The standard Peregrine soliton corresponds to $\omega = -1$, so (3.35) constitutes a family of such solitons, scaled by the spectral parameter. Solitons (3.35) have a maximum amplitude $A(t = 0) = 3\sqrt{|\omega|}$, which is three times the mean wave-height $\sqrt{|\omega|}$. (Note that the mean or background waves are given by $\sqrt{|\omega|}e^{-i\omega t}$.) It shall be most useful to define a shifted solution $\hat{\psi}_\omega = \psi_\omega - \sqrt{|\omega|}e^{-i\omega t}$ to remove the background. (This shifting was done for the spectrally transformed version of the soliton [1] where it was shown that the Peregrine soliton has a triangular spectrum at every stage of its development, which points to a possible application where one might identify the occurrence of such rogue waves by detecting their spectral signatures.) Initial mass is conserved with respect to the spectral parameter, $M = \int_{-\infty}^{\infty}|\psi_\omega(x,0)|dx = 2\pi$. Yet, as $|\omega|$ increases, A increases while M remains fixed, so larger amplitude waves allocate a greater proportion of their mass near the origin. This suggests that waves of greater amplitude may have greater decay rates, and indeed this is true. Let t_* be the time taken for the wave to decay to an amplitude $A(t_*) = \alpha\sqrt{|\omega|}$, where $1 < \alpha < 3$. One finds that $t_* = \frac{1}{2|\omega|}\sqrt{\frac{9-\alpha^2}{\alpha^2-1}} = \frac{9}{2A^2}\sqrt{\frac{9-\alpha^2}{\alpha^2-1}}$ and hence the greater the initial amplitude, the greater the rate of decay. For instance, the time taken for a soliton (3.35) to decay to one-half the initial wave height ($\alpha = 1.5$) is $t_* = 10.4571/A^2$. Since the solitons (3.35) are

94

symmetric with respect to $t = 0$, this value is equivalent to the time it takes a wave to grow (in particular, to double its height).

The time-evolution of one such soliton, corresponding to $\omega = -0.2$, is given in Fig. 3.5. The influence of the spectral parameter ω on the envelope profiles is demonstrated in Fig. 3.6.
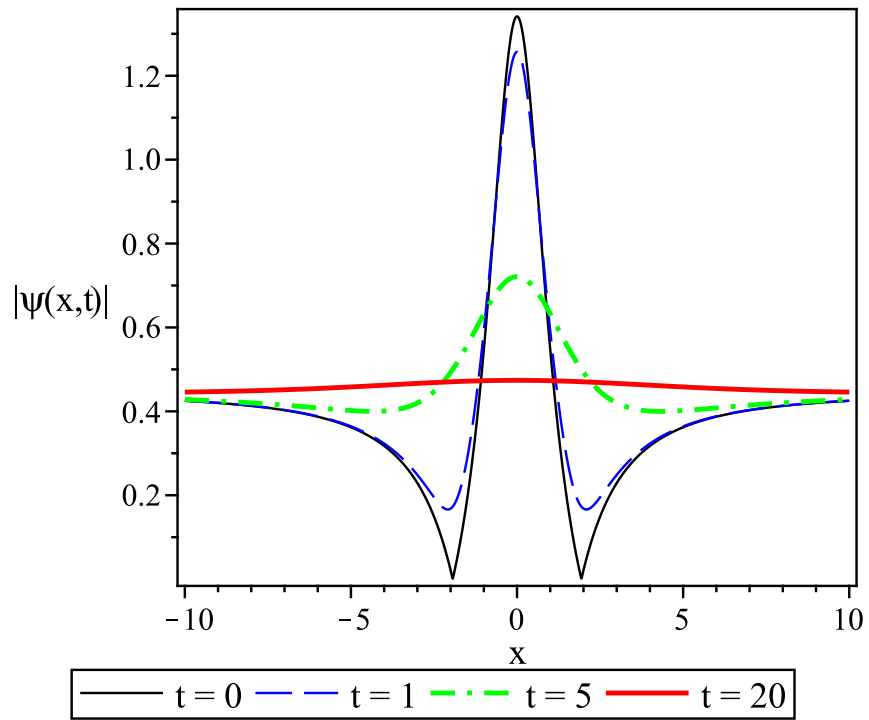
Figure 3.5: Time-evolution of the localized soliton (3.35) corresponding to $\omega = -0.2$.
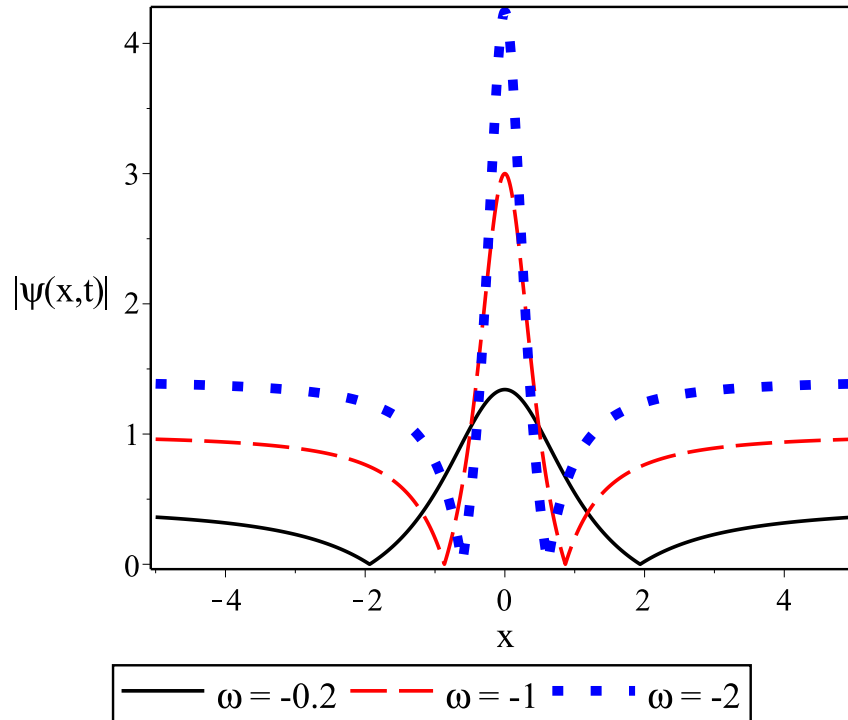
Figure 3.6: Influence of the spectral parameter, $\omega < 0$, on the wave envelopes. As $|\omega|$ increases, the amplitude increases like $3\sqrt{|\omega|}$ yet the mass of the wave remains fixed. Hence, a greater proportion of mass is allocated near the center of the wave, in the case of large amplitude solitons. Note that by amplitude, we refer to deviation of the mean wave-height (which is $\sqrt{|\omega|}$) - the total height of the wave, in this model, is $4\sqrt{|\omega|}$.

3.3.3 Orbital stability analysis

The inclusion of the spectral parameter has given us some indication how a Peregrine soliton should behave depending on amplitude. While the wave naturally has a tendency to decay asymptotically in time, one may wonder if the wave is robust against spectral perturbations, and for this the inclusion of the spectral parameter in (3.35) is essential. To demonstrate that the Peregrine soliton is orbitally unstable we apply the Vakhitov-Kolokolov stability criterion [97], which has been applied to discuss the stability of stationary solutions in one or many spectral parameters; see [61, 87, 58, 66] for some applications. The criterion has been applied to a variety of integrable equations [63], and relates the change in the soliton charge with respect to the spectral parameter to the orbital stability of that soliton.

Define the soliton charge or momentum by

$$P(\psi) = \frac{1}{2} \int_{-\infty}^{\infty} |\psi(x,t)|^2 dx\,. \tag{3.36}$$

Since (3.35) includes a background, we use the shifted function $\hat{\psi}_\omega$ (which results in the charge relative to and not including the background). A straightforward calculation shows

$$P(\hat{\psi}_\omega) = 2\pi[|\omega|(1 + 4\omega^2 t^2)]^{-1/2}\,. \tag{3.37}$$

When applicable, the Vakhitov-Kolokolov stability criterion implies that $\frac{d}{d\omega}P(u_\omega) < 0$ is a necessary condition for linear stability of the orbit. On the other hand, if $\frac{d}{d\omega}P(u_\omega) > 0$, then the solution is orbitally unstable (in such a case, the linear stability analysis shows the existence of spectral values on the right half of the complex plane, implying linear instability).

We find

$$\frac{dP}{d\omega} = \pi(1 + 12\omega^2 t^2)[|\omega|(1 + 4\omega^2 t^2)]^{-3/2} > 0 \qquad (3.38)$$

for finite t. So, we expect the family of solitons (3.35) to be orbitally unstable. Mathematically, this means that given a rogue wave solution (3.35), say $\psi(x,t)$, the difference between ψ and a perturbation of this function, say ψ_{pert}, will grow so that ψ and ψ_{pert} are drastically different. (Contrast this to the orbitally stable case, where the two functions can be made to remain arbitrarily close, under sufficiently small perturbations.) Regarding the specific manner of instability, the waves must collapse under perturbations. This is consistent with the fact that the Peregrine soliton is considered one possible model of rogue waves, and that such structures are highly localized phenomenon which are highly sensitive to initial data and hence perturbations.

The result is interesting since the VK-type criterion is usually applied to solitons with the modulus $|\psi|$ strictly a function of x. Often, a soliton with time-dependent modulus is much harder to study in a spectral sense, because the spectrum becomes time-dependent. Of course, the instability here could be determined by introducing a small perturbation to the soliton (3.35), $\Psi = (\rho_\omega + a(x,t) + ib(x,t))e^{-i\omega t}$, where $|a|, |b| << 1$ and ρ_ω is the rational factor of (3.35). The evolution of these small perturbations is governed by (see, e.g.,)
$\frac{\partial}{\partial t}\begin{pmatrix} a \\ b \end{pmatrix} = \mathcal{J}\begin{pmatrix} a \\ b \end{pmatrix}$, where the operator matrix $\mathcal{J}$ is given by

$$\mathcal{J} = \begin{pmatrix} 0 & -\frac{1}{2}\frac{\partial^2}{\partial x^2} - \omega - |\rho_\omega|^2 \\ -\left(-\frac{1}{2}\frac{\partial^2}{\partial x^2} - \omega - 3|\rho_\omega|^2\right) & 0 \end{pmatrix}. \qquad (3.39)$$

99

The spectrum of $\mathcal{J}$ is in general time-dependent, since ρ_ω depends not only on space (as is often the case) but also on time. Still, for a desired value of ω, we may numerically determine the spectrum of the operator $\mathcal{J}$ [22], which upon calculation implies linear instability (when $\omega < 0$) due to the small perturbation $(a(x,t) + ib(x,t))e^{-i\omega t}$ at all finite times. Note that this calculation is possible since ρ_ω is well-behaved, even though it depends on time. Indeed, we may show that $\omega^2 \le |\rho_\omega|^2 \le 9\omega^2$ for all $x \in \mathbb{R}$ and all $t \ge 0$. It is also possible to study the rate of soliton instability [45] by calculating the maximal eigenvalue of $\mathcal{J}$, though this is complicated again by the appearance of the time variable in the operator $\mathcal{J}$. However, note that the instability rate is not related to the magnitude of $\frac{dP}{d\omega}$ [45].

3.3.4   Discussion

In summary, we have constructed a family of scaled Peregrine solitons, where the scaling is due to a spectral parameter $\omega < 0$. The initial mass of the wave is invariant under this spectral parameter, while the initial amplitude scales as the square of the spectral parameter, $A \sim \omega^2$. Therefore, large amplitude solitons of this type concentrate a greater percentage of their mass near the origin. We calculate that the rate of decay of the solitons scales as A^{-2}, so large-amplitude solitons decay quickly. The important contribution is that we were able to show that a family of scaled Peregrine soltons are orbitally unstable using a concise analytical approach. Such an approach (typically used for stationary solitons - solitons for which the complex modulus is time-independent) was successful here since the temporal behavior of

the solitons is rather tame. The analytical results are in agreement with a numerical linear stability analysis, which suggests linear instability of the solitons under small perturbations.

While the eigenvalues of $\mathcal{J}$ are time-dependent, and hence the rate of instability is too complicated for an analytical analysis, it is reasonable to say that larger amplitude solitons are less stable than their small-amplitude counterparts. This is evident, since the large-amplitude solitons have faster growth and decay rates (the time for such rogue waves to form and dissipate is small, and scales as $\sim A^{-2}$ with the amplitude A). Since the amplitude of the rogue waves modeled by the Peregrine solitons are three times the ambient wave-heights, this means that the Peregrine solitons exhibit a higher rate of instability in the presence of large ambient wave-heights. On the other hand, when ambient wave-heights are rather small, the Peregrine soliton survives longer (though not eternally like many solitons, since it is still a localized phenomenon).

CHAPTER 4

BREAKDOWN OF SINGLE VALUED SOLUTIONS AND VORTEX COLLAPSE

4.1 Scaling laws and accurate small-amplitude stationary solution for the LIA

We provide a formulation of the local induction approximation (LIA) for the motion of a vortex filament in the Cartesian reference frame (the extrinsic coordinate system) which allows for scaling of the reference coordinate. For general monotone scalings of the reference coordinate, we derive an equation for the planar solution to the derivative nonlinear Schrödinger equation governing the LIA. We proceed to solve this equation perturbatively in small amplitude through an application of multiple scales analysis, which allows for accurate computation of the period of the planar vortex filament. The perturbation result is shown to agree strongly with numerical simulations, and we also relate this solution back to the solution obtained in the arclength reference frame (the intrinsic coordinate system). The scaling laws and matched / self-intersecting solutions considered in this and the next section were first considered in Van Gorder [105].

4.1.1 Formulation and scaling the LIA

Alternate scaling of the LIA can be useful both for physical analysis and for computational reasons. For instance, the infinite domain due to $x \in \mathbb{R}$ can be mapped into a closed and bounded interval, which can assist with analytical and numerical analysis. We first determine the influence of such transforms. Let us consider the scaled position vector

$$\mathbf{r} = f(x)\mathbf{i}_x + y(x,t)\mathbf{i}_y + z(x,t)\mathbf{i}_z \,, \tag{4.1}$$

where $f(x)$ denotes a general scaling of the x-coordinate. This is one of two possible equivalent such scalings, with the other being

$$\mathbf{r} = x\mathbf{i}_x + y(f^{-1}(x),t)\mathbf{i}_y + z(f^{-1}(x),t)\mathbf{i}_z \tag{4.2}$$

provided f^{-1}, the inverse map of f, exists. For this reason, we will often be interested in monotone scalings f so that the inversion f^{-1} is well-defined. We chose to work with (4.1) as opposed to (4.2) since it gives more computationally tractable results. From (4.1), we compute

$$\mathbf{t} = \frac{d\mathbf{r}}{ds} = \frac{d\mathbf{r}}{dx}\frac{dx}{ds} = (f', y_x, z_x)\frac{dx}{ds} \tag{4.3}$$

and $\mathbf{v} = (0, y_t, z_t)$, where

$$\frac{dx}{ds} = \frac{1}{\sqrt{f'^2 + y_x^2 + z_x^2}}\,. \tag{4.4}$$

We then have $\kappa\mathbf{n} = \frac{d\mathbf{t}}{ds} = \frac{d\mathbf{t}}{dx}\frac{dx}{ds}$, giving

$$\kappa\mathbf{n} = \left[f''(y_x^2 + z_x^2) - f'(y_x y_{xx} + z_x z_{xx})\right]\frac{dx}{ds}\mathbf{i}_x$$
$$+ \left[y_{xx}z_x - y_x z_x z_{xx} + y_{xx}f'^2 - f'f''y_x\right]\frac{dx}{ds}\mathbf{i}_y \tag{4.5}$$
$$+ \left[z_{xx}y_x^2 - z_x y_x y_{xx} + z_{xx}f'^2 - f'f''z_x\right]\frac{dx}{ds}\mathbf{i}_z\,,$$

so that $\mathbf{v} = \gamma\kappa\mathbf{t} \times \mathbf{n} = \gamma\mathbf{t} \times (\kappa\mathbf{n})$ becomes

$$\mathbf{v} = \gamma(y_x z_{xx} - z_x y_{xx})\left(\frac{dx}{ds}\right)^3 \mathbf{i}_x$$
$$- \gamma(f'z_{xx} - f''z_x)\left(\frac{dx}{ds}\right)^3 \mathbf{i}_y \tag{4.6}$$
$$+ \gamma(f'y_{xx} - f''y_x)\left(\frac{dx}{ds}\right)^3 \mathbf{i}_z\,.$$

Matching the two representation of $\mathbf{v}$, we obtain the constraint $y_x z_{xx} - z_x y_{xx} = 0$ and the real-valued system

$$y_t = -\gamma(f'z_{xx} - f''z_x)\left(\frac{dx}{ds}\right)^3\,, \tag{4.7}$$

$$z_t = \gamma(f'y_{xx} - f''y_x)\left(\frac{dx}{ds}\right)^3\,. \tag{4.8}$$

Introducing the complex potential function

$$\Phi(x, t) = y(x, t) + iz(x, t)\,, \tag{4.9}$$

the PDE system reduces to

$$i\Phi_t + \gamma\left(f'\Phi_{xx} - f''\Phi_x\right)\left(f'^2 + |\Phi_x|^2\right)^{-3/2} = 0\,. \tag{4.10}$$

Note that (4.10) is a complicated nonlinear Schrödinger equation with variable coefficients (f' and f'' in general depend on x). However, with the scaling $\Phi(x, t) = \Psi(\mu, t)$ where

$\mu = f(x)$, we may reduce (4.10) to

$$i\Psi_t + \gamma \left(1 + |\Psi_\mu|^2\right)^{-3/2} \Psi_{\mu\mu} = 0 \,, \tag{4.11}$$

for non-degenerate f. Hence, (4.10) yields solutions of the LIA. The transformed equation (4.11) matches exactly that studied in [98, 99].

The form of (4.10) (and hence (4.11)) is $U(1)$-invariant, just like many of its derivative NLS relatives, hence it makes sense to consider stationary solutions of the form $\Phi(x, t) = e^{-i\gamma t}\phi(x)$ to (4.10) (and $\Psi(\mu, t) = e^{-i\gamma t}\psi(\mu)$ to (4.11)).

To summarize, the permitted scalings are that for which:

(i) the LIA is invariant under monotone scalings of the x coordinate;

(ii) the LIA is invariant under scalings of the form $e^{-i\gamma t}$.

Together, these conditions guarantee the existence of planar vortex filaments described by $\Psi(x, t) = e^{-i\gamma t}\psi(\mu(x))$. In the extrinsic three-dimensional Cartesian frame, the position of the planar vortex filament at any time t is then given by

$$\mathbf{r} = \mu(x)\mathbf{i}_x + \cos(\gamma t)\psi(\mu(x))\mathbf{i}_y - \sin(\gamma t)\psi(\mu(x))\mathbf{i}_z \,, \tag{4.12}$$

To better visualize such vortex filaments, see Fig. 4.1, where we consider a periodic function $\psi(\mu(x))$. The vortex filament rotates about the x-axis as time increases. So, by determining $\psi(\mu(x))$, we determine the spatial structure of the planar vortex filament completely, the inclusion of a factor $e^{-i\gamma t}$ providing the motion of such a filament in time.
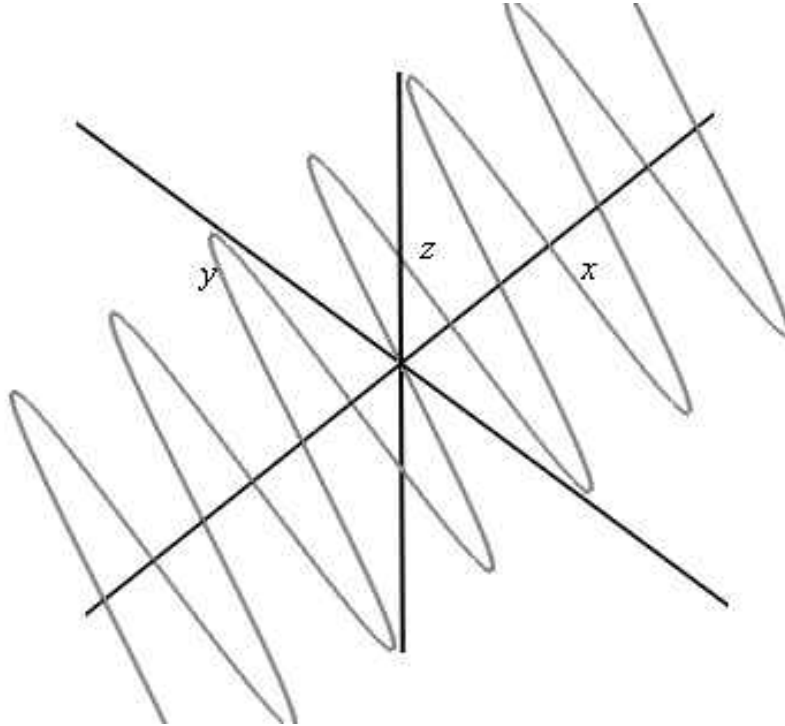
Figure 4.1: Plot of the spatial geometry. The curve represents the planar vortex filament described by $\Phi(x,t) = e^{-i\gamma t}\phi(\mu(x))$ for periodic $\psi(\mu(x))$. As time increases, the structure rotates about the x-axis.

4.1.2 Accurate perturbation approach for the stationary solution

Let us consider the stationary solution $\Psi(\mu, t) = Ae^{-i\gamma t}\psi(\mu)$ to the scaled equation (4.11), where we let the parameter $A > 0$ be the amplitude and normalize $\max \psi = 1$. Then, we obtain the ordinary differential equation

$$\psi + \left(1 + A^2\psi'^2\right)^{-3/2}\psi'' = 0\,. \tag{4.13}$$

The simplest nonlinear approximation to equation (**??**) takes the form

$$\psi + \left(1 - \frac{3}{2}A^2\psi'^2\right)\psi'' = 0\,. \tag{4.14}$$

As discussed in a forthcoming work, (4.14) has periodic real-valued solutions for $A < 1/\sqrt{3} \approx 0.577$. For small A, (4.14) is a good approximation to (4.13). It then makes sense to consider a perturbation solution, in terms of the small parameter A^2. However, standard perturbation will yield inaccurate solutions which fall out of resonance with the true solution due to the appearance of secular terms. Hence, we shall be interested in applying the method of multiple scales to (4.14). To proceed, assume there exists parameter $\delta(A^2)$ such that $d/d\mu = \delta(A^2)(d/d\eta)$ where $\eta = \delta(A^2)\mu$. Then, we consider the perturbation solution $\psi(\mu) = \hat{\psi}(\eta; A^2) = \psi_0(\eta; A^2) + A^2\psi_1(\eta; A^2) + O(A^4)$, $\delta(A^2) = \delta_0 + A^2\delta_1 + O(A^4)$. Equation (4.14) becomes

$$\hat{\psi} + \delta^2\left(1 - \frac{3}{2}A^2\delta^2\hat{\psi}_\eta^2\right)\hat{\psi}_{\eta\eta} = 0\,, \tag{4.15}$$

giving

$$\delta_0^2\psi_{0,\eta\eta} + \psi_0 = 0\,, \quad \psi_0(0) = 1\,, \quad \psi_{0,\eta}(0) = 0\,, \tag{4.16}$$

$$\delta_0^2 \psi_{1,\eta\eta} + \psi_1 = \frac{3}{2}\delta_0^4 \psi_{0,\eta}^2 (\psi_0)_{\eta\eta} - 2\delta_0\delta_1\psi_{0,\eta\eta},$$

$$\psi_1(0) = 0 = (\psi_1)_\eta(0).$$

(4.17)

The quantities at $\eta = 0$ follow from the fact that we desire space-periodic ψ with amplitude A. As we assume a solution $\Psi = A\psi \exp(-i\gamma t)$, it follows that the amplitude of ψ must be 1 (then the amplitude of Ψ is A). Without loss of generality, we take $\eta = 0$ to correspond to a peak (this can be translated by $\eta \mapsto \eta' + \eta_0$ if need be). Thus, $\psi_\eta(x) = 0$. Assuming $\psi = \psi_0 + A^2\psi_1 + \cdots$, it follows that $\psi_0(0) = 1$, $\psi_{0,\eta}(0) = 0$, $\psi_1(0) = 1$ and $\psi_{1,\eta}(0) = 0$.

Normalizing to get 2π-periodic solutions, we pick $\delta_0 = 1$, obtaining $\psi_0(\eta) = \cos(\eta)$. From here, we have

$$(\psi_1)_{\eta\eta} + \psi_1 = \left(2\delta_1 - \frac{3}{8}\right)\cos(\eta) + \frac{3}{8}\cos(3\eta),$$

(4.18)

so picking $\delta_1 = 3/16$ prevents any secular terms. We then obtain

$$\psi_1(\eta) = \frac{3}{64}\left(\cos(\eta) - \cos(3\eta)\right) = \frac{3}{16}\sin^2(\eta)\cos(\eta).$$

(4.19)

Therefore, we have obtained the perturbation solution

$$\psi(\mu) = \cos\left(\left[1 + \frac{3}{16}A^2\right]\mu\right)$$
$$+ \frac{3}{16}A^2 \sin^2\left(\left[1 + \frac{3}{16}A^2\right]\mu\right)\cos\left(\left[1 + \frac{3}{16}A^2\right]\mu\right).$$

(4.20)

Consider the standard case $\mu(x) = x$. From Eq. (4.20), we see that the approximate period of small-amplitude solutions satisfies

$$T(A) \approx 2\pi\left[1 + \frac{3}{16}A^2\right]^{-1} \approx 2\pi - \frac{3\pi}{8}A^2 + \frac{9\pi}{128}A^4.$$

(4.21)

In order to demonstrate the agreement between the solution (4.20) and the true solution, we plot the numerical solution along with the perturbation solution in Fig. 4.2. Since the perturbation and numerical results agree so nicely, the difference between the two is not easily ascertainable, so we plot their errors separately, in Fig. 4.3.
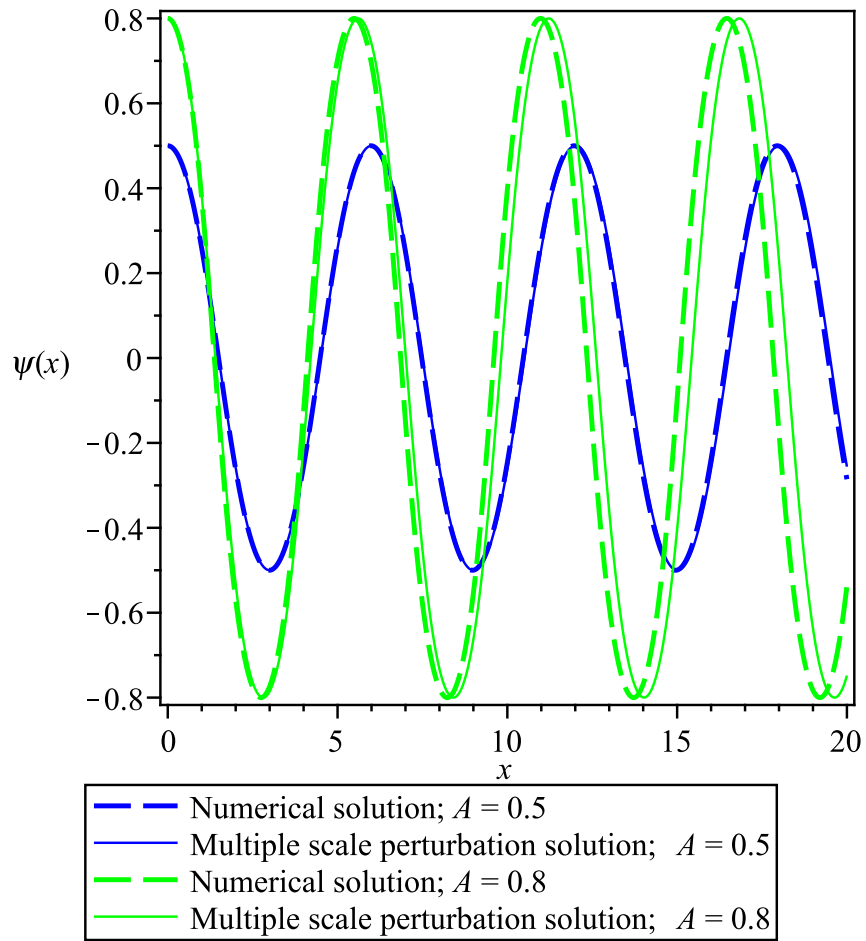
Figure 4.2: Plot of the perturbation solutions (4.20) for $\psi(x)$ obtained through the method of multiple scales against numerical solutions obtained via the Runge-Kutta-Fehlberg method (RKF45) [29]. The valid region for the approximation (4.14) is $A < 1/\sqrt{3} \approx 0.577$, and in this region the results agree nicely. For larger A, the agreement breaks down, as the solutions fall out of resonance with the true solutions.
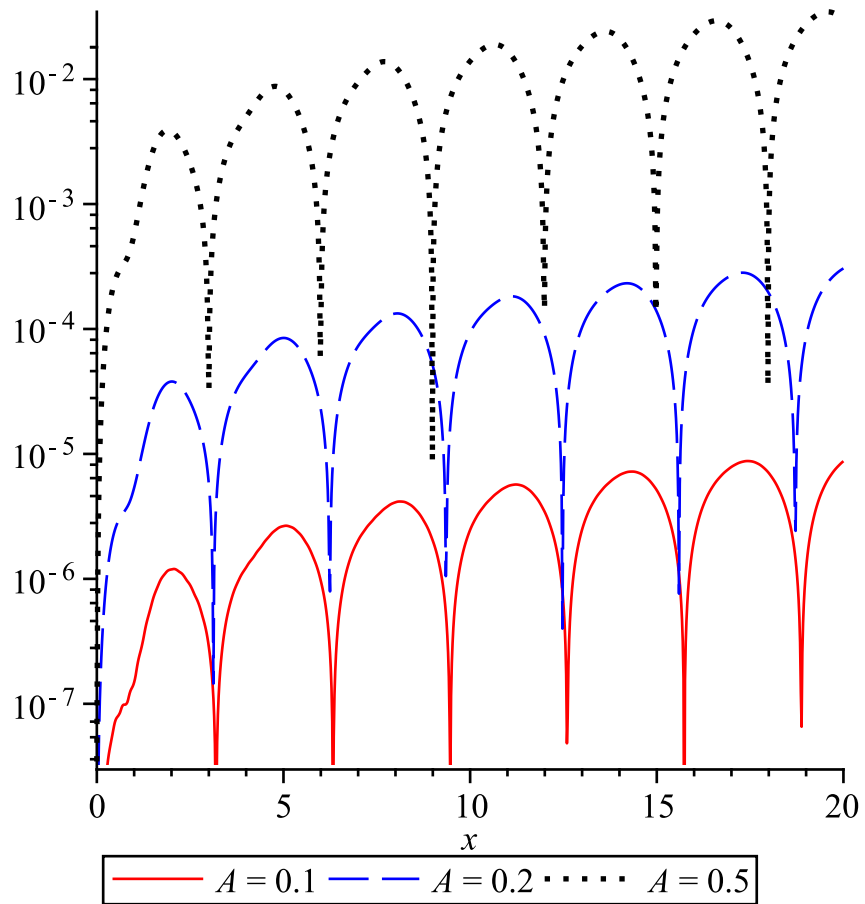
Figure 4.3: Plot of the absolute error between the perturbation solutions (4.20) for $\psi(x)$ obtained through the method of multiple scales and the numerical solutions obtained via the Runge-Kutta-Fehlberg method (RKF45) [29]. The agreement is strong for small amplitude solutions, while the agreement gradually breaks down for larger amplitudes.

4.1.3 Connection with arclength solution and implicit solution

In this section, take $\mu(x) = x$, so that $\Phi(x, t) = \Psi(\mu, t)$. In Van Gorder [100], an exact stationary solution for the arclength formulation of the LIA was given by

$$v(s, t) = e^{-it}q(s) = Be^{-it}\text{sn}\left(\frac{s - \hat{s}}{\sqrt{1 - B^2}}, Bi\right),\tag{4.22}$$

where B is the amplitude (in the arclength frame), $\hat{s}$ is a constant, and s is the arclength element. It was shown in [95] that the Cartesian quantity $\Phi(x, t)$ and the arclength quantity $v(s, t)$ are related by

$$|\Phi_x|^2 = \frac{2|v|^2}{(1 - |v|^2)^2}, \quad \frac{dx}{ds} = \frac{1 - |v|^2}{1 + |v|^2}.\tag{4.23}$$

Noting that $|\Phi_x| = \phi'(x)$ and $|v| = q(s)$, we have that $\phi'^2 = 2q^2(1 - q^2)^{-2}$. Separating variables, and using the form of dx/ds given in (4.23), we obtain

$$\phi(x) = \sqrt{2}\int_{\hat{s}}^{s(x)} \frac{B\text{sn}\left(\frac{s-\hat{s}}{\sqrt{1-B^2}}, Bi\right)}{1 + B^2\text{sn}^2\left(\frac{s-\hat{s}}{\sqrt{1-B^2}}, Bi\right)}ds.\tag{4.24}$$

Performing the integration exactly is not possible (in closed form). And then, one must still contend with the arclength variable $s(x)$. So, while this formula offers a connection between the exact arclength solution to the planar vortex filament problem and that of the Cartesian problem, it is not very practical. We can compare this formula to the direct solution for $\phi(x)$. A first integral of (4.13) (when $\mu = x$ and hence $\psi(\mu) = \phi(x)$) is

$$\phi^2 - \frac{2}{A^2\sqrt{1 + A^2\phi'^2}} = -\mathcal{E}.\tag{4.25}$$

If $\phi(0) = 1$, $\phi'(0) = 0$, then $\mathcal{E} = (2 - A^2)/A^2 > 0$ since $|A| < \sqrt{2}$ for any periodic solution.

Solving (4.25) for ϕ' and separating variables as needed,

$$x = \pm \int_\phi^1 \frac{A^3(\zeta^2 + \mathcal{E})}{\sqrt{4 - A^4(\zeta^2 + \mathcal{E})^2}} d\zeta . \tag{4.26}$$

Changing variables to $\xi = \zeta^2 + \mathcal{E}$,

$$x = \pm \frac{A^3}{2} \int_{\phi^2 + \mathcal{E}}^{2/A^2} \frac{\xi d\xi}{\sqrt{(\xi - \mathcal{E})(2 - A^2\xi)(2 + A^2\xi)}} . \tag{4.27}$$

Eq. (4.27) is an implicit solution which is not easily inverted. However, we may still extract information out of this relation more easily than is the case when dealing with (4.24). In the previous section, we approximated the period of a space-periodic planar vortex filament using perturbation. We shall now be interested in comparing that approximation with a true exact relation between the period T and amplitude A for a space-periodic solution to the vortex filament problem.

If we consider the phase portrait, a quarter-period $T(A)/4$ occurs when ϕ goes from $\phi = 0$ to $\phi = 1$, so from Eq. (4.27) we obtain the exact yet implicit relation

$$T(A) = 2A^3 \int_{\mathcal{E}}^{2/A^2} \frac{\xi d\xi}{\sqrt{(\xi - \mathcal{E})(2 - A^2\xi)(2 + A^2\xi)}} . \tag{4.28}$$

Now, in the valid region $0 < A < \sqrt{2}$, the definite integral (4.28) can be evaluated in terms of elliptic integrals to give the relation

$$T(A) = 8E\left(A/2\right) - 4K\left(A/2\right) , \tag{4.29}$$

where K is the complete elliptic integral of the first kind and E is the complete elliptic integral of the second kind. Recall that the period of the solutions in the arclength representation

[100], the period of the space-periodic solution was a bit simpler, involving only the elliptic integral K.

In order to extract more information from Eq. (4.29), we turn to the small-θ asymptotics

$$K(\theta) = \frac{\pi}{2}\left(1 + \frac{1}{4}\frac{\theta^2}{1-\theta^2} - \frac{1}{8}\frac{\theta^4}{1-\theta^2}\right), \tag{4.30}$$

$$E(\theta) = \frac{\pi}{2}\left(1 - \frac{1}{4}\theta^2 - \frac{3}{64}\theta^4\right). \tag{4.31}$$

Using (4.30)-(4.31) in (4.29), and approximating where needed,

$$T(A) \approx 2\pi - \frac{3\pi}{8}A^2 - \frac{7\pi}{256}A^4. \tag{4.32}$$

Note that the approximation (4.32) to the period $T(A)$ obtained through the fully nonlinear relation (4.27) for ϕ is in extremely good agreement with the approximation obtained through the method of multiple scales (4.21) for the period $T(A)$. In Fig. 4.4, we plot the exact period $T(A)$ found in (4.29), along with the approximations shown in (4.21) and (4.32). In Fig. 4.5, we plot the relative error between the approximations and the exact values.
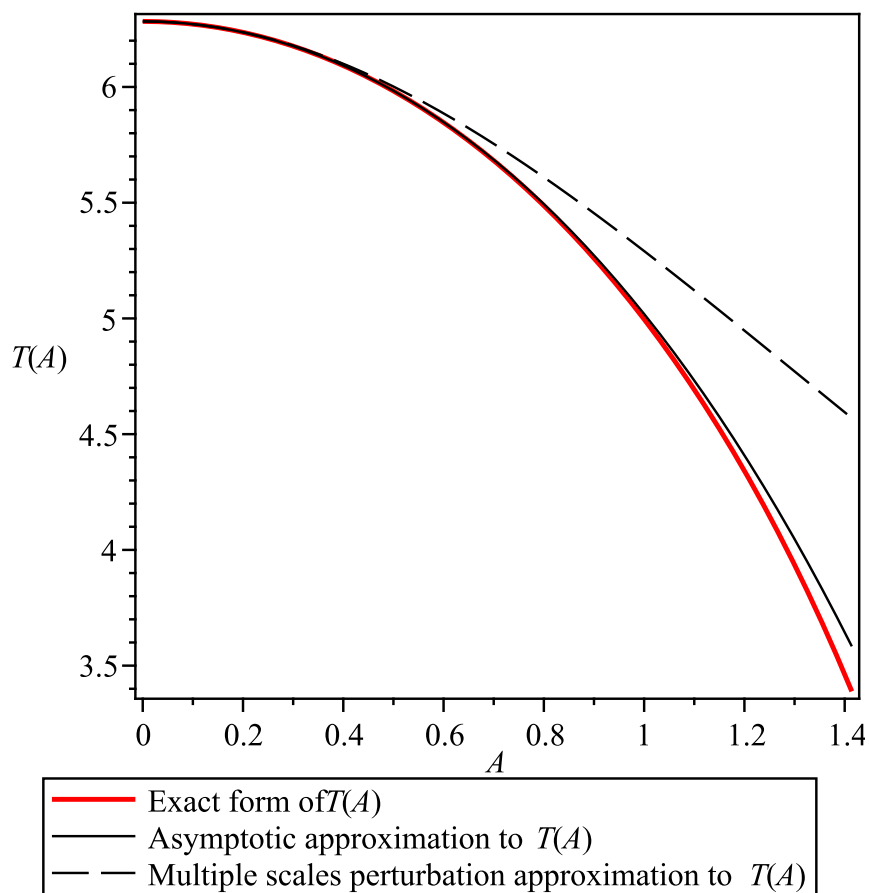
Figure 4.4: Plot of the x-period $T(A)$ for the stationary solution x-dependence function $\phi(x)$. In addition to the exact value (4.29), we plot two approximate quantities, namely the approximation found through multiple scales (4.21) and the asymptotic approximation (4.32) to the true result (4.29). We consider $A \in [0, \sqrt{2}]$.
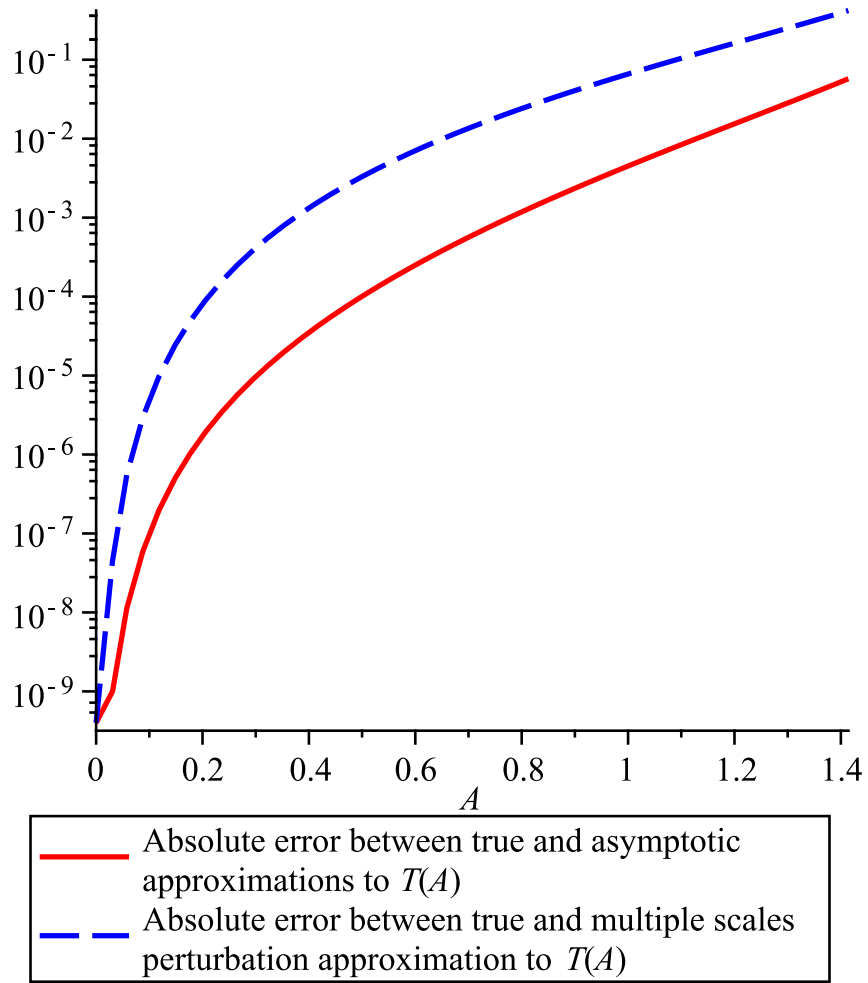
Figure 4.5: We demonstrate the relative error between the approximations to the period $T(A)$ and the true solution (4.29). Both are extremely accurate for small A, and gradually lose accuracy for larger A, though the asymptotic approximation (4.32) outperforms the multiple scale approximation (4.21) nicely. That said, in its region of validity $(A < 1/\sqrt{3})$, the multiple scale approximation (4.21) is rather accurate for only a first order perturbation result.

4.1.4 Discussion

We have derived the fully nonlinear form of the local induction approximation (LIA) governing the motion of a vortex filament. Permitting a scaling of the free coordinate along which the vortex is aligned (x, in our case) permits us to have greater flexibility in computing solutions, both analytically and numerically. Such vortex solutions are a variation on the theme of planar vortex filaments, and take the form

$$\mathbf{r} = (f(x), \cos(\gamma t)\phi(x), -\sin(\gamma t)\phi(x)) . \tag{4.33}$$

The main analytical benefit is that such a solution form can capture a greater range of physical behaviors (particularly when the scale is non-monotone), while numerical simulations can be made easier by taking a scale $f : \mathbb{R} \to \mathcal{I}$ where $\mathcal{I}$ is a compact interval (numerical integration on such a compact interval can often be simpler than on an unbounded domain such as the real line).

In the case of monotone scalings $f(x) = \mu$, we have a very elegant way to determine the planar contribution $\phi(x) = \psi(\mu)$ to the vortex filament structure, obtaining a nonlinear ordinary differential equation (ODE) governing ψ; see (4.13). For monotone scalings, we therefore find that ψ is a strict function of μ and therefore the ODE (4.13) has only constant coefficients, making its solution possible. The planar solution is equivalent to a stationary solution of the form $\Phi = e^{-\gamma t}\psi(\mu)$. The main stationary solution of interest is periodic for small amplitudes A, so this is the solution we focus on next. While numerical solutions can be obtained, we compute a perturbation solution, scaling both the function and

117

the variable by the amplitude A of solutions through a multiple scales approach. We compare the perturbation solution to numerical solutions, finding that the perturbation solution accurately captures the structure of the planar vortex filament (in particular, the spacial period of oscillation for such solutions). We find that the spatial period $T(A)$ is given by the approximation

$$T(A) \approx 2\pi \left(1 + \frac{3}{16}A^2\right)^{-1} , \tag{4.34}$$

for small A.

Properties of the planar vortex filament in the arclength system (the intrinsic coordinate frame) were considered in [100], and we have compared the two formulations. The primary benefit of the arclength frame is that it allows for exact solutions, in terms of elliptic sn functions. The Cartesian framework, however, gives us a clearer view of exactly what is going on with the structure of the vortex filament. While there is no exact solution, the perturbation result does work nicely for small amplitude periodic solutions. Despite the fact that there is no exact closed-form solution for $\psi(\mu)$, we are able to derive an exact relation for the period $T(A)$ in terms of elliptic integrals, obtaining

$$T(A) = 8E\left(A/2\right) - 4K\left(A/2\right) , \tag{4.35}$$

which agrees nicely with the approximation found through perturbation for small A; see Fig. 4.4. This is also reminiscent of the period for the arclength representation of the planar solution discussed in [100]. Note that there is a bound $A < \sqrt{2}$ on the amplitude A of the space-periodic function $\psi(\mu)$, as will be discussed in a forthcoming work. As such, the

maximal period occurs with amplitude $A = 0$ and is $T(0) = 2\pi$ while the minimal period solution occurs with amplitude $A = \sqrt{2}$ and is $T(\sqrt{2}) = 3.3886$. Hence, the period $T(A)$ of a space-periodic solution is related in an inverse manner to the amplitude A of such a solution.

4.2 Non-monotone space scales and self-intersection of filaments

We now discuss non-monotone coordinate scalings and their application for finding self-intersections of vortex filaments. These self-intersecting vortex filaments are likely unstable and collapse into other structures or dissipate completely.

Up to this point we have considered only monotone scalings $f(x)$ in (4.1), since these permit well-behaved solutions to (4.11). As we've shown, such solutions can be studied analytically, and in some cases exactly. However, in situations where $f(x)$ is non-monotone, we may still assume a stationary solution of the form $\Phi(x,t) = e^{-i\gamma t}\phi(x)$. While $\psi(\mu)$ from (4.13) was defined on the real μ-axis in the case of monotone $\mu = f(x)$, for non-monotone $f(x)$ it is possible that the domain of $\phi(x)$ will be restricted. Assuming a solution $\Phi(x,t) = e^{-i\gamma t}\phi(x)$, (4.10) reduces to

$$\phi + \frac{f'\phi'' - f''\phi'}{\left(f'^2 + \phi'^2\right)^{3/2}} = 0 \,. \tag{4.36}$$

The ordinary differential equation (4.36) is degenerate when f is not strictly monotone, i.e. if there exists a point $x = a$ at which $f'(a) = 0$. In order for a planar vortex filament

119

to have self-intersections, there should exist points $x_* < x^*$ such that $f(x_*) = f(x^*)$ and $\phi(x_*) = \phi(x^*)$, but for $x_* < x_1 < x_2 < x^*$, $f(x_1) = f(x_2)$ and $\phi(x_1) = \phi(x_2)$ can not hold simultaneously. If such x_1 and x_2 exist, then there can be a loop (if not, then we just have a constant valued function). Then from (4.1) we must have $\mathbf{r}(x_*, t) = \mathbf{r}(x^*, t)$ for all $t \geq 0$. If we have such points $x_* < x_1 < x_2 < x^*$, there there is at least one loop formed. This loop is parametrized by $\theta \in [x_*, x^*]$ as

$$r(\theta, t) = f(\theta)\mathbf{i}_x + \cos(\gamma t)\phi(\theta)\mathbf{i_y} - \sin(\gamma t)\phi(\theta)\mathbf{i}_z , \tag{4.37}$$

with the loop closing since $\mathbf{r}(x_*, t) = \mathbf{r}(x^*, t)$. In Fig. 4.6 we provide a schematic of the planar loop vortex filament. Now that we have some conditions on parametrized crossings and loop strictures on a vortex filament, we provide some examples to show that these structures can actually occur as solutions to the equation governing a vortex filament of planar type.
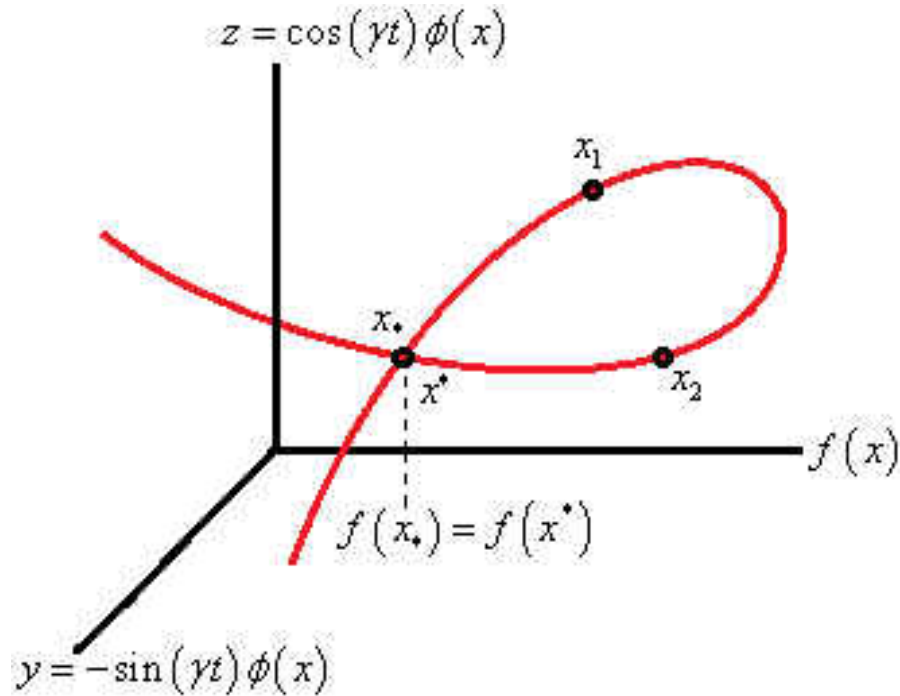
Figure 4.6: Schematic of a self-intersection for the planar vortex filament governed by a solution $\phi(x)$ to equation (4.36). Self-intersection occurs at spatial coordinate $f(x_*)$ where the parametrization x attains the value x^* such that $f(x_*) = f(x^*)$ and $\phi(x_*) = \phi(x^*)$. It is necessary for $\phi(x_1) \neq \phi(x_2)$ for all $x_* < x_1 < x_2 < x^*$ in order to have a single loop. For multiple loops, similar yet more complicated conditions must hold.

4.2.1 Single loop case

As our first numerical case, we consider an example of a parametrized single loop on a vortex filament. Let us consider the scaling $f(x) = x^2/2$. We then have

$$\phi + \frac{x\phi'' - \phi'}{\left(x^2 + \phi'^2\right)^{3/2}} = 0 \,. \tag{4.38}$$

Unlike in the simpler case of monotone f, here we cannot easily solve the differential equation (4.38) analytically. So, we resort to numerical solutions. It is useful to assign a specific x_N as a numerical initial point. Picking $x_N = 0$ is problematic, since (4.38) is degenerate at that point. So, we shall take x_N to be small yet positive. We find that loops are not obtained for many parameter values. However, they can occur for our choice of f. Taking, for instance, $x_N = 0.1$, $\phi(x_N) = 0.6$, $\phi'(x_N) = -0.1$, we find that $\phi(2.059) = \phi(-2.059)$ while $f(x) = f(-x)$ by the form of f selected, so we pick $x_* = -2.059$ and $x^* = 2.059$. To make sure the loop is closed, the derivatives should differ at each point. We calculate $\phi'(x_*) = 3.589$ while $\phi'(x^*) = 0.857$, so the loop does close. So, in the prescribed geometry, we have found a closed filament loop. As mentioned above, the loop must remain closed for all $t \geq 0$. The resulting single loop planar vortex filament is displayed in Fig. 4.7.
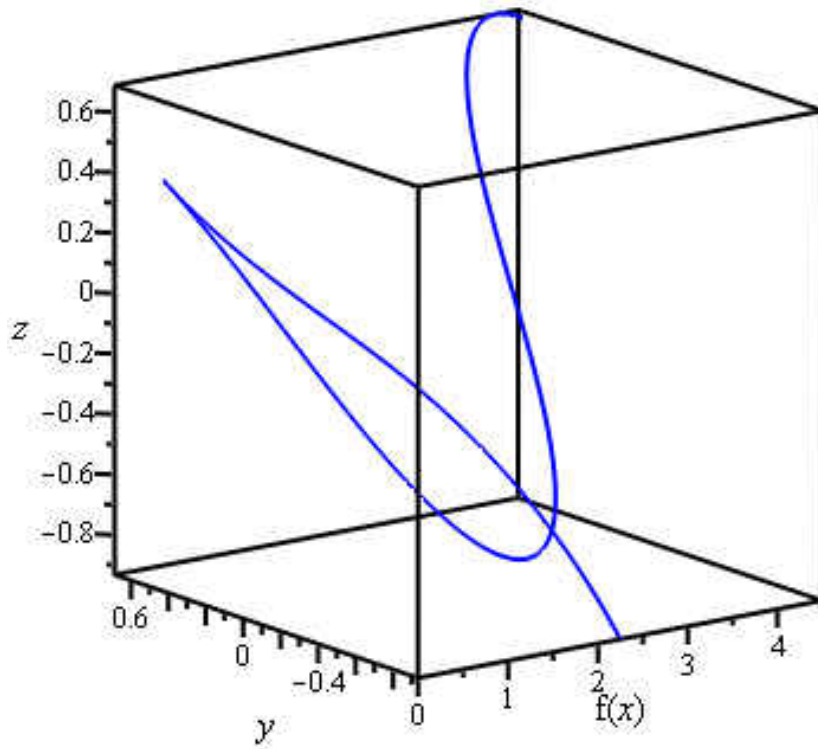
Figure 4.7: Plot of the numerical solution for a single loop vortex filament described by $\phi(x)$ when $\phi(x)$ satisfies (4.38), $\phi(0.1) = 0.6$, $\phi'(0.1) = -0.1$. The x scaling is $f(x) = x^2/2$. The space coordinate is parametrized by $x \in [-2.12, 3.00]$.

4.2.2   Double loop case

Let us now consider a double loop structure on a vortex filament. Let us take the scaling $f(x) = \cos(x)$. We then have

$$\phi + \frac{-\sin(x)\phi'' + \cos(x)\phi'}{\left(\sin^2(x) + \phi'^2\right)^{3/2}} = 0 \,. \tag{4.39}$$

Taking $x_N = 0.1$, $\phi(x_N) = 0.5$, $\phi'(x_N) = -0.095$, we numerically solve (4.39). Defining $-x_*^{[1]} = 2.35 = x^{*[1]}$, $x_*^{[2]} = -3.89$, $x^{*[2]} = 2.395$, we have that $\phi(x_*^{[1]}) = \phi(x^{*[1]})$ and $\phi(x_*^{[2]}) = \phi(x^{*[2]})$. Yet, since $f(x) = \cos(x)$, we have $f(x_*^{[1]}) = f(x^{*[1]})$ and $f(x_*^{[2]}) = f(x^{*[2]})$. So, the conditions for crossing are satisfied at spatial coordinates $\cos(x_*^{[1]}) = -0.70$ and $\cos(x_*^{[2]}) = -0.73$. We verify that the derivatives differ at each point, so the loop structures close off at the required points. (If the derivatives do not differ, then the filament my become tangent to itself, and therefore not close to form a loop, at the required point.) Hence, we have obtained a double loop structure on a vortex filament. The resulting double loop planar vortex filament is displayed in Fig. 4.8.

One may continue with multi-loop structures, but these get progressively harder to construct, since one must guess an appropriate transform of space variable $f(x)$ and deduce values of the crossings. Further, since this is done numerically (such analytical constructions are very challenging), there is a bit of guess work involved in the initial conditions which permit solutions $\phi(x)$ which allow for the crossings.
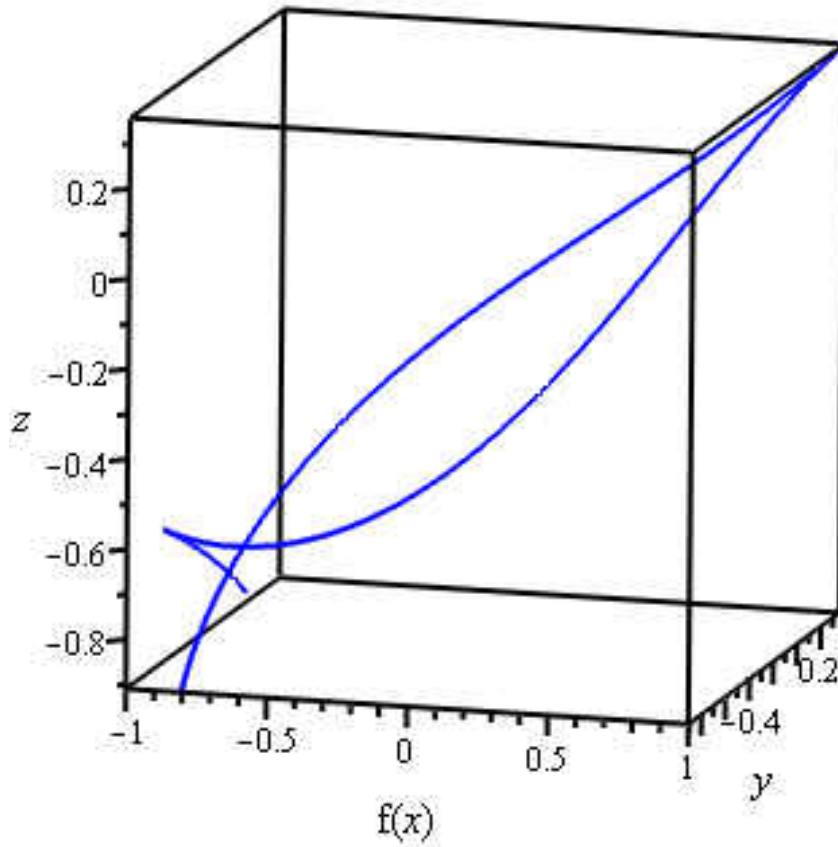
Figure 4.8: Plot of the numerical solution for a double loop vortex filament described by $\phi(x)$ when $\phi(x)$ satisfies (4.39), $\phi(0.1) = 0.5$, $\phi'(0.1) = -0.095$. The x scaling is $f(x) = \cos(x)$. The space coordinate is parametrized by $x \in [-4.0, 2.5]$.

While these loop structures have been shown to exist numerically for appropriate scales f and planar components ϕ, in practice one would not expect these structures to persist. A more physically relevant situation would be for a vortex filament to cross (or come close to crossing, since physically the vortex core has non-trivial diameter), a loop structure is monentarily formed, and then the filament is disrupted. Depending on the ambient fluid, one could have that:

(i) the vortex filament sheds the loop, and realign as a non-crossing well-defined curve;

(ii) the loop collapses, with the filament stretching laterally to realign as a non-intersecting curve;

(iii) the loop dominates, with the "tails" decaying, resulting in a vortex ring.

While the present results point toward either of those outcomes, note that one would need to retain more structure than the LIA permits in order to fully model the dynamics of such vortex filament crossings. In order to study such complicated dynamics, the full integral form of the BiotSavart law would be required. At best, the LIA provides a sort of first order approximation to such behavior, though it fails to pick up on the complicated dynamics of these situations, which would lead from a vortex filament crossing to one of the possible outcomes listed. That the LIA can pick up on the occurrence of such interactions, given its simplicity relative to the full Biot-Savart law, is still beneficial.

4.2.3 Analytical calculation

While numerical results are easiest for the case of self-intersections, we remark that analytical approximations can be obtained, at a cost. Indeed, when $f'(x_0) = 0$ for some x_0, then (4.36) degenerates (the coefficient of ϕ'' vanishes, decreasing the order of the equation). To counter this, we must have two solution branches, which we match at x_0. However, while the matching preserves continuity, it cannot preserve continuity of the first derivative (on each side of x_0, that is $x < x_0$ and $x > x_0$, the slope of the branches must differ). Without loss of generality, take $x_0 = 0$. Then, in order to match a positive and negative branch, we consider the following piecewise defined solution:

$$\phi(x) = \begin{cases} -\psi(f(x)) & x_* < x < 0\,, \\ 0 & x = 0\,, \\ \psi(f(x)) & 0 < x < x^*\,, \end{cases} \tag{4.40}$$

where $\psi(\mu)$ is a solution as was found in the monotone case and $x_* < 0 < x^*$ such that $f(x_*) = f(x^*) = T/2$ where T is the period of ψ. From the form of (4.36), if ψ is a solution, then so is $-\psi$. Hence, each branch is a solution (when $f' \neq 0$). This representation is not unique, as we could have reversed the signs in (4.40). To get both functions to match at $x = 0$, we use a modified form of (4.20) where $\psi(0) = 0$, $\psi'(0) = 1$ (which gives a sine, as opposed to cosine, representation). This is equivalent to translation of the solution in (4.20) by $-\pi/2$ on the x-axis. So, to lowest order (one can add higher order corrections, but we

suppress them for brevity) (4.40) becomes

$$\phi(x) = \begin{cases} -\sin\left(\left[1 + \frac{3}{16}A^2\right]f(x)\right) & x_* < x < 0\,, \\ 0 & x = 0\,, \\ \sin\left(\left[1 + \frac{3}{16}A^2\right]f(x)\right) & 0 < x < x^*\,. \end{cases} \tag{4.41}$$

Note that $\phi(x_*) = -\psi(f(x_*)) = -\psi(T/2) = 0 = \psi(T/2) = \psi(f(x^*)) = \phi(x^*)$ by construction, so $\phi(x_*) = \phi(x^*)$.

For example, consider again the $f(x) = x^2/2$ case. We pick

$$x_*(A) = -\sqrt{2\pi\left[1 + \frac{3}{16}A^2\right]^{-1}}\,, \tag{4.42}$$

$$x^*(A) = \sqrt{2\pi\left[1 + \frac{3}{16}A^2\right]^{-1}}\,. \tag{4.43}$$

We then get (to lowest order)

$$\phi(x) = \begin{cases} -\sin\left(\left[1 + \frac{3}{16}A^2\right]\frac{x^2}{2}\right) & x_*(A) < x < 0\,, \\ 0 & x = 0\,, \\ \sin\left(\left[1 + \frac{3}{16}A^2\right]\frac{x^2}{2}\right) & 0 < x < x^*(A)\,. \end{cases} \tag{4.44}$$

Note that $\phi(x_*(A)) = -\sin(\pi) = 0 = \sin(\pi) = \phi(x^*(A))$. Furthermore, let

$$x_1(A) = -\sqrt{\pi\left[1 + \frac{3}{16}A^2\right]^{-1}}\,, \tag{4.45}$$

$$x_2(A) = \sqrt{\pi\left[1 + \frac{3}{16}A^2\right]^{-1}}\,. \tag{4.46}$$
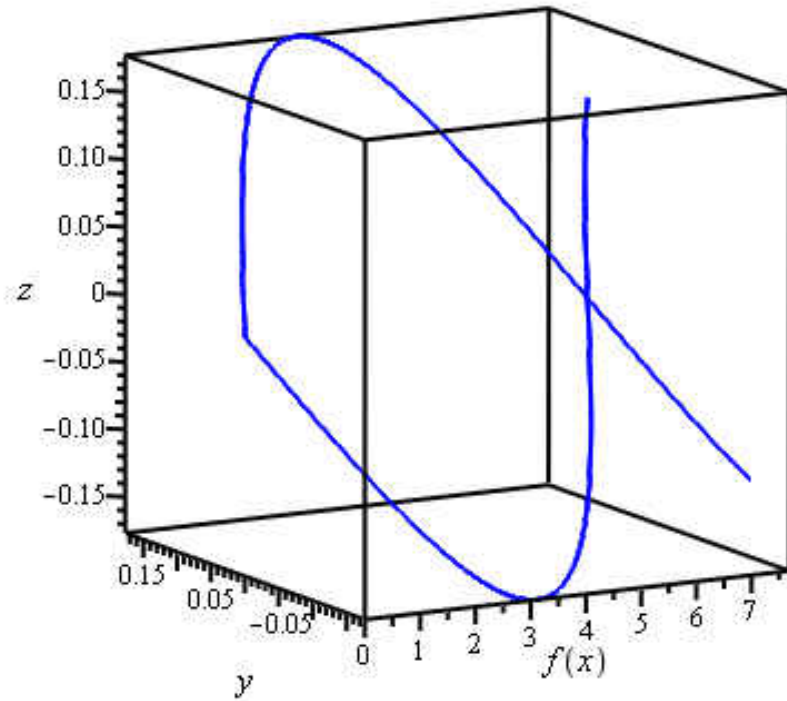
Figure 4.9: Plot of the analytical solution for a single loop vortex filament described by $\phi(x)$ when $\phi(x)$ satisfies (4.44). The x scaling is $f(x) = x^2/2$, while the amplitude of the solution is taken to be $A = 0.25$. The space coordinate is parametrized by $x \in [x_*(A), x^*(A)]$ while on the loop.

Then $\phi(x_1(A)) = -\sin(\pi/2) = -1 \neq 1 = \sin(\pi/2) = \phi(x_2(A))$. So, there exist $x_1(A)$ and $x_2(A)$ such that $x_*(A) < x_1(A) < x_2(A) < x^*(A)$, $\phi(x_*(A)) = \phi(x^*(A))$, and $\phi(x_1(A)) \neq \phi(x_2(A))$, so a loop is indeed formed. The solution (4.44) is shown in Fig. 4.9, in the case of $A = 0.25$. The single-loop structure is prominent.

We remark that since ϕ is continuous on $x \in [-\sqrt{\pi}, \sqrt{\pi}]$, yet ϕ' has a discontinuity at a single point $x = 0$, the matched solution is a class of "weak" solution.

4.2.4 Discussion

For monotone scalings f we were able to obtain the nice analytical results discussed above. We also discuss non-monotone coordinate scalings f and their application for finding self-intersections of vortex filaments. An equation governing the stationary solution $\phi(x)$ was given in (4.36). This equation becomes singular at points where monotonicity of f fails, yielding solutions which, in some cases, permit self-intersection of the curve $\mathbf{r}$ given in (4.1). Such a self-intersection results in a vortex filament loop. While such a situation is not tractable analytically, we provide numerical simulations to demonstrate that such results are at the very least mathematically possible. We also outline some general criteria which would permit a loop filament structure. These self-intersecting vortex filaments essentially "break" the LIA formulation, meaning that once intersection occurs, the LIA is not sufficient to study the dynamics of the loop solutions. Such solutions are likely unstable and collapse into other structures or dissipate completely. These types of dynamics are quite interesting,

and would certainly merit future work. Analytical results, under weaker conditions than monotonicity, yet stronger conditions than just arbitrary non-monotone transforms, could be possible, maybe in the case of the specific examples considered here. Some analytical results were given for the non-monotone scalings, and it was shown that such solutions may be constructed in a piecewise manner. These analytical solutions are continuous, yet fail to have a continuous derivative. In this sense, we may view such solutions as weak solutions. Nevertheless, these analytical results agree qualitatively with the numerical simulations.

4.3   Scaling laws and unsteady solutions under the integrable 2D local induction approximation

We give a formulation of the 2D LIA (2.25) that accounts for functional scalings of the spatial variable, as was done recently for stationary states of the LIA by Van Gorder [105] (and this was shown in the previous two sections). In the present section, we focus on scalings of unsteady vortex filaments, in particular rotating and self-similar vortex filaments. Conditions for self-intersections of filaments under this formulation are given, which enables us to study the formation of loops that arise when unsteady filaments intersect. Furthermore, we are able to study the time evolution of kinks that may form along a vortex filament, and we show that such kink solutions can persist in time. The results presented for unsteady vortex filaments were considered in Van Gorder [111].

4.3.1 Spatial scalings for the 2D LIA

The scaled position vector describing the vortex is

$$\mathbf{r} = \mu(x)\mathbf{i}_x + y(x,t)\mathbf{i}_y + z(x,t)\mathbf{i}_z \,, \tag{4.47}$$

where $\mu(x)$ denotes a general scaling of the x-coordinate. This is one of two possible equivalent such scalings, with the other being

$$\mathbf{r} = x\mathbf{i}_x + y(\mu^{-1}(x),t)\mathbf{i}_y + z(\mu^{-1}(x),t)\mathbf{i}_z \tag{4.48}$$

provided μ^{-1}, the inverse map of μ, exists.

The form of $\mu(x)$ strongly impacts the structure of the vortex filament. The unscaled LIA corresponds to $\mu(x) = x$. For monotone scalings $\mu' > 0$, the dual mapping (4.48) exists. However, for non-monotone scaling, the situation becomes more complicated.

Introducing the complex potential function $\Phi(x,t) = y(x,t) + iz(x,t)$ and taking the 2D LIA discussed in Chapter 2, one obtains the dispersion equation

$$i\Phi_t + \gamma\frac{\mu'\Phi_{xx} - \mu''\Phi_x}{[\mu'^2 + |\Phi_x|^2]^{3/2}} + \frac{\gamma}{2\mu'}\frac{|\Phi_x|^2\Phi_{xx} - \Phi_x^2\Phi_{xx}^*}{[\mu'^2 + |\Phi_x|^2]^{3/2}} = 0 \,. \tag{4.49}$$

Defining the function Ψ so that $\Phi(x,t) = \Psi(\mu,t)$, (4.10) reduces to

$$
\begin{aligned}
0 &= i\Psi_t + \gamma\frac{\Psi_{\mu\mu}}{[1 + |\Psi_\mu|^2]^{3/2}} + \frac{\gamma}{2}\frac{|\Psi_\mu|^2\Psi_{\mu\mu} - \Psi_\mu^2\Psi_{\mu\mu}^*}{[1 + |\Psi_\mu|^2]^{3/2}} \\
&= i\Psi_t + \gamma\frac{\partial}{\partial\mu}\left(\frac{\Psi_\mu}{\sqrt{1 + |\Psi_\mu|^2}}\right) .
\end{aligned}
\tag{4.50}
$$

This gives a conservation law for Ψ. Note that when $\mu(x) = x$, (4.50) is the 2D LIA (2.25).

132

In addition to these scalings, note that every solution to (4.11) is $U(1)$-invariant in time (invariant under scalings $\Psi(\mu, t) \mapsto e^{i\alpha t}\Psi(\mu, t)$. Furthermore, solutions are invariant under addition by complex constants, $\Psi(\mu, t) \mapsto \Psi(\mu, t) + C$. From both properties, we see that if $\Psi(\mu, t)$ is a solution then so is $C - \Psi(\mu, t)$. Physically, this means that there is a type of superposition principle

$$\mathbf{r}(x, t) = \mathbf{r}_0(x) + \mathbf{r}_\Psi(x, t), \tag{4.51}$$

where $\mathbf{r}_0(x)$ is an arbitrary line filament and $\mathbf{r}_\Psi(x, t)$ is any filament solution to the potential form of the LIA.

4.3.2 The scaled helix

To model helical vortex filaments, we take $\Psi(\mu, t) = A \exp(k\mu(x) - \omega\gamma t)$, where A is the amplitude of the helical solution, k is the wave number, and ω is the frequency. In terms of the vortex filament, A represents the maximal deviation from the central axis of rotation, while ω gives the rotational motion. Hence, for the helical filament we have that the distance between the filament and the central axis of rotation remains constant for all time. Under such an assumption, we necessarily find that

$$\left\{\omega - \frac{k^2}{(1 + A^2 k^2)^{1/2}}\right\} A \exp(kx - \omega\gamma t) = 0, \tag{4.52}$$

hence we have the exact dispersion relation

$$\omega = \frac{k^2}{(1 + A^2 k^2)^{1/2}} > 0. \tag{4.53}$$

Then, for a choice of scaling $\mu(x)$, we have the exact solution

$$\Phi(x,t) = A \exp\left(i\left[k\mu(x) - \frac{k^2\gamma t}{(1+A^2k^2)^{1/2}}\right]\right). \tag{4.54}$$

The vortex filament (in Cartesian coordinates) is then given by

$$\begin{aligned}
\mathbf{r}(x,t) &= \mu(x)\mathbf{i}_x + A\cos\left(k\mu(x) - \frac{k^2\gamma t}{(1+A^2k^2)^{3/2}}\right)\mathbf{i}_y \\
&+ A\sin\left(k\mu(x) - \frac{k^2\gamma t}{(1+A^2k^2)^{3/2}}\right)\mathbf{i}_z.
\end{aligned} \tag{4.55}$$

Such a solution is useful, since it permits us to study irregular helical filaments. Indeed, by appropriately choosing the scaling $\mu(x)$, one may obtain a variety of various helical filaments. While such filaments always remain a fixed distance from the reference axis, their spatial behaviors can vary wildly. Such filaments are the simplest time-dependent filaments.

4.3.3   Self-similar filament structures

Let us turn our attention to self-similar vortex filament structures under the scaled LIA. Unlike helical or planar filaments which exist at certain specific scales, the self-similar structures correspond to solutions with a type of scale independence (that is, solutions appear the same at different scales). Such solutions are sometimes referred to as quasi-stationary solutions, since they satisfy such a scaling property yet depend strongly on time at a fixed spatial coordinate (unlike stationary states). We consider a solution of the form

$$\Psi(\mu,t) = \sqrt{2\gamma t}\,\phi(\eta), \quad \eta = \frac{\mu(x)}{\sqrt{2\gamma t}}. \tag{4.56}$$

Equation (4.11) is then put into the form

$$i \left(\phi - \eta \phi' \right) + \left(\frac{\phi'}{\sqrt{1 + |\phi'|^2}} \right)' = 0 \,. \tag{4.57}$$

It is clear that (4.57) always admits a solution of the form $\phi(\eta) = C\eta$, where C is a complex-valued constant. In turn, this gives $\Phi(x,t) = \sqrt{2\gamma t}C\eta = C\mu(x)$. Hence, the filament $\mathbf{r}(x,t) = (\mu(x), \mathrm{Re}(C)\mu)x), \mathrm{Im}(C)\mu(x))$ is a solution. In this case the solution is stationary. If $\mu(x) = x$, this corresponds to a line filament, while for $\mu(x) \neq x$, more interesting behaviors are possible. Note that this solution is time-independent, demonstrating what we mean by quasi-steady solutions. In this particular case, the exact filament solution ends up independent of time due to the self-similarity assumption. However, for more complicated solutions, we do not expect completely time-independent filament motion.

As it turns out, this linear solution in μ is an indicator of the average behavior along a perturbed filament. It is possible to show numerically that solutions behave like $\phi(\eta) = C\eta + \epsilon\hat{\phi}(\eta)$, where the linear term gives something like the line filament, and the $\hat{\phi}(\eta)$ perturbation gives deviations of a realistic filament from this more idealized linear trend. Under such an assumption on the form of $\phi(\eta)$, we find that (neglecting higher-order terms in ϵ)

$$i \left(\hat{\phi} - \eta \hat{\phi}' \right) + \left(1 + |C|^2 \right)^{-1/2} \hat{\phi}'' = 0 \,, \tag{4.58}$$

where prime denotes differentiation with respect to the similarity variable η. The solution is found to be

$$\hat{\phi}(\eta) = \exp \left(\frac{i}{2} \left(1 + |C|^2 \right)^{1/2} \eta^2 \right) \,. \tag{4.59}$$

In the small ϵ limit, we therefore have

$$\phi(\eta) = C\eta + \epsilon \exp\left(\frac{i}{2}\sqrt{1 + |C|^2}\eta^2\right).$$ (4.60)

Converting this back into the x, t coordinate system, we have

$$\begin{aligned} \Phi(x,t) &= \Psi(\mu(x), t) \\ &= C\mu(x) + \epsilon\sqrt{2\gamma t} \exp\left(\frac{i}{2}\sqrt{1 + |C|^2}\frac{\mu(x)^2}{2\gamma t}\right), \end{aligned}$$ (4.61)

where we neglect order ϵ^2 and higher terms. The self-similar filament is then given in Cartesian coordinates by

$$\begin{aligned} \mathbf{r}(x,t) = {}& \mu(x)\mathbf{i}_x \\ &+ \left[\text{Re}(C)\mu(x) + \epsilon\sqrt{2\gamma t} \cos\left(\sqrt{1 + |C|^2}\frac{\mu(x)^2}{4\gamma t}\right)\right]\mathbf{i}_y \\ &+ \left[\text{Im}(C)\mu(x) + \epsilon\sqrt{2\gamma t} \sin\left(\sqrt{1 + |C|^2}\frac{\mu(x)^2}{4\gamma t}\right)\right]\mathbf{i}_z \end{aligned}$$ (4.62)

when we neglect order ϵ^2 and higher perturbations.

The large-time dynamics of these filaments will depend strongly on the form of the similarity function ϕ. If $\phi(0) = 0$, then the filament remains bounded as $t \to \infty$ provided $\mu(x)\phi'(0)$ exists and is finite. If $\phi'(0) = 0$, then the solution converges to the zero solution in the asymptotic time limit. This means that the self-similar solution does not persist, and dissipates to the line filament oriented along the x axis. In other words, the self-similar perturbations along such a filament gradually decay for large time.

In the case where $\phi'(0) \neq 0$ yet is finite, and $\phi(0) = 0$, the vortex filament persists. In the limit $t \to 0$, we must then have

$$\lim_{t \to \infty} \sqrt{2\gamma t}\phi(\eta) = \lim_{\sigma \to \infty} \sigma\phi(\mu(x)/\sigma) = \lim_{\sigma^* \to 0} \frac{\phi(\mu(x)\sigma^*)}{\sigma^*}$$
$$= \lim_{\sigma^* \to 0} \mu(x)\phi'(\mu(x)\sigma^*) = \mu(x)\phi'(0).$$
(4.63)

In this case, the self-similar filament persists and asymptotically approaches the line filament $\mathbf{r}(x,t) = (\mu(x), \mathrm{Re}(\phi'(0))\mu(x), \mathrm{Im}(\phi'(0))\mu(x))$.

In the case where $\phi(0) \neq 0$, we have $|\Phi(x,t)| \to \infty$ as $t \to \infty$. So, $\phi(0) = 0$ is necessary condition for a self-similar filament to be bounded. This would give the kink-type solutions previously studied for the quantum LIA in the presence of superfluid friction parameters.

4.3.4 Self-intersection and vortex kinks

As was previously discussed in Van Gorder, vortex filaments which cross (self-intersect) can be constructed as a limiting case of the LIA. The example used previously was an approximation to the planar filaments (obtained using a multiple scales approach). It was shown that, in the small-amplitude regime, certain scaled planar filaments can be constructed which exhibit self-intersection. While solutions exist mathematically at and past the point of intersection, physically we expect that the filament will break, with a vortex ring type structure developing.

In the present section, we shall study the self-intersection of these vortex filaments without making the assumption of small amplitude filament solutions. Recall that small amplitude solutions correspond to filaments which exhibit only small deviations from the reference axis. In fact, vortex filament breakdown, reconnection, and self-intersection can be in response to large deviations from the reference axis. Hence, it makes sense to consider self-intersection of filaments which have non-small deviations from the reference axis.

Let $\Psi_1(\mu, t)$ and $\Psi_2(\mu, t)$ be distinct solutions to the scaled LIA. It then makes sense to consider a weak solution

$$\Phi(x, t) = \begin{cases} \Psi_1(\mu(x), t), & x \geq 0, \\ \\ \Psi_2(\mu(x), t), & x < 0. \end{cases} \tag{4.64}$$

The function $\Phi(x, t)$ is continuous for all x and t provided that $\Phi(0, t) = \Psi_1(\mu(0), t) = \Psi_2(\mu(0), t)$. However, Φ is not in general differentiable in x at $x = 0$.

It is important to recall that the LIA permits a very useful property: if $\Psi(\mu, t)$ is a solution to (4.11), then so is $-\Psi(\mu, t)$, $\Psi(-\mu, t)$ and $-\Psi(\mu, t)$. It makes sense to take $\Psi_1 = \Psi$, $\Psi_2 = -\Psi$ for some solution Ψ to the scaled LIA. Indeed, $\Psi_\mu(\mu(0), t)\mu'(0) = 0$ is a required condition for $\Phi_x(0, t)$ to be continuous. This can hold if either $\mu'(0) = 0$ or if $\Psi_\mu(\mu(0), t) = 0$. If either of these conditions hold, we have a solution $\Phi \in C^1(\mathbb{R} \times (0, \infty))$ with continuous partial derivatives. On the other hand, if $\Psi_\mu(\mu(0), t)\mu'(0) \neq 0$ (which is true in general, unless we pick very specific functional forms of μ), then we have a solution $\Phi \in C^0(\mathbb{R} \times (0, \infty))$ which is continuous yet does not have continuous partial derivatives. To enforce the existence of Φ_{xx}, we need additional conditions resulting in $\Phi_{xx} = 0$ at $x = 0$. So,

it is not feasible to have a classical solution with continuous second order partial derivatives in x. Hence, (4.64) is a weak solution.

While a solution such as (4.64) loses regularity at $x = 0$, this should make physical sense. At $t = 0$, we essentially make a sharp turn or kink in the vortex filament, which under appropriate conditions will result in a self-intersection of the filament.

Note that the helical filaments, even with a rescaling of x, cannot self-intersect if we take $\Psi_1 = \Psi$, $\Psi_2 = -\Psi$, where Ψ is some helical solution. This lies in the fact that the complex modulus of such solutions is always a positive constant, which simply means that a purely helical filament will always remain at a constant positive distance from the reference axis. Yet, recalling that solutions are preserved under the scaling $\Psi \mapsto C - \Psi$, let us define

$$\Phi(x, t) = \begin{cases} A \exp(i[k\mu(x) - \omega t]), & x \geq 0, \\ 2A - A \exp(i[k\mu(x) - \omega t]), & x < 0. \end{cases} \tag{4.65}$$

This is a weak solution to the scaled LIA. This function is continuous at $x = 0$ provided $t = 0$. Then when $t > 0$, the function becomes discontinuous. This solution can be used to model an event where two filament sections approach ($t < 0$), intersect ($t = 0$) and then separate ($t > 0$). Interestingly, in this case at $t = 0$ a loop filament can be formed. To see such a solution, in Figs. 4.10-4.11 we take $\mu(x) = \cos(x)$ and $k = 2\pi$. At $t = 0$, a loop is formed when both parts of the vortex filament intersect at $(-1, A, 0)$ and $(1, A, 0)$. The filament sections are also tangent at the point $(0, A, 0)$. When $t > 0$ in general, the two filament sections do not agree at $(-1, A, 0)$ and $(1, A, 0)$, so the loop breaks down.

139
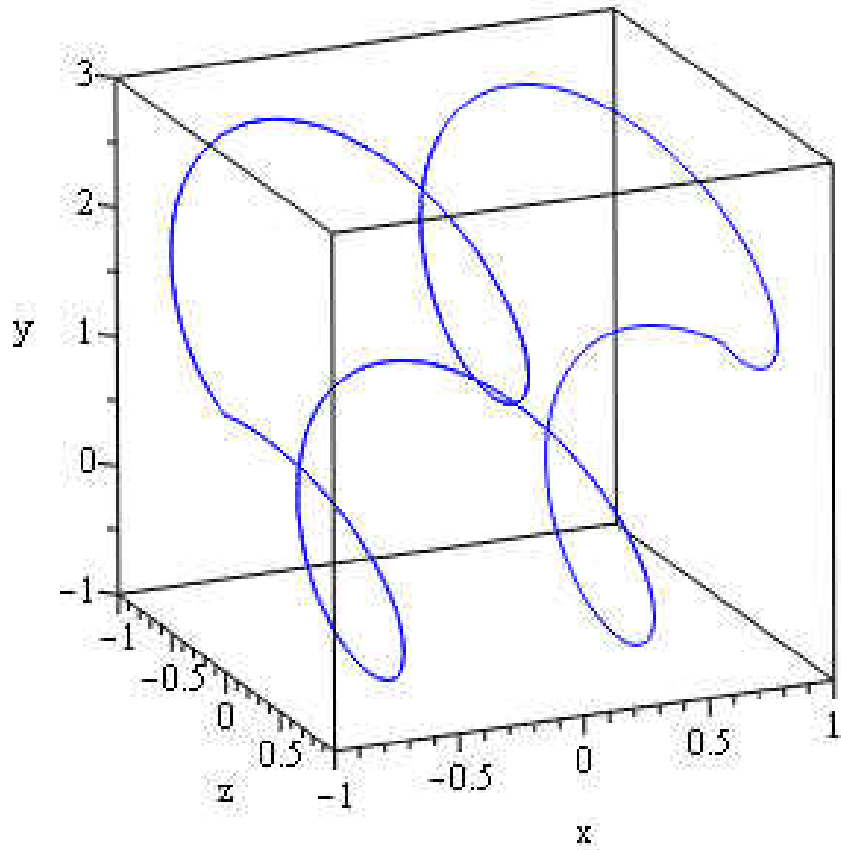
Figure 4.10: A vortex filament loop formed at $t = 0$ by two scaled helical vortex filament segments as defined in (4.65). Before $t = 0$, the two filament sections do not form a closed loop, and for $t > 0$ the filaments separate and the loop is broken. Therefore, the loop is a highly localized temporal event. The loop can redevelop at a later time. Here the scaling is $\mu(x) = \cos(x)$, and to illustrate the results graphically we take $k = 2\pi$, $A = 1$, $\gamma = 1$. For time, we take $t = 0$.
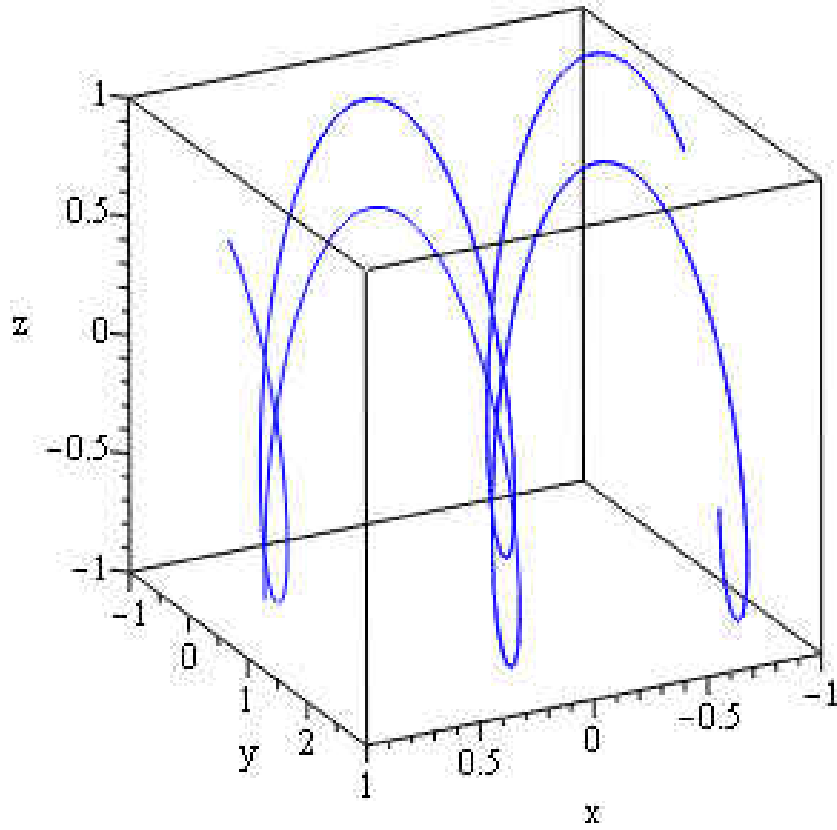
Figure 4.11: A vortex filament loop formed at $t = 0$ by two scaled helical vortex filament segments as defined in (4.65). Before $t = 0$, the two filament sections do not form a closed loop, and for $t > 0$ the filaments separate and the loop is broken. Therefore, the loop is a highly localized temporal event. The loop can redevelop at a later time. Here the scaling is $\mu(x) = \cos(x)$, and to illustrate the results graphically we take $k = 2\pi$, $A = 1$, $\gamma = 1$. For time, we take $t = 10$.

141

Due to the scaling function $\mu(x) = \cos(x)$, the vortex filament in Figs. 4.10-4.11 was confined to the interval $[-1, 1]$ along the x-axis. In this case, the entire filament forms a closed loop at $t = 0$. However, it is possible to have vortex filaments of arbitrary length which still form a loop along part of their length. A general solution to the LIA will take values on $x \in \mathbb{R}$, and even in infinite length vortex filaments can we construct loops. In fact, it is possible to construct filaments with any number of loops in this manner. To demonstrate this, we take the weak solution (4.65) with the scaling $\mu(x) = |x|$ and plot the resulting vortex filament in Fig. 4.12. At $t = 0$, this solution gives a vortex filament intersection when $x = 0, 1, 2, \ldots$. When t increases, the filament no longer have self-intersections, so the loops dissipate, as was the case in Figs. 4.10-4.11.
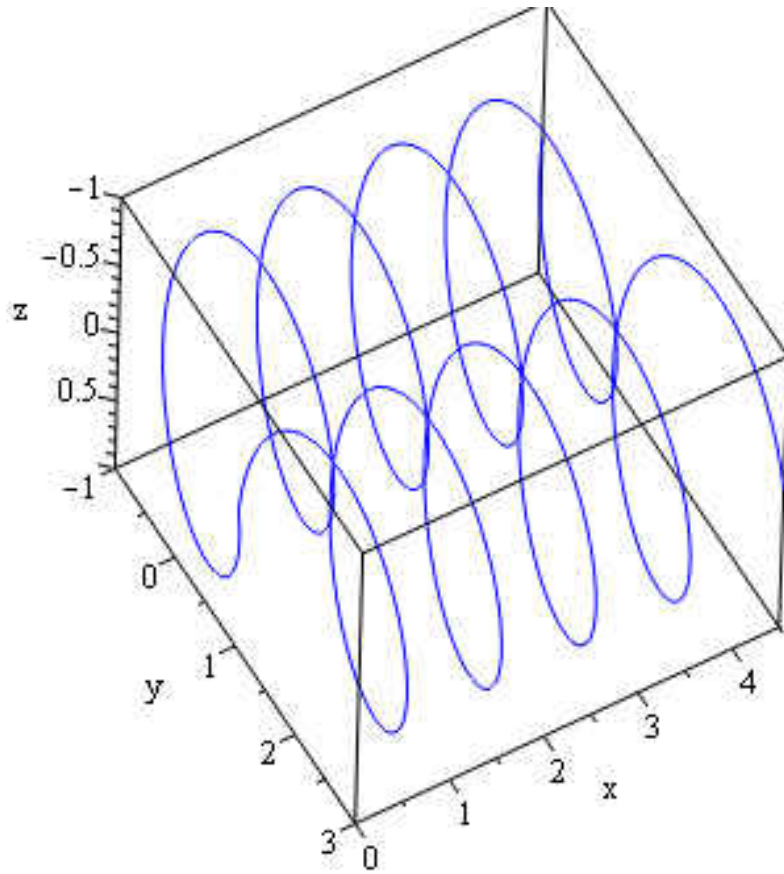
Figure 4.12: A vortex filament loop formed at $t = 0$ by two scaled helical vortex filament segments as defined in (4.65). Before $t = 0$, the two filament sections do not form a closed loop, and for $t > 0$ the filaments separate and the loop is broken. Therefore, the loop is a highly localized temporal event. The loop can redevelop at a later time. Here the scaling is $\mu(x) = \cos(x)$, and to illustrate the results graphically we take $k = 2\pi$, $A = 1$, $\gamma = 1$.

4.3.5 Self-similar vortex filaments and kink solutions

In the case of a vortex filament which exhibits self-similarity, we can construct a kink solution using the same method employed above to demonstrate self-intersecting filaments. Let $\Phi(x,t) = \sqrt{2\gamma t}\phi(\eta)$ denote a self-similar solution to (4.11). Then, there exists a weak solution (4.64) with a kink at $x = 0$ which we may construct from the formula

$$\Phi(x,t) = \begin{cases} \sqrt{2\gamma t}\phi(\mu(x)/\sqrt{2\gamma t})\,, & x \geq 0\,, \\ \\ -\sqrt{2\gamma t}\phi(\mu(x)/\sqrt{2\gamma t})\,, & x < 0\,, \end{cases} \tag{4.66}$$

provided that $\phi(\mu(0)/\sqrt{2\gamma t}) = 0$ for all $t > 0$. This makes sense only if $\mu(0) = 0$, so we may recast this solution as

$$\Phi(x,t) = \begin{cases} \sqrt{2\gamma t}\phi(\eta)\,, & \eta \geq 0\,, \\ \\ -\sqrt{2\gamma t}\phi(\eta)\,, & \eta < 0\,, \end{cases} \tag{4.67}$$

where $\phi(0) = 0$. The condition $\phi(0) = 0$ is not excessive. Indeed, as was shown earlier, this condition is necessary for a self-similar vortex filament to remain bounded as $t \to \infty$.

So, in the $t \to \infty$ limit, we have that the self-similar filament takes the form

$$\lim_{t\to\infty}\Phi(x,t) = \hat{\Phi}(x) = \begin{cases} \phi'(0)\mu(x)\,, & x \geq 0\,, \\ \\ -\phi'(0)\mu(x)\,, & x < 0\,, \end{cases} \tag{4.68}$$

Hence, we have shown that a self-similar vortex filament with a kink will tend towards a steady state solution in the asymptotic time limit. Since such a solution is distinct from the zero solution (which itself is the line filament oriented along the x axis), the self-similar

solution persists in time. This limiting solutions is in general discontinuous. However, there are some exceptions. Clearly, when $\psi'(0) = 0$ the function $\hat{\Phi}(x)$ is zero and hence continuous. This corresponds to a line filament. On the other hand, if $\mu(0) = 0$, then $\hat{\Phi}(x)$ is continuous. So, continuous asymptotic behavior of the kink solutions is possible provided μ is appropriately selected.

In the case where $\phi(0) \neq 0$, such as what occurs when there are small oscillations along a line filament (such as when we have a solution of the form (4.60)), the kink vortex filament formed by the piecewise solution (4.67) is continuous at $t = 0$ alone. For $t > 0$, such an initial kink solution breaks into two separate filaments. However, there is a way to construct a kink filament which remains continuous. Let us define the function

$$\Phi(x,t) = \begin{cases} C\mu(x) + \epsilon\sqrt{2\gamma t}\hat{\phi}\left(\frac{\mu(x)}{\sqrt{2\gamma t}}\right), & x \geq 0\,, \\[3mm] -C\mu(x) + \epsilon\sqrt{2\gamma t}\hat{\phi}\left(\frac{\mu(x)}{\sqrt{2\gamma t}}\right), & x < 0\,, \end{cases} \tag{4.69}$$

where $\hat{\phi}$ is as defined in (4.59). For $x > 0$ the filament is aligned along

$$\mathbf{r}(x) = (\mu(x), \operatorname{Re}(C)\mu(x), \operatorname{Im}(C)\mu(x))\,, \tag{4.70}$$

while when $x < 0$ the filament is aligned along

$$\mathbf{r}(x) = (\mu(x), -\mathbf{Re}(C)\mu(x), -\mathbf{Im}(C)\mu(x))\,. \tag{4.71}$$

For $\mu(x)$ such that $\mu(0) = 0$, we have that (4.69) maintains continuity for all $t > 0$. (The case of (4.67) would have included a $-$ sign in front of the small ϵ amplitude perturbations, which would have broken continuity of $\Phi(x,t)$ at $x = 0$ for all $t > 0$.) One may verify that,

in the limit $t \to \infty$,

$$\lim_{t \to \infty} \Phi(x,t) = \begin{cases} C\mu(x), & x \geq 0, \\ \\ -C\mu(x), & x < 0. \end{cases} \tag{4.72}$$

In Figs. 4.13-4.15 we demonstrate one such vortex kink solution of the form (4.69). For small time, the oscillations along the curve persist, while for large time the filament gradually becomes linear, as suggested by (4.72).
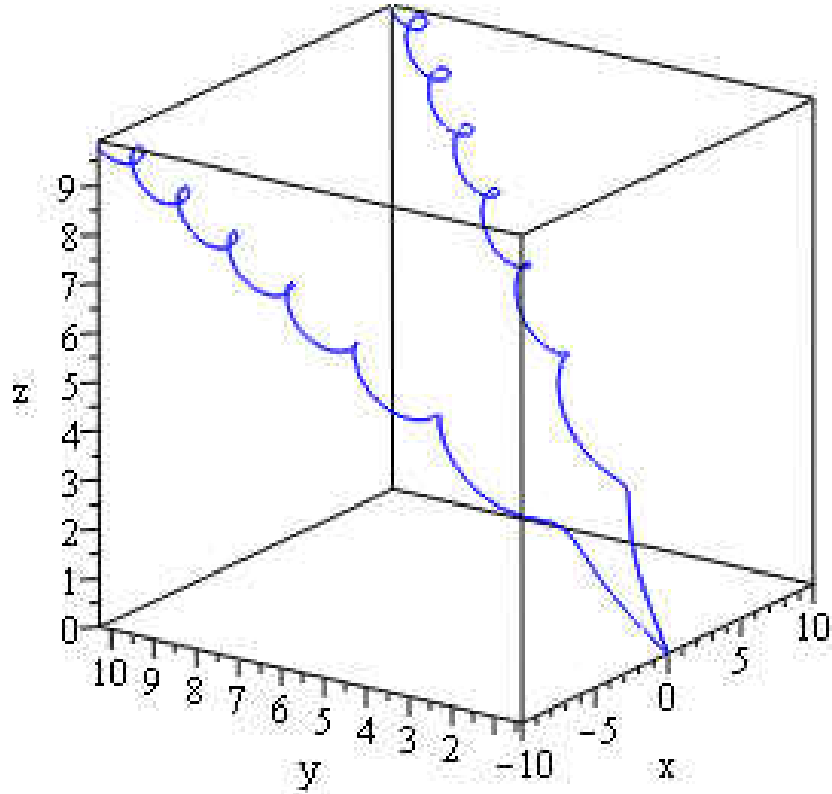
Figure 4.13: Time evolution of a vortex filament kink solution of the type described by (4.69). We set $t = 1$, and we have taken $C = 1 + i$, $\gamma = 1$, $\epsilon = 0.25$. While oscillations initially appear along the filament, these die off as time becomes large, and therefore the filament tends to the limit (4.72) as time grows.
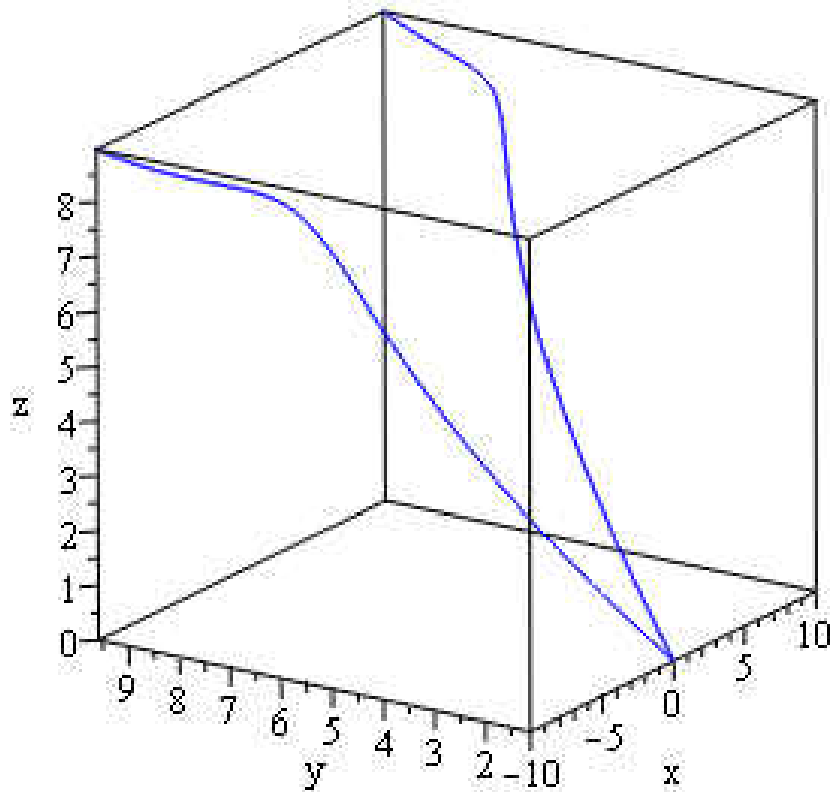
Figure 4.14: Time evolution of a vortex filament kink solution of the type described by (4.69). We set $t = 10$, and we have taken $C = 1 + i$, $\gamma = 1$, $\epsilon = 0.25$. While oscillations initially appear along the filament, these die off as time becomes large, and therefore the filament tends to the limit (4.72) as time grows.
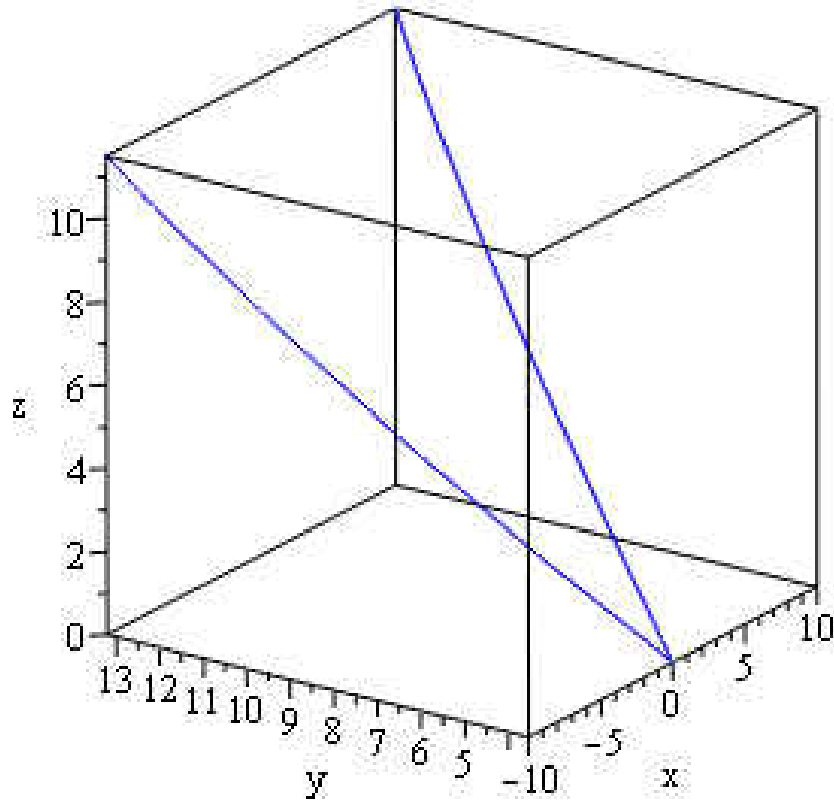
Figure 4.15: Time evolution of a vortex filament kink solution of the type described by (4.69). We set $t = 100$, and we have taken $C = 1 + i$, $\gamma = 1$, $\epsilon = 0.25$. While oscillations initially appear along the filament, these die off as time becomes large, and therefore the filament tends to the limit (4.72) as time grows.

CHAPTER 5

POTENTIAL FORMULATIONS FOR SUPERFLUID MODELS

5.1 Potential equation describing the motion of a vortex filament in superfluid ^{4}He in the Cartesian frame of reference

We obtain the fully nonlinear local induction equation describing the motion of a vortex filament in superfluid ^{4}He. As the relevant friction parameters are small, we linearize terms involving such parameters, while keeping the remaining nonlinearities, which accurately describe the curvature of the vortex filament, intact. The resulting equation is a type of nonlinear Schrödinger equation, and, under an appropriate change of variables, this equation is shown to have a first integral. This is in direct analogy to the simpler equation studied previously in Chapter 2. While this first integral is mathematically interesting, it is not particularly useful for actually computing solutions to the nonlinear partial differential equation which governs the vortex filament. As such, we introduce a new change of dependent variable, which results in a nonlinear four-dimensional system that can be numerically integrated. Integrating this system, we recover solutions to the fully nonlinear local induction equation describing the motion of a vortex filament in superfluid ^{4}He. We find that the

150

qualitative features of the solutions depend not only on the superfluid friction parameters, but also strongly on the initial conditions taken, the curvature and the normal fluid velocity. The formulation and results present in this section are due to Van Gorder [102].

5.1.1 Background

One current area of research interest lies in superfluids, a state of matter which behaves like a fluid without viscosity and with extremely high thermal conductivity. Along these lines, Shivamoggi [85] considered vortex motion in superfluid ^{4}He by reformulating the Hall-Vinen equation in the extrinsic vortex filament coordinate space. As mentioned in Shivamoggi [85], vortices in superfluids are perhaps better suited for applications of the LIE/LIA compared with their ordinary fluid counterparts, as the thin cores of such vortices correspond more readily to the asymptotic nature of the LIA; see also Schwarz [81]. In Shivamoggi [85], a first-order approximation to the nonlinearities was considered. We shall now obtain the fully nonlinear LIE for superfluid ^{4}He describing the motion of a vortex filament in such a superfluid. As the relevant friction parameters are small, we linearize such terms, while keeping the remaining nonlinearities, which accurately describe the curvature of the vortex filament, intact. The resulting equation is a type of nonlinear Schrödinger equation, and, under an appropriate change of variables, this equation is shown to have a first integral. This is in direct analogy to the simpler equation studied in Van Gorder [99]; indeed, in the limit where the superfluid parameters are taken to zero, we recover the results of Van Gorder

[99]. While this first integral is mathematically interesting, it is not particularly useful for actually computing solutions to the nonlinear partial differential equation which governs the vortex filament. As such, we introduce a new change of dependent variable, resulting in a nonlinear four-dimentional system which can be numerically integrated. The influence of the physical parameters on solutions to these equations can then be studied.

5.1.2 LIA for vortex filament in a superfluid

Including the effect of frictional force exerted the normal fluid on a vortex, recall that the self-induced velocity of the vortex in the reference frame moving with the superfluid according to the local induction equation is given in the non-dimensional form

$$\mathbf{v} = \gamma\kappa\mathbf{t} \times \mathbf{n} + \alpha\mathbf{t} \times (\mathbf{U} - \gamma\kappa\mathbf{t} \times \mathbf{n}) - \alpha'\mathbf{t} \times (\mathbf{t} \times (\mathbf{U} - \gamma\kappa\mathbf{t} \times \mathbf{n})), \qquad (5.1)$$

where $\mathbf{U}$ is the dimensionless normal fluid velocity, $\mathbf{t}$ and $\mathbf{n}$ are the unit tangent and unit normal vectors to the vortex filament, κ is the dimensionless average curvature, $\gamma = \Gamma \ln(c/\kappa a_0)$ is a dimensionless composite parameter (Γ is the dimensionless quantum of circulation, c is a scaling factor of order unity, $a_0 \approx 1.3 \times 10^{-8}$ is the effective core radius of the vortex), α and α' are dimensionless friction coefficients which are small (except near the λ-point; for reference, the λ-point is the temperature (≈ 2.17K) below which normal fluid Helium transitions to superfluid Helium (Landau and Lifshitz [51])).

If we consider the vortex to be aligned along the x axis and set $\mathbf{U} = U_1 \mathbf{i}_x$, (5.1) reduces to

$$\mathbf{v} = (1 - \alpha')\gamma\kappa\mathbf{t} \times \mathbf{n} + \alpha\mathbf{t} \times \mathbf{U} + \alpha\gamma\kappa\mathbf{n} - \alpha'U_1\mathbf{t} + \alpha'U_1\mathbf{i}_x \,, \tag{5.2}$$

assuming the deviations along the x axis to be sufficiently bounded in variation. We assume a solution of the form

$$\mathbf{r} = x\mathbf{i}_x + y(x,t)\mathbf{i}_y + z(x,t)\mathbf{i}_z \,. \tag{5.3}$$

By bounded in variation, we mean that we only consider solutions which may be expressed in the form (5.3). This means that solutions must be uniquely expressed in terms of functions of x. In the case of a vortex filament which folds back on itself, clearly the resulting solutions will be multi-valued in x, and hence cannot be expressed in the form (5.3). This also excludes the possibility of singularities at finite x. Thus, only single-branched non-singular solutions are discussed under the present framework. That said, we are not required to make any assumptions on the growth rate of $\|\mathbf{r}\|$, and such a solution is permitted to grow fast provided it is of bounded variation. Note that this restriction also prevents the strong bending or twisting of a vortex.

Employing the relations

$$\mathbf{v} = \frac{d\mathbf{r}}{dt} = y_t\mathbf{i}_y + z_t\mathbf{i}_z \,, \tag{5.4}$$

$$\mathbf{t} = \frac{d\mathbf{t}}{ds} = (\mathbf{i}_x + y_x\mathbf{i}_y + z_x\mathbf{i}_z)\frac{dx}{ds} \,, \tag{5.5}$$

$$\kappa \mathbf{n} = - \left(y_x y_{xx} + z_x z_{xx} \right) \frac{dx}{ds} \mathbf{i}_x$$

$$+ \left(y_{xx} \frac{dx}{ds} - \left(y_x^2 y_{xx} + y_x z_x z_{xx} \right) \right) \frac{dx}{ds} \mathbf{i}_y \tag{5.6}$$

$$+ \left(z_{xx} \frac{dx}{ds} - \left(z_x y_x y_{xx} + z_x^2 z_{xx} \right) \right) \frac{dx}{ds} \mathbf{i}_z \,,$$

$$\frac{dx}{ds} = \frac{1}{\sqrt{1 + y_x^2 + z_x^2}} \,, \tag{5.7}$$

and making the change of dependent variable

$$\Phi(x, t) = y(x, t) + i z(x, t) \,, \tag{5.8}$$

we find that (5.2) becomes

$$i \left(\Phi_t + \frac{\alpha' U_1 \Phi_x}{\left(1 + |\Phi_x|^2 \right)^{1/2}} \right) - \alpha U_1 \Phi_x$$

$$+ \left(\frac{(1 + \alpha') \gamma}{\left(1 + |\Phi_x|^2 \right)^{3/2}} - i \frac{\alpha \gamma}{\left(1 + |\Phi_x|^2 \right)^2} \right) \Phi_{xx} = 0 \,. \tag{5.9}$$

This is the fully nonlinear LIE describing the motion of a vortex filament in a superfluid. In the $(\alpha, \alpha') \to (0, 0)$ limit, note that (5.9) becomes (2.7). As was shown in Chapter 2, the nonlinear term in (2.7) plays a strong role in shaping solutions and hence should not be neglected. However, α and α' are small in value and hence nonlinear terms involving these terms are negligible. Then, linearizing the terms with α and α' coefficients, we reduce (5.9) into the more tractable equation

$$i \Phi_t + \left(\alpha' + i \alpha \right) \left(i U_1 \Phi_x + \gamma \Phi_{xx} \right) + \frac{\gamma \Phi_{xx}}{\left(1 + |\Phi_x|^2 \right)^{3/2}} = 0 \,. \tag{5.10}$$

5.1.3 First integral

In Chapter 2, we showed that the $\alpha, \alpha' \to 0$ reduction had both first and second integrals, which permitted implicit exact solutions in terms of elliptic integrals. Before proceeding further, we should show that (5.10) has a similar, albeit more complicated and less physically intuitive, first integral. To this end, map x into ξ where $\xi = x - (\alpha' + i\alpha)U_1 t$ and map $\Phi(x, t)$ into $\Psi(\xi, t)$, giving a coordinate change

$$\xi = x - (\alpha' + i\alpha) U_1 t,$$

$$\Psi(\xi, t) = \Phi(x - (\alpha' + i\alpha) U_1 t, t).$$

(5.11)

We then obtain from (5.10) the modified equation

$$i\Psi_t + \gamma \left[(\alpha' + i\alpha) + \frac{1}{(1 + |\Psi_\xi|^2)^{3/2}} \right] \Psi_{\xi\xi} = 0.$$

(5.12)

Equation (5.12) is in the form $i\Psi_t + \gamma F(|\Psi_\xi|) \Psi_{\xi\xi} = 0$, so as in Van Gorder (2011) let us assume a solution of the form $\Psi(\xi, t) = \psi(\xi)e^{-i\gamma t}$. Then, we obtain the ordinary differential equation

$$\psi + \left[(\alpha' + i\alpha) + \frac{1}{\left(1 + \psi'^2\right)^{3/2}} \right] \psi'' = 0.$$

(5.13)

Multiplying (5.13) by $2\psi'$ and integrating over an appropriate contour, we obtain the first integral

$$\psi^2 + (\alpha' + i\alpha)\psi'^2 - \frac{2}{\sqrt{1 + \psi'^2}} = C,$$

(5.14)

where $C \in \mathbb{C}$ is a constant of integration. From (5.14), we see that

$$P^2 V^3 + 2(Q - P)PV^2 + (Q - P)^2 V - 4 = 0,$$

(5.15)

where for simplicity we have taken $P = \alpha' + i\alpha$, $Q = \psi^2 - C$ and $V = 1 + \psi'^2$. Then, (5.15) has three solutions V_1, V_2, V_3 in V, which are functions of ψ and system parameters. For each V_k there exist two solutions for ψ', namely $\psi' = \pm\sqrt{V_k(\psi) - 1}$. Hence, there are six possible solutions to (5.14). However, in the $P \to 0$ limit (i.e., the $(\alpha, \alpha') \to (0, 0)$ limit), (5.15) becomes $Q^2 V = 4$, and hence we recover the solutions of Chapter 2, which satisfy the nonlinear ordinary differential equation

$$\psi'^2 = \frac{4 + C - \psi^2}{\psi^2 - C}. \tag{5.16}$$

5.1.4   4D dynamical system

The form of (5.14) suggests that, as in the simpler case (2.7), periodic solutions to (5.10) should be possible, at the very least in the small α, α' limits. To this end, let us assume a more physically reasonable solution $\Phi(x, t) = e^{-it}(\rho(x) + i\sigma(x))$. Equation (5.10) then yields the four dimensional ordinary differential system

$$
\begin{aligned}
\rho'' =& \frac{\gamma^{-1}\alpha\left(U_1\left(\alpha\sigma' - \alpha'\rho'\right) - \sigma\right)}{\left[\alpha^2 + \alpha'^2 + 2\alpha'\left(1 + \rho'^2 + \sigma'^2\right)^{3/2} + \left(1 + \rho'^2 + \sigma'^2\right)^3\right]} \\
&+ \frac{\gamma^{-1}\left(\left(1 + \rho'^2 + \sigma'^2\right)^{3/2} + \alpha'\right)\left(U_1\left(\alpha'\sigma' + \alpha\rho'\right) - \rho\right)}{\left[\alpha^2 + \alpha'^2 + 2\alpha'\left(1 + \rho'^2 + \sigma'^2\right)^{3/2} + \left(1 + \rho'^2 + \sigma'^2\right)^3\right]} \\
\sigma'' =& \frac{\gamma^{-1}\left(\left(1 + \rho'^2 + \sigma'^2\right)^{3/2} + \alpha'\right)\left(U_1\left(\alpha'\sigma' - \alpha\rho'\right) - \sigma\right)}{\left[\alpha^2 + \alpha'^2 + 2\alpha'\left(1 + \rho'^2 + \sigma'^2\right)^{3/2} + \left(1 + \rho'^2 + \sigma'^2\right)^3\right]} \\
&- \frac{\gamma^{-1}\alpha\left(U_1\left(\alpha\sigma' + \alpha'\rho'\right) - \rho\right)}{\left[\alpha^2 + \alpha'^2 + 2\alpha'\left(1 + \rho'^2 + \sigma'^2\right)^{3/2} + \left(1 + \rho'^2 + \sigma'^2\right)^3\right]}
\end{aligned}
\tag{5.17}
$$

which can be integrated numerically.

We then recover the solutions

$$y(x,t) = \mathcal{R}\mathrm{e}(\Phi) = \rho(x)\cos(\gamma t) + \sigma(x)\sin(\gamma t)\,,$$

$$z(x,t) = \mathcal{I}\mathrm{m}(\Phi) = \sigma(x)\cos(\gamma t) - \rho(x)\sin(\gamma t)\,.$$

(5.18)

Clearly, these solutions are 2π-periodic in t. Note that, due to the form of (5.10), γ is not distributed among all terms other than the Φ_t term, hence we cannot simply assume that Φ contains a factor of $e^{-i\gamma t}$. This is why γ still appears in the equations, despite the fact that it can be scaled out of the simpler model for a standard fluid. As we shall see, γ strongly influences the form of the vortex filament.

Solving (5.17) numerically, we obtain the solutions (5.18). In order to do so, we shall need reasonable values of the physical parameters. From Table 1 of Schwarz (1985) we obtain reasonable value for α and α': at temperature $T = 1$K we have $\alpha = 0.005$ and $\alpha' = 0.003$, while at temperature $T = 1.5$K we have $\alpha = 0.073$ and $\alpha' = 0.018$. Note that that α' can scale as order α, and hence it can have an important contribution. In Figs. 5.1-5.4, we reconstruct the full solutions using (5.18). Note that the results display strong sensitivity to initial conditions.
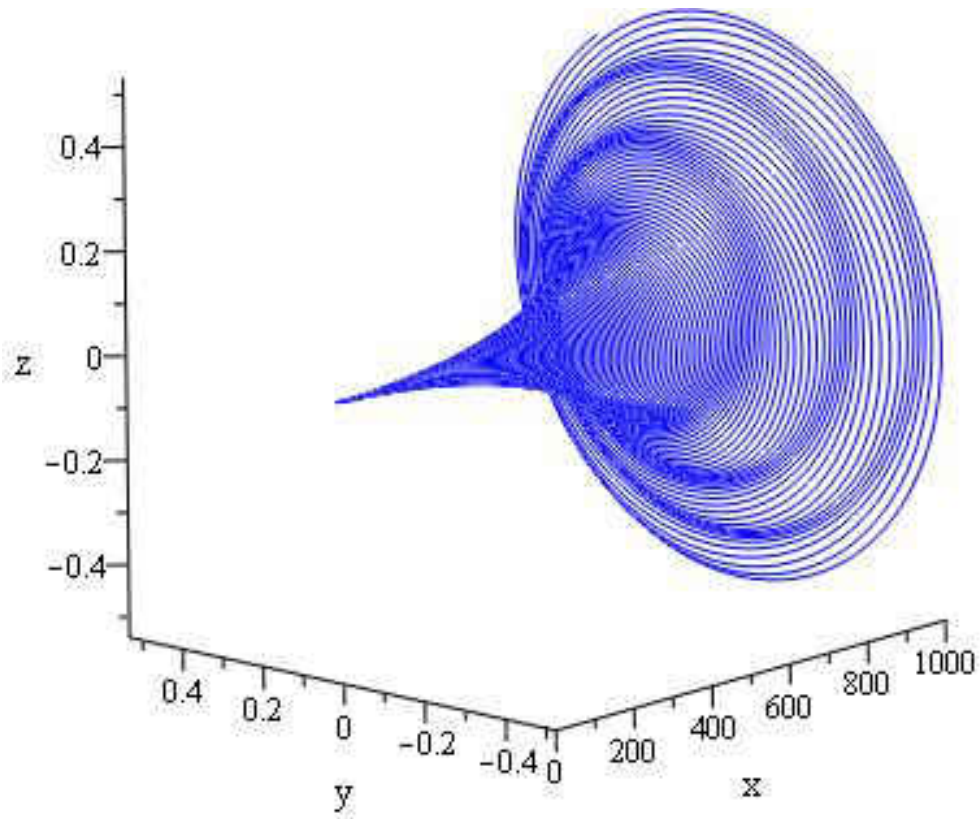
Figure 5.1: Vortex filament at temperature $T = 1$K where we have $\alpha = 0.005$ and $\alpha' = 0.003$.

We set $U_1 = \gamma = t = 1$ and $\rho(0) = \sigma(0) = 0.01$, $\rho'(0) = \sigma'(0) = 0$.
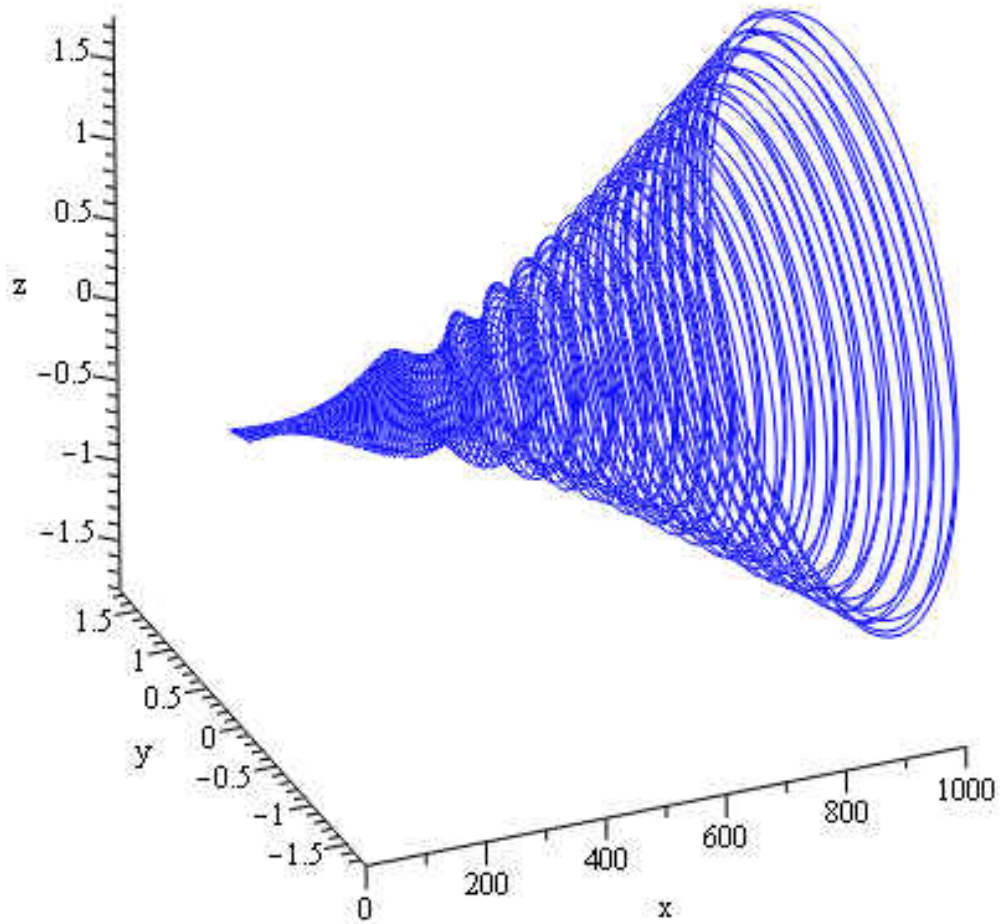
Figure 5.2: Vortex filament at temperature $T = 1K$ where we have $\alpha = 0.005$ and $\alpha' = 0.003$. We set $U_1 = \gamma = t = 1$ and $\rho(0) = \sigma(0) = 0.1$, $\rho'(0) = \sigma'(0) = 0$. Note the influence of the initial condition (compared with Fig. 5.1).
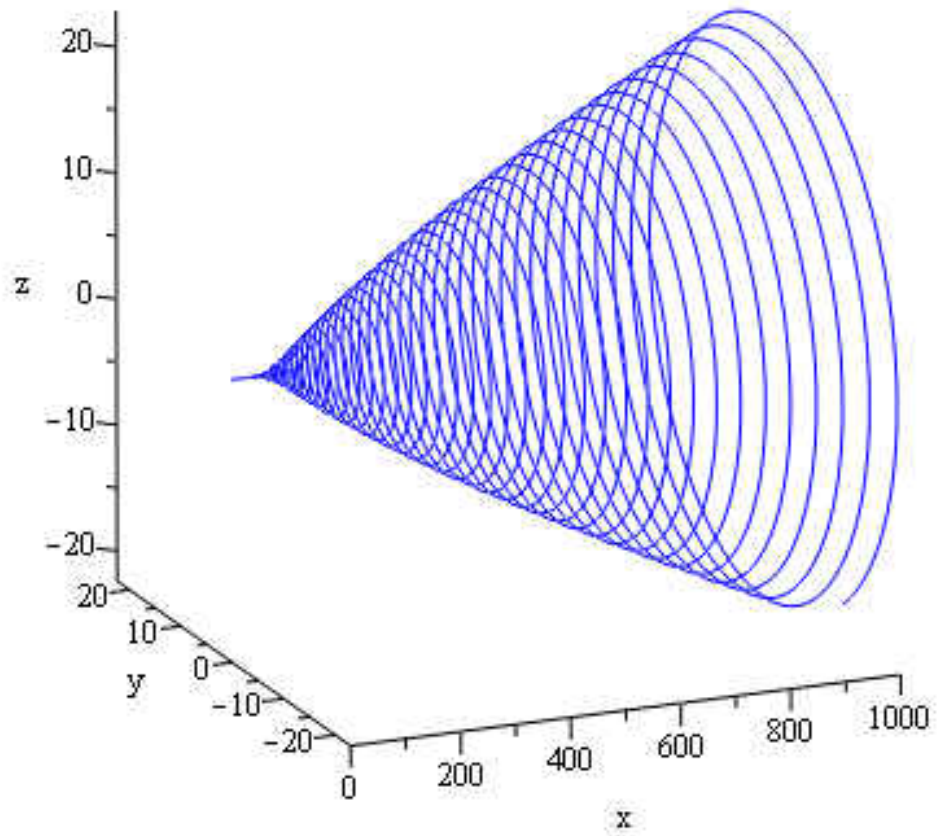
Figure 5.3: Vortex filament at temperature $T = 1.5$K we have $\alpha = 0.073$ and $\alpha' = 0.018$. We set $U_1 = \gamma = t = 1$ and $\rho(0) = \sigma(0) = 0.01$, $\rho'(0) = \sigma'(0) = 0$.
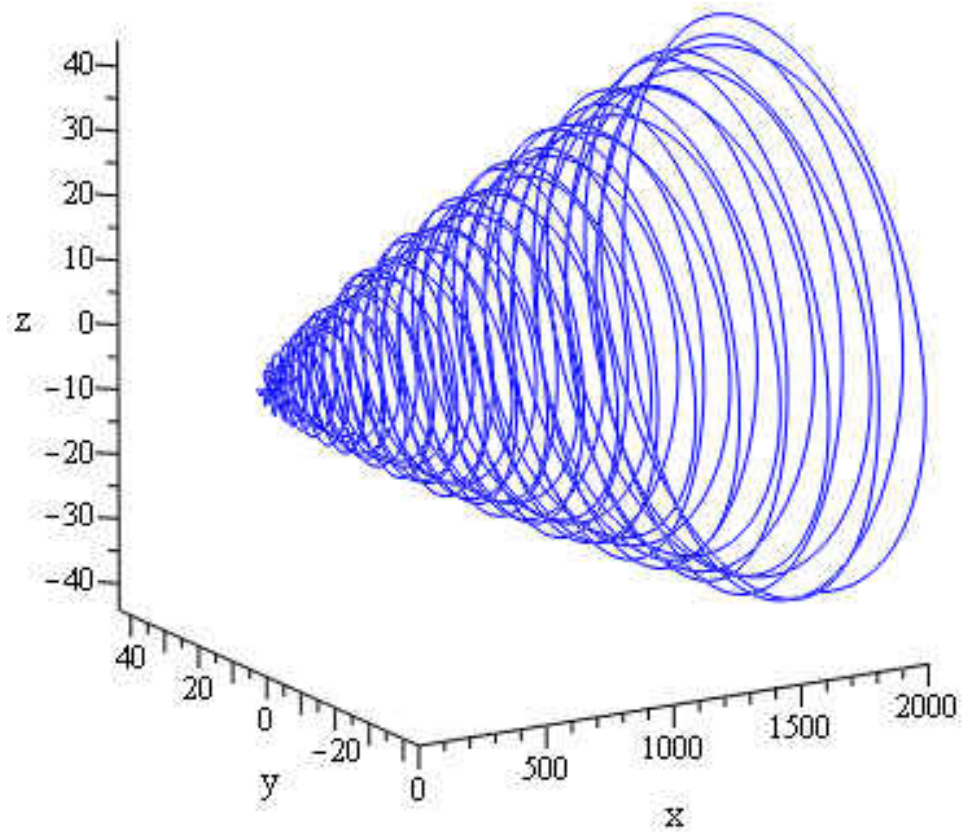
Figure 5.4: Vortex filament at temperature $T = 1.5$K we have $\alpha = 0.073$ and $\alpha' = 0.018$. We set $U_1 = \gamma = t = 1$ and $\rho(0) = \sigma(0) = 2$, $\rho'(0) = \sigma'(0) = 0$. Again, we see that the solutions do depend strongly in the initial condition. Here the filament exhibits far less regularity in structure than in the "small initial condition" case.

In Fig. 5.5, we plot the modulus $|\Phi| = \sqrt{\rho^2 + \sigma^2}$. Observe the intermittent behavior in the plots for cases II and III corresponding to $T = 1.5\mathrm{K}$. Thus, at this higher thermal level, the regular oscillatory behavior apparent at lower temperatures gives way to a more complicated pattern. Similarly, the numerical findings suggest that an increase in the normal fluid velocity can destabilize the circular form of the vortex filament (in the $y - z$-plane), mirroring the effect seen in Fig. 5.4, where the solutions exhibit a far less uniform circular structure. For large enough values of the normal fluid velocity, we find numerical solutions that become asymmetric in the $y - z$-plane (see Fig. 5.6). Meanwhile, increasing the parameter γ has the reverse effect: circular symmetry is maintained and even reinforced as γ is increased, whereas the solutions become asymmetric when $\gamma << 1$ (Fig. 5.7).
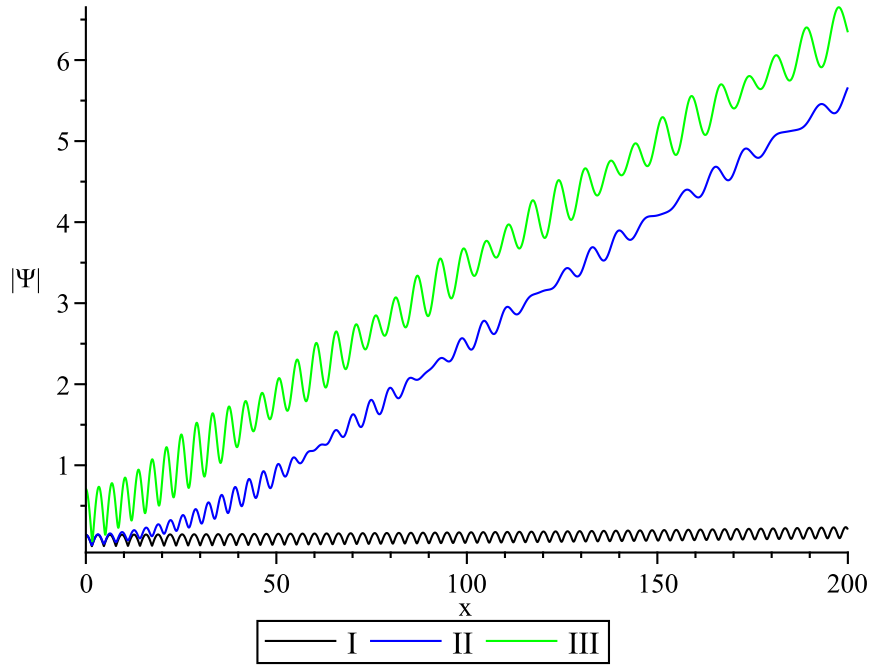
Figure 5.5: Plot of the modulus $|\Phi| = \sqrt{\rho^2 + \sigma^2}$ given I: $T = 1$K, $\alpha = 0.005$, $\alpha' = 0.003$, $\rho(0) = \sigma(0) = 0.1$; II: $T = 1.5$K, $\alpha = 0.073$, $\alpha' = 0.018$, $\rho(0) = \sigma(0) = 0.1$; II: $T = 1.5$K, $\alpha = 0.073$, $\alpha' = 0.018$, $\rho(0) = \sigma(0) = 0.5$. We set $U_1 = \gamma = t = 1$, $\rho'(0) = \sigma'(0) = 0$ in all plots. Note the intermittent behavior apparent in II and III.
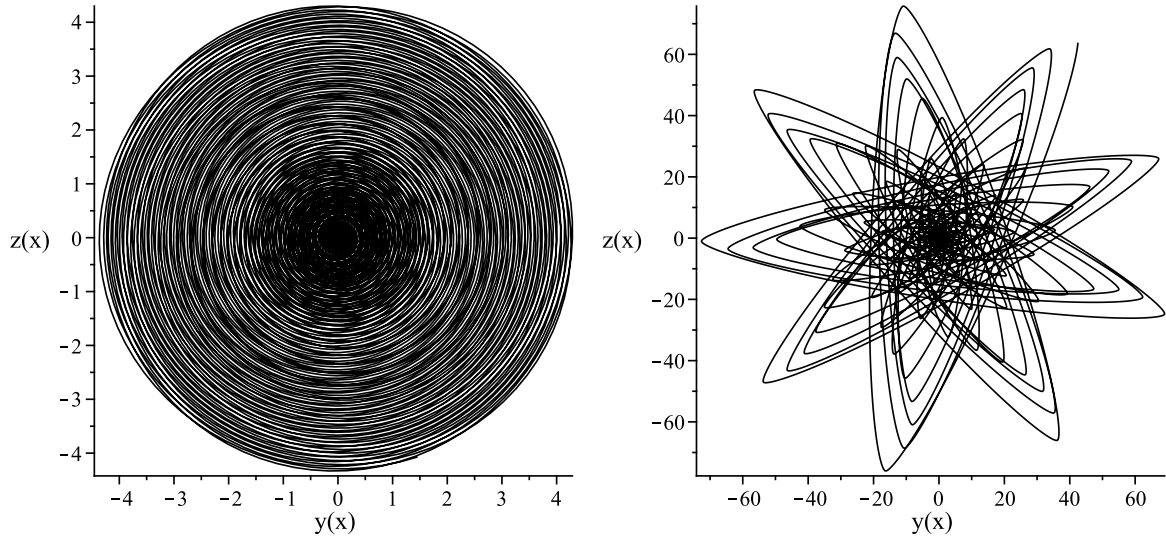
Figure 5.6: Phase portrait of $(y(x), z(x))$ for $x \in [0, 2000]$ given $T = 1K$, $\alpha = 0.005$, $\alpha' = 0.003$, $\rho'(0) = \sigma'(0) = 0$ $\rho(0) = \sigma(0) = 0.1$, $\gamma = t = 1$. We have taken $U_1 = 1$ (left image) to demonstrate a radially symmetric solution and $U_2 = 20$ (right image) to demonstrate the structures that may develop when the normal fluid velocity, U_1, becomes large.
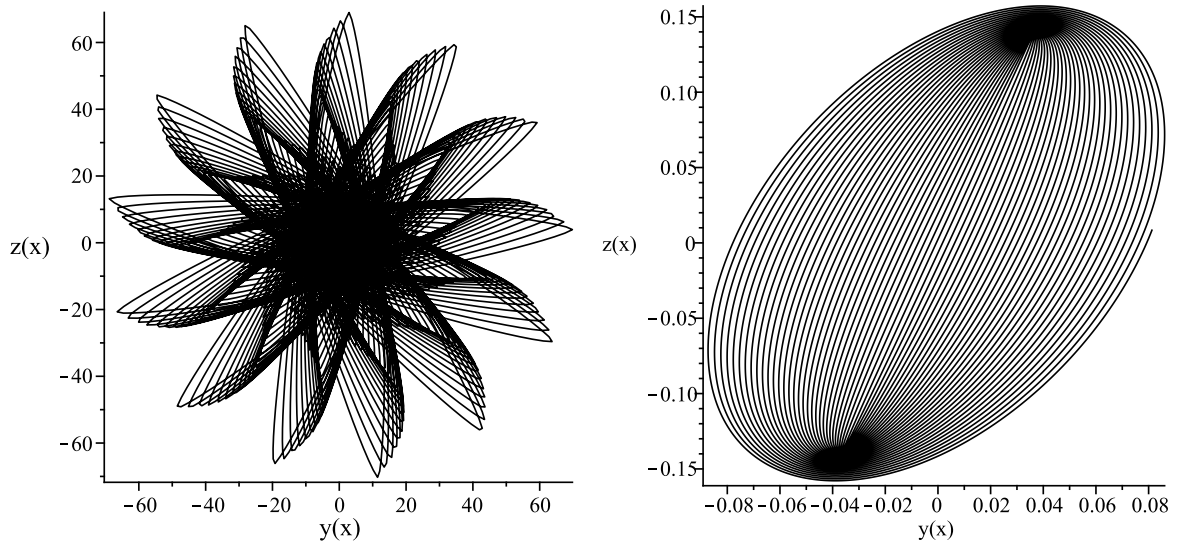
Figure 5.7: Phase portrait of $(y(x), z(x))$ for $x \in [0, 2000]$ given $T = 1\text{K}$, $\alpha = 0.005$, $\alpha' = 0.003$, $\rho'(0) = \sigma'(0) = 0$ $\rho(0) = \sigma(0) = 0.1$, $U_1 = t = 1$. We have taken $\gamma = 0.001$ (left image) and $\gamma = 100$ (right image) to demonstrate the spectrum of structures possible.

5.1.5 Discussion

We've derived the fully nonlinear local induction equation describing the motion of a vortex filament in superfluid ^{4}He. Upon linearizing terms involving the two superfluid parameters, a less nonlinear form of this equation was studied. The resulting equation is a type of potential-less nonlinear Schrödinger equation, and, under an appropriate change of variables, this equation is shown to have a first integral. This property is shared with the analogous equation governing the motion of a vortex in a standard fluid, as was studied in Chapter 2. Indeed, in the limit where $(\alpha, \alpha') \to (0, 0)$, equation (5.10) reduces to the equation studied in Chapter 2. In the limit $(\alpha, \alpha') \to (0, 0)$, the six possible formal solutions to (5.10) reduce to the two solution branches found in Chapter 2. While this first integral is mathematically interesting, it involves a plane-wave type function with a complex wave-speed, and hence it is not particularly useful for actually computing solutions to the nonlinear partial differential equation which governs the vortex filament. Introducing a new change of dependent variable, $\Phi(x, t) = e^{-it} (\rho(x) + i\sigma(x))$, we obtained a nonlinear four-dimentional ODE system governing $\rho(x)$ and $\sigma(x)$, which we were then able to numerically integrate. Unlike the special exact solution in (Shivamoggi [85]), the present solutions are valid for a far wider region of physical parameters: for instance, for large values of γ and U. Integrating this system, we recover solutions to the fully nonlinear local induction equation describing the motion of a vortex filament in superfluid ^{4}He. We find that the qualitative features of

the solutions depend not only on the superfluid parameters, but also strongly on the initial conditions, the curvature, and the normal fluid velocity.

5.2 Motion of a helical vortex filament in superfluid ^{4}He under the extrinsic potential form of the LIA

We study the motion of helical vortex filaments in superfluid ^{4}He under the exact fully nonlinear LIA considered in potential form discussed in the previous section. Nonlinear dispersion relations governing the helical Kelvin wave on such a vortex filament are derived in exact form, from which we may exactly calculate the phase and group velocity of the Kelvin wave. With this, we classify the motion of a helical Kelvin wave on a vortex filament under the LIA. The dispersion relations and results which follow are exact in nature, in contrast to most results in the literature, which are usually numerical approximations. As such, our results accurately capture the qualitative behavior of the Kelvin waves under the LIA. Extensions to other frameworks are discussed. The results on helical vortex filaments under the potential form of the quantum LIA present in this section are due to Van Gorder [106].

5.2.1 Background

The superfluid regime is one in which the LIA can usefully be applied as a reasonable approximation, due to zero viscosity which allows the persistence of vortex filament structures[39, 40]. In this setting, the LIA can be used to model Kelvin waves on a vortex filament in superfluid ^{4}He. In the present section, we study a vortex filaments under the Cartesian reference frame (the extrinsic coordinate system[102]) for the LIA. Recently, a cubic approximation to this model was considered[85]. The fully nonlinear form of the LIA, however, is required in order to pick up the full qualitative features of the solutions under the LIA.

Kelvin waves have previously been considered in a number of settings [85] in order to study superfluid turbulence. That said, exact solutions for either the fully nonlinear or the approximate forms of the Hall-Vinen form of the LIA including superfluid friction parameters are rare. However, classification of solutions to such models are useful, as they set the foundation for numerical solutions under more complicated conditions, such as reconnection. The approximate (some terms with α, α' were dropped) solution presented by Shivamoggi [85] was that of a propagating damped Kelvin kink on a vortex, which is reminiscent of the soliton on a vortex filament studied by Hasimoto [42]. Some results for Hasimoto-type [41] planar vortex filaments have also been given [100]. Helical waves are a useful type of solution, and have been considered for the standard LIA [89] (corresponding to setting the superfluid friction parameters to zero).

It should be noted, however, that for non-zero values of the superfluid friction parameters, there are no helical solutions studied for any of the models in the literature, full or approximate. Upon writing the LIA for a superfluid in potential form, we are able to construct helical Kelvin wave solutions, and accordingly determine the relevant exact dispersion relations between the frequency ω and wave number k. In the case where the friction parameters are non-zero, the amplitude A of a helical Kelvin wave is bounded and depends non-linearly on the wave number k. A degenerate case is also mentioned, which highlights a qualitative difference in the two friction parameters introduced by Hall and Vinen[40]. Comparisons of the present results with those for approximating models [85, 55] related to the fully nonlinear LIA are made; while such models agree with the fully nonlinear LIA for small wave number solutions, the agreement breaks down for larger values of the wave number, both quantitatively and qualitatively. We are able to determine the helical solutions exactly in terms of the model parameters, and for each case we are able to determine the phase and group velocity of the solutions in closed form. Therefore, we are able to completely classify the motion of a helical filament in superfluid ^{4}He under the LIA. For the Laurie et al. [55] model, we also give results for the planar vortex filament.

The present results allow us to see exactly how the inclusion of the superfluid friction parameters influences the qualitative behavior of filament solutions in general, and the quantitative behavior of helical structures in particular. Such a solution is fundamental, and serves as a baseline of comparison with other analytical solutions, and also for more

complicated solutions which must be found numerically. For these reasons, the results here further our understanding of solutions occurring at the onset of superfluid turbulence.

As discussed above, Van Gorder[102] determined the derivative NLS equation resulting from the LIA:

$$i\Phi_t + \frac{\alpha' U i \Phi_x}{(1 + |\Phi_x|^2)^{1/2}} - \frac{\alpha \gamma i \Phi_{xx}}{(1 + |\Phi_x|^2)^2} - \alpha U \Phi_x + \frac{(1 - \alpha')\gamma \Phi_{xx}}{(1 + |\Phi_x|^2)^{3/2}} = 0 \,. \tag{5.19}$$

This describes the motion of a type of vortex filament which moves about the x-axis. Propagation of a wave along the x-axis is made possible as the filament rotates in a corkscrew manner: the filament rotates, with an excitation propagating in the x-direction. Again, this formulation is useful if the filament is aligned along the x-axis, for which the above relations are well-defined. If the filament alignment deviates too much from this (for instance, if the filament bends back on itself), then the formulation breaks down, and a full three-dimensional simulation may be needed. Still, in the regime where this form of the LIA is valid, exact solutions are possible, which are of course the most preferred.

5.2.2 Helical vortex filament

We shall now be interested in helix solutions to the LIA, of the form $\Phi(x, t) = A \exp(i(kx - \omega t + x_0))$. These can describe the propagation of a Kelvin wave on a helical vortex filament under the LIA. Mapping the potential form of a solution into the Cartesian representation, one obtains $\mathbf{r} = x\mathbf{i}_x + A\cos(kx - \omega t + x_0)\mathbf{i}_y + A\sin(kx - \omega t + x_0)\mathbf{i}_z$. Such a solution takes

the form of a helix oriented along the x-axis which rotates in time; see Fig. 5.8. Assuming such a helical solution, we arrive at necessary and sufficient conditions (separating real and imaginary parts) on the model parameters:

$$-\omega + \frac{\alpha' U k}{(1 + A^2 k^2)^{1/2}} + \frac{\gamma(1 - \alpha')k^2}{(1 + A^2 k^2)^{3/2}} = 0 \,, \tag{5.20}$$

$$\alpha i \left(-U k + \frac{\gamma k^2}{(1 + A^2 k^2)^2} \right) = 0 \,. \tag{5.21}$$

When these conditions are satisfied, a helical solution exists. In order to determine the precise motion, one needs to determine the angular frequency as a function of the wave number and the physical parameters. With this information, the position of the helix structure can be determined at any time t.

We have two cases, one degenerate and one non-degenerate, depending on α. In the degenerate case where $\alpha = 0$, it is condition (5.21) that degenerates, leaving the wave number k and the amplitude A arbitrary (unlike in the $\alpha \neq 0$ case, where they are related in a fixed manner). However, since physically we should have $\alpha > \alpha'$, then both friction parameters should vanish in this case. Hence, we reduce to the standard LIA, which has been studied elsewhere.
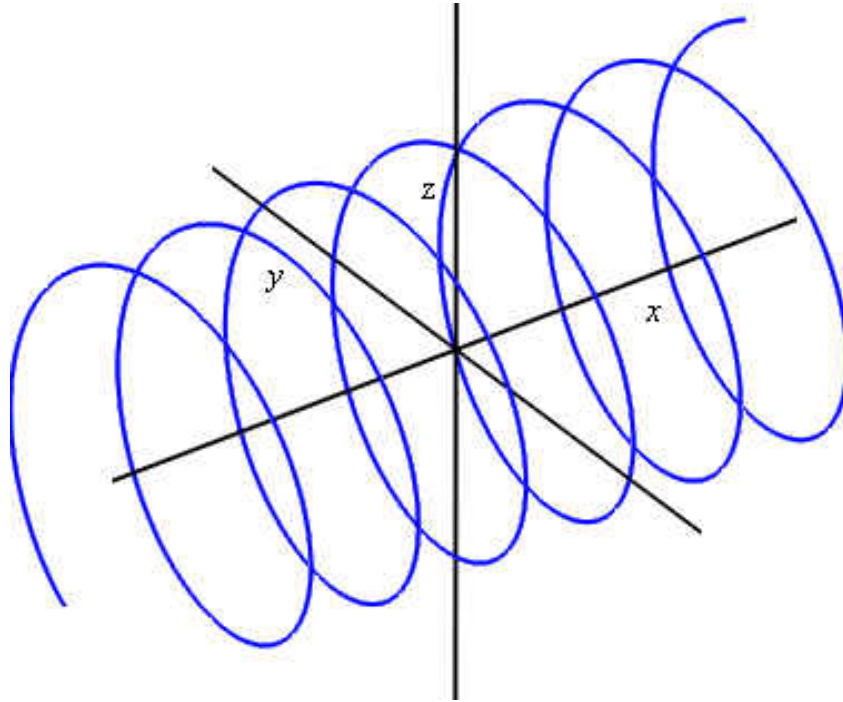
Figure 5.8: Schematic of the problem geometry for a prototypical helical vortex filament. The helical vortex filament is oriented along the x-axis, with amplitude A and wave-number k. The angular frequency, ω, will dictate the motion of this helical vortex filament.

If $\alpha \neq 0$, condition (5.21) implies $k(1 + A^2k^2)^{-2} = U/\gamma$, a condition fixing A and k in terms of one another. It is simpler to solve for amplitude in terms of wave number, and thus this condition implies that the amplitude must satisfy the condition

$$A = \frac{1}{k}\sqrt{\sqrt{\gamma k/U} - 1}\,, \tag{5.22}$$

provided $k > U/\gamma$; such solutions do not exist for $k \leq U/\gamma$. Placing (5.22) into (5.20), we find

$$\omega = U^{5/4}\gamma^{-1/4}k^{5/4}\left(\frac{\alpha'}{\sqrt{k}} + (1 - \alpha')\sqrt{\frac{\gamma}{U}}\right). \tag{5.23}$$

We then find that the phase velocity is

$$v_p = \frac{\omega}{k} = U^{5/4}\gamma^{-1/4}k^{1/4}\left(\frac{\alpha'}{\sqrt{k}} + (1 - \alpha')\sqrt{\frac{\gamma}{U}}\right), \tag{5.24}$$

while the group velocity is

$$v_g = \frac{\partial \omega}{\partial k} = U^{5/4}\gamma^{-1/4}k^{1/4}\left(\frac{3\alpha'}{4\sqrt{k}} + \frac{5}{4}(1 - \alpha')\sqrt{\frac{\gamma}{U}}\right). \tag{5.25}$$

From the condition (5.22), we see that for large wave numbers, the amplitude must be small. Meanwhile, for large normal velocity flows, the wave number, obeying $k > U/\gamma$ must be sufficiently large, leading to solutions of sufficiently small amplitude.

We plot the amplitude of a helical solution in the $\alpha \neq 0$ regime in Fig. 5.9 for various values of normal fluid velocity (normalizing $\gamma = 1$). As expected, the increased instability due to higher normal fluid velocities decreases the permitted size of the helical solutions (an increase in U decreases the amplitude A). Interestingly, a maximal amplitude solution exists for wave number k_A, where $k_A = \frac{16U}{9\gamma}$. This maximal value of A is given by $A_{\max} = \frac{3\sqrt{3}\gamma}{16U}$.

The dispersion relation $\omega(k)$ for the angular frequency given by (5.23) scales as $k^{5/4}$ for large k, so the phase and group velocities scale as $k^{1/4}$. An increase in the superfluid friction parameter α serves to increase the angular frequency, along with the phase and group velocities. The dispersion relation $\omega(k)$ is plotted in Fig. 5.10.

We should remark that, in the case where $\alpha \neq 0$ yet $U = 0$, condition (5.21) implies $k = 0$, so the only helical solution is a constant. In this case, the solution simply corresponds to a line vortex filament $\mathbf{r} = (x, 0, 0)$ (a zero-curvature solution). This is reasonable: the normal fluid velocity is driving the helical structure through the friction parameters, so without the normal flow, a non-zero friction parameter makes no sense. Mathematically, the degenerate case has the following properties.

First, the angular frequency is then given by

$$\omega = \frac{\alpha' U k}{(1 + A^2 k^2)^{1/2}} + \frac{\gamma(1 + \alpha')k^2}{(1 + A^2 k^2)^{3/2}} \, . \tag{5.26}$$

The phase velocity in this case is

$$v_p = \frac{\alpha' U}{(1 + A^2 k^2)^{1/2}} + \frac{\gamma(1 + \alpha')k}{(1 + A^2 k^2)^{3/2}} \, , \tag{5.27}$$

while the group velocity is

$$v_g = \frac{\alpha' U}{(1 + A^2 k^2)^{3/2}} + \frac{\gamma(1 + \alpha')(2 - A^2 k^2)k}{(1 + A^2 k^2)^{5/2}} \, . \tag{5.28}$$

Note that v_g changes sign once as k increases from zero to infinity, so there exists a finite wave number, say k^*, at which ω attains a unique maximum. Setting $v_g(k^*) = 0$, we find that k^* satisfies the complicated cubic expression

$$\alpha' U + 2\gamma(1 - \alpha')k^* + \alpha' U A^2 k^{*2} - \gamma(1 - \alpha')A^2 k^{*3} = 0 \, . \tag{5.29}$$
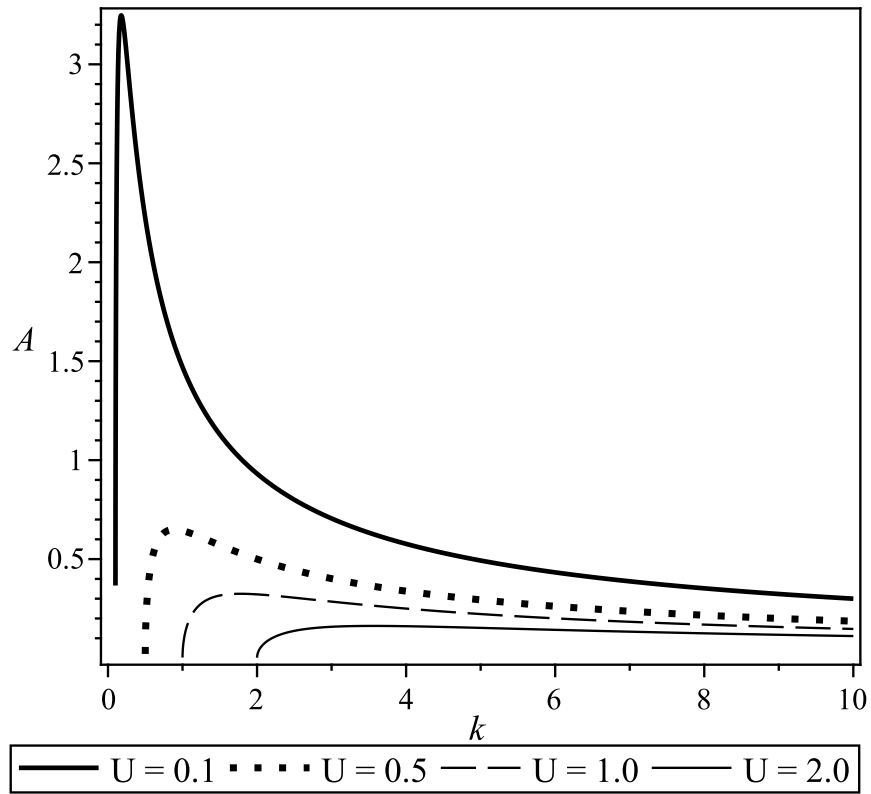
Figure 5.9: Plot of the nonlinear dependence of the amplitude A given in Eq. (5.22) on the wave number k and the normal fluid velocity U. The permissible wave numbers satisfy $k > U/\gamma$, and for the sake of demonstration we normalize $\gamma = 1$. As the normal fluid velocity increases, the permitted amplitude values decrease, owing to the added instability induced by the normal fluid. We observe a unique peak value in amplitude at some wave number k_A for each fixed value of U.
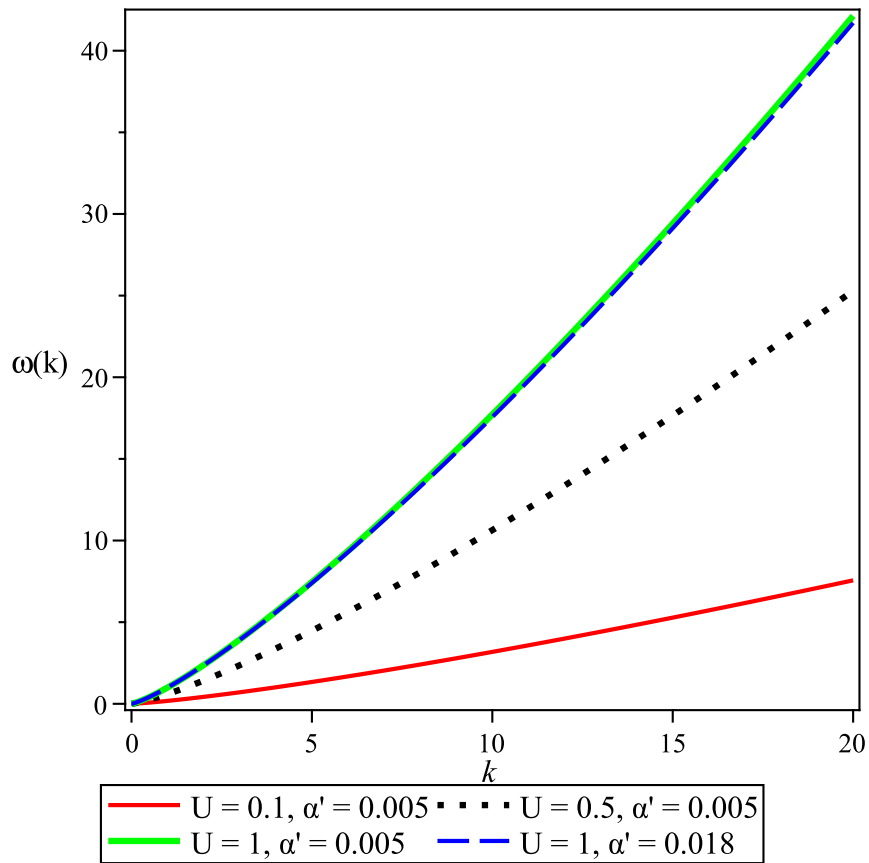
Figure 5.10:   Plots of the nonlinear dispersion relation Eq. (5.23) for $\omega(k)$ in the non-de-

generate case $\alpha \neq 0$. When $k = 0$, $\omega(0) = 0$ while $\omega > 0$ for $k > 0$.

Note that when $\alpha' = 0$, we have $k^* = \sqrt{2}/A$. So, since α' is small, it makes sense to consider a perturbation expansion for k^* in α'. Doing so, we find that maximal amplitude solutions correspond to the wave number given by

$$k^* = \frac{\sqrt{2}}{A} + \frac{3U}{4\gamma}\alpha' + \left(\frac{3U}{4\gamma} - \frac{3\sqrt{2}U^2 A}{64\gamma^2}\right)\alpha'^2 + O(\alpha'^3). \tag{5.30}$$

In the case of $\alpha = 0$, the LIA model admits helical solutions with bounded angular frequency ω. Unlike in the $\alpha \neq 0$ case, here the amplitude A is unrestricted, so large-amplitude solutions are possible. Furthermore, there are no restrictions on the wave number, so negative wave numbers are even possible.

Regarding the asymptotics of the dispersion relation, in the $k \to +\infty$ limit, we find that

$$\omega \sim \frac{\alpha'U}{A} + \frac{\gamma(1 + \alpha')}{A^3}\frac{1}{k}, \tag{5.31}$$

while in the $k \to -\infty$ limit, we find

$$\omega \sim -\frac{\alpha'U}{A} - \frac{\gamma(1 + \alpha')}{A^3}\frac{1}{|k|}. \tag{5.32}$$

So, there is some negative wave number $k_- < 0$ at which $\omega(k_-) = 0$.

5.2.3 Approximations to the LIA

In the present section, we shall consider two approximations to the fully nonlinear form of the LIA used above. We highlight the utility and shortcomings of each reduced model.

Taking an approximation to the LIA, Shivamoggi[85] obtained a linearized model, which preserved up to cubic nonlinearity affiliated with the curvature of a vortex filament while linearizing the superfluid friction terms α and α'. An approximate locally stationary wave solution was then presented.

If one takes a cubic approximation of the nonlinear contribution due to arclength, and drops nonlinear terms which are multiplied with superfluid friction parameters, we arrive at the cubic derivative NLS equation

$$i\Phi_t + (\alpha'i - \alpha)U\Phi_x + (1 - \alpha' - \alpha i)\gamma\Phi_{xx} - \frac{3\gamma}{2}|\Phi_x|^2\Phi_{xx} = 0 \,. \tag{5.33}$$

Assuming a helical Kelvin wave, we obtain the conditions

$$\omega - \alpha'Uk - (1 - \alpha')\gamma k^2 + \frac{3\gamma}{2}A^2k^4 = 0 \,, \tag{5.34}$$

$$\alpha i(-Uk + \gamma k^2) = 0 \,. \tag{5.35}$$

Here, a few features of the solutions are apparent. First, if $\alpha \neq 0$, the wave number depends only on U (the normal velocity) and γ (the strength of the filament). If $\alpha = 0$, the wave number is arbitrarily determined. In either case, α does not enter into the helical solution. Now, in the $\alpha \neq 0$ case, $k = U/\gamma$, so the angular frequency is

$$\omega = \frac{U^2}{\gamma}\left\{1 - \frac{3A^2U^2}{2\gamma^2}\right\} \,. \tag{5.36}$$

Some observations are in order. Note that there is no amplitude restriction on the solution. Also, when $U = 0$ and $\alpha \neq 0$, note that $k = 0$ necessarily, in which case $\Phi = $ constant.

In the case where $\alpha = 0$, (5.35) becomes degenerate and the angular frequency reads

$$\omega = \alpha' U k + (1 - \alpha')\gamma k^2 - \frac{3\gamma}{2}A^2 k^4 \,. \tag{5.37}$$

In contrast to the fully nonlinear LIA, note that for the cubic approximation to the LIA, the angular frequency is unbounded in wave number k. For helical vortex filaments satisfying (5.37), the phase velocity is given by

$$v_p = \alpha' U + (1 - \alpha')\gamma k - \frac{3\gamma}{2}A^2 k^3 \,, \tag{5.38}$$

whereas the group velocity is given by

$$v_g = \alpha' U + 2(1 - \alpha')\gamma k - 6\gamma A^2 k^3 \,. \tag{5.39}$$

Laurie et al. [55] derived a local nonlinear equation (LNE) from the Biot-Savart law, which was proposed as a simple model for the motion of Kelvin waves. The LNE is simpler than the fully nonlinear LIA, yet permits energy exchange between Kelvin waves, unlike the linearized LIA. The LNE of Laurie et al. [55] reads

$$i\Psi_t + \hat{\gamma}\frac{\partial}{\partial x}\left\{\left(\Lambda - \frac{1}{4}|\Psi_x|^4\right)\Psi_x\right\} = 0 \,. \tag{5.40}$$

Here $\hat{\gamma} = \kappa/(4\pi) > 0$ (κ is the quantum of velocity circulation) and $\Lambda > 0$ scales as the natural logarithm of the mean intervortex distance over the vortex core radius. Nonlinearity in this equation is responsible for the energy transfer among the Kelvin wave modes. Making the change of variable $\Phi(x,t) = (4\Lambda/5)^{-1/4}\Psi(x,t)$, and letting $\gamma = \hat{\gamma}\Lambda$, we obtain the scaled equation

$$i\Phi_t + \gamma\left(1 - |\Phi_x|^4\right)\Phi_{xx} = 0 \,. \tag{5.41}$$

Assuming a helical solution, $\omega = \gamma k^2 \left(1 - A^4 k^4\right)$. Like in the case of the cubic approximation to the LIA, the angular frequency is unbounded for the helix solution to the LNE. However, like in the case of the full nonlinear LIA, there exists a maximum value of ω (beyond this value, ω decays to $-\infty$). The phase velocity is $v_p = \gamma k \left(1 - A^4 k^4\right)$, while the group velocity is $v_g = 2\gamma k \left(1 - 3A^4 k^4\right)$. Setting the group velocity to zero, we find that ω attains a unique maximum value at $k^* = 3^{-1/4}/A$, which is approximately half the value of k^* found for the fully nonlinear LIA. Thus, while the LNE picks up the qualitative maximum, the quantitative agreement is quite off.

5.2.4 Rotating planar filaments

For small-amplitude space-periodic planar vortex filaments, we shall now show that the LNE (5.41) provides an accurate approximation.

Consider the stationary solution

$$\Phi(x, t) = A e^{-i\gamma t} \phi(x), \tag{5.42}$$

for real-valued $\phi(x)$, which describes a distinct structure from that of the helical Kelvin waves discussed above: namely, it gives a rotating planar vortex filament; see Fig. 5.11 for the problem geometry. In particular, from the form of the time-dependence, Eq. (5.42) describes a rotating planar vortex filament, which moves around the x-axis as time progresses.
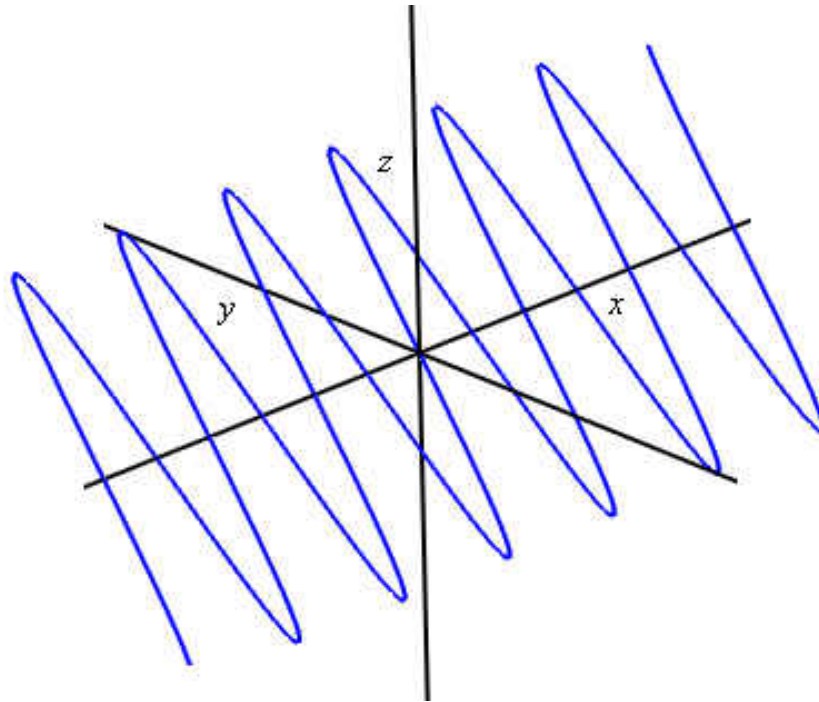
Figure 5.11: Schematic of the problem geometry for a planar vortex filament. The planar vortex filament is oriented along the x-axis, with radius A and x-period $T(A)$. The angular frequency, $\omega = \gamma$ (by assumption (5.42)) determined the motion of the vortex filament with time. The temporal period is then $2\pi/\gamma$.

Both of the LIA models (5.33) and (5.19) do not permit real-fields ϕ due to the appearance of α and α', as previously discussed by Van Gorder [102]. Since the LNE was derived differently than the LIA models, it can support such structures. With an assumption (5.42), the planar vortex filament can be described in Cartesian coordinates as

$$\mathbf{r} = x\mathbf{i}_x + A\cos(\gamma t)\phi(x)\mathbf{i}_y - A\sin(\gamma t)\phi(x)\mathbf{i}_z \,. \tag{5.43}$$

Under the assumption of such a stationary solution (5.42), (5.41) gives

$$\phi + \left(1 - A^4\phi'^4\right)\phi'' = 0 \,. \tag{5.44}$$

Without loss of generality, consider ϕ normalized such that $\phi(0) = 1$, $\phi'(0) = 0$. A first integral for (5.44) is then

$$\phi^2 + \phi'^2 - \frac{A^4}{3}\phi'^6 = 1 \,. \tag{5.45}$$

In order to have a helical solution of the form (5.42), we need ϕ to be periodic and continuous. Then, there must exist some $x \in \mathbb{R}$ at which $\phi = 0$. At such a point, $\phi'^2 - \frac{A^4}{3}\phi'^6 = 1$, which is an algebraic equation for the derivative of ϕ at such a point. This condition is equivalent to the existence of a positive root to $\frac{A^4}{3}\mu^3 - \mu + 1 = 0$, or, in transformed coordinates, $\nu^3 - \nu + \frac{A^2}{\sqrt{3}} = 0$. We find that a necessary and sufficient condition for the existence of a positive root $\nu > 0$ is $A \leq \sqrt{2/3}$. Hence, $A \leq \sqrt{2/3}$ is a necessary condition for the existence of a periodic solution ϕ for (5.44).

In order to directly solve (5.45), we would need to separate variables, which involves solving a cubic for ϕ'^2, and then performing an integration over the positive branch. To make matters worse, the integral cannot be evaluated in closed form (which is expected,

182

from the non-integrability of the LNE (5.41); see [55]). We therefore bypass such an exact method, and we instead seek a perturbation solution. Primitive perturbation theory does not adequately capture the periodicity of the true solution, so we consider the method of multiple scales. To do so, let us assume a solution of the form

$$\phi(x) = \hat{\phi}(\eta, A^4) = \hat{\phi}_0(\eta) + A^4 \hat{\phi}_1(\eta) + O(A^8) \tag{5.46}$$

where

$$\eta = \delta(A^4)x \quad \text{and} \quad \delta(A^4) = \delta_0 + A^4 \delta_1 + O(A^8) \,. \tag{5.47}$$

Eq. (5.44) is then reduced to

$$\hat{\phi} + \delta^2(A^4)(1 - \delta^4(A^4)A^4 \hat{\phi}_\eta^4)\hat{\phi}_{\eta\eta} = 0 \,, \tag{5.48}$$

which results in the terms

$$\delta_0^2(\hat{\phi}_0)_{\eta\eta} + \hat{\phi}_0 = 0 \,,$$
$$\hat{\phi}_0(0) = 1 \,, (\hat{\phi}_0)_\eta(0) = 0 \,, \hat{\phi}_0(\eta + 2\pi) = \hat{\phi}_0(\eta) \,, \tag{5.49}$$

$$\delta_0^2(\hat{\phi}_1)_{\eta\eta} + \hat{\phi}_1 = \left(\delta_0^6(\hat{\phi}_0)_\eta^4 - 2\delta_0\delta_1 \right)(\hat{\phi}_0)_{\eta\eta} \,,$$
$$\hat{\phi}_1(0) = 0 \,, (\hat{\phi}_1)_\eta(0) = 0 \,, \hat{\phi}_1(\eta + 2\pi) = \hat{\phi}_1(\eta) \,, \tag{5.50}$$

where the periodic condition is to ensure that the solutions are 2π-periodic in η (and hence $2\pi/\delta(A^4)$-periodic in x). The periodicity requirement forces $\delta_0 = 1$, and thus the zeroth order solution is found to be $\hat{\phi}_0(\eta) = \cos(\eta)$.

Using this solution in Eq. (5.50), we have

$$(\hat{\phi}_1)_{\eta\eta} + \hat{\phi}_1 = \left(2\delta_1 - \frac{1}{8} \right)\cos(\eta) + \frac{3}{16}\cos(3\eta) - \frac{1}{16}\cos(5\eta) \,. \tag{5.51}$$

183

In order to remove secular contributions, we set $\delta_1 = 1/16$ so that $\delta(A^4) = 1 + A^4/16 + O(A^8)$.

Then, using the initial conditions in (5.50), we obtain

$$\begin{aligned}
\hat{\phi}_1(\eta) &= \frac{1}{48} \cos(\eta) - \frac{3}{128} \cos(3\eta) + \frac{1}{384} \cos(5\eta) \\
&= \frac{1}{48} \sin^2(\eta) \left(5 - 2\cos^2(\eta) \right) \cos(\eta) .
\end{aligned}$$
(5.52)

From here, the perturbation solution reads

$$\begin{aligned}
\phi(x) = &\left\{ 1 + \frac{A^4}{48} \sin^2 \left(\left[1 + \frac{A^4}{16} \right] x \right) \right. \\
&\left. \times \left(5 - 2\cos^2 \left(\left[1 + \frac{A^4}{16} \right] x \right) \right) \right\} \cos \left(\left[1 + \frac{A^4}{16} \right] x \right) .
\end{aligned}$$
(5.53)

The period $T(A)$ of the solution is then approximated as

$$T(A) \approx 2\pi \left(1 + \frac{A^4}{16} \right)^{-1} = 2\pi - \frac{\pi}{8} A^4 + \frac{\pi}{128} A^8 + O(A^{12}) .$$
(5.54)

Comparing the period $T(A)$ computed in Eq. (5.54) with an exact value is useful in determining the accuracy of the approximation (5.53). From Eq. (5.45), we find

$$\phi' = \sqrt{\mu(\phi^2 - 1, A)} ,$$
(5.55)

where

$$\mu(\zeta, A) = \frac{4 + \left\{ 12A^2\zeta + 4\sqrt{9A^4\zeta^2 - 4} \right\}^{2/3}}{2A^2 \left\{ 12A^2\zeta + 4\sqrt{9A^4\zeta^2 - 4} \right\}^{1/3}}$$
(5.56)

is the branch of the cubic $\zeta + \mu - A^4\mu^3/3 = 1$ giving real solutions for small A. Separating variables in (5.55) and integrating, we obtain

$$x = \int_\phi^1 \frac{d\xi}{\sqrt{\mu(\xi^2 - 1, A)}} .$$
(5.57)
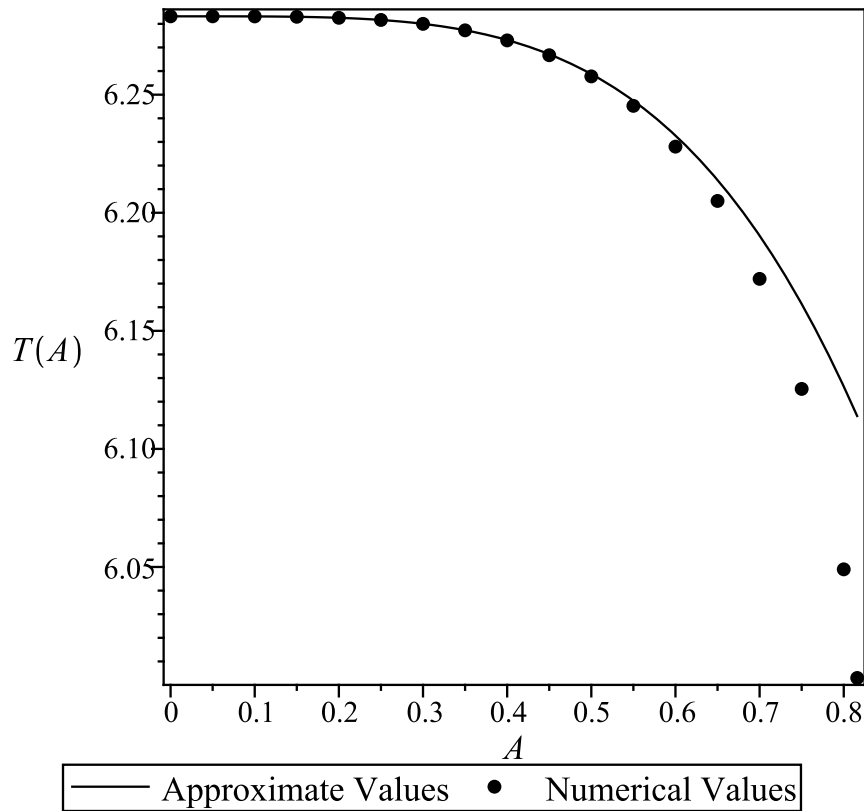
Figure 5.12: Plot of the approximation (5.54) to the space period $T(A)$ of the planar vortex filament given by the method of multiple scales. Also plotted are the exact numerical values for $T(A)$ that may be found by numerically integrating (5.44) in order to construct a solution. Clearly, the multiple scales approximation is a very good fit for small-amplitude solutions. Periodic solutions exist for $A < \sqrt{2/3} \approx 0.81649$.
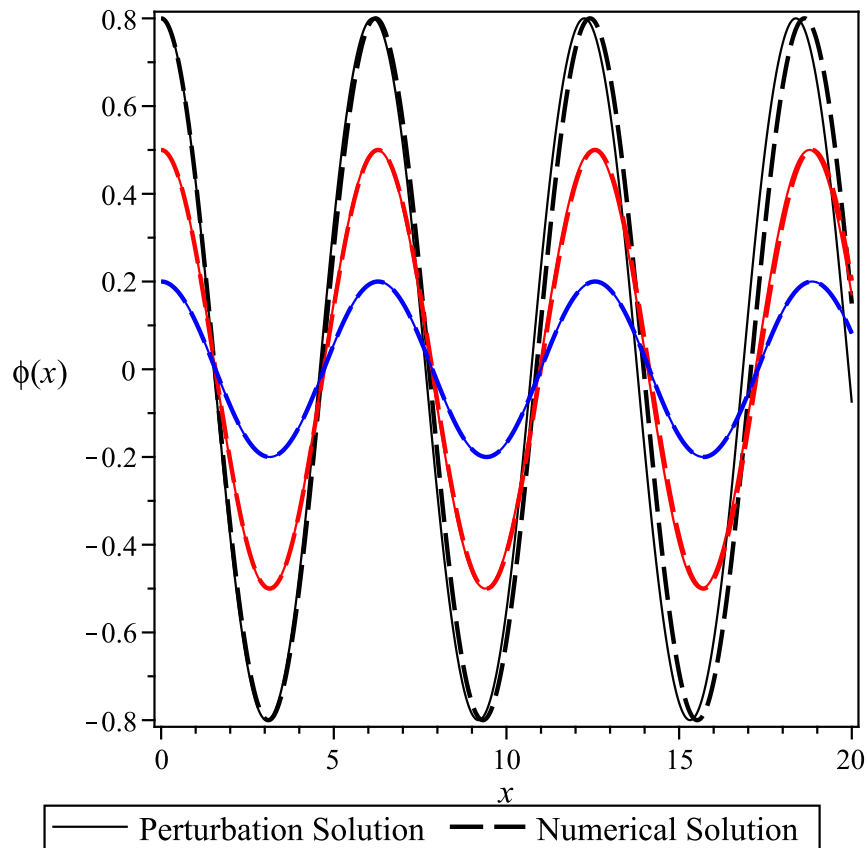
Figure 5.13: Plot of the space periodic part of the planar vortex filament, for various values of A. Solid lines denote the perturbation approximation (5.53) while the dashed lines denote numerical simulations via RKF45 method of numerical integration. We see remarkable agreement for small amplitude solutions. For the large amplitude solutions, the numerics and analytics begin to go out of phase for large x, due to the small error in the approximate period (5.54) and the true period.

Now, integrating over one quarter-period,

$$T(A) = 4 \int_0^1 \frac{d\xi}{\sqrt{\mu(\xi^2 - 1, A)}} \, . \tag{5.58}$$

The integral (5.58) is too complicated to evaluate exactly. However, it may certainly be plotted numerically as a function of A. In Fig. 5.12, we plot the exact relation for the period $T(A)$ given in (5.58) along with the approximate value obtained by multiple scales analysis in Eq. (5.54). As expected, for small A, the agreement between the approximate solution and the exact relation is good. With this, we have enough information to accurately determine the motion of a planar vortex filament. In Fig. 5.13, we plot the planar part ($\phi(x)$) of such a vortex filament, for various values of A. To recover the three-dimensional structure, one would use ϕ in (5.43) to recover a structure like that shown in Fig. 5.11.

We have demonstrated that the LNE permits a planar vortex filament solution of the Hasimoto type, in addition to the class of helical vortex filaments presented in the previous section.

5.2.5 Discussion

Under the assumption of a helical vortex filament, we have determined the dispersion relations describing the motion of this helical vortex filament in superfluid ^{4}He under the fully nonlinear form of the LIA (which is the most true form of the LIA to the Biot-Savart formulation) corresponding to the Hall and Vinen [39, 40] formulation. With this we have been

able to determine the phase and group velocities, effectively classifying all possible motions of a helical vortex filament under the LIA. Our results include the effect of both superfluid friction parameters, as well as normal fluid velocity, along the lines of the Hall and Vinen [39, 40] framework.

The helical vortex filaments are free of α (yet depend on α') due to the orientation of the filaments. However, as we've shown, there is a qualitative disconnect between the $\alpha = 0$ and $\alpha \neq 0$ solutions. This is in agreement with a finding of Shivamoggi [85], where in the case of a Hasimoto-type 2D planar vortex solution[41], "the friction term associated with α appears again to be able to change the vortex motion aspects in a qualitative way." The $\alpha = 0$ (zero temperature limit) has already been considered by Sonin [89]. While α' enters into the helix solution explicitly, its effects are relatively minor. In the $\alpha \neq 0$ and $\alpha' \to 0$ limit, we have $\omega = U^{3/4}\gamma^{1/2}k^{5/4}$ and for small non-zero α' we simply have a linear perturbation of this quantity.

There are two sensible reductions of the fully nonlinear form of the LIA:
(i) an integrable cubic reduction preserving lowest order nonlinearity [85];
(ii) a non-integrable quintic reduction useful for studying Kelvin wave interactions [55].

For sake of comparison with the fully nonlinear LIA, we may determine the dispersion relations (and other associated quantities) for these two reduced models. The three models considered become exactly comparable in the limit $\alpha = \alpha' = U = 0$, which corresponds to the standard LIA. For small values of the wave number k the agreement between the angular frequency, phase velocity, and group velocity all agree qualitatively in the case of helical

Kelvin waves. However, for the cubic approximating model, there is a fixed wave number $k = U/\gamma$, while for the other models there is a continuous spectrum. For large values of the wave number k, both approximating models break down, as they fail to capture enough of the nonlinearity governing the vortex filament motion. For the two approximating models, the angular frequency becomes unbounded for large k in the $\alpha = 0$ degenerate case, while the fully nonlinear LIA (5.19) ensures bounded angular frequency for all k in the degenerate case. For very small k, the cubic approximation to the LIA is the best fit. However, for intermediate k, the angular frequency from the local nonlinear equation produces the qualitative peak observed in the full nonlinear LIA (5.19). Hence there is utility in each model, though one must be mindful of the parameter regimes for which each simplified model is used.

In summary, some qualitative results are:

- the fully nonlinear LIA demonstrates that the amplitude A of a helical wave is strongly related to the wave number k;

- the approximating models lose the dependent of the amplitude A on the wave number k;

- the cubic approximation is valid for the unique wave number $k = U/\gamma$, while the fully nonlinear LIA is valid for an unbounded continuous spectra of wave numbers k;

- in the $k \to 0$, $U \to 0$ limit, the full and approximating models are in qualitative agreement, while for $k \to \infty$, only the fully nonlinear model is physically consistent;

189

- the amplitude of a helical wave under the fully nomlinear model is always bounded, and assumes a maximal value of $A_{\max} = \frac{3\sqrt{3}\gamma}{16U}$ at wave number $k_A = \frac{16U}{9\gamma}$.

Rotating planar Kelvin waves have also been shown to exist for the LNE, and explicit perturbation solutions have been developed for the small amplitude regime. This formulation is much simpler than that given previously for the fully nonlinear LIA[102]. In particular, by considering a multiple scales analysis, we have been able to accurately construct perturbation solutions for these planar vortex filaments. Using the results, we can determine the nonlinear dependence of the spatial period of such planar filaments on their amplitude. In the $\alpha, \alpha' \to 0$ regime (i.e., the low-temperature regime), we have therefore obtained accurate planar filaments. Unlike the helical filaments, the planar filaments lie on a plane which rotates about the x-axis, along the same lines as the Hasimoto filament which was related to elastica [41].

5.3 Self-similar vortex dynamics in superfluid ^{4}He under the Cartesian representation of the quantum LIA

We determine conditions under which the fully nonlinear form of the local induction approximation (LIA) governing the motion of a vortex filament in superfluid ^{4}He (that is, the Hall-Vinen model) in the Cartesian frame of reference permits the existence of self-similar solutions, even in the presence of superfluid friction parameters. Writing the Cartesian Hall-

Vinen LIA in potential form for the motion of a vortex filament, we find that a necessary condition for self-similarity is that the normal-fluid component vanishes (which makes sense in the low temperature limit), and we reduce the potential form of the Hall-Vinen LIA to a complex nonlinear ordinary differential equation governing the behavior of a similarity solution. In the limit where superfluid friction parameters are negligible, we provide some analytical and asymptotic results for various regimes. While such analytical results are useful for determining the qualitative behavior of the vortex filament in the limit where superfluid friction parameters vanish, numerical simulations are needed to determine the true behavior of the filaments in the case of non-zero superfluid friction parameters. While the superfluid friction parameters are small, the numerical results demonstrate that the influence of the superfluid friction parameters on the self-similar vortex structures can be strong. We classify two types of filaments from the numerical results: singular filaments (which demonstrate growing oscillations and hold kink-type solutions as a special case) and bounded filaments (whose behavior is a bounded function of x). We also comment on how to include the case where there is a non-zero normal fluid, and we find a transformation of the self-similar solutions into non-similar solutions that can account for this. The results considered here on self-similar vortex dynamics under the potential form of the quantum LIA were first published in Van Gorder [107].

5.3.1 Background

We shall demonstrate that self-similar solutions exist to the vortex filament problem (2.12) for superfluid ^{4}He, even in the presence of superfluid friction parameters, under the Hall-Vinen model in the natural Cartesian coordinate frame (hereafter referred to as the Cartesian form of the LIA, or the extrinsic coordinate model). We shall then explore various properties of these vortex filament solutions. Previously, Lipniacki [56, 57] demonstrated self-similarity for a version of the corresponding local induction equation where the dependent quantities were curvature and torsion (this is the classical intrinsic coordinate frame). In both studies, the normal fluid flow was taken to be zero, and the influence of the superfluid parameters on the curvature and torsion was studied. Thus, while self-similar solutions have been shown for the intrinsic coordinate system with curvature and torsion, self-similar solution have not been considered for the extrinsic Cartesian form of the LIA. Such solutions for the extrinsic form of the LIA would be useful, since the extrinsic frame of reference corresponds directly to the physical geometry of the problem in Cartesian coordinates. For a mathematical treatment of similarity solutions in the curvature-torsion reference frame, see [38]. The case studied therein was for the standard fluid model, corresponding to the $\alpha, \alpha' \to 0$ limit. Additionally, note that the $\alpha, \alpha' \to 0$ limit corresponds to the zero temperature limit. Svistunov explored this case in [92], and proposed a model in Cartesian coordinates.

We obtain the potential form of the Hall-Vinen model and reduce it, through an appropriate similarity transformation, into a complex-valued ordinary differential equation

with appropriate choice of similarity variable. To do so, we must assume that the normal fluid velocity is zero, as way done by Lipniacki [56, 57] in the curvature-torsion frame. In the case of very small superfluid friction, the parameters α and α' drop out, and we may obtain some analytical results corresponding to the temperature zero limit. These results allow us to understand the qualitative features of some of the interesting solutions, and are highlighted next in this section. Most interesting are the small amplitude solutions (which measure small deviations of the vortex filament from its central axis of rotation) and asymptotic solutions, valid for large values of the similarity variable. We then obtain numerical solutions for the self-similar solutions in the presence of the superfluid friction parameters α and α'. These solutions display a strong sensitivity to both initial conditions and the superfluid friction parameters. These solutions are classified as either singular or non-singular, depending on their behavior as time goes to infinity. The singular solutions can be used to construct vortex filament kinks, while the non-singular solutions can exhibit more exotic behavior. Finally, we discuss various aspects of the solutions obtained. We also discuss why it is necessary to set the normal fluid velocity to zero for the self-similar filament solutions.

We shall again use the potential form of the quantum LIA

$$i\Phi_t + \frac{\alpha' U i\Phi_x}{(1+|\Phi_x|^2)^{1/2}} - \frac{\alpha\gamma i\Phi_{xx}}{(1+|\Phi_x|^2)^2} - \alpha U\Phi_x + \frac{(1+\alpha')\gamma\Phi_{xx}}{(1+|\Phi_x|^2)^{3/2}} = 0\,. \tag{5.59}$$

In the general, the nonlinear equation (5.59) does not admit a self-similar solution (as may be verified; we revisit this point later in the discussions). However, in the slightly less general case of $U = 0$, we have a similarity solution. While this may seem excessively

193

restricting, note that superfluid turbulence in the absence of a normal-fluid component is still of physical relevance [5]. It has been shown that bundle reconnections are possible (at temperature 1.65K) in the case where the normal fluid velocity is zero [3]. Actually, the $U = 0$ limit corresponds to the low temperature limit, where there is physically little or no normal fluid influence [117]. Later, we shall discuss a way by which we may include the case of non-zero normal fluid velocity. To do so, we will transform the self-similar solution into a new solution, which breaks the self-similarity at larger time scales.

To see this, we introduce what can be verified as being a unique (up to multiplicative scaling) similarity transformation

$$\Phi(x,t) = \sqrt{\gamma t} f(\eta) \qquad \text{where} \qquad \eta = \frac{x}{\sqrt{\gamma t}}\,. \tag{5.60}$$

Despite the reduction $U = 0$, this solution still takes into account the superfluid friction parameters α and α', and hence is still of relevance. Invoking the similarity transformation (5.60), we obtain from (5.59) the ordinary differential equation

$$\frac{i}{2}\left(f - \eta f'\right) + \left(\frac{1 + \alpha'}{\left(1 + |f'|^2\right)^{3/2}} - i\frac{\alpha}{\left(1 + |f'|^2\right)^2}\right) f'' = 0\,, \tag{5.61}$$

where prime denotes differentiation with respect to η. Next, writing $f(\eta)$ in the form

$$f(\eta) = R(\eta) \exp\left(i\Theta(\eta)\right)\,, \tag{5.62}$$

we obtain the coupled system

$$\frac{\eta}{2}R\Theta' + (1 + \alpha')\frac{R'' - R\Theta'^2}{\left(1 + R^2\Theta'^2 + R'^2\right)^{3/2}} + \alpha\frac{R\Theta'' - 2R'\Theta'}{\left(1 + R^2\Theta'^2 + R'^2\right)^2} = 0\,, \tag{5.63}$$

194

$$\frac{1}{2}\left(R - \eta R'\right) + \left(1 + \alpha'\right)\frac{R\Theta'' - 2R'\Theta'}{\left(1 + R^2\Theta'^2 + R'^2\right)^{3/2}} - \alpha\frac{R'' - R\Theta'^2}{\left(1 + R^2\Theta'^2 + R'^2\right)^2} = 0\,. \qquad (5.64)$$

For space-time variables (x, t), solutions can be plotted in the Cartesian reference frame $\mathbf{r} = (x, y, z)$ given by

$$\mathbf{r} = \left(x, \sqrt{\gamma t}R\left(\frac{x}{\sqrt{\gamma t}}\right)\cos\left(\Theta\left(\frac{x}{\sqrt{\gamma t}}\right)\right), \sqrt{\gamma t}R\left(\frac{x}{\sqrt{\gamma t}}\right)\sin\left(\Theta\left(\frac{x}{\sqrt{\gamma t}}\right)\right)\right)\,. \qquad (5.65)$$

5.3.2 Analytical properties in the $\alpha, \alpha' \to 0$ limit

The behavior of solutions to the standard and superfluid models are qualitatively similar, with quantitative differences arising from the inclusion of the superfluid friction parameters. To recover the standard fluid case, we set $\alpha = \alpha' = 0$ in (5.63)-(5.64) to obtain

$$\frac{\eta}{2}R\Theta' + \frac{R'' - R\Theta'^2}{\left(1 + R^2\Theta'^2 + R'^2\right)^{3/2}} = 0\,, \qquad \frac{1}{2}\left(R - \eta R'\right) + \frac{R\Theta'' - 2R'\Theta'}{\left(1 + R^2\Theta'^2 + R'^2\right)^{3/2}} = 0\,. \quad (5.66)$$

Since the standard and superfluid solutions are qualitatively similar (since the derivative NLS equation arising from the superfluid case is a type of structural perturbation of the derivative NLS equation arising from the standard fluid case), and since the standard fluid equations are amenable to analysis, we shall consider analytical properties of self-similar solutions governed by (5.66).

We should note that self-similar solutions in the case where $U = 0$ have been studied previously. Lipniacki [56, 57] has studied such self-similar solutions in the intrinsic formulation of the LIA (the curvature-torsion frame). Svistunov [92] obtained a formulation for Cartesian frame in the temperature zero limit, corresponding to the $\alpha, \alpha' \to 0$ limit.

5.3.3 Constant phase solution yielding a linear filament

In the special case where the phase is constant, say $\Theta(\eta) = \Theta_0$, we obtain the equations $R'' = 0$ and $R - \eta R' = 0$. These equations are satisfied only for $R(\eta) = C\eta$, where C is an arbitrary scaling constant. As such, we recover

$$f(\eta) = Ce^{i\Theta_0}\eta = (C_1 + iC_2)\eta, \tag{5.67}$$

for appropriate real-valued constants C_1 and C_2. Mapping back to $\Phi(x,t)$, we have

$$\Phi(x,t) = \sqrt{\gamma t}(C_1 + iC_2)\frac{x}{\sqrt{\gamma t}} = (C_1 + iC_2)x, \tag{5.68}$$

hence $y(x,t) = C_1 x$ and $z(x,t) = C_2 x$. With this, we have shown that any constant phase solution must be linear in x and constant in t. Note that this case corresponds to $R(0) = 0$. Physically, this solution corresponds to the unperturbed line filament $\mathbf{r} = (x, C_1 x, c_2 x)$.

5.3.4 Non-constant phase as a function of amplitude

From the form of (5.66), it is clear that the phase Θ and amplitude R of a solution (5.62) are strongly coupled. From (5.66), we find

$$\frac{\frac{\eta}{2}R\Theta'}{R'' - R\Theta'^2} = -\frac{1}{\left(1 + R^2\Theta'^2 + R'^2\right)^{3/2}} = \frac{\frac{1}{2}(R - \eta R')}{R\Theta'' - 2R'\Theta'}. \tag{5.69}$$

Note that the middle term in (5.69) is always negative and finite (for any real-valued R and Θ), and hence so are the left and right terms. Setting the left and right hand sides equal,

and then manipulating the resulting equation (including multiplying the final expression by 2η), we have

$$2\eta^2 R^2 \Theta' \Theta'' - 6\eta^2 R R' \Theta'^2 + 2\eta R^2 \Theta'^2 = 2\eta(R - \eta R') R'' . \tag{5.70}$$

Observe that the left hand side of (5.70) is nearly a total derivative. Indeed, we find that (5.70) is equivalent to

$$R^8 \frac{d}{d\eta} \left\{ \eta^2 \Theta'^2 R^{-6} \right\} = 2\eta(R - \eta R') R'' . \tag{5.71}$$

Cross multiplying and integrating, we obtain

$$\eta^2 \Theta'^2 R^{-6} = \int_0^\eta \frac{2\xi(R(\xi) - \xi R'(\xi)) R''(\xi)}{R^8(\xi)} d\xi . \tag{5.72}$$

Solving equation (5.72) for Θ'^2 gives

$$\Theta'^2 = \frac{R^6(\eta)}{\eta^2} \int_0^\eta \frac{2\xi(R(\xi) - \xi R'(\xi)) R''(\xi)}{R^8(\xi)} d\xi , \tag{5.73}$$

which is an exact relation for the change of the phase Θ (in η) as a function of the amplitude R and its derivatives. We then have the local representation

$$\Theta(\eta) = \Theta_0 + \int_0^\eta \Theta'(\xi) d\xi = \Theta_0 + \int_0^\eta \sqrt{\frac{R^6(\xi)}{\xi^2} \int_0^\xi \frac{2\zeta(R(\zeta) - \zeta R'(\zeta)) R''(\zeta)}{R^8(\zeta)} d\zeta} \, d\xi . \tag{5.74}$$

For small η, we write $R(\eta) = R(0) + R'(0)\eta + \frac{R''(0)}{2}\eta^2 + O(\eta^3)$, so (5.74) becomes

$$\Theta(\eta) \approx \Theta_0 + \int_0^\eta \sqrt{\frac{R(0)^6}{\xi^2} \int_0^\xi \frac{2\zeta R''(0)}{R(0)^7} d\zeta} \, d\xi = \Theta_0 + \int_0^\eta \sqrt{\frac{R''(0)}{R(0)}} d\xi = \Theta_0 + \sqrt{\frac{R''(0)}{R(0)}} \eta . \tag{5.75}$$

Since this holds true in the small-η regime, it is clear, then, that

$$\Theta'(0) = \sqrt{\frac{R''(0)}{R(0)}} . \tag{5.76}$$

197

Hence the initial data $R''(0)$, $R(0)$ and $\Theta'(0)$ are closely related. In particular, when $R(0) \neq 0$, this relation allows us to determine $R''(0)$ in terms of $R(0)$ and $\Theta'(0)$ alone. While this follows from (5.75), it could have also been obtained from setting $\eta = 0$ in equation (5.66). As such, we see that the local solution (5.74) is consistent with the system (5.66). Likewise, from (5.66), we can determine $\Theta''(0)$ as

$$\Theta''(0) = 2\frac{\Theta'(0)R'(0)}{R(0)} - 2\left(1 + R(0)^2\Theta'(0)^2 + R'(0)^2\right)^{3/2}, \tag{5.77}$$

and making use of (5.76), we see that $\Theta''(0)$ can be completely described in terms of R and its derivative at $\eta = 0$, to wit:

$$\Theta''(0) = 2\frac{R'(0)\sqrt{R''(0)/R(0)}}{R(0)} - 2\left(1 + R(0)R''(0) + R'(0)^2\right)^{3/2}. \tag{5.78}$$

Therefore, we can completely determine the curvature of a filament at the origin $\eta = 0$ in terms of the initial data $R(0)$, $R'(0)$, $\Theta(0)$, and $\Theta'(0)$.

5.3.5 Constant modulus solution $R(\eta) = R_0$

Let us now consider the case where $f(\eta) = R_0 \exp(i\Theta(\eta))$, a constant modulus solution to (5.61). (Of course, we pick $R_0 > 0$ to avoid the zero solution.) Equation (5.70) then reduces to

$$2\eta(\eta\Theta'' + \Theta') = 0, \tag{5.79}$$

which admits a solution

$$\Theta(\eta) = \Theta_0 + C\ln(|\eta|) \tag{5.80}$$

for $\eta \neq 0$. So, a constant amplitude solution f takes the form

$$f(\eta) = R_0 \exp(i\Theta_0 + iC \ln(|\eta|)) = R_0 \cos(\Theta_0 + C \ln(|\eta|)) + iR_0 \sin(\Theta_0 + C \ln(|\eta|)). \quad (5.81)$$

The $R(\eta) = R_0$ solution then corresponds to a filament of the form

$$\mathbf{r} = \left(x, R_0 \sqrt{\gamma t} \cos\left(\Theta_0 + C \ln\left|\frac{x}{\sqrt{\gamma t}}\right|\right), R_0 \sqrt{\gamma t} \sin\left(\Theta_0 + C \ln\left|\frac{x}{\sqrt{\gamma t}}\right|\right) \right). \quad (5.82)$$

5.3.6 Small oscillation solutions

The obtained self-similar solution $f(\eta)$ scales as a linear function of η for large η. About this linear function appear oscillations, and in the present section we shall attempt to describe this behavior analytically. Let us assume a solution of the form

$$f(\eta) = q\eta + Ag(\eta), \quad (5.83)$$

where q is the coefficient of the linear dominating term for $|\eta| \to \infty$, $g(\eta)$ is the function holding the deviations from this linear function (in particular, the oscillations), and A the the maximal magnitude of the deviations. As seen in the numerical simulations, the deviations are small. So, it make quantitative sense to consider A as a perturbation parameter. Assuming a solution of the form

$$g(\eta) = g_0(\eta) + Ag_1(\eta) + O(A^2), \quad (5.84)$$

we find

$$\frac{i}{2}(g_0 - \eta g_0') + \frac{1}{(1+q)^{3/2}} g_0'' = 0, \quad (5.85)$$

$$\frac{i}{2}(g_1 - \eta g_1') + \frac{1}{(1+q)^{3/2}} g_1'' = \frac{3}{2(1+q)^{5/2}}(g_0 + g_0^*) g_0'', \tag{5.86}$$

To solve (5.85), let us make the substitution $G(\eta) = g_0(\eta) - \eta g_0'(\eta)$, which reduces (5.85) to

$$G'(\eta) = \frac{i}{2}(1+q)^{3/2} \eta G(\eta), \tag{5.87}$$

hence

$$G(\eta) = \exp\left(\frac{i}{4}(1+q)^{3/2}\eta^2 + c_0\right). \tag{5.88}$$

Then $G(\eta) = g_0(\eta) - \eta g_0'(\eta)$ yields the solution

$$
\begin{aligned}
g_0(\eta) &= c_1\eta + c_2\eta \int^\eta \frac{1}{\xi^2} \exp\left(\frac{i}{4}(1+q)^{3/2}\xi^2\right) d\xi \\
&= \left\{ c_1 - c_2\sqrt{i}\frac{\sqrt{\pi}}{2}\mathrm{erfi}\left(\frac{\sqrt{i}}{2}(1+q)^{3/4}\eta\right) - \frac{c_2}{\eta}\exp\left(\frac{i}{4}(1+q)^{3/2}\eta^2\right)\right\}\eta.
\end{aligned}
\tag{5.89}
$$

Since we want only the oscillatory contribution as $\eta \to \infty$, we compute the asymptotics

$$
\begin{aligned}
g_0(\eta) &= \left(c_1 + \frac{\sqrt{-i\pi}}{2}c_2\right)\eta \\
&+ \exp\left(\frac{i}{4}(1+q)^{3/2}\eta^2\right)\left\{-\left(1 + (1+q)^{3/4}\right)c_2 + \frac{2ic_2}{(1+q)^{9/4}}\frac{1}{\eta^2} + O\left(\frac{1}{\eta^4}\right)\right\}.
\end{aligned}
\tag{5.90}
$$

Picking $c_1 = -\sqrt{-i\pi}c_2/2$, we remove the linear growth term. The constant c_2 becomes a scaling, so we take $c_2 = 2/\sqrt{i\pi}\hat{c}(q)$ (where $\hat{c}(q)$ is a scaling factor) to simplify the resulting expression, obtaining

$$g_0(\eta) = \hat{c}(q)\left\{i - \mathrm{erfi}\left(\frac{\sqrt{i}}{2}(1+q)^{3/4}\eta\right)\right\}\eta - \hat{c}(q)\sqrt{\frac{2}{\pi}}(1-i)\exp\left(\frac{i}{4}(1+q)^{3/2}\eta^2\right). \tag{5.91}$$

Observe that the linear growth rate, q, of these solutions strongly influences the manner of oscillation. Picking $\hat{c}(q)$ appropriately, the function $g_0(\eta)$ has maximal modulus equal to unity.
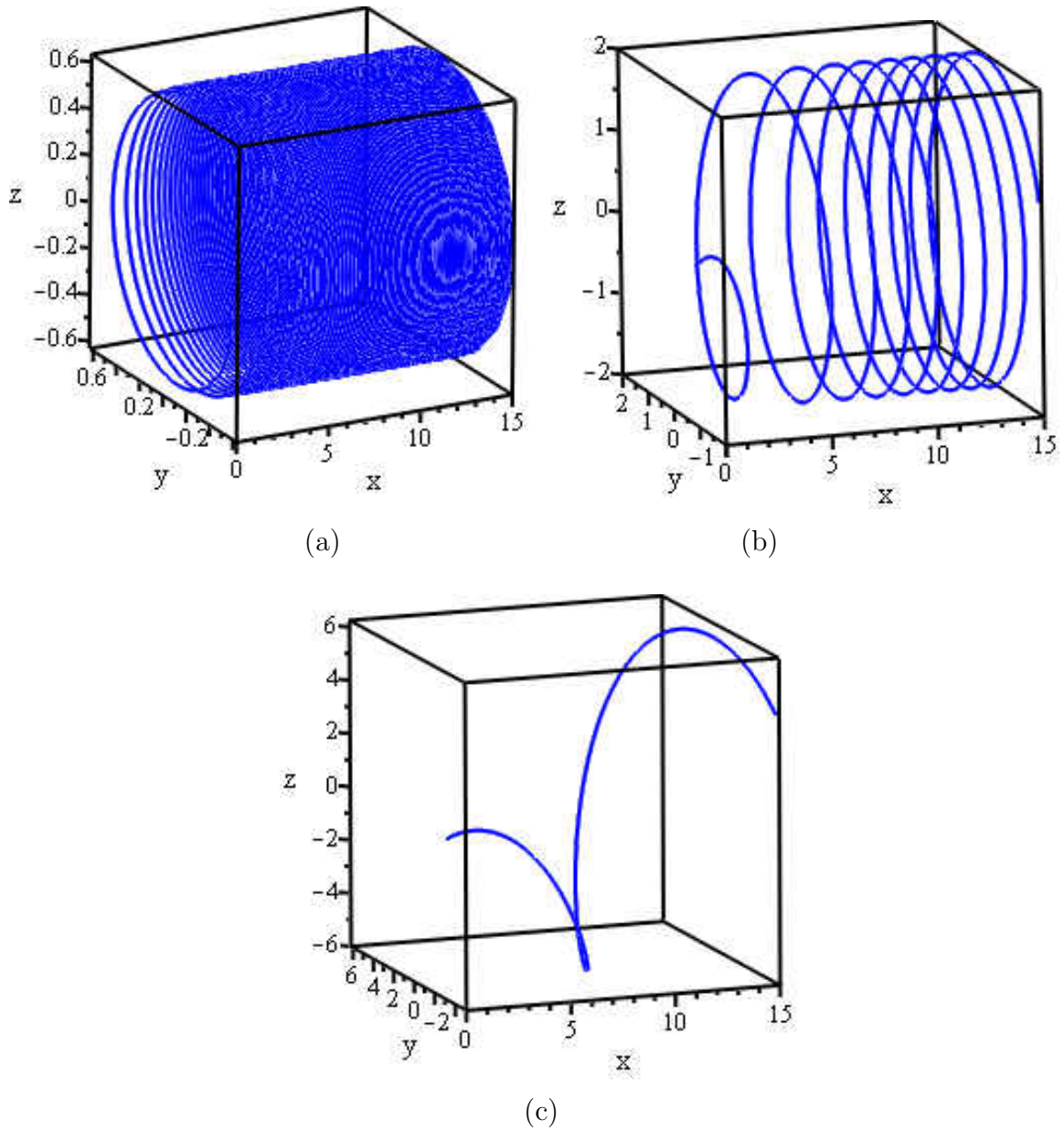
Figure 5.14: Plot of small-amplitude solutions (5.93) corresponding to (4.13) over space $x \in [0, 15]$ given (a) $t = 0.1$, (b) $t = 1$, and (c) $t = 10$. We fix $\gamma = 1$; changes in γ would simply manifest as a dilation of the temporal variable t, thereby altering (up to a scale) the temporal variation shown in (a) - (c).

Using this perturbation result, up to order $O(A^2)$ we have that the vortex filament is described by

$$\mathbf{r} = \left(x, \sqrt{\gamma t}\, \mathrm{Re}\, g_0(\eta), \sqrt{\gamma t}\, \mathrm{Im}\, g_0(\eta)\right)$$
$$= (1, \mathrm{Re}\, q, \mathrm{Im}\, q)\, x + \left(0, \mathrm{Re}\, g_0\left(\frac{x}{\sqrt{\gamma t}}\right), \mathrm{Im}\, g_0\left(\frac{x}{\sqrt{\gamma t}}\right)\right) A\sqrt{\gamma t} + O(A^2). \tag{5.92}$$

In order to get a better feeling for the oscillations, let us take $q = 0$ to remove the linear trend. Then we obtain

$$\mathbf{r} = \left(x, A\sqrt{\gamma t}\, \mathrm{Re}\, g_0\left(\frac{x}{\sqrt{\gamma t}}\right), A\sqrt{\gamma t}\, \mathrm{Im}\, g_0\left(\frac{x}{\sqrt{\gamma t}}\right)\right) + O(A^2). \tag{5.93}$$

Taking $q = 0$, we see that $|g_0(\eta)| \leq |g_0(0)|$ for all $\eta \geq 0$. So, to normalize our expression, we take $\hat{c}(0) = 1/g_0(0) = \sqrt{2\pi}(1 + i)/4$. Then

$$g_0(\eta) = \frac{\sqrt{2\pi}(1 + i)}{4}\left\{i - \mathrm{erfi}\left(\frac{\sqrt{i}}{2}(1 + q)^{3/4}\eta\right)\right\}\eta - \exp\left(\frac{i}{4}(1 + q)^{3/2}\eta^2\right) \tag{5.94}$$

and $g_0(\eta)$ has maximum modulus equal to unity on $\eta \geq 0$. Replacing $\eta = x/\sqrt{\gamma t}$, we can plot the similarity solution (5.93), and we do so in Fig. 5.14. Note that we have scaled the solution so that $A = 1$ in the latter two components, since we are only interested in the qualitative shape of the vortex filament at this juncture.

5.3.7 Asymptotic solution for large η

Let us consider the asymptotics for the singular solution. We substitute $R(\eta) = \eta^{-1}r(\eta)$, and keeping highest order contributions in (5.66) η (that is, we discard terms of order $O(\eta^{-2})$)

we find

$$r'' + \frac{\eta}{2}r\Theta - r\Theta'^2 = 0 \qquad \text{and} \qquad r\Theta'' - \left(\frac{\eta}{2} + 2\Theta'\right)r' + r = 0\,. \tag{5.95}$$

Defining $\zeta = r'/r$ and $\xi = \Theta'$, we have the coupled system of first order differential equations

$$\zeta' + \zeta^2 + \left(\frac{\eta}{2} - \xi\right)\xi = 0 \qquad \text{and} \qquad \xi' - 2\zeta\xi - \frac{\eta}{2}\zeta + 1 = 0\,. \tag{5.96}$$

We find the solution $\zeta(\eta) = 1/\eta$ and $\xi(\eta) = \eta/2$. Then, $r(\eta) = r_0\eta$ so $R(\eta) = r_0$, a constant. Meanwhile, $\Theta(\eta) = \Theta_0 + \eta^2/4$. So, in the large η limit, we have $f(\eta) = r_0 e^{i\Theta_0} \exp(i\eta^2/4)$. Picking $\Theta_0 = 0$, we have $f(\eta) = r_0\cos(\eta^2/4) + ir_0\sin(\eta^2/4)$. The solution in the large η regime is then given as

$$\mathbf{r} = \left(x, r_0\sqrt{\gamma t}\cos\left(\frac{x^2}{4\gamma t}\right), r_0\sqrt{\gamma t}\sin\left(\frac{x^2}{4\gamma t}\right)\right)\,. \tag{5.97}$$

Note that this solution is in complete agreement with the complex exponential term which gives oscillations to the small-amplitude solution (5.94). This makes complete sense for the present case, as the solutions tend toward pure oscillations for large magnitudes $|\eta|$. Hence this asymptotic result agrees completely with the large η limit of the small-amplitude case when the linear trend is removed. We shall see that this also agrees with the numerical solutions presented in the following section.

5.3.8 Numerical simulations

At this point, we solve the transformed version of the LIA (5.63)-(5.64). Instead of using (5.65), however, note that if we consider the transformed coordinate system (η, τ) in place

of (x, t), where η is the similarity variable and τ is the transformed time $\tau = \sqrt{\gamma} t$ (under which η reads $\eta = x/\tau$), we have the simpler expression

$$\hat{\mathbf{r}} = (\eta, R(\eta) \cos \Theta(\eta), R(\eta) \sin \Theta(\eta)) \tag{5.98}$$

where $\hat{\mathbf{r}} = \mathbf{r}/\tau$ is the time-normalized position vector. Thus, through a numerical simulation of solutions $R(\eta)$ and $\Theta(\eta)$ to (5.63)-(5.64), we can recover the vortex structure $\hat{\mathbf{r}}$ for the superfluid ^{4}He case (and, if need be, convert the results back to the original coordinates (x, t)). We shall therefore obtain numerical solutions to (5.63)-(5.64) and plot them in the natural coordinates (5.98).

The influence of the superfluid friction parameters α and α' will be of most interest, since these were excluded from the analytical results. Although the superfluid friction parameters are small, as we shall demonstrate, they are certainly not negligible.

Before we begin, let us take a look at the linearized system. We find that (5.63)-(5.64) has a linearized form

$$\begin{bmatrix} 1 + \alpha' & \alpha R \\ -\alpha & 1 + \alpha R \end{bmatrix} \begin{bmatrix} R'' \\ \Theta'' \end{bmatrix} + M(R, R', \Theta, \Theta') = 0 \,, \tag{5.99}$$

where M is a vector with entries consisting of R, R', Θ and Θ'. We see that

$$\det \begin{bmatrix} 1 + \alpha' & \alpha R \\ -\alpha & 1 + \alpha R \end{bmatrix} = [\alpha^2 + (1 + \alpha')^2] R \,, \tag{5.100}$$

so the system is non-degenerate for all α and α', provided that $R \neq 0$. If, however, $R = 0$ (for instance, if we invoke the initial condition $R(0) = 0$), then the linearized system (5.99) for the

204

nonlinear system (5.63)-(5.64) becomes degenerate. This must be taken into consideration as we proceed, when we desire solutions satisfying $R(0) = 0$, as this condition is needed for the non-singular solutions.

5.3.9 Singular solutions $R(0) > 0$

The first order of business is calibrating initial conditions. We should take $R(0) > 0$ for singular solutions, but the remaining three condition can be selected somewhat arbitrarily. We therefore take $R(0) = 1$ for the singular solutions, so that solutions become singular in the $t \to \infty$ limit.

In Fig. 5.15, we provide solutions which oscillate for small η and in the limit $\eta \to \pm\infty$ tend toward a line. The solutions satisfy $R'(0) = \Theta'(0) = 0$ and $\Theta(0) = 2$. These are kink-solutions: at $\eta = 0$ they alter their position (turning in the reverse direction). Note that the solutions are very sensitive to the superfluid friction parameters. Both the $(\alpha, \alpha') = (0,0)$ and $(\alpha, \alpha') = (0.005, 0.003)$ cases give rapid oscillations near the origin, yet they diverge from one another, with the filaments ending up with drastically different orientations. Meanwhile, for the $(\alpha, \alpha') = (0.073, 0.018)$ case, the solutions oscillate far less rapidly and the vortex filament rapidly diverges from the other two cases. Note that, in the small α, α' limit, the numerical results agree well with the analytical formula (5.75). In particular, note that for small η, the phase is accurately approximated by (5.75). On the other hand, in the large η case, the numerical solutions agree well with the asymptotic formula (5.97).
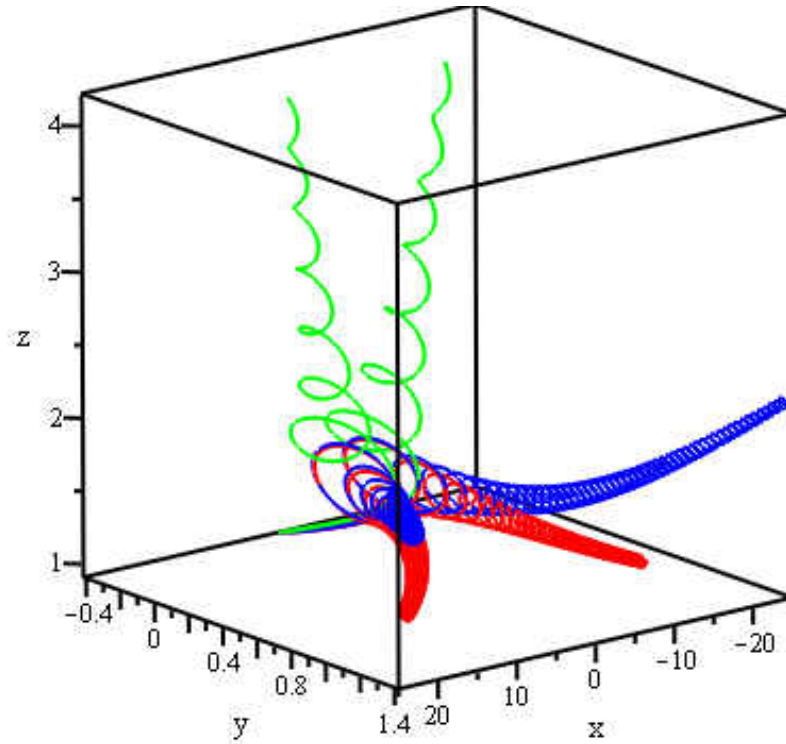
Figure 5.15: Plot of singular self-similar solutions $\hat{\mathbf{r}}$ for (5.63)-(5.64). The red (lower) solution denotes $(\alpha, \alpha') = (0, 0)$, the blue (middle) solution denotes $(\alpha, \alpha') = (0.005, 0.003)$, and the green (upper) solution denotes $(\alpha, \alpha') = (0.073, 0.018)$. Here $R(0) = 1$, $R'(0) = \Theta'(0) = 0$, $\Theta(0) = 2$.
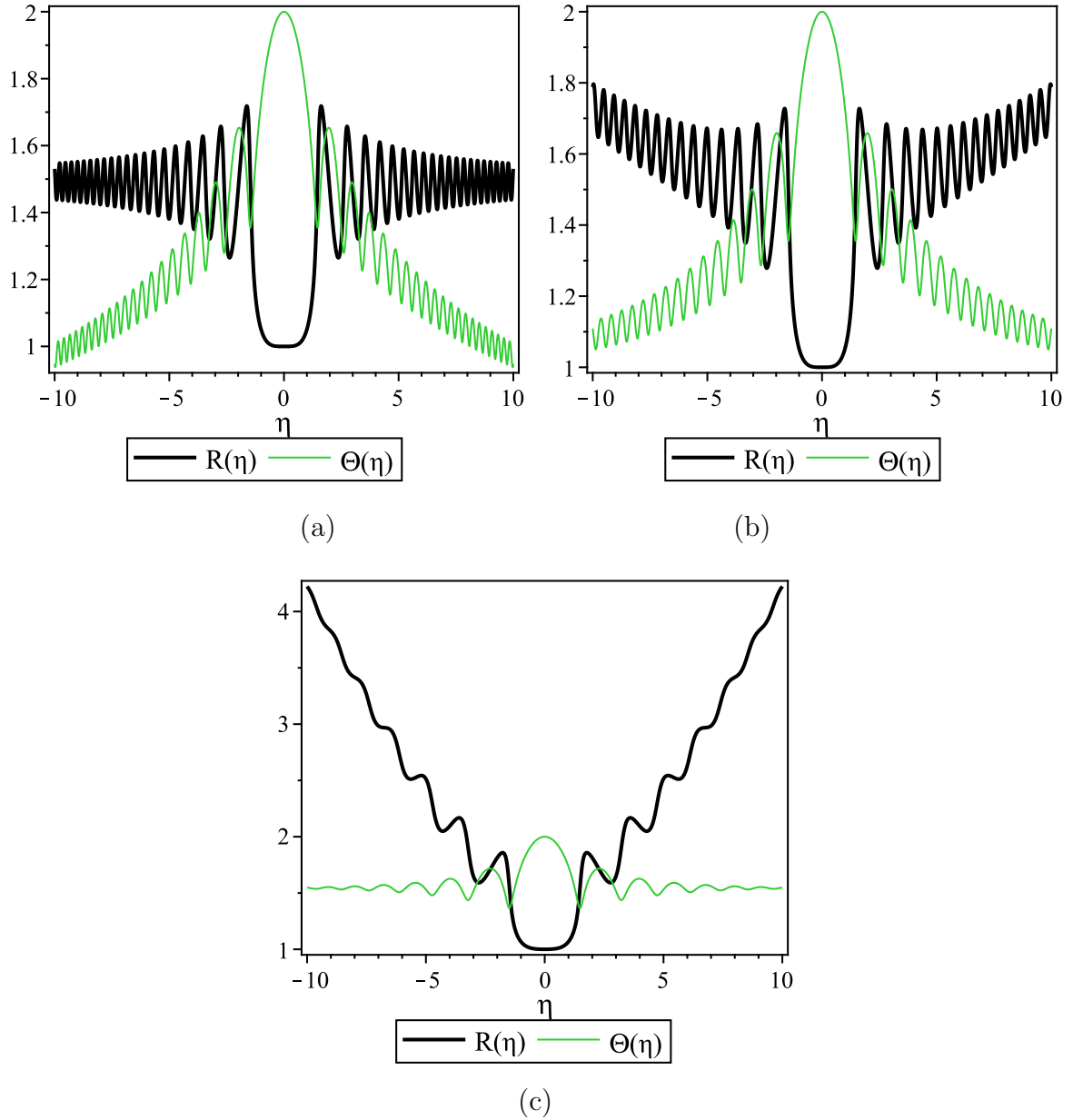
Figure 5.16: Plot of self-similar solutions $R(\eta)$ and $\Theta(\eta)$ for (5.63)-(5.64) given (a) $(\alpha, \alpha') = (0,0)$, (b) $(\alpha, \alpha') = (0.005, 0.003)$, and (c) $(\alpha, \alpha') = (0.073, 0.018)$. When the superfluid friction parameters are zero, the solution $R(\eta)$ oscillates about a fixed point. Yet, with the addition as even small superfluid friction parameters, the solution $R \to \infty$ as $|\eta| \to \infty$. Here $R(0) = 1$, $R'(0) = \Theta'(0) = 0$, $\Theta(0) = 2$.

The difference in these three vortex filaments lies in the behavior of $R(\eta)$. To demonstrate this, we plot $R(\eta)$ and $\Theta(\eta)$ in Fig. 5.16, for each parameter set in Fig. 5.15. Again, we see the small η agreement with the formula (5.75) and the large η agreement with the asymptotic formula (5.97). Compare these solutions with Figs. 3-4 of [56], where relatively large values of the superfluid friction parameters were taken. For large values of α, the oscillations along the mean curve die off, leaving a V-shaped filament. As α is made progressively closer to zero, the oscillations increase in frequency, yielding the behavior we see in Fig. 5.15. In the curvature-torsion model studied by Lipniacki, the filament becomes more wavy as α is decreased toward zero.

5.3.10 Non-singular solutions $R(0) = 0$

For the non-singular solutions, we require $R(0) = 0$ so that $\lim_{t \to \infty} |\sqrt{\gamma t} f(x/\sqrt{\gamma t})| < \infty$. That is, so that $\|(y(x,t), z(x,t))\| < \infty$ as $t \to \infty$. As shown previously, the linearized system (5.99) is degenerate at $R = 0$, which will naturally complicate the numerical solution for the non-singular case since the needed initial condition results in such a degeneracy. To get around this, we introduce a slight perturbation $0 < \epsilon << 1$ so that $R(0) = \epsilon$. This will permit us to approximate the non-singular vortex filament. We find that taking $\epsilon = 10^{-3}$ will suffice; for $\epsilon < 10^{-3}$, we notice no qualitative difference in the solutions. The other initial conditions are again taken to be $R'(0) = \Theta'(0) = 0$ and $\Theta(0) = 2$, which provides us with symmetric solutions.

208
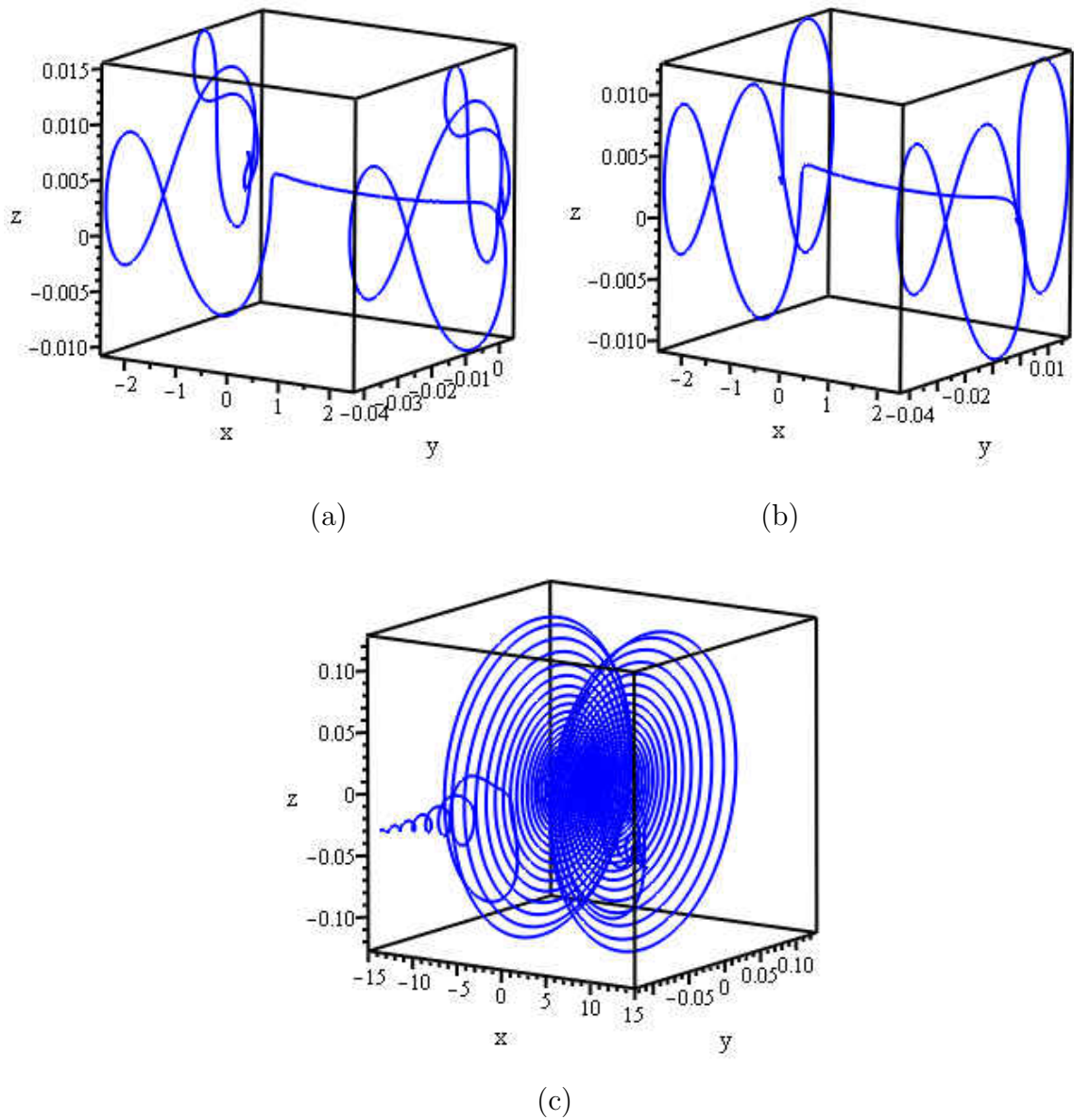
Figure 5.17: Plot of non-singular self-similar solutions $\hat{\mathbf{r}}$ for (5.63)-(5.64) given (a) $(\alpha, \alpha') = (0, 0)$, (b) $(\alpha, \alpha') = (0.005, 0.003)$, and (c) $(\alpha, \alpha') = (0.073, 0.018)$. Here $R(0) = \epsilon = 10^{-3}$, $R'(0) = \Theta'(0) = 0$, $\Theta(0) = 2$. Taking $\epsilon = 10^{-3}$ is sufficient to numerically approximate the non-singular vortex filament solution.

In Fig. 5.17, we plot the non-singular solutions for various values of the superfluid friction parameters. Note that these solutions appear similar to those in Fig. 5 of Lipniacki [56]. The plots of Lipniacki appear more well-behaved, since $\alpha = 1$ is taken. Since α scales positively with temperature, this large value of α corresponds to warmer temperatures. Indeed, we see that for small $\alpha << 1$, the behavior of the solutions for the Cartesian model similar: the solutions are bounded, and appear to have two attractive regions.

5.3.11   Discussion

After a series of reasonable assumptions and transformations, we have reduced the fully non-linear local induction approximation (2.12) for the motion of a vortex filament in superfluid ^{4}He derived in [102] to an ordinary differential equation of the form

$$\frac{i}{2}\left(f - \eta f'\right) + \left(\frac{1 + \alpha'}{(1 + |f'|^2)^{3/2}} - i\frac{\alpha}{(1 + |f'|^2)^2}\right) f'' = 0\,, \tag{5.101}$$

where $\eta = x/\sqrt{\gamma t}$ is a similarity variable. The vortex filament in the Cartesian frame is then given by

$$\mathbf{r} = \left(x, \sqrt{\gamma t}\,\mathrm{Re}\,f(\eta), \sqrt{\gamma t}\,\mathrm{Im}\,f(\eta)\right)\,. \tag{5.102}$$

From this formulation of the self-similar solution, we have been able to study various properties of the resulting vortex filament. Analytical solutions have been considered for the $\alpha, \alpha' \to 0$ regime, which is the limit under which the superfluid model reduces to the standard fluid model. In this case, we have been able to study the filament solutions in a

qualitative manner. Of course, in order to determine the influence of superfluid friction parameters on the self-similar solutions, we need to consider numerical simulations. These simulations demonstrate the existence of two classes of solutions, depending on whether the solution is singular or not. (A singular solution is one in which $f(0) \neq 0$, since this implies that the limit $\sqrt{\gamma t} f(x/\sqrt{\gamma t})$ is unbounded as $t \to \infty$).

The results corresponding to the $\alpha, \alpha' \to 0$ limit were considered, and effectively describe self-similar solutions to the Cartesian form of the LIA for a standard fluid. This model was previously considered in [98, 99] where planar and helical vortex filaments were obtained by Van Gorder. The self-similar solutions obtained here are distinct from those solutions. We were able to determine that solutions grow linearly in η, the similarity variable. The solutions are shown to oscillate about a linear curve of the form $\mathbf{s} = (\eta, A\eta, B\eta)$. Note that $\mathbf{s}$ is the form of a constant-phase solution ($\Theta(\eta) = \Theta_0$). For the non-constant phase solutions, an elegant representation for the phase $\Theta(\eta)$ has been given in terms of the amplitude $R(\eta)$:

$$\Theta(\eta) = \Theta_0 + \int_0^\eta \sqrt{\frac{R^6(\xi)}{\xi^2} \int_0^\xi \frac{2\zeta(R(\zeta) - \zeta R'(\zeta))R''(\zeta)}{R^8(\zeta)} d\zeta} d\xi. \qquad (5.103)$$

In this case, we also find that the boundary data is related like $\Theta'(0) = \sqrt{R''(0)/R(0)}$.

The case of small-amplitude oscillations was considered perturbatively, and an analytic form of the oscillations (with the linear trend removed) was given to order $O(A)$, where A is the bound on the amplitude of the oscillations. We prove that the oscillations should

go as

$$\exp\left(\frac{i}{4}(1+q)^{3/2}\eta^2\right) \tag{5.104}$$

once the linear trend is removed. While this analytic form of the oscillations was given in the $\alpha, \alpha' \to 0$ limit, it agrees completely with what we see in the numerics for the $\alpha \neq 0$, $\alpha' \neq 0$ case.

In order to better understand this behavior, we consider an asymptotic approximation of the solution in the $\eta \to +\infty$ limit. The resulting asymptotic solutions (with linear trend removed) take the form

$$\mathbf{r} = \left(x, r_0\sqrt{\gamma t}\cos\left(\frac{x^2}{4\gamma t}\right), r_0\sqrt{\gamma t}\sin\left(\frac{x^2}{4\gamma t}\right)\right), \tag{5.105}$$

which is in complete agreement with the $O(A)$ perturbation result.

While our numerical study is far from exhaustive, we have shown that the solution to the system (5.63)-(5.64) is very sensitive to the values of the superfluid friction parameters α and α'. Furthermore, in the case of singular solutions (those solutions with $R(\eta) > 0$ as $\eta \to 0^+$, the normalized filament tends infinitely far from the origin as $\eta \to \pm\infty$. In other words, $\|\hat{\mathbf{r}}\| \to \infty$ as $\eta \to \pm\infty$ for the singular solutions. For the non-singular solutions (those solutions with $R \to 0$ as $\eta \to 0^+$), we observe that $\|(y(x,t), z(x,t))\| < \infty$ as $\eta \to \pm\infty$. Hence, the non-singular solutions are bounded for all η.

We thus recover singular solutions, which grow as x becomes large, when $f(0) \neq 0$. Kink-type solutions fall within this class [57]. Such solutions are strongly influenced by the values of the superfluid friction parameters. Even a small increase in the superfluid friction

parameters can lead to a drastic increase in where the filament is positioned at large x. These are the solutions which agree qualitatively well with the analytical solutions in the $\alpha, \alpha' \to 0$ limit. The difference in parameteric values of α and α' influences orientation as $x \to \pm\infty$ and in the frequency of oscillations. In particular, as α and α' increase, the frequency of oscillations diminishes, owing to the increased friction and hence energy loss.

On the other hand, we recover a second class of solutions when $f(0) = 0$. For any fixed x, this class of solutions remains bounded for all time. These solutions are of small magnitude, and exhibit more exotic forms of oscillations than do the singular solutions: the solutions exhibit small oscillatory excitations at some small positive value of η, before decaying back down toward zero. Such solutions are effectively small excitations of the solution $\mathbf{r} = (x, 0, 0)$. Note that when α and α' are sufficiently large (such as in the $T = 1.5K$ case), these solutions appear very similar in form to a class of solutions obtained by Lipniacki [57], though those solutions were obtained in a different manner than the solutions presented here.

Note that, in principle, there exists a correspondence between the curvature-torsion solutions and the Cartesian solutions discussed here. Going from the Cartesian frame to the curvature-torsion frame is relatively straightforward, since the curvature and torsion along an arclength element can be calculated directly in terms of the Cartesian solutions. Going int he reverse direction is more complicated. There is an additional frame, the tangent-arclength frame proposed by Umeki [96], which can be seen as a natural bridge between the two. Mapping from the curvature-torsion frame into the tangent-arclength frame is more

straightforward. Then, one may use the maps provided by Umeki to connect the tangent-arclength frame solutions to Cartesian solutions. While the solutions are more complicated for the case where superfluid friction is considered (as opposed to the standard LIA), the transformations between the various coordinate frames are identical.

5.3.12 Remark on self-similarity in other frames of reference

Solutions also exist in the literature for the arclength form of the LIA; helical solutions were previously obtained by Umeki [95]-[96] while planar vortex filaments were constructed by Van Gorder [100]. We are not aware of any self-similar solutions to the arclength formulation of the LIA for either a standard fluid or a superfluid. The arclength frame is one of two extrinsic real space frames (the other being the Cartesian frame discussed here). In the intrinsic frame, in particular the related torsion-curvature framework, Lipniacki [56]-[56] demonstrated the existence of self-similar solutions in a superfluid formulation of the LIA (retaining one of the superfluid friction parameters). As such, we find it likely that self-similar solutions are possible for the arclength form of the LIA for a superfluid.

Note that, for the Cartesian frame, the similarity transform used for the superfluid was the same as that used for the regular fluid: $\Phi(x,t) = \sqrt{\gamma t} f(\eta)$ with $\eta = x/\sqrt{\gamma t}$. It makes sense, then, to determine whether the arclength form of the LIA for a standard fluid

permits self-similar solutions. Recall [95, 100] that the LIA in the arclength frame reads

$$iv_t + v_{ss} - \frac{2v^*v_s^2}{1+|v|^2} = 0 \,, \tag{5.106}$$

where * denotes complex conjugation, $v(s,t) : \mathbb{R} \times (0,\infty) \to \mathbf{C}$, s is the arclength and t remains the time. The assumption $v(s,t) = g(\hat{\eta})$ where $\hat{\eta} = s/\sqrt{t}$ leads to a similarity solution, which is governed by the equation

$$-\frac{i}{2}\hat{\eta}g' + g'' - \frac{2g^*g'^2}{1+|g|^2} = 0 \,. \tag{5.107}$$

Hence, the curvature-torsion form of the LIA, the Cartesian form of the LIA, and the arclength form of the LIA all share the same similarity transform, which is simply that of the heat equation: $\eta = x/\sqrt{t}$. The differences in the outer scaling factors (the t^ν factor in the similarity solution $t^\nu f(\eta)$) are dependent on the frame taken. Clearly, the appearance of self-similar solutions, such as those presented here, are intrinsic to the LIA and completely independent of the reference frame taken.

Owing to the rather simple representation for a planar filament in the arclength frame [100] compared to the more complicated result for the Cartesian frame, it may be possible that some vortex filaments in superfluid ^{4}He may be more succinctly described in an arclength coordinate frame. The derivation of the Hall-Vinen model in the arclength frame will yield a generalization of (5.106), which shall account for superfluid friction parameters. This will be taken up in a subsequent work.

5.3.13 Remark on the destruction of similarity by a normal flow impinging on the vortex

We mentioned that the normal fluid velocity must be zero in order to permit self-similarity; indeed, including terms with $U\Phi_x$ would remove the possibility of similarity for any transform $\Phi(x,t) = t^\nu f(xt^\beta)$. It is natural, then, to wonder what effect a small perturbation in U (i.e., $|U| << 1$) would have on destroying similarity. Assuming a solution (5.60) for (5.59) with $U \neq 0$, we find that (5.61) becomes

$$\frac{i}{2}\left(f - \eta f'\right) + \left(\frac{1+\alpha'}{(1+|f'|^2)^{3/2}} - i\frac{\alpha}{(1+|f'|^2)^2}\right) f'' + U\sqrt{\gamma t}\left\{\frac{\alpha'}{(1+|f'|^2)^{1/2}} - \alpha\right\} f' = 0\,.$$

$$(5.108)$$

What this shows is that deviations from the self-similar solution, for even small yet fixed normal fluid velocity U, will deviate as $\sqrt{t}$ due to the addition of non-zero normal flow. Hence, the normal flow destroys the self-similarity. If we view the term with $U\sqrt{\gamma t}$ as a structural perturbation to equation (5.61), the perturbation grows with order $O(t^{1/2})$ in t. So, there is no reasonable way to view such a term as a small perturbation of the self-similar solution for all time, and similarity is destroyed with the introduction of $U \neq 0$.

With all of that said, there is a way to obtain solutions to the $U \neq 0$ problem, and, in fact, we can describe such solutions in terms of the similarity solutions already obtained in previous sections. Consider the $\alpha > 0$ and $\alpha' = 0$ case (which is physically relevant and is considered in a number of studies. Instead of assuming a purely self-similar solution, let us consider a solution with a self-similar contribution that is allowed to drift in time. To that

end, let us assume a solution

$$\Phi(x,t) = \sqrt{\gamma t}F(\sigma) \quad \text{where} \quad \sigma = \frac{x}{\sqrt{\gamma t}} - iw(t) = \eta - iw(t)\,. \tag{5.109}$$

Here, the new variable σ modifies the pure similarity variable η by adding a drift term $w(t)$ (which itself takes the form of a Wick rotation). Then, in the place of (5.108), we obtain

$$\frac{i}{2}\left(F - \sigma F'\right) + \left(\frac{1}{(1 + |F'|^2)^{3/2}} - i\frac{\alpha}{(1 + |F'|^2)^2}\right)F'' = 0\,, \tag{5.110}$$

where prime denotes differentiation with respect to σ, while $w(t)$ satisfies

$$w + 2\gamma t\frac{dw}{dt} - 2\alpha U\sqrt{\gamma t} = 0\,. \tag{5.111}$$

The drift term must then read

$$w(t) = \frac{2\alpha U}{1 + \gamma}\sqrt{\gamma t}\,. \tag{5.112}$$

Here, terms in the derivative Φ_t has cancelled the contribution of the form $2\alpha U\sqrt{\gamma t}\Phi_x$. Note that (5.110) is simply (5.61) under the replacement $f \to F$ and $\eta \to \sigma$. Hence, one may use the solutions derived above in order to obtain solutions to $F(\sigma)$.

We may use this new transformation to determine the asymptotic behavior of a solution $F(\sigma)$. Assume that $f(\eta) \approx r_0\exp(i\eta^2/4)$ asymptotically. Then, $F(\sigma) \approx r_0\exp(i\sigma^2/4)$ asymptotically, and hence $\Phi(x,t)$ goes as

$$\Phi(x,t) \approx r_0\sqrt{\gamma t}\exp\left(i\left[\frac{x^2}{4\gamma t} - \frac{\alpha^2 U^2\gamma}{(1 + \gamma)^2}t\right]\right)\exp\left(\frac{\alpha U}{1 + \gamma}x\right)\,. \tag{5.113}$$

asymptotically. Due to the fact that σ is the addition of a pure similarity variable and a Wick rotation of a scaling of time, the asymptotic properties of this solution differ in a subtle

yet significant way from the $U = 0$ case considered before. While the oscillatory behavior is still present in the asymptotic result, there is now a real-values exponential, which makes the filament arbitrarily large as $x \to \infty$. However, this is not inconsistent with the numerical results, where for the singular filaments, taking $\eta \to \infty$ yielded unbounded limits. Therefore, the addition of $U \neq 0$ has not altered the qualitative properties of the asymptotic behavior of the vortex filaments. However, it has modified the type of solution. Instead of pure self-similar solutions which are quasi-static, we obtain filaments which drift and deform at a rate depending on the strength of the normal fluid flow U.

The actual manner in which U influences the filament can be seen through two effects. First, there is a modification to the local behavior, such as the types of waves or oscillations which form along the vortex filament. Since there is now a term which scales as $\frac{\alpha^2 U^2 \gamma}{(1+\gamma)^2} t$ influencing the oscillations, large time scales and small time scales have strong effects on the manner of oscillations. Previously, only small time scales had significant effects. The second effect is what we alluded to above. The manner of growth of the singular vortex filament away from the center axis of rotation was of the order $\sqrt{t}$ in the $U = 0$ case. Now, with the inclusion of $U \neq 0$, the growth rate is more accurately approximated by $\sqrt{\gamma t} \exp\left(\frac{\alpha U}{1+\gamma} x\right)$. Hence, there is now growth in space and time.

These modifications are completely consistent with what one might expect from (5.108). Indeed, in the limit where $t << 1$, the results obtained here are essentially the same as for the $U = 0$ case. So, the influence of the normal fluid on a similarity solution is

felt at larger times, and the similarity breaks down for those times. The manner in which similarity is lost is best seen through the function $F(\sigma)$ ans its asymptotics.

5.3.14 Physical Implications

The solutions obtained (through both the asymptotic and the numerical results) are in agreement with the studies by Lipniacki and Svistunov in the $\alpha, \alpha' \to 0$ limit. What we have done here is show that self-similarity is still inherent in vortex solutions to the LIA, even when superfluid friction parameters are included. Hence, the Hall-Vinen formulation of vortex dynamics in superfluid ^{4}He admits self-similarity of solutions when there is no normal flow impinging on the vortex. Such a normal flow disrupts the vortex. Even when solutions do exist in the presence of normal flow impinging on the vortex, the resulting solutions do not maintain self-similarity. In other words, the behavior of the vortex filament may vary strongly with the size of the length scale. In the no normal fluid case, the self-similarity inherent in the obtained solutions physically implies that the solutions exhibit the same general behavior at arbitrary length scales.

While the addition of the superfluid friction parameters complicated the form of the nonlinear PDE we must solve, including such terms is necessary, as we have seen from the numerical simulations that such parameters strongly influence the vortex filament solutions. Indeed, as was shown in Figures 2-4, rather drastic quantitative changes can appear given seemingly minor increases in the superfluid friction parameters. Since the parameters scale

positively with temperature, what we have really done here is demonstrate the influence of temperature on the self-similar motion of a vortex filament in superfluid ^{4}He. As the temperature increases, the singular filaments take on a sharp V-shape (a kink-shape) toward the z axis. Furthermore, the waves or oscillations on these vortex filament solutions diminish for larger temperatures. In a way, this is in qualitative agreement with the finding in [94] that for multiple vortex filaments, the vortex tangle is smoother for positive temperatures than for the zero temperature case. For the non-singular solutions which are always bounded in distance from the axis of orientation, the solutions appear as excitations near the origin, and then tend toward the line filament $\mathbf{r} = (x, 0, 0)$ for larger x. The form of these local excitations depends strongly on the superfluid friction parameters.

Many of the numerical plots agree with the results for the curvature-torsion model studied by Lipniacki. While many of the solutions are given for the "warm" case of $\alpha = 1$ (recall that α scales positively with temperature), many qualitative features remain. The singular solutions feature kinks near the origin. As the filament travels away from the origin on either side, the filament will develop waves or oscillations, depending on the size of the superfluid friction parameter α. Indeed, as α increases, the waves or oscillations tend to dissipate. On the other hand, the non-singular vortex filament solutions remain confined to a bounded region.

Since the Hall-Vinen model is an extension of the LIA which includes superfluid effects, it is natural to question whether the solutions are reasonable approximations to the non-local model governing the vortex filaments. This point was discussed by Lipniacki [56],

and it was argued that for increasing spatial scales, the similarity solutions are reasonable, whereas for decreasing spatial scales, the similarity solutions fail to be accurate representations of the true vortex filament motions, and nonlinear effects are needed. More accurate solutions in the decreasing scale case can be obtained through the simulation of a generalized Biot-Savart law which accounts for superfluid friction. The comments hold for the Cartesian case, as well.

Since the LIA, and therefore the Hall-Vinen model, are approximations to the true motion of vortex filaments, the degree to which these self-similar solutions approximate the true solutions is worth considering. In cases where the filaments are not tightly coiled, vortex filament interactions would involve local crossings. While the full Biot-Savart law is needed to understand arbitrary crossings, simple crossing can be approximated locally for this basic case. For more complicated filaments, such as those with many waves or oscillations, or those featuring many loops (as is true of some of the non-singular vortex filaments), interactions may occur at a number of places, so LIA will not be as useful an approximation.

As remarked before, a normal fluid impinging on the vortex filament will destroy self-similarity. This does not mean that the solution is completely destroyed, only that it is modified. Indeed, the solution may simply be perturbed by some quantity. If this perturbation or excitation is small, it is likely that the solution can, more-or-less, maintain its form, modified only by a perturbation term. This would make sense in the context of the stability results of Banica and Vega [11], who consider the standard ($\alpha = \alpha' = 0$) model under the curvature-torsion frame and determine that the kink-type similarity solutions are

indeed stable under sufficiently small perturbations. While the proof for the $\alpha > 0$, $\alpha' > 0$ case has never been considered, it is reasonable that, under small enough perturbations and small enough superfluid friction parameters, the solutions will remain robust. For very large perturbations (i.e., large normal fluid velocity) the similarity solutions likely break down, but this is also physically reasonable.

As addressed in the previous subsection, if we introduce a new variable σ which shifts the similarity variable by a function of time alone, then we can study the influence of a normal fluid impinging on the solutions. What we find is that the similarity solutions are transformed into functions of this new variable. The greatest differences occur for large values of time, whereas for small time, the solutions are essentially the same as the purely self-similar ones. For large time, the singular solutions exhibit a faster rate of growth away from the central axis along which the vortex is aligned. These effects are only in the presence of superfluid friction; when $\alpha \to 0$, we have $\sigma \to \eta$, and the normal fluid influence is nil.

In the small temperature limit (under 1K), the normal fluid effects are negligible, as stated previously. It has been shown experimentally that the vortex lines are able to decay under these conditions [25]. It was assumed that occasional vortex reconnection gives rise to kinks on the vortex line. These kinks were considered as superpositions of Kelvin waves. Kelvin waves can lose energy by emitting sound (phonons), hence the observed decay even in the absence of friction effects due to the normal fluid. For future work, it may be interesting to study the dynamics of Kelvin waves related to such filament kinks. In principle, these might best be modeled as the superposition of solitons on the filament (with the solitons

representing decaying Kelvin waves), which makes sense in light of the fact that the standard LIA is integrable. This also has possible topological implications for the propagation of Kelvin waves along vortex filaments which demonstrate breakdown and reconnection. In particular, such solutions would break the similarity observed here. However, such similarity breaking would be of a distinct kind from that observed when U becomes non-negligible. In such a case, the addition of a drift term is not likely to be sufficient, and a more involved approach to representing such solutions would be required.

5.4 Quantum vortex dynamics under the tangent representation of the LIA

We derive the Local Induction Approximation (LIA) for a quantum vortex filament in the arclength coordinate frame where the tangent vector is the unknown function. The equation for the tangent vector to the filament is then converted to a potential form, which ends up being a type of nonlinear Schrödinger equation that governs the tangential LIA model (T-LIA). Such a formulation was previously derived by Umeki for the standard fluid model (in the absence of superfluid friction terms). While it is challenging to generalize many of the exact solutions found for the standard LIA to the quantum LIA model, we demonstrate that the T-LIA model actually facilitates this generalization nicely. Indeed, under the T-LIA model, we are able to construct a variety of solutions. The Hasimoto solution related to

elastica is one of the fundamental solutions present for the standard fluid model; however, using the T-LIA model, we are able to demonstrate the existence of such a solution, thereby extending the Hasimoto solution to the superfluid case. In the zero temperature limit, purely self-similar solutions are shown to exist for the T-LIA model. As the superfluid warms (so that the influence of the normal flow is no longer negligible), the analogue to the self-similar solution is a new class of solutions, which depend on the similarity variable as well as a time-dependent additive scaling. In other words, the self-similar structures gradually deform as the magnitude of the normal fluid velocity increases, which makes complete physical sense. When dealing with small deviations from the central axis of alignment, we can describe such solutions analytically. There exists a family of helical vortex filaments in the presence of a normal fluid impinging on the vortex, in complete agreement with the previously studied results for the LIA model. Finally, a number of soliton solutions are shown to exist in different regimes of the T-LIA model. The present results for the T-LIA model were considered in Van Gorder [108].

Perhaps the most standard form of the LIA and quantum LIA models would be the curvature-torsion form, which is one type of intrinsic form. A natural extrinsic form would be the Cartesian form of these models (Boffetta [17]; Van Gorder [98]), which has the advantage of yielding vortex filament solutions which are easily viewed geometrically. A less studied form of the LIA was derived by Umeki [95], who put the LIA into a form strictly involving the tangent vector to a filament. The resulting vector PDE admits a natural potential form, resulting in a new type of nonlinear Schrödinger equation (where the space variable is

arclength). One very natural benefit to such an approach was that certain solutions become much easier to represent, with even closed form solutions possible (Umeki [96]; Van Gorder [100]).

Due to the fact that this formulation appears very natural for the LIA, it is reasonable to apply such a tangent-arclength formulation to the quantum LIA model, and this shall be our focus. We derive two explicit potential forms of this Tangent-LIA (T-LIA) model. We consider the low temperature limit when the influence of **U** is negligible, and demonstrate the existence and properties of two very fundamental solutions: planar filaments (along the lines of the Hasimoto solution related to elastica) and self-similar structures. Then, we include the effects of the normal fluid velocity **U**, and demonstrate the existence of helical and soliton solutions, which are driven by the normal fluid velocity. In addition, we determine the manner in which self-similar structures are disrupted under the inclusion of the normal fluid impinging on the quantum vortex. So, the T-LIA model is shown to be useful for understanding the qualitative structure of a variety of quantum LIA solutions.

5.4.1 Formulation including normal and binormal friction

In the low temperature limit, the influence of the normal fluid impinging on the filament is often neglected, so we set $U \to 0$, where U is the magnitude of the normal fluid velocity **U**. This condition is vacuously satisfied when $\alpha, \alpha' \to 0$, and this limit corresponds to the zero temperature limit. Svistunov [92] explored this case, and Boffetta et al. [17] proposed

a model in Cartesian coordinates. Many studies on specific structures in the quantum LIA model have taken the normal fluid velocity to zero, as it permits one to study such structures without the influence of drift or other distorting effects on the filaments [5, 3, 117].

Setting $U = 0$, differentiating with respect to the arclength variable s, and performing several vector manipulations, we have that the quantum LIA model (2.12) becomes

$$\dot{\mathbf{t}} = \mathbf{t} \times \mathbf{t}_{ss} - \alpha[\mathbf{t}_s \times (\mathbf{t} \times \mathbf{t}_s) - \mathbf{t} \times (\mathbf{t} \times \mathbf{t}_{ss})]$$

$$+ \alpha'[\mathbf{t}_s \times (\mathbf{t} \times (\mathbf{t} \times \mathbf{t}_s)) + \mathbf{t} \times (\mathbf{t}_s \times (\mathbf{t} \times \mathbf{t}_s)) + \mathbf{t} \times (\mathbf{t} \times (\mathbf{t} \times \mathbf{t}_{ss}))]$$

$$= \mathbf{t} \times \mathbf{t}_{ss} - \alpha[(|\mathbf{t}_s|^2 + \mathbf{t} \cdot \mathbf{t}_{ss})\mathbf{t} - (\mathbf{t} \cdot \mathbf{t}_s)\mathbf{t}_s - |\mathbf{t}|^2 \mathbf{t}_{ss}] - \alpha'[2(\mathbf{t} \cdot \mathbf{t}_s)\mathbf{t} \times \mathbf{t}_s + |\mathbf{t}|^2 \mathbf{t} \times \mathbf{t}_{ss}]$$

$$= \frac{\partial}{\partial s} \left\{ \mathbf{t} \times \mathbf{t}_s - \alpha[(\mathbf{t} \cdot \mathbf{t}_s)\mathbf{t} - |\mathbf{t}|^2 \mathbf{t}_s] + \alpha'|\mathbf{t}|^2 \mathbf{t} \times \mathbf{t}_s \right\}$$

$$\tag{5.114}$$

$$\dot{\mathbf{t}} = \frac{\partial}{\partial s} \left\{ (1 - \alpha'|\mathbf{t}|^2)\mathbf{t} \times \mathbf{t}_s - \alpha[(\mathbf{t} \cdot \mathbf{t}_s)\mathbf{t} - |\mathbf{t}|^2 \mathbf{t}_s] \right\} . \tag{5.115}$$

We have also rescaled relevant quantities to remove the γ factor. Forcing $\mathbf{t}$ to be a unit tangent vector, the equation simplifies slightly to

$$\dot{\mathbf{t}} = \frac{\partial}{\partial s} \left\{ (1 - \alpha')\mathbf{t} \times \mathbf{t}_s - \alpha[(\mathbf{t} \cdot \mathbf{t}_s)\mathbf{t} - \mathbf{t}_s] \right\} . \tag{5.116}$$

This gives us a representation of the quantum LIA dynamics strictly in terms of the tangent vector to the filament, $\mathbf{t}$. Next, we introduce the potential function $v \in \mathbb{C}$, where for $\mathbf{t}(t, x) = (t_1(x, t), t_2(x, t), t_3(x, t))$ we set

$$t_1 + it_2 = \frac{2v}{1 + |v|^2}, \qquad t_3 = \frac{1 - |v|^2}{1 + |v|^2} . \tag{5.117}$$

This v is the same potential function used by Umeki in the standard fluid ($\alpha = \alpha' = 0$) case. We obtain (scaling $t \mapsto (1 - \alpha')t$)

$$iv_t + v_{ss} - \frac{2v_s^2 v^*}{1 + |v|^2} - \hat{\alpha}i \left[v_{ss} - \frac{2v_s^2 v^*}{1 + |v|^2} - \frac{4vv_s v_s^*}{1 - |v|^4} \right] = 0 \,, \tag{5.118}$$

where $\hat{\alpha} = \alpha/(1 - \alpha')$. This formulation is a clear generalization of the Umeki formulation of the standard LIA (Umeki 2010). Indeed, taking $\alpha, \alpha' \to 0$, we recover that model. It was shown that the Umeki formulation admits several exact solutions (Umeki 2013).

We should note that while a plane wave of the form $v(s,t) = Ae^{i(ks-\omega t)}$ exists for the standard LIA (even in the arclength form; see Umeki [96]), such a simple solution cannot exist for the model (5.118). The reason for this discrepancy is that such a helical solution's development is fundamentally associated with the normal fluid velocity (Van Gorder [106]). We shall then show that including a non-zero magnitude for the normal fluid velocity grants us the existence of a family of helical filaments.

5.4.2   Perturbation of the planar filament due to superfluid friction terms

A planar vortex filament is one of the important general forms of a vortex filament which can be given analytically and was studied in Chapter 2. For the arclength-tangent frame, Van Gorder [100] obtained an exact solution in the case corresponding to $\alpha, \alpha' = 0$. Here the results shall be extended to the non-zero α, α' regime.

A planar filament in the Umeki formulation takes the form of a stationary state $v(s, t) = e^{-i\omega t}q(s)$. In Chapter 2, it was shown that an exact solution exists for the $\hat{\alpha} = 0$ case and takes the form

$$v(s, t) = e^{-i\omega t}q_\omega(s) = Ae^{-i\omega t}\,\text{sn}\,\left(\sqrt{\frac{\omega}{1 + A^2}}(s - s_0), Ai\right). \qquad (5.119)$$

If we assume a first order perturbation solution, we find that the order one correction is purely complex, that is $v(s, t) = e^{-i\omega t}[q_\omega(s) + i\hat{\alpha}Q(s)]$, where $Q(s)$ satisfies

$$\omega Q + Q'' + \frac{2q_\omega'^2 Q - 4q_\omega' q_\omega Q'}{1 + q_\omega^2} = q_\omega'' + \frac{2q_\omega'^2 q_\omega}{1 - q_\omega^2}. \qquad (5.120)$$

The first order correction due to $\hat{\alpha}$ then takes the form

$$Q(s) = -q_\omega(s)\int_0^s \frac{(1 + q_\omega(\zeta)^2)^2}{q_\omega(\zeta)^2}\int_0^\zeta \frac{4q_\omega(\xi)^2 q_\omega'(\xi)^2 + \omega q_\omega(\xi)(1 - q_\omega(\xi)^4)}{(1 + q_\omega(\xi)^2)^3(1 - q_\omega(\xi)^2)}d\xi d\zeta. \qquad (5.121)$$

The modified form of the planar vortex filament due to the superfluid friction parameters is then

$$v(s, t) = e^{-i\omega t}q_\omega(s)$$
$$\times \left[1 - i\hat{\alpha}\int_0^s \frac{(1 + q_\omega(\zeta)^2)^2}{q_\omega(\zeta)^2}\int_0^\zeta \frac{4q_\omega(\xi)^2 q_\omega'(\xi)^2 + \omega q_\omega(\xi)(1 - q_\omega(\xi)^4)}{(1 + q_\omega(\xi)^2)^3(1 - q_\omega(\xi)^2)}d\xi d\zeta\right],$$
$$(5.122)$$

where $q_\omega(s)$ is the Jacobi sn function defined in (5.119).

Some notes are in order. The qualitative change in the planar filament is primarily due to α and not α', and α' is often neglected and set to zero in the literature. We see from the planar vortex filament that the first order correction due to α is rather drastic, highlighting the complications in extending the LIA to the superfluid case.

As A goes to zero, note that the first order correction (5.121) does not diverge. The inner integral scales as A, the outer integral gives a contribution of at worst order A^{-2}, so performing both integrations we have a term of order at worst A^{-1}. The factor $q_\omega(s)$ outside of the integral gives another multiplicative factor of A, and this the first order correction (5.121) is (at worst) of order $O(1)$ as A tends toward zero. Actually performing the integrations for the appropriately defined $q_\omega(s)$, we find that the correction should go as order A. This makes sense, as the correction should tend toward zero as the unperturbed parent term goes to zero. Another way to more easily see this is to consider (5.120) directly when A is small. This gives $\omega Q + Q'' = A q_\omega''(s) + O(A^2)$. The correction can be shown to then take the form

$$Q(s) = \frac{A}{\sqrt{\omega}} \int_0^s \sin(\sqrt{\omega}[s - \xi]) q_\omega''(\xi) d\xi \,. \tag{5.123}$$

Physically, the inclusion of superfluid friction parameters disrupts the planar filament in such a way that the resulting filament curves or bends so that it no longer lies on a plane. Indeed, while the unperturbed filament lies along a plane described by $(\cos(t), \sin(t))$ for any t (the plane itself rotates), the stationary part of the perturbed solution is complex (with non-trivial real and imaginary parts) which means that the solution no longer lies on a plane.

It is natural to wonder if such filaments are spectrally stable. The planar filament in the standard fluid LIA is orbitally stable (as was shown in Chapter 3), however this deformation of the planar filament is not simply a perturbed solution to the same nonlinear Schrödinger equation. Rather, the entire governing equation is changed (for $\alpha > 0$), so we are dealing with a structural perturbation of the problem as well. Hence, the question of

stability is not as simple as treating the solution (5.119) as a perturbation of (5.122). Rather, such a stability analysis should be performed on general perturbations of solutions to (5.118) directly.

5.4.3 Purely self-similar filament structures

Similarity solutions (solutions which maintain their form independent of scale) have been considered for the curvature-torsion and Cartesian reference frames in the absence of a normal fluid impinging on the filament. These results are reviewed in the previous section. Here we shall consider self-similar solution to the T-LIA model.

Let us take the similarity variable $\eta = s/\sqrt{t}$ and the similarity solution $v(s,t) = g(\eta)$. The potential equation (5.118) reduces to

$$-\frac{i}{2}\eta g' + g'' - \frac{2g'^2 g^*}{1+|g|^2} - \hat{\alpha}i\left[g'' - \frac{2g'^2 g^*}{1+|g|^2} - \frac{4g|g'|^2}{1-|g|^4}\right] = 0\,, \qquad (5.124)$$

where prime denotes differentiation with respect to the similarity variable. From here one can separate real and imaginary parts of g and solve numerically. In order to determine the qualitative properties of the solution dependence on $\hat{\alpha}$, we shall consider a small-amplitude solution (corresponding to a vortex filament with small deviation in s and t). Doing so, we neglect terms of order two or higher, obtaining the linearized expression

$$-\frac{i}{2}\eta g' + (1 - \hat{\alpha}i)g'' = 0\,. \qquad (5.125)$$

230

We find that

$$g'(\eta) = \epsilon \exp\left(-\frac{\hat{\alpha}}{1+\hat{\alpha}^2}\eta^2\right)\left\{\cos\left(\frac{\eta^2}{1+\hat{\alpha}^2}\right) + i\sin\left(\frac{\eta^2}{1+\hat{\alpha}^2}\right)\right\}, \qquad (5.126)$$

where ϵ is a small parameter of the order of magnitude of the small-amplitude solution. From here, we recover the approximation to the small amplitude solution,

$$\begin{aligned}
g(\eta) = \delta_1 &+ \epsilon \int_0^\eta \cos\left(\frac{\nu^2}{1+\hat{\alpha}^2}\right)\exp\left(-\frac{\hat{\alpha}\nu^2}{1+\hat{\alpha}^2}\right)d\nu \\
&+ i\left[\delta_2 + \epsilon\int_0^\eta \sin\left(\frac{\nu^2}{1+\hat{\alpha}^2}\right)\exp\left(-\frac{\hat{\alpha}\nu^2}{1+\hat{\alpha}^2}\right)d\nu\right],
\end{aligned} \qquad (5.127)$$

where δ_1, δ_2 are sufficiently small parameters. So, in the absence of the normal fluid, purely self-similar filament structures can exist.

What we have therefore shown is that, in the absence of a normal fluid impinging on the vortex, there exist filament structures which are completely self-similar in nature. These self-similar structures are completely determined by (5.124). In the situation where deviations of the filament from a reference axis are small, the self-similar filaments can be approximated according to formula (5.127).

In terms of the physics of the problem, the existence of such solutions implies that, in the low temperature limit where $U \to 0$, well-organized structures are possible. The natural scaling for the similarity goes as $x \sim \sqrt{t}$. At large length and time scales, the solutions mirror their own behavior at small time scales. For small deviations from a central axis, the behaviors manifest as solutions which oscillate about this central axis, at all scales. This self-similarity is rather idealized. In the following section, we shall see what is preserved of the self-similarity when a non-zero normal fluid velocity is introduced. Fonda [32] demonstrate

the agreement of the self-similar solutions obtained under LIA with experiments on Kelvin waves (at a temperature of 1.98K).

5.4.4 Formulation including normal fluid flow

For larger temperatures, the normal fluid impinging on the vortex matters qualitatively, and should be included. On the other hand, the friction parameter α' does not influence the behavior of the solutions strongly (much less so than α), and shall be neglected in this section. One may write $\mathbf{U} = U\mathbf{t} + U_a\mathbf{n} + U_b\mathbf{b}$ where $\mathbf{b}$ is the binormal vector. As discussed in Shivamoggi [86], the transverse velocity components U_a and U_b often result in an algebraic rescaling of the Kelvin waves along the filament, while U (the velocity component along the filament) influences the filament in a qualitative manner. Therefore, we consider consider $U \neq 0$ and $U_a = U_b = 0$ to determine the qualitative features of the filament solutions to the quantum LIA model. Umeki [96] developed a transformation between the Cartesian LIA and the arclength LIA variables. Making use of this transformation, we can derive the arclength form of the quantum LIA model including the normal fluid, through the Cartesian form of the quantum LIA model. We find that, upon setting $\alpha' = 0$ and differentiating (2.12) with respect to s, the quantum LIA model becomes (making use of the same potential function v defined in (5.117))

$$iv_t + v_{ss} - \frac{2v_s^2 v^*}{1 + |v|^2} - \alpha i \left[v_{ss} - \frac{2v_s^2 v^*}{1 + |v|^2} - \frac{4vv_s v_s^*}{1 - |v|^4} \right] - \alpha U \left(\frac{1 + |v|^2}{1 - |v|^2} \right)^2 v_s = 0, \quad (5.128)$$

where the final term is the influence due to the normal fluid impinging on the vortex. If the magnitude of the normal fluid velocity is small, it is sufficient to consider the results of the previous section. On the other hand, if the magnitude U is large, the final term is more dominant than the term involving only α. The model is most useful when perturbations along the vortex filament are small. When they are large, one may wish to use the full form of the quantum LIA given in (2.12).

5.4.5 Helical filaments

Unlike in the zero normal flow case, when $U \neq 0$ there exists an exact planar wave solution to (5.128). Such a solution manifests as a helical structure when plotted in the coordinate frame (t_1, t_2). Assuming $v(s,t) = A \exp(i[kx - \omega t])$, we have

$$\omega - k^2 + \frac{2A^2 k^2}{1+A^2} - \alpha i \left[\left(\frac{1+A^2}{1-A^2} \right) k^2 - U \left(\frac{1+A^2}{1-A^2} \right)^2 k \right] = 0. \qquad (5.129)$$

Separating real and imaginary parts, $\omega = \left(\frac{1-A^2}{1+A^2} \right) k^2$, $A = \sqrt{\frac{k-U}{k+U}}$, so $\omega = kU$. The solution is then

$$v(s,t) = \sqrt{\frac{k-U}{k+U}} e^{ik(x-Ut)}. \qquad (5.130)$$

Note that while this solution does not explicitly depend on the superfluid friction parameter, α, it does require that $\alpha > 0$, which yields a unique value of the amplitude A. This solution also requires $k > U$. On the other hand, if $\alpha = 0$, the amplitude would not be specified, so

there would exist an infinite family of solutions, one for each value of $A \in (0, 1)$. In that case, the solution does not involve U.

The existence of such a helical structure is to be expected. Such solutions naturally exist in the Cartesian frame of reference. In the zero-temperature limit of the Cartesian frame, helical filaments were studied by Sonin [89]. More recently, helical filament solutions for the positive temperature case (which includes $\alpha > 0$ and $\alpha' > 0$) have also been studied (Van Gorder [106]). Like in the Cartesian frame (Van Gorder [106]), there exists a relation between the permitted region for the wave number and the magnitude of the normal fluid velocity. In particular, if the magnitude of the normal fluid velocity is high, the vortex filament exists only if the wave number is sufficiently large. In other words, there can be no slowly rotating helical vortices in the presence of strong normal fluid flow.

The exact solution (5.130) also demonstrates that this rotating helix cannot exist for $U = 0$. Indeed, in the absence of a normal fluid contribution, we would be left with a helix $v(s, t) = e^{iks}$. However, such a helix is time-independent (so there can be no rotation). Such a standing solution would be highly unlikely for the physical problem. Hence, the rotation helical solution is actually driven by the normal fluid flow. There is no explicit dependence on α, in complete agreement with the Cartesian formulation (Van Gorder [106]). However, the existence of this solution does depend on $\alpha > 0$; from (5.129), if $\alpha > 0$, then we may determine the exact form of the amplitude in terms of k and U. Without such a specification, the amplitude of the helix is undetermined.

5.4.6 A soliton in the small-amplitude regime when the normal fluid flow dominates

One of the more famous solutions for the standard fluid LIA is the Hasimito 1-soliton [42]. However, finding such a general soliton in the quantum LIA model in either the curvature-torsion or Cartesian frames has not been done, due to the added complication of the highly nonlinear terms associated with superfluid friction. If one is willing to linearize such equations, it is possible to obtain locally stationary structures which behave as solitary waves (Shivamoggi [85, 86]).

Let us now consider a soliton in the small α, large U limit where (5.128) reduces to

$$iv_t + v_{ss} - \frac{2v_s^2 v^*}{1 + |v|^2} - \alpha U \left(\frac{1 + |v|^2}{1 - |v|^2} \right)^2 v_s = 0 \,. \tag{5.131}$$

In particular, consider $v(s,t) = e^{-i\omega\alpha^2 U^2 t} p(S)$, where $S = \alpha U s$. The resulting equation is rather complicated to solve, even numerically. Under the assumption of a small-amplitude solution, with $\epsilon << 1$ the maximal deviation of the filament from the reference axis, we find (neglecting terms of nonlinearity order greater than three) that

$$\omega p + \frac{d^2 p}{dS^2} - 2p \left(\frac{dp}{dS} \right)^2 - (1 + 4p^2)\frac{dp}{dS} = 0 \,. \tag{5.132}$$

The choice of ω is ours, since we use it as a scaling parameter. In the case of $\omega = -6$, we have $p(S) = \epsilon e^{-2S}$ as an exact solution. So, when deviations from the reference axis are small, we have soliton solutions which scale like $v(s,t) = \epsilon e^{6i\alpha^2 U^2 t} e^{-2S} = \epsilon e^{6i\alpha^2 U^2 t} e^{-2\alpha U s}$ for $s \geq 0$. Such solutions have maximal amplitude at zero arclength and gradually decay as the

arclength becomes large. Therefore, the time evolution of a small soliton-type perturbation localized at $s = 0$ can be determined in the case where U dominates α, that is, for the case of strong normal fluid flow. Note that, in the Cartesian geometry, one can view $s = 0$ as occurring at a wall. As s increases and one moves away from the wall, the filament gradually decays to a straight line filament.

5.4.7 A soliton in the intermediate regime

For the intermediate regime, where neither small α nor large U dominate, it is still possible to seek a soliton solution. Assume $v(s,t) = e^{-(\omega_1 + i\omega_2)\alpha^2 U^2 t} p(S)$, where $S = \alpha U s$. Note that the time dependence is no longer only a phase contribution. For solutions to remain bounded in time, it is necessary that $\omega_1 > 0$. We again assume small deviations from the reference axis, of magnitude $\epsilon << 1$. The equation governing p then becomes

$$(\omega_2 - i\omega_1)p + (1 - \alpha i)\frac{d^2p}{dS^2} - 2(1 - \alpha i)p^*\left(\frac{dp}{dS}\right)^2 + 4\alpha i p \frac{dp}{dS}\left(\frac{dp}{dS}\right)^* - (1 + 4|p|^2)\frac{dp}{dS} = 0. \quad (5.133)$$

It makes sense to seek a solution $p(S) = \epsilon e^{(r_1 + ir_2)S}$. We obtain an algebraic system of four equations for the four unknowns ω_1, ω_2, r_1 and r_2, resulting in the solution

$$v(s,t) = \epsilon \exp\left(\frac{6i\alpha U}{1 + 9\alpha^2}\left[s + \alpha U\frac{1 + \alpha^2}{1 + 9\alpha^2}t\right]\right)\exp\left(-\frac{2\alpha U}{1 + 9\alpha^2}\left[s + \alpha^2 U\frac{13 + 45\alpha^2}{1 + 9\alpha^2}t\right]\right).$$

$$(5.134)$$

What we see is that, in the intermediate regime (where neither α nor U dominate), the soliton solution decays both a arclength and time increase. This is in contrast to the soliton

236

in the large U regime, where there is only decay for large s and persistence of a non-zero perturbation for all time. Hence, in this intermediate case, the filament asymptotically decays so that is has no deviation from the reference axis, as $t \to \infty$. Furthermore, due to the damping term involving α, as α increases in value the soliton decays more rapidly.

5.4.8 Quasi-similarity solution with temporal drift

For non-zero U, there is not a pure similarity solution. The break-down of self-similarity in the $U \neq 0$ case was previously highlighted in Van Gorder [107]. However, there does exist a transformation which maps a pseudo-similarity solution into the similarity solution obtained for the $U = 0$ case. Let us consider a solution of the form $v(s,t) = h(\zeta)$, where $\zeta = \eta + \chi(t)$ and $\eta = s/\sqrt{t}$ is the similarity variable introduced before. Neglecting terms of order two or higher (valid for small deviations from the centralized axis),

$$-\frac{i}{2}\zeta h' + (1 - \alpha i)h'' + \left(\frac{i}{2}\chi'(t) + i\chi(t) - \alpha U \sqrt{t}\right)h' = 0 \,. \tag{5.135}$$

When the rightmost term is zero, this equation reduces to an equation of the form (5.125). This, in turn, means that the function χ must satisfy the first order ODE $\frac{i}{2}\chi'(t) + i\chi(t) - \alpha U \sqrt{t} = 0$, the solution of which reads

$$\chi(t) = -2i\alpha U \left\{\sqrt{t} - \sqrt{2}F\left(\sqrt{\frac{t}{2}}\right)\right\}, \quad \text{where} \quad F(\sigma) = e^{-\sigma^2}\int_0^\sigma e^{\xi^2}d\xi \tag{5.136}$$

is Dawson's integral. Therefore, for filaments with small deviation from the centralized axis, we have that $h(\zeta) = g(\zeta)$, g is the function given in (5.126) (which will need to have real

and imaginary parts regrouped) and

$$\zeta = \eta - 2i\alpha U \left\{ \sqrt{t} - \sqrt{2}F\left(\sqrt{\frac{t}{2}}\right) \right\} = \frac{s}{\sqrt{t}} - 2i\alpha U \left\{ \sqrt{t} - \sqrt{2}F\left(\sqrt{\frac{t}{2}}\right) \right\}. \qquad (5.137)$$

Thus, we have obtained a variation of the pure similarity solution given in the previous section, which includes the influence of the non-zero normal fluid velocity. The influence of the normal fluid velocity is to induce a sort of drift term, which adds a temporal correction to the similarity variable.

Since $\alpha << 1$, and the correction to η is of the order $\sqrt{t}$, the similarity solutions are disrupted for only large time scales. For the small time scales (when the solution is like that of the purely self-similar case), the filaments remain bounded for all t and all s. However, for large time-scales, the similarity solutions give way to solutions involving the composite variable ζ. If s is particularly large, the influence of the correction is small. However, for time scales much larger than the arclength scale, the correction dominates. The growth of this correction is like $O(t^{1/2})$, while the decay of the similarity part of ζ goes like $O(t^{-1/2})$.

5.4.9 Discussion

We obtain the quantum LIA model in terms of the tangent vector to the vortex filament. Under an appropriate transformation, this vector PDE is put into potential form, resulting in a type of nonlinear Schrödinger equation (NLS). This is in analogy to the result of Umeki [95] for the LIA. We demonstrate that this formulation is actually rather useful, as it permits us

to construct a number of solutions analytically. Many of these solutions (the planar, helical, and self-similar filaments) were known for the standard LIA, yet had not been analytically extended to the quantum LIA model in the presence of superfluid friction or a normal fluid impinging on the filament. Additionally, some solitary wave perturbations were constructed, which model soliton Kelvin waves along the filament. Note that we considered two reductions of the quantum LIA (2.12), namely (5.118) and (5.128), each of which models a qualitatively distinct situation.

The primary utility in using the tangent form of the quantum LIA model developed here lies in the fact that it permits one to construct solutions, either analytically or numerically, with relative ease, since the quantum LIA model is put into a potential equation which is a kind of NLS. Both the influence of superfluid friction and the normal fluid are taken into account through such a model. The main drawback to this formulation is that the solutions are given for the tangent vector to the filament, as opposed to a more obviously useful quantity. However, using the transformation of Umeki [96], it is possible to map every solution obtained here into a solution in the Cartesian reference frame. It is noteworthy that this procedure is apparently simpler than attempting to obtain the solutions directly in the Cartesian frame, as the potential equation obtained there (Van Gorder [102]) is not so simple to solve in the case of some of the filaments obtained here (for instance, the deformations of the planar filaments). In Figs. 5.18-5.21, we provide some of the solutions obtained here, after they have been mapped back to the Cartesian frame of reference. We demonstrate the

effect of the superfluid friction parameters on the planar filament, the self-similar filament, the helical filament, and one of the soliton filaments.

One qualitative feature we notice is that solutions can essentially be separated into two groups: those which exist in the low-temperature limit ($U = 0$), and those which require $U > 0$. The former include the self-similar vortex filament; when $U \neq 0$, these filaments are strongly perturbed by the oncoming flow, resulting in a loss of pure self-similarity. On the other hand, the helical and soliton solutions are driven by this flow. This becomes very clear when one considers the tangent form of the quantum LIA model.
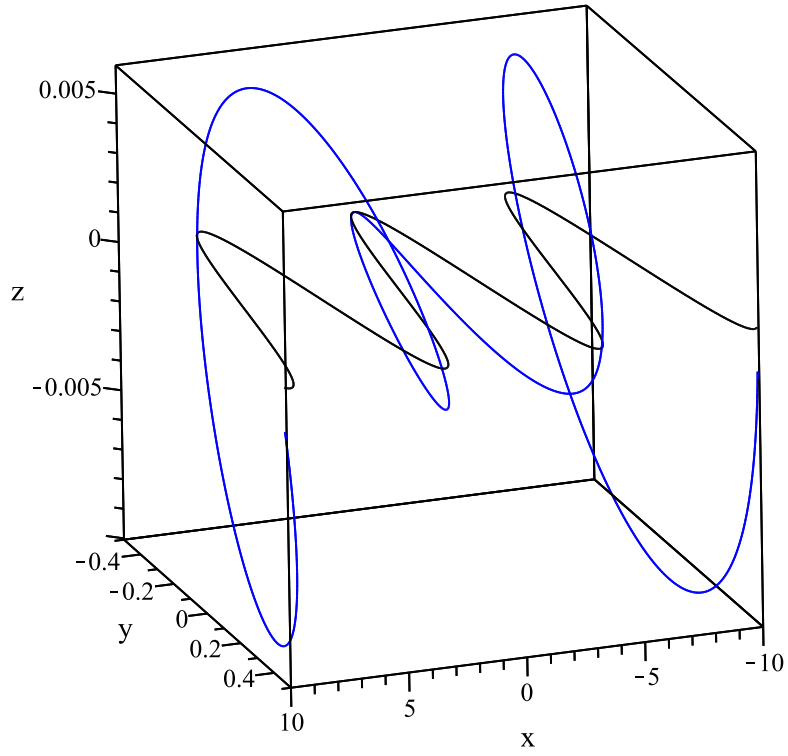
Figure 5.18: The deformation of planar filaments due to superfluid friction as given analytically by (5.122). The black line represents $\alpha = \alpha' = 0$, while the blue line represents $\alpha = 0.005, \alpha' = 0.003$.
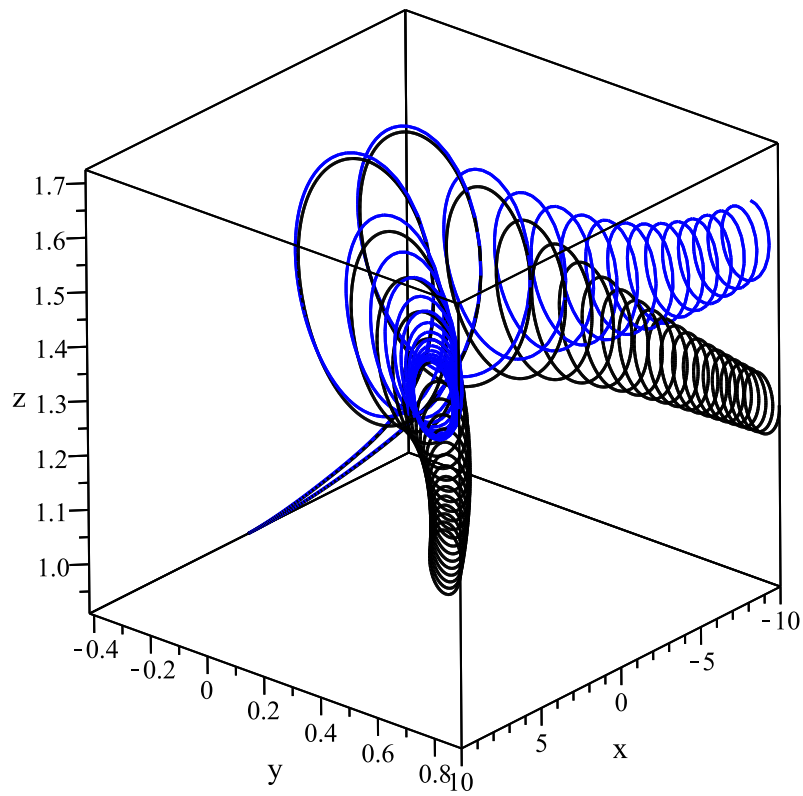
Figure 5.19: The self-similar solutions for $\alpha = \alpha' = 0$ (black line), $\alpha = 0.005, \alpha' = 0.003$ (blue line) corresponding to the fully nonlinear equation (5.124).
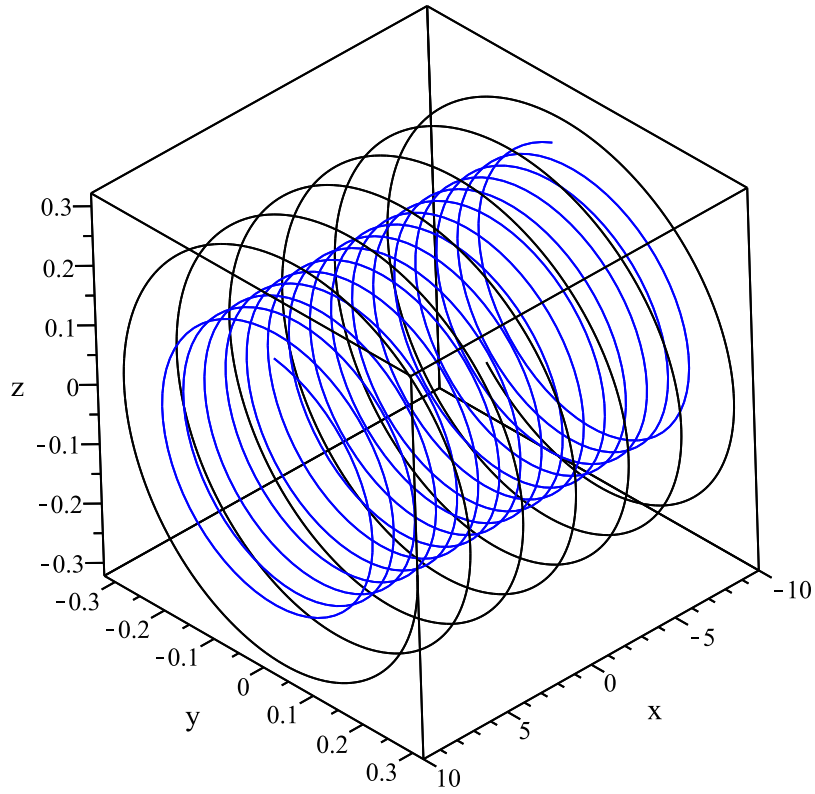
Figure 5.20: Helical solutions are plotted for $U = 1, k = 2$ (black line) and $U = 1, k = 5$ (blue line). As the wave number k increases, the period increases while the amplitude (in Cartesian coordinates) decreases.
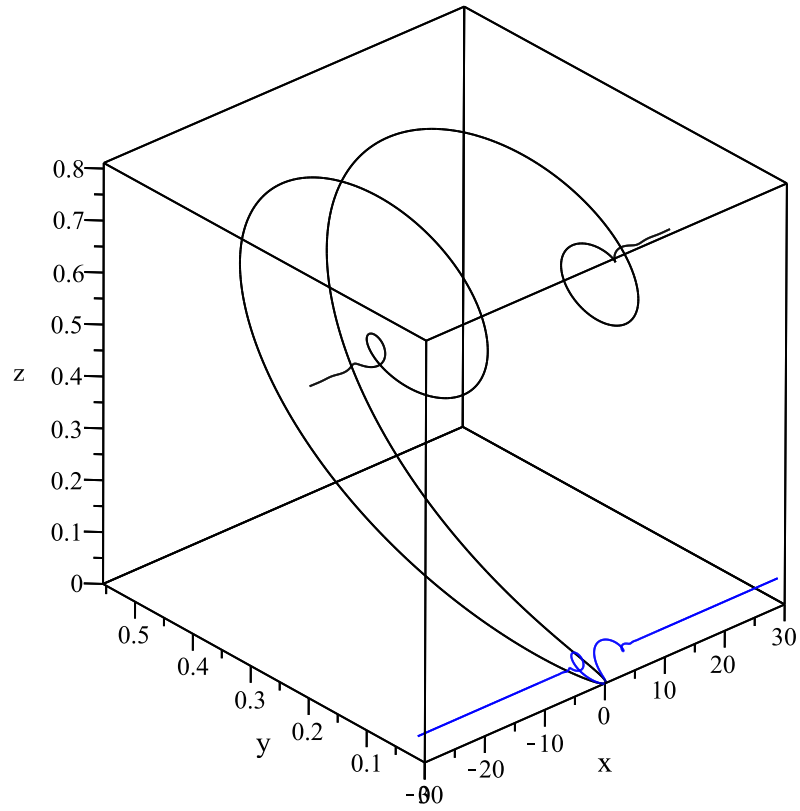
Figure 5.21: Soliton solutions (5.134) are given in (d), for $\alpha = 0.005$ (black line) and $\alpha = 0.073$ (blue line) in the presence of a normal fluid ($U = 1$). The perturbation size of these soliton excitations of the tangent filament is $\epsilon = 0.01$ (though the corresponding value of the perturbation is much larger in the Cartesian frame).

CHAPTER 6

SOLUTIONS UNDER THE EXACT (NON-POTENTIAL) 3D

VECTOR QUANTUM LIA

In the previous chapters, we have thus far studied potential formulations of vortex models, which allow for the vortex filament solution to be recast as the solution of a scalar nonlinear dispersive partial differential equation. As mentioned before, such an approach in general neglects certain features of the true solutions. The most general approach to study quantum LIA vortex filament solutions would then be to consider nonlinear dispersive partial differential equation where the unknown function is a vector-valued function, rather than a scalar-valued function. This shall be the focus of the present chapter.

6.1 Decay of helical Kelvin waves on a vortex filament under the quantum LIA

We study helical Kelvin waves driven by a normal fluid moving along a vortex filament in the quantum form of the local induction approximation (LIA) in vector form (without additional simplifications, and including friction terms). The motion of such Kelvin waves is both

translational (along a reference axis) and rotational (in the plane orthogonal to the reference axis). We first present an exact closed form solution for the motion of these Kelvin wanes in the case of a constant amplitude helix. Such solutions exist for a critical wave number and correspond exactly to the Donnelly-Glaberson instability, so perturbations of such solutions either decay to line filaments or blow-up (the latter is non-physical). This leads us to consider helical Kelvin waves which decay to line filaments. Unlike in the case of constant amplitude helical solutions, the dynamics are much more complicated for the decaying helical waves, owing to the fact that the rate of decay of the helical perturbations along the vortex filament is not constant in time. We give an analytical and numerical description of the motion of decaying helical Kelvin waves, from which we are able to ascertain the influence of the physical parameters on the temporal decay, translational motion along the filament, and rotational motion, of these waves. The results presented here originate from Van Gorder [112].

6.1.1 Background

We will now work with the vector equation

$$\mathbf{v} = \gamma\kappa\mathbf{t} \times \mathbf{n} + \alpha\mathbf{t} \times (\mathbf{U} - \gamma\kappa\mathbf{t} \times \mathbf{n}) - \alpha'\mathbf{t} \times (\mathbf{t} \times (\mathbf{U} - \gamma\kappa\mathbf{t} \times \mathbf{n})) \tag{6.1}$$

which was introduced earlier. We shall study the motion of helical Kelvin waves along a quantum vortex filament under the Schwarz model (6.1). The time evolution of the vortex filament will be described in the Cartesian reference frame, as this permits one to view the

filaments directly. There are three main components of the time evolution for such nonlinear waves: translation along a central axis, rotation about the central axis, and decay. In the case of no decay (i.e., the amplitude of the waves remains constant in time, so the waves are eternal), the filament can be described exactly - in closed form. This solution corresponds to the critical wave number for the Donnelly-Glaberson instability [23, 36, 71]. When the Kelvin waves are allowed to decay, which is more physically relevant yet much harder to investigate mathematically, we are able to obtain a dynamical system which governs the time evolution of the translational and rotational motion, in addition to the decay rate. Unlike what may be inferred from the eternal solution, the decay of the Kelvin waves is not constant in time, and we are able to demonstrate mathematically that the rate of decay should gradually increase until the helical Kelvin waves dissipate, leaving a line filament. Numerical simulations verify the analytical results. The influence of the normal fluid velocity, the superfluid friction parameters, and the wave number of the Kelvin waves on the time evolution is discussed in detail.

While a number of studies on helical filaments exist, they can gradually be split into two groups. First, there are studies on helical filaments in the classical LIA (see for instance Kida [49]; Sonin [89]), which correspond to the zero temperature limit ($\alpha, \alpha' = 0$). Of course, there is no dissipation in such limits, yet dissipative waves are the physically interesting case. Secondly, there are a number of approximations to the full vector equation (6.1). Assuming that translational effects are small (or negligible, through a change of the spatial coordinate), one may define a potential form of the quantum LIA. This has been

done for the Cartesian (Van Gorder [102]) and arclength-tangent (Van Gorder [108]) frames. In such formulations, the filaments are assumed to satisfy some constraints (for instance, they should be of sufficient bounded variation - see (Van Gorder [106])). The benefit of the present study is that we consider the full vector equation (6.1) without making any such simplifying assumptions. This allows us to take into account strong translation of Kelvin waves along the filament. Furthermore, we are able to consider decay of the Kelvin waves in time, which is not accessible under potential forms of the quantum LIA. As we shall see, the translation and decay are not constant in time, so the approach taken here is required in order to study such quantum vortex dynamics.

6.1.2 Propagation of a helical filament driven by the normal fluid

Assume that the filament is aligned on the same axis along which the normal fluid is directed. Choosing our geometry in this way, we may write the normal fluid velocity as $\mathbf{U} = (U, 0, 0)$ and the vortex filament as $\mathbf{r} = (x, y(x, t), z(x, t))$. A line filament will take the form $\mathbf{r}_0 = (x, 0, 0)$. We shall show that under the Schwarz quantum LIA model (6.1), the normal fluid velocity $\mathbf{U}$ induces helical perturbations in the line filament. To do so, we equivalently demonstrate the existence of a helical filament of the form

$$\mathbf{r} = (x + \beta t, A\cos(kx - \omega t + x_0), A\sin(kx - \omega t + x_0)) \tag{6.2}$$

to the Schwarz model. Here, A is the amplitude, β is the translation of the central axis along which the filament is aligned due to time, k is the wavenumber, ω is the frequency, and x_0 is some constant which may be calibrated subject to any helical initial condition

For simplicity, denote $\eta = kx - \omega t + x_0$. We compute several quantities needed for the right hand side of (6.1):

$$\frac{dx}{ds} = \frac{1}{\sqrt{1 + A^2 k^2}}, \tag{6.3}$$

$$\mathbf{t} = \frac{(1, -Ak\sin(\eta), Ak\cos(\eta))}{\sqrt{1 + A^2 k^2}}, \quad \kappa\mathbf{n} = \frac{(0, -Ak^2\cos(\eta), -Ak^2\sin(\eta))}{(1 + A^2 k^2)}, \tag{6.4}$$

$$\kappa\mathbf{t} \times \mathbf{n} = \frac{(A^2 k^3, Ak^2\sin(\eta), -Ak^2\cos(\eta))}{(1 + A^2 k^2)^{3/2}}, \tag{6.5}$$

$$\mathbf{t} \times (\kappa\mathbf{t} \times \mathbf{n}) = -\kappa\mathbf{n}, \quad \mathbf{t} \times [\mathbf{t} \times (\kappa\mathbf{t} \times \mathbf{n})] = -\kappa\mathbf{t} \times \mathbf{n}, \tag{6.6}$$

$$\mathbf{t} \times \mathbf{U} = \frac{(0, AkU\cos(\eta), AkU\sin(\eta))}{\sqrt{1 + A^2 k^2}}, \tag{6.7}$$

$$\mathbf{t} \times (\mathbf{t} \times \mathbf{U}) = \frac{(-A^2 k^2 U, -AkU\sin(\eta), AkU\cos(\eta))}{1 + A^2 k^2}. \tag{6.8}$$

On the other hand, the left hand side of (6.1) is given by

$$\mathbf{r}_t = (\beta, A\omega\sin(\eta), -A\omega\cos(\eta)). \tag{6.9}$$

Placing these into (6.1), we obtain three equations, one for each of the x, y and z components. Simplifying these, and noting that the z equation is equivalent to the y equation, we obtain the three parameter restrictions

$$\beta = \frac{(1 - \alpha')\gamma A^2 k^3}{(1 + A^2 k^2)^{3/2}} + \frac{\alpha' A^2 k^2 U}{1 + A^2 k^2}, \tag{6.10}$$

$$A\omega = \frac{(1 - \alpha')\gamma A k^2}{(1 + A^2 k^2)^{3/2}} + \frac{\alpha' AkU}{1 + A^2 k^2}, \tag{6.11}$$

$$0 = \frac{\alpha A k U}{\sqrt{1 + A^2 k^2}} - \frac{\alpha \gamma A k^2}{1 + A^2 k^2} \,. \tag{6.12}$$

Equation (6.10) gives the translation of the first coordinate. The remaining two conditions determine the frequency ω and the wave number k. Compared to helical solutions found in Chapter 5, note that the result for the potential form of the quantum LIA accurately gave the first term for ω, but the second term involving U is off by a factor, since the term giving this factor was approximated. From (6.12), we find that the wave number must take the critical value

$$k^* = \frac{U}{\sqrt{\gamma^2 - A^2 U^2}} \,. \tag{6.13}$$

Using (6.13) and (6.10) in (6.11), we find that

$$\omega^* = \frac{U^2}{\gamma^2} \sqrt{\gamma^2 - A^2 U^2} \,. \tag{6.14}$$

Equation (6.10) should then read $\beta = A^2 k^* \omega^* = A^2 U^3 \gamma^{-2}$. The constant-amplitude helical filament driven by the normal fluid velocity $\mathbf{U}$ is then given by

$$\mathbf{r}(x, t) = \left(x + \frac{A^2 U^3}{\gamma^2} t, A \cos(\eta), A \sin(\eta) \right) , \tag{6.15}$$

where

$$\eta = \frac{U}{\sqrt{\gamma^2 - A^2 U^2}} x + \frac{U^2}{\gamma^2} \sqrt{\gamma^2 - A^2 U^2} t + x_0 \,. \tag{6.16}$$

A necessary condition for the existence of such a helical vortex filament solution to the quantum LIA is that $A < \gamma/|U|$, so the amplitude of the helical perturbations to the line filament must be bounded.

In either the small amplitude or small U limit, the vortex filament (6.16) collapses to a line filament. So, it is clear that the helical perturbations that rise along the line filament are

driven by the normal fluid impinging on the superfluid. The normal fluid flow also induces a drift, which manifests in the t-dependence of the x-coordinate of (6.16). This drift is of order U^3, so if the magnitude of the velocity is small, the drift is very small, whereas if the velocity is large, the translational motion greatly exceeds the rotational motion.

Note that such filaments solutions are eternal, in the sense that they do not decay. These solutions correspond to the onset of the Donnelly-Glaberson instability of Kelvin waves driven by the normal fluid flow. The critical value of $k = k^*$ therefore corresponds to the critical wave number for this instability. Such helical structures, while eternal, should be unstable. This means that, under small perturbations, the helical filaments will not maintain their form. This makes sense, in light of the fact that there are dissipation effects (such as the friction parameters) in contrast to the driving force due to the normal fluid flow. At $k = k^*$, these effects are balanced, whereas under a small perturbation one or the other effects on the vortex filament may dominate.

Blow-up of this type of filament is non-physical, but the decay of such a filament into a line filament (that is, the dissipation of the helical waves along the filament) is physically relevant. Therefore, we should generalize the particular solution in this section (corresponding to the critical wave number for the Donnelly-Glaberson instability) to account for dissipation. In order to obtain solutions which exhibit both translational and rotational motion in addition to decay, a more complicated analysis is required, and we perform this analysis in the next section.

6.1.3 Constructing the decaying helical filament

The solution obtained in the previous section does not decay in time: the motion of the helical vortex filament is rotational and translational, but there is no dissipation of the helical waves. In order to account for the decay, it may be tempting to simply include terms of the form $\exp(-rt)$, where r is some positive constant, to (6.15) (multiplying the sine and cosine terms). Unfortunately, things are not so simple: doing so, one obtains factors of $\exp(-2rt)$ in the expressions for ω, implying that ω is not a constant parameter. In order to avoid such contradictions, we must assume that ω is not a constant in time, nor do we assume the decay rate is constant in time. To this effect, let us consider a filament solution of the form

$$\mathbf{r}(x,t) = (x + \beta(t), A\exp(-\mu(t))\cos(\nu(x,t)), A\exp(-\mu(t))\sin(\nu(x,t))) , \tag{6.17}$$

where $\nu(x,t) = kx - \omega(t) + x_0$. Following similar derivations to those in the previous section, we find that such a decaying vortex filament solution (6.17) exists provided that

$$\frac{d\beta}{dt} = \left\{ \frac{(1-\alpha')\gamma A^2 k^3}{(1 + A^2 k^2 \exp(-2\mu(t)))^{3/2}} + \frac{\alpha' A^2 k^2 U}{1 + A^2 k^2 \exp(-2\mu(t))} \right\} \exp(-2\mu(t)) , \tag{6.18}$$

$$\frac{d\omega}{dt} = \frac{(1-\alpha')\gamma k^2}{(1 + A^2 k^2 \exp(-2\mu(t)))^{3/2}} + \frac{\alpha' kU}{1 + A^2 k^2 \exp(-2\mu(t))} , \tag{6.19}$$

$$\frac{d\mu}{dt} = \frac{\alpha\gamma k^2}{1 + A^2 k^2 \exp(-2\mu(t))} - \frac{\alpha kU}{\sqrt{1 + A^2 k^2 \exp(-2\mu(t))}} . \tag{6.20}$$

Equations (6.18)-(6.20) constitute a system of differential equations governing the translational ($\frac{d\beta}{dt}$), rotational ($\frac{d\omega}{dt}$), and decay ($\frac{d\mu}{dt}$) effects on the helix in the quantum LIA. The

first two of these equations give us

$$\beta(t) = A^2 k \int_0^t \frac{d\omega}{dt}(\tau) \exp(-2\mu(\tau))d\tau \,, \tag{6.21}$$

$$\omega(t) = \int_0^t \left\{ \frac{(1-\alpha')\gamma k^2}{(1 + A^2 k^2 \exp(-2\mu(t)))^{3/2}} + \frac{\alpha' kU}{1 + A^2 k^2 \exp(-2\mu(t))} \right\} d\tau \,. \tag{6.22}$$

Hence, provided we can find $\mu(t)$, the quantities $\beta(t)$ and $\omega(t)$ are able to be calculated.

From (6.20), we can separate variables and obtain an implicit relation for $\mu(t)$:

$$\int_0^{\mu(t)} \frac{1 + A^2 k^2 \exp(-2w)}{\gamma k^2 - kU \sqrt{1 + A^2 k^2 \exp(-2w)}} dw = \alpha t \,. \tag{6.23}$$

Note that when $\alpha = 0$, the decay rate is zero. Therefore, the helical solutions to the classical LIA do not decay.

In the case where the amplitude is very small, $A << 1$, we ignore the order A^2 terms, obtaining $\beta(t) = \beta_0$ (a constant, meaning that there is no translation),

$$\omega(t) = \left\{ (1-\alpha')\gamma k^2 + \alpha' kU \right\} t \,, \tag{6.24}$$

and

$$\mu(t) = \alpha k (\gamma k - U) t \,. \tag{6.25}$$

From the latter, we see that a necessary condition for decay of the filament is $k > U/\gamma$.

6.1.4 Properties of the decay term $\mu(t)$

Assume that $\gamma > |U|$. Then, (6.20) has an equilibrium μ^* which is given by the formula

$$\mu^* = \frac{1}{2} \ln \left(\frac{U^2}{\gamma^2 - (1 + A^2)U^2} \right) \,. \tag{6.26}$$

253

In order to μ^* to exist and be positive, we must have the condition

$$\frac{\gamma^2 - 2U^2}{U^2} < A^2 < \frac{\gamma^2 - U^2}{U^2} \tag{6.27}$$

on the initial amplitude A. As may be verified easily, the positive equilibrium μ^* is always unstable.

Even without the condition $\gamma > |U|$, the function $\mu(t)$ can be shown to increase under reasonable conditions. From the form of (6.20), if the right hand side of (6.20) is initially positive, then it should remain positive for all time. Since we take $\mu(0) = 0$, this means that we should have

$$\frac{\alpha\gamma k^2}{1 + A^2 k^2} - \frac{\alpha k U}{\sqrt{1 + A^2 k^2}} > 0, \quad \text{or, equivalently,} \quad \frac{k}{\sqrt{1 + A^2 k^2}} > \frac{U}{\gamma}. \tag{6.28}$$

For small time, we have that $\mu(t)$ is approximately given by

$$\mu(t) \approx \alpha k \left(\frac{\gamma k - U\sqrt{1 + A^2 k^2}}{1 + A^2 k^2} \right) t. \tag{6.29}$$

Since $\mu(t)$ is increasing in time, we should have that $\exp(-2\mu(t)) \to 0$ as $t \to \infty$. This is equivalent to taking the amplitude to zero, so in this limit the solutions is equivalent to (6.25). In Fig. 6.1, we plot a numerical solution to (6.20) in addition to the small-time approximation (6.29) and the large-time approximation (6.25). We see that the approximation (6.29) is reasonable for $t < \alpha^{-1}$, whereas the approximation (6.25) is a good fit to the true solution provided $t > \alpha^{-1}$. These solutions indicates an interesting facet of the decay of the helical filament, namely, that the exponential rate of decay is not constant. Instead, the filament decays more slowly for small time values and decays more rapidly for large time.

This suggests that such vortex filaments would be observed on small time scales, before decaying to line filaments when time increases.

6.1.5 The case of vanishing normal fluid velocity

In the small U limit, note that we obtain

$$\frac{d\mu}{dt} = \frac{\alpha\gamma k^2}{1 + A^2 k^2 \exp(-2\mu(t))} \tag{6.30}$$

which admits the exact solution

$$\mu(t) = \frac{1}{2}\text{LambertW}\left(A^2 k^2 \exp(A^2 k^2 - 2\alpha\gamma k^2 t)\right) + \alpha\gamma k^2 t - \frac{1}{2}A^2 k^2. \tag{6.31}$$

This function is approximately linear (as seen by plotting the first term), and an accurate linear approximation is given by

$$\mu(t) \approx \frac{\alpha\gamma k^2}{1 + A^2 k^2} t. \tag{6.32}$$

When $U = 0$, (6.19) reduces to

$$\frac{d\omega}{dt} = \frac{(1-\alpha')\gamma k^2}{(1 + A^2 k^2 \exp(-2\mu(t)))^{3/2}} = \frac{1-\alpha'}{\alpha} \frac{1}{\sqrt{1 + A^2 k^2 \exp(-2\mu(t))}} \frac{d\mu}{dt}. \tag{6.33}$$

Integrating both sides of this equation once, and performing relevant algebraic manipulations, we find

$$\omega(t) = \frac{1-\alpha'}{\alpha}\mu(t) + \frac{1-\alpha'}{\alpha}\ln\left\{\frac{1 + \sqrt{1 + A^2 k^2 \exp(-2\mu(t))}}{1 + \sqrt{1 + A^2 k^2}}\right\}. \tag{6.34}$$
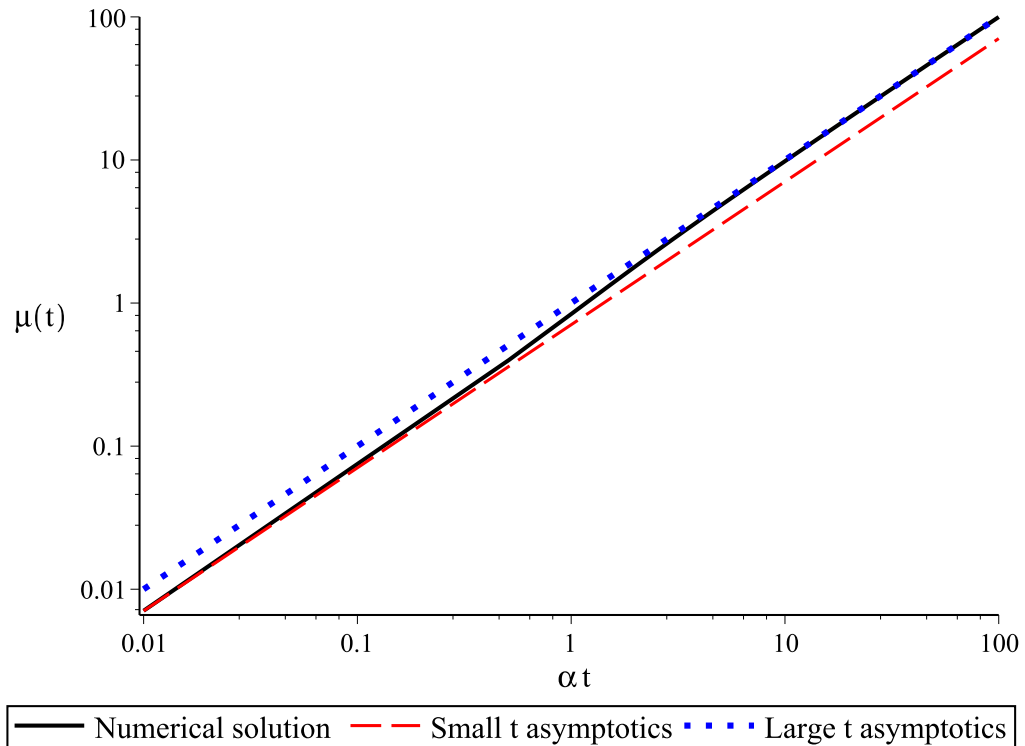
Figure 6.1: Plot of the numerical solution for $\mu(t)$ governed by equation (6.20) along with the small time asymptotic solution (6.29) and the large time asymptotic solution (6.25). Parameter values are fixed at $A = 0.5$, $k = U = 1$, $\gamma = 2$. For small time $(t < \alpha^{-1})$, the approximation (6.29)) is a good fit to the numerical solution, whereas when time is large $(t > \alpha^{-1})$, the approximation (6.25) accurately describes the numerical solution. With this, we find that helical perutrbations along the line vortex filament decay slowly on small time scales, and then more rapidly for larger time scales.

Obtaining the linear approximation like that of (6.32), we have

$$\omega(t) \approx \frac{(1 - \alpha')\gamma k^2}{(1 + A^2 k^2)^{3/2}} t \,, \tag{6.35}$$

which is completely consistent with the dispersion relation obtained under LIA for a standard fluid when we set $\alpha' = 0$.

When $U = 0$, the translation effects (6.18) should be given by

$$\frac{d\beta}{dt} = \frac{(1 - \alpha')\gamma A^2 k^3}{(1 + A^2 k^2 \exp(-2\mu(t)))^{3/2}} \exp(-2\mu(t)) = \frac{1 - \alpha'}{\alpha} \frac{A^2 k \exp(-2\mu(t))}{\sqrt{1 + A^2 k^2 \exp(-2\mu(t))}} \frac{d\mu}{dt} \,, \tag{6.36}$$

which gives a solution of the form

$$\beta(t) = \frac{1 - \alpha'}{\alpha k} \left\{ \sqrt{1 + A^2 k^2} - \sqrt{1 + A^2 k^2 \exp(-2\mu(t))} \right\} \,. \tag{6.37}$$

Up to first order, this solution is approximated like

$$\beta(t) \approx \frac{(1 - \alpha')\gamma A^2 k^3}{(1 + A^2 k^2)^{3/2}} t \tag{6.38}$$

when t is small enough. Setting $\alpha' = 0$, we again recover the expected result from the standard fluid LIA. When t is large, we should have $\exp(-2\mu(t)) \to 0$ and therefore

$$\beta(t) \approx \frac{1 - \alpha'}{\alpha k} \left\{ \sqrt{1 + A^2 k^2} - 1 \right\} \,. \tag{6.39}$$

What we find is that, when the effects of the normal fluid velocity are negligible $(U = 0)$, we obtain the helical filament

$$\mathbf{r}(x, t) \approx \left(x + \frac{(1 - \alpha')\gamma A^2 k^3}{(1 + A^2 k^2)^{3/2}} t \right) \mathbf{i}_x + A \exp\left(-\frac{\alpha\gamma k^2}{1 + A^2 k^2} t \right) \cos\left(kx - \frac{(1 - \alpha')\gamma k^2}{(1 + A^2 k^2)^{3/2}} t \right) \mathbf{i}_y$$

$$+ A \exp\left(-\frac{\alpha\gamma k^2}{1 + A^2 k^2} t \right) \sin\left(kx - \frac{(1 - \alpha')\gamma k^2}{(1 + A^2 k^2)^{3/2}} t \right) \mathbf{i}_z \,, \tag{6.40}$$

which gradually decays to a line filament with exponential rate of decay $\frac{\alpha\gamma k^2}{1+A^2k^2} = O(\alpha)$ as time increases. Quantum vortex filaments in the $U = 0$ case are still physically relevant (Vinen 2001; Araki, Tsubota & Nemirovskii 2002; Alamri, Youd & Barenghi 2008), and the results here show that small helical excitations along such filaments should still decay despite the absence of the normal fluid.

6.1.6   The role of normal fluid velocity on vortex motion and persistence

While exact solutions for $\mu(t)$ are not forthcoming in the presence of a non-zero normal fluid velocity, we observe that the solutions should be approximately linear, with the slope gradually increasing as t increases (as discussed above). For small t ($t < \alpha^{-1}$), we obtain

$$\beta(t) \approx \left\{ \frac{(1-\alpha')\gamma A^2 k^3}{(1+A^2k^2)^{3/2}} - \frac{\alpha' A^2 k^2 U}{1+A^2k^2} \right\} t, \tag{6.41}$$

$$\omega(t) \approx \left\{ \frac{(1-\alpha')\gamma k^2}{(1+A^2k^2)^{3/2}} - \frac{\alpha' kU}{1+A^2k^2} \right\} t, \tag{6.42}$$

$$\mu(t) \approx \left\{ \frac{\alpha\gamma k}{1+A^2k^2} - \frac{\alpha kU}{\sqrt{1+A^2k^2}} \right\} t, \tag{6.43}$$

while for large t ($t > \alpha^{-1}$) we have the approximations $\beta(t) \approx \beta_0, \omega(t) \approx \{(1-\alpha')\gamma k^2 + \alpha' kU\} t$, and $\mu(t) \approx \alpha k(\gamma k - U)t$ (which is exactly what we found previously, in the small amplitude limit).

Both attributes of the vortex motion, namely translation and rotation, are increased when we increase the normal fluid velocity. Increasing the normal fluid velocity, we see that solutions will decay more slowly, and therefore persist for longer periods of time. Both of

these observations make sense in light of the fact that the normal fluid velocity is expected to drive the vortex. Therefore, increasing the normal fluid velocity results in faster-moving and longer-lasting helical vortex filaments.

In Fig. 6.2, we plot the time evolution of a helical vortex filament as described by the solution of the system of nonlinear differential equations (6.18)-(6.20). We take the normal fluid velocity to be zero. In Fig. 6.3 we do the same, while taking a non-zero normal fluid velocity.

From Fig. 6.4, we see that the translational motion of the helical Kelvin waves along the vortex filament is strongly influenced by both the normal fluid velocity and the magnitude of the superfluid friction parameters. Naturally, in increase in the normal fluid velocity results in an increase in the rate of propagation of a helical Kelvin wave along the x-axis. On the other hand, an increase in the superfluid friction parameters slows the propagation of such helical Kelvin waves. While these results are completely intuitive, an analysis of the nonlinear system (6.18)-(6.20) is needed to justify these conclusions for a filament in the LIA. Meanwhile, the effective frequency ($\omega(t)/t$) is not strongly influenced by the normal fluid velocity, nor is it strongly influenced by the superfluid friction parameters. This follows from the fact that the leading order term in the dispersion relation (6.19) does not depends on either α, α' or on U, and the only term involving U has the multiplication $\alpha'U$ so that any effects of U are small.
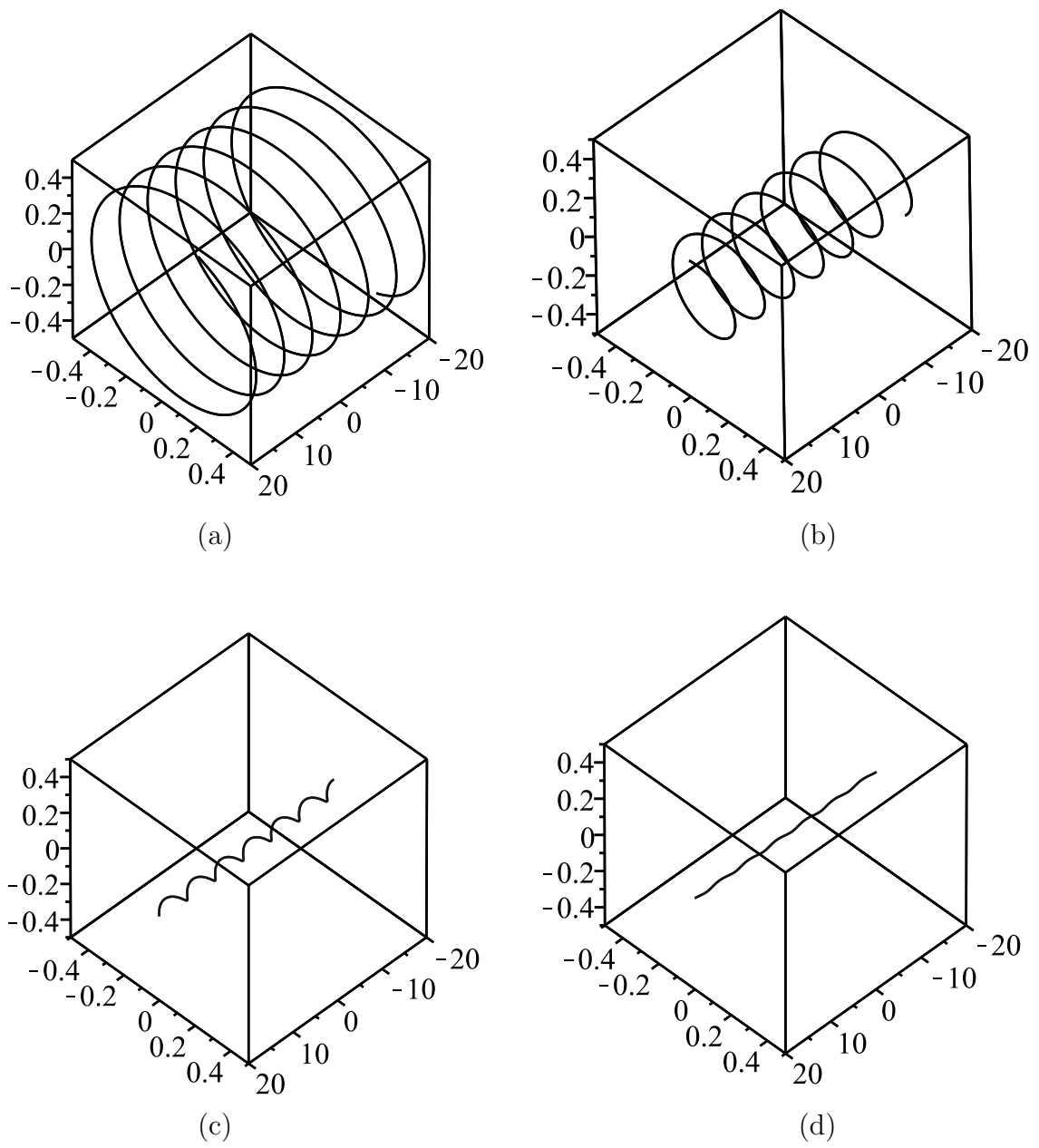
Figure 6.2: Plot of the time evolution of a helical filament solution corresponding to $A = 0.5$, $\gamma = 2$, $k = 1$, T=1K (i.e., $\alpha = 0.005$, $\alpha' = 0.003$) and $U = 0$. Times referenced are (a) $t = 0$, (b) $t = 100$, (c) $t = 300$, (d) $t = 500$.
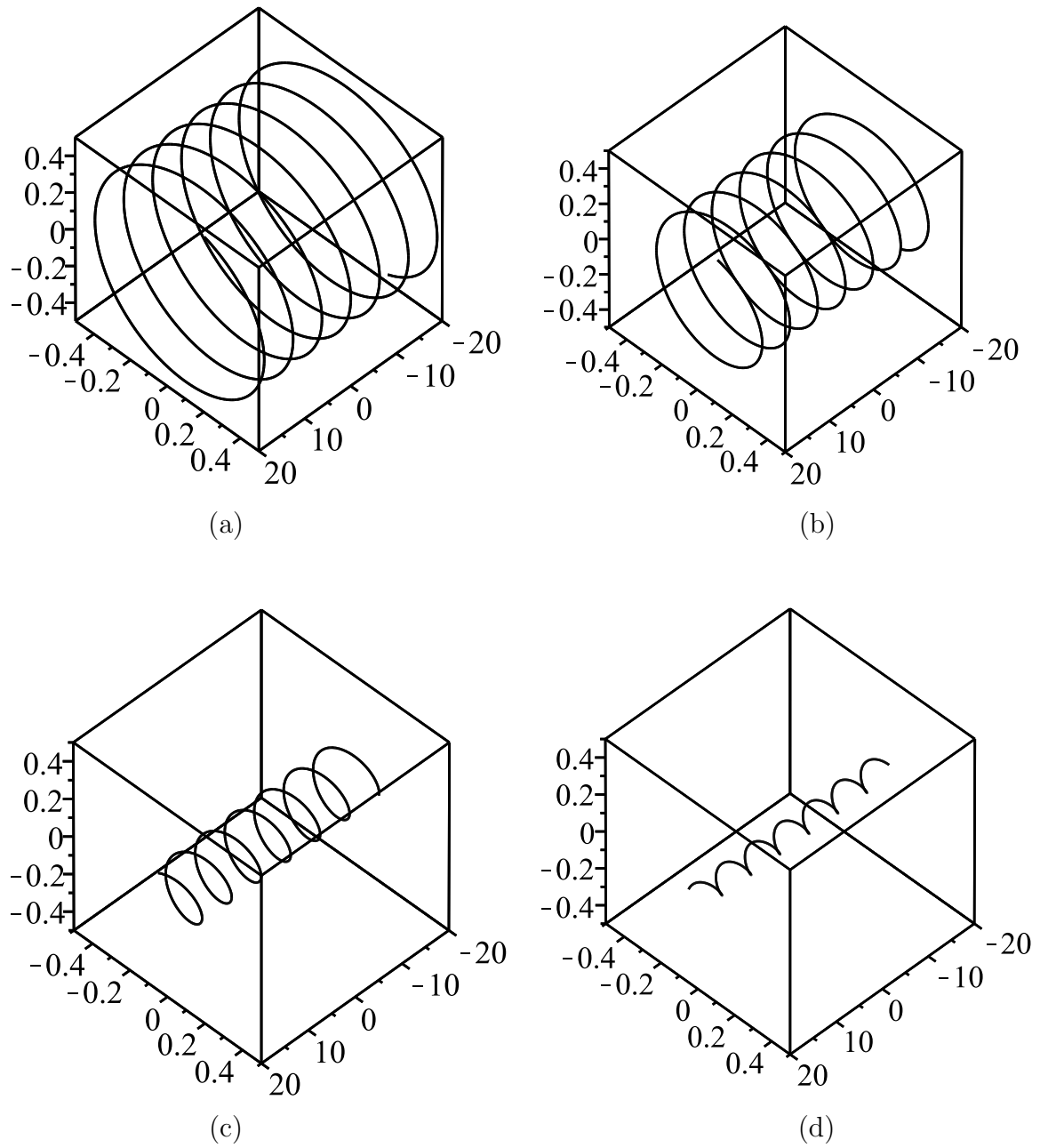
Figure 6.3: Plot of the time evolution of a helical filament solution corresponding to $A = 0.5$, $\gamma = 2$, $k = 1$, T=1K (i.e., $\alpha = 0.005$, $\alpha' = 0.003$) and $U = 1$. Times referenced are (a) $t = 0$, (b) $t = 100$, (c) $t = 300$, (d) $t = 500$. Note that the decay of the helical perturbations along the filament is markedly slower than in the case of $U = 0$ (which was considered in Fig. 6.2).

261
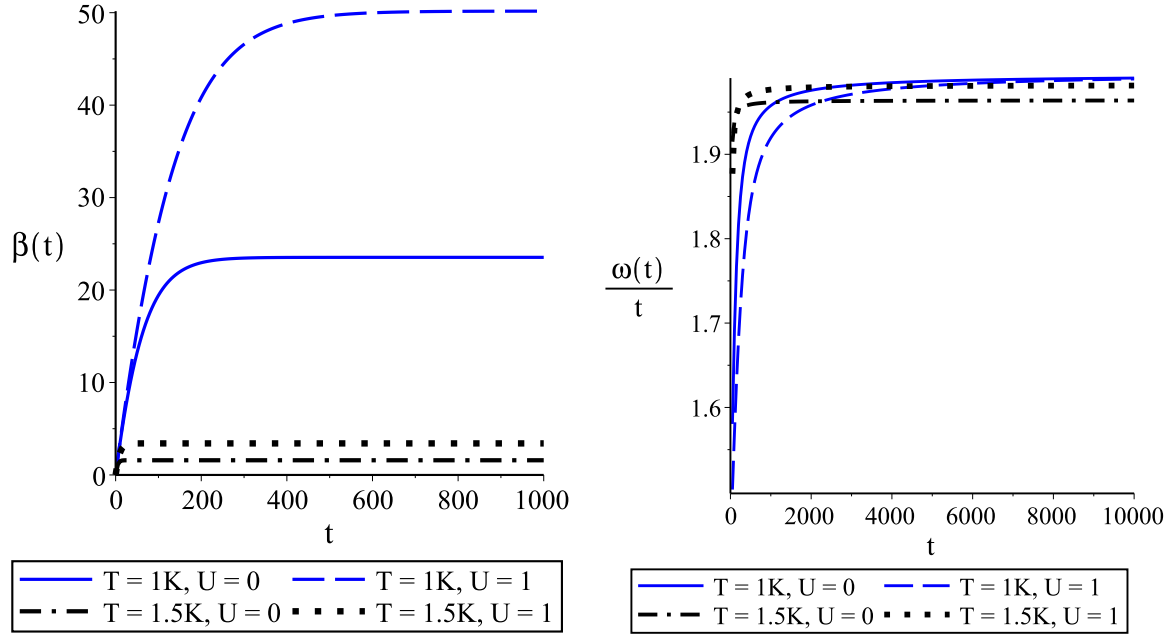
(a)

(b)

Figure 6.4: Plot of the (a) translation $\beta(t)$ of the x-coordiate (the translational motion of the helical waves along the filament) and (b) the effective frequency $\omega(t)/t$ for a helical filament solution corresponding to $A = 0.5$, $\gamma = 2$, $k = 1$, for various temperatures and normal fluid velocity. The temperature T $=$ 1K correspond to $\alpha = 0.005$, $\alpha' = 0.003$, while T $=$ 1.5K corresponds to $\alpha = 0.073$, $\alpha' = 0.018$.

6.1.7 Discussion

For the eternal solutions (which do not decay in time), there is a requirement that the wave number is fixed. In other words, for fixed values of the parameters A, γ, U there is a unique wave number $k = k^*$ given by (6.13) such that a constant-amplitude helical filament solution exists. This restriction in turn implies that the amplitude of such a helical filament must be bounded like $A < \gamma/|U|$. This still allows the amplitude to be large enough for the helix to exhibit translational motion in addition to pure rotation, as is evident from the solution form presented in (6.15). The dispersion relation is close to that obtained in Van Gorder [106], though the dispersion relation ω obtained here is exact, while that of Van Gorder [106] was approximate (since an approximate potential form of the quantum LIA was assumed).

For the solutions which are permitted to decay in time, some observations are in order. The rate of decay of the filament, $\mu(t)/t$, is not constant in time but rather varies according to (6.20). We see from the asymptotics of μ that the greatest rate of decay is for large time, so the helical perturbations along the filament decay slowly at first and more rapidly as time progresses. Since the translational effects are tied to the decay rate of the filament through a term of the form $\exp(-2\mu(t))$, the greatest translation of the filament occurs for small time, while translation of the filament ceases for asymptotically large time. This makes sense: as the helical filament decays into a line filament, translational effects diminish since there is no translation of a line filament. This is demonstrated in Fig. 6.4. Therefore, the Kelvin waves rotate and also move along the x-axis while decaying. The more

they decay in amplitude, the slower the motion along the x-axis. Meanwhile, the rotational motion persists, even as the waves decay.

In the case of constant-amplitude helical waves along a filament (i.e., eternal solutions), the wave number is fixed (at a value corresponding to the Donnelly-Glaberson instability), while when the helical filament is allowed to decay to a line filament we have no such restriction on the wave number. However, we do still have a restriction on the possible value of k which permit the filament to decay, $k/\sqrt{1 + A^2 k^2} > \frac{U}{\gamma}$. Rearranging this, we obtain a condition on A: $A < \sqrt{\frac{\gamma^2}{U^2} - \frac{1}{k^2}} < \frac{\gamma}{|U|}$. Therefore, the restriction on the amplitude is stronger when we permit the helical waves to decay. This is physically reasonable, as it is sensible to describe small-amplitude Kelvin waves along a vortex filament using LIA. For large-amplitude perturbations, non-local effects will influence the solutions, so the full Biot-Savart law under the HVBK model would be more reasonable for describing the filament dynamics.

6.2 Dynamics of a planar vortex filament under the quantum LIA

The Hasimoto planar vortex filament is one of the rare exact solutions to the classical local induction approximation (LIA). This solution persists in the absence of friction or other disturbances, and is hence rather idealized, as it maintains its form over time. As such, the

dynamics of such a filament have not been extended to more complicated physical situations. We consider the planar vortex filament under the quantum LIA, which accounts for superfluid friction and the velocity of a normal fluid impinging on the filament. We show that, for most interesting situations, a filament which is planar in the absence of friction and normal fluid at zero temperature will gradually deform due to friction effects and the normal fluid flow corresponding to warmer temperatures. The influence of friction is to induce torsion, so the filaments bend as they rotate. Furthermore, the flow of a normal fluid along the vortex filament length will have an amplifying effect on the initial planar perturbations of a line filament, reminiscent of the Donnelly - Glaberson instability seen in helical filament structures. For warmer temperatures, these effects increase in magnitude. A number of nice qualitative results are analytical in nature, and these results are verified numerically for physically interesting cases. The results on the deformed planar filaments present under the quantum LIA were considered in Van Gorder [113].

6.2.1 Background

While the planar filament has been studied under multiple models, for the quantum LIA such filaments have so far been approximated (numerically or analytically) under potential forms of the LIA (as discussed in Chapter 5). These are approximations to the LIA, valid under certain restrictions such as that deviations from a reference axis must remain small of be of sufficient bounded variation, and thus a more direct approach could be enlightening. In

particular, while such potential formulations are useful in some parameter regimes, there are often restrictions (such as on amplitude of any waves along a filament, on the wave number of solutions, and so on) that must be obeyed. In the present section, we work directly with the LIA, as opposed to any approximating potential form. While this means that the mathematics may not be as elegant, we benefit from having a precise representation of the solutions. We shall consider the quantum LIA directly in Cartesian coordinates, since this allows for easy visualization of the vortex filament solutions. Our goal in doing this is to determine both qualitative and quantitative effects of the superfluid friction parameters and the normal fluid velocity on the planar vortex filaments. In this way, we extend the planar filaments of Hasimoto valid under the classical LIA to a new type of filament under the quantum form of the LIA.

We review the planar filament in the classical fluid model, and attempt to extend such a solution to the quantum fluid model directly. A solution of this type is possible only when the normal fluid velocity varies in space and takes a particular form, meaning that such a solution is of narrow applicability. Next, we overcome such difficulties by defining a different type of filament, which happens to be planar at $\alpha, \alpha' = 0$ yet non-planar away from the origin when $\alpha, \alpha' > 0$. Such a solution is the true generalization of the planar filament for the quantum LIA, and indeed this solution allows us to study the dynamics of a planar filament in the quantum LIA. The influence of the normal fluid velocity and of the superfluid friction parameters on this family of solutions is discussed both through analytical approximation and numerical simulation. The results suggest that the friction parameters

266

result in a twisting of the filaments, while the normal fluid directed along the filament results in a type of amplification, reminiscent of the Donnelly - Glaberson instability [23, 36, 71] for helical filaments under the quantum LIA.

6.2.2 A purely planar vortex filament

The general form of a rotating planar vortex filament under LIA is given by

$$\mathbf{r}(x,t) = (x, \cos(\gamma t)\psi(x), -\sin(\gamma t)\psi) , \tag{6.44}$$

where ψ is some unknown function to be determined. Note that the solution lies on a plane which intersects the x-axis and rotates in time around the x-axis. We shall be most interested in a normal fluid velocity vector oriented along the vortex filament, $\mathbf{U} = (U, 0, 0)$, since this will often drive Kelvin waves along the filament.

Placing the solution representation (6.44) into the classical LIA (2.14), we find that

$$\gamma \kappa \mathbf{t} \times \mathbf{n} = \gamma(0, \sin(\gamma t), \cos(\gamma t)) \frac{\psi''}{(1 + \psi'^2)^{3/2}} \tag{6.45}$$

while

$$\mathbf{r}_t = \gamma(0, -\sin(\gamma t), -\cos(\gamma t))\psi ; \tag{6.46}$$

Therefore, (6.44) is a solution to the classical LIA provided that

$$\psi + \frac{\psi''}{(1 + \psi'^2)^{3/2}} = 0 . \tag{6.47}$$

If we carry out similar computations for the quantum LIA (2.12), and set all three components of the resulting vectors equal, we shall find

$$0 = -\alpha \frac{\psi'\psi''}{(1+\psi'^2)^2} + \alpha'V\frac{\psi'^2}{1+\psi'^2}\,, \tag{6.48}$$

$$\sin(\gamma t)\psi = -\sin(\gamma t)\left\{\frac{(1-\alpha')\psi''}{(1+\psi'^2)^{3/2}} - \frac{\alpha V\psi'}{(1+\psi'^2)^{1/2}}\right\} + \cos(\gamma t)\left\{\frac{\alpha\psi''}{(1+\psi'^2)^2} - \frac{\alpha'V\psi'}{1+\psi'^2}\right\}\,, \tag{6.49}$$

$$-\cos(\gamma t) = \cos(\gamma t)\left\{\frac{(1-\alpha')\psi''}{(1+\psi'^2)^{3/2}} - \frac{\alpha V\psi'}{(1+\psi'^2)^{1/2}}\right\} - \sin(\gamma t)\left\{\frac{\alpha\psi''}{(1+\psi'^2)^2} - \frac{\alpha'V\psi'}{1+\psi'^2}\right\}\,, \tag{6.50}$$

where $V = U/\gamma$. Each of these equations has a term of the form

$$\frac{\alpha\psi''}{(1+\psi'^2)^2} - \frac{\alpha'V\psi'}{1+\psi'^2}\,, \tag{6.51}$$

which vanishes in the $\alpha, \alpha' \to 0$ limit. Meanwhile, the analogue to (6.47) in the quantum case is apparently

$$\psi + \frac{(1-\alpha')\psi''}{(1+\psi'^2)^{3/2}} - \frac{\alpha V\psi'}{(1+\psi'^2)^{1/2}} = 0\,. \tag{6.52}$$

Let us assume that (6.51) holds equal to zero. This would then imply that (6.52) takes the form

$$\psi + \left(1 - \alpha' - \frac{\alpha^2}{\alpha'}\right)\frac{\psi''}{(1+\psi'^2)^{3/2}} = 0\,. \tag{6.53}$$

Let $\hat{\psi}(x)$ be a bounded and periodic solution of (6.47). Then, the scaling

$$\psi(x) = \sqrt{1 - \alpha' - \frac{\alpha^2}{\alpha'}}\,\hat{\psi}\left(\frac{x}{\sqrt{1 - \alpha' - \alpha^2/\alpha'}}\right) \tag{6.54}$$

is a solution of (6.53). This provides a nice link between the classical and quantum LIA solutions, and shows that a purely planar solution is possible, provided that the consistency

term (6.51) vanishes. That said, the consistency term (6.51) does not, in general vanish. To see why, note that a planar filament solution to (6.47) is periodic. On the other hand, let us rescale the coefficients in (6.51) to obtain the differential equation

$$h'' = h' + h'^3 \,. \tag{6.55}$$

After obtaining a first integral, we should have

$$h' = \pm \frac{1}{\sqrt{Ce^{-2x} - 1}} \,, \tag{6.56}$$

and therefore at some finite value of x, h should become singular. Since this incompatible with a planar solution, we conclude that (6.51) does not vanish when ψ is a bounded and periodic function as given in (6.54). Note that a solution (6.54) may still remain a very good approximation to a true filament solution. In this case, the consistency term should be sufficiently small. Indeed, the consistency term is of order α, whereas the solution (6.54) is determined by an equation of order unity.

There is a fix that allows us to obtain a solution (6.54) while also satisfying the consistency condition (6.51), but this involves picking the normal fluid velocity in a very specific way. In particular, if instead of considering a constant velocity for the normal fluid flow, we were to pick $\mathbf{U} = (U(x), 0, 0)$, then we can use (6.51) to determine conditions on such a function $U(x)$. Doing so, one finds

$$U(x) = \frac{\alpha}{\alpha'\gamma} \frac{\psi''}{\psi'(1 + \psi'^2)} \,. \tag{6.57}$$

While this is, of course, a rather narrow restriction on the form of $\mathbf{U}$, it does permit a very elegant solution (6.54).

As it turns out, a purely planar vortex filament moving without change in form is simply too specialized to exist in a superfluid under normal conditions (the exact solution we get when $U = U(x)$ takes a specific form is certainly not what one would call general in any sense). Rather, it makes more sense to consider a family of vortex filaments what generalize the planar filament in the sense that they reduce to the planar filament in the limit $\alpha, \alpha' = 0$. For $\alpha, \alpha' > 0$, such filaments would not be confined to a plane which rotates about the reference axis, but would rather exhibit planar behavior in a local sense, while exhibiting other behaviors asymptotically for large $|x|$. In a way, we could view such vortex filaments as deformations of the planar filaments, with the deformations do the the influence of both the superfluid friction parameters and the normal fluid velocity.

6.2.3 Deformation of a planar filament due to superfluid parameters

When attempting to construct a purely planar quantum generalization of the planar filament found in the classical LIA, it became clear that in most cases (for instance, when $\mathbf{U}$ is a constant vector) there are too few degrees of freedom if we assume that the time evolution of the vortex filament follows (6.44). In order to obtain the most useful generalization of the classical planar filament, we need to consider that the superfluid parameters can cause the filament to become non-planar in a variety of ways. Amplification or deamplification of waves along a quantum vortex filament is possible, while modified torsion due to the superfluid friction parameters is also an issue. To account for such effects, we propose a

solution of the form

$$\mathbf{r}(x,t) = (x, \cos(\gamma t)\phi(x) + \sin(\gamma t)\psi(x), \cos(\gamma t)\psi(x) - \sin(\gamma t)\phi(x)) \,. \tag{6.58}$$

Placing (6.58) in (2.12), we obtain the differential equations

$$\phi + \frac{(1-\alpha')\phi''}{(1+\phi'^2+\psi'^2)^{3/2}} + \frac{\alpha\psi''}{(1+\phi'^2+\psi'^2)^2} - \frac{\alpha V\phi'}{(1+\phi'^2+\psi'^2)^{1/2}}$$
$$- \frac{\alpha'V\psi'}{(1+\phi'^2+\psi'^2)} - \frac{\alpha\phi'(\psi'\phi''-\phi'\psi'')}{(1+\phi'^2+\psi'^2)^2} = 0 \,, \tag{6.59}$$

$$\psi + \frac{(1-\alpha')\psi''}{(1+\phi'^2+\psi'^2)^{3/2}} - \frac{\alpha\phi''}{(1+\phi'^2+\psi'^2)^2} - \frac{\alpha V\psi'}{(1+\phi'^2+\psi'^2)^{1/2}}$$
$$+ \frac{\alpha'V\phi'}{(1+\phi'^2+\psi'^2)} - \frac{\alpha\psi'(\psi'\phi''-\phi'\psi'')}{(1+\phi'^2+\psi'^2)^2} = 0 \,. \tag{6.60}$$

By including two unknown functions, we obtain two differential equations for two unknown functions, as opposed to two differential equations for one unknown function (as was the case for the purely planar filament). The motion of the filament (6.58) is not purely planar, though it contains the pure planar filament as a reduction (taking $\psi \to 0$ gives the pure planar filament).

Since we should have a planar filament when $\alpha, \alpha' \to 0$, we should take ϕ to be of order unity and ψ to be of order α. While a complete analytical analysis of (6.59)-(6.60) is not possible since the equations are too complicated, we can make some qualitative observations. If we assume $\psi = \alpha\Psi$ for some function Ψ of order unity, and we neglect order α^2 and higher terms, we should have

$$\phi + \frac{(1-\alpha)\phi''}{(1+\phi'^2)^{3/2}} - \frac{\alpha V\phi'}{(1+\phi'^2)^{1/2}} = 0 \,, \tag{6.61}$$

$$\Psi + \frac{(1-\alpha)\Psi''}{(1+\phi'^2)^{3/2}} - \frac{\alpha V\Psi'}{(1+\phi'^2)^{1/2}} = \frac{\phi''}{(1+\phi'^2)^2} - \frac{\alpha'V}{\alpha}\frac{\phi'}{1+\phi'^2} \,. \tag{6.62}$$

While simplified from (6.59)-(6.60), these equations are still too complicated to solve exactly, owing to the fact that (6.61) does not have a first integral for $\alpha \neq 0$. In the case where the amplitude A of a solution ϕ is sufficiently small, we should find

$$\phi(x) = A \cos\left(\frac{\sqrt{4(1-\alpha') - \alpha^2 V^2}}{2(1-\alpha')}x\right) \exp\left(\frac{\alpha V}{2(1-\alpha')}x\right) + O(A^3). \qquad (6.63)$$

For small A, the order A^3 corrections are negligible. Near the origin, the solutions maintain a planar appearance, since the exponential growth or decay rate is of order α. The solutions will amplify for either $x > 0$ or $x < 0$, depending on the sign of V. So, there is amplification driven by the normal fluid along the direction in which the normal fluid points. This is analogous to the Donnelly - Glaberson instability seen when a normal fluid flow is directed along a helical vortex filament.

In the case where $V = 0$, there is no amplification in the lowest-order term. However, as we shall see later, nonlinear terms will cause amplification for both large negative and large positive values of x. Such effects are only captured by considering higher order terms in A.

It is possible to exploit the symmetry of equations (6.59)-(6.60) to obtain a single complex equation. Defining $W = \phi + i\psi$, and adding i times (6.60) to (6.59), we obtain

$$\begin{aligned}
W &+ \frac{(1-\alpha')W''}{(1+|W'|^2)^{3/2}} - \frac{\alpha V W'}{(1+|W'|^2)^{1/2}} \\
&+ i\left\{\frac{\alpha' V W'}{1+|W'|^2} - \frac{\alpha W''}{(1+|W'|^2)^2} - \frac{\alpha}{2}\frac{W'(W'^*W'' - W'W''^*)}{(1+|W'|^2)^2}\right\} = 0.
\end{aligned} \qquad (6.64)$$

Here, * denotes complex conjugation. Note that (6.64) implies that (6.59)-(6.60) can be mapped to a three-dimensional real system, despite the fact that (6.59)-(6.60) is a four-

dimensional real dynamical system. This is due to a certain type of symmetry that exists in the equations (6.59)-(6.60) which is inherited from the LIA itself. To demonstrate this, let us consider the representation $W(x) = R(x)\exp(i\int_0^x \theta(\sigma)d\sigma)$, where R and θ are real-valued functions. Placing this representation into (6.64), and separating the resulting equation into real and imaginary parts, we obtain

$$R + \frac{(1-\alpha')(R''-R\theta^2)}{(1+R'^2+R^2\theta^2)^{3/2}} + \frac{\alpha(2R'\theta+R\theta')}{(1+R'^2+R^2\theta^2)^2} - \frac{\alpha V R'}{(1+R'^2+R^2\theta^2)^{1/2}}$$
$$- \frac{\alpha'V R\theta}{(1+R'^2+R^2\theta^2)} + \frac{\alpha R'[(2R'^2-RR'')\theta+R^2\theta^2+RR'\theta']}{(1+R'^2+R^2\theta^2)^2} = 0\,,$$
(6.65)

$$\frac{(1-\alpha')(2R'\theta+R\theta')}{(1+R'^2+R^2\theta^2)^{3/2}} - \frac{\alpha(R''-R\theta^2)}{(1+R'^2+R^2\theta^2)^2} - \frac{\alpha V R\theta}{(1+R'^2+R^2\theta^2)^{1/2}}$$
$$+ \frac{\alpha'V R'}{(1+R'^2+R^2\theta^2)} + \frac{\alpha R\theta[(2R'^2-RR'')\theta+R^2\theta^2+RR'\theta']}{(1+R'^2+R^2\theta^2)^2} = 0\,.$$
(6.66)

Equations (6.65)-(6.66) constitute a three-dimensional dynamical system. This system can be solved provided that it is non-degenerate. Writing the system in the form

$$[(1-\alpha')\sqrt{1+R'^2+R^2\theta^2} - \alpha RR'\theta]R'' + \alpha R(1+R'^2)\theta = F_1(R,R',\theta)\,, \tag{6.67}$$

$$-\alpha(1+R^2\theta^2)R'' + [(1-\alpha')R\sqrt{1+R'^2+R^2\theta^2} - \alpha R^2 R'\theta]\theta' = F_2(R,R',\theta)\,, \tag{6.68}$$

for appropriately defined F_1 and F_2. The determinant of the Jacobian of the left hand side of (6.67)-(6.68) must not vanish, which is equivalent to the condition

$$(\alpha R^2 R'\theta + (1-\alpha'))\sqrt{1+R'^2+R^2\theta^2} - R[\alpha R'\theta + (\alpha'-\alpha'^2-\alpha^2)(1+R'^2+R^2\theta^2)] \neq 0\,. \tag{6.69}$$

In the limit $\alpha, \alpha' \to 0$, this condition becomes

$$\sqrt{1+R'^2+R^2\theta^2} \neq 0\,, \tag{6.70}$$

which is always true. Therefore, given small enough α and α', the system (6.65)-(6.66) is non-degenerate, and a solution does exist.

Equations (6.65)-(6.66) are no simpler to study than (6.59)-(6.60). However, let us assume that any deviations from the reference axis are small, so that $|R| \leq \epsilon << 1$. Let us also define the function $\xi(x) = R'(x)/R(x)$, which itself should be of order unity. Then, neglecting terms of order ϵ^2 and higher, equations (6.65)-(6.66) are reduced to

$$1 + (1 - \alpha')(\xi' + \xi^2 - \theta^2) + \alpha(2\xi\theta + \theta') - \alpha V\xi - \alpha'V\theta = 0, \tag{6.71}$$

and

$$(1 - \alpha')(2\xi\theta + \theta') - \alpha(\xi' + \xi^2 - \theta^2) - \alpha V\theta + \alpha'V\xi = 0, \tag{6.72}$$

respectively. To study the qualitative effects of the remaining nonlinearity, we set $V = 0$, which is physically relevant in the low-temperature limit and also in the case of superfluid Helium 3. We obtain

$$\beta + 2\xi\theta + \theta' = 0, \tag{6.73}$$

$$\beta' + \xi' + \xi^2 - \theta^2 = 0, \tag{6.74}$$

where

$$\beta = \frac{\alpha}{\alpha^2 + (1 - \alpha')^2} \quad \text{and} \quad \beta' = \frac{1 - \alpha'}{\alpha^2 + (1 - \alpha')^2}. \tag{6.75}$$

This system admits two equilibrium points when $\beta > 0$: $(\xi^*, \theta^*) = (-\beta/(2\nu), \nu)$ and $(\xi^*, \theta^*) = (\beta/(2\nu), -\nu)$, where

$$\nu = \sqrt{\frac{\beta' + \sqrt{\beta'^2 + \beta^2}}{2}}. \tag{6.76}$$

A linear stability analysis shows that the equilibrium $(-\beta/(2\nu), \nu)$ is unstable, whereas $(\beta/(2\nu), -\nu)$ is linearly stable. Eigenvalues of the Jacobian for system (6.73)-(6.74) take the form $\lambda_\pm = \frac{\beta}{\theta^*} \pm 2i\theta^*$, so the stable solutions should spiral inward toward the equilibrium, while the unstable solutions should spiral outward from the equilibrium, in the (ξ, θ) phase space. If we consider the time reversal (more accurately, "space-reversal" since ξ and θ depend on space variable x), the equilibrium points switch stability properties. This suggests that on one half of the x-axis, the perturbations along the vortex filament decay, whereas for the opposite half of the x-axis such perturbations amplify. Therefore, the amplification of planar perturbations along the vortex filament is possible even without the normal fluid velocity.

From the analysis above, we draw several conclusions about the deformation of a planar vortex filament in the quantum form of the LIA. First, the effect of V, the scaled normal fluid velocity, is to amplify the planar wave along the direction which the normal fluid velocity vector is pointing. The rate of amplification is moderated by the friction parameter α, which is small. The smaller the parameter α, the slower the amplification (in the perturbative limit). Amplification is still possible when $V = 0$. The inclusion of superfluid friction parameters results in a non-trivial phase term, θ. This feature implies that there are torsion effects not present in the classical planar filament. If the initial condition is $\theta(0) = 0$, then such effects are small near the origin, but can become large for large values of $|x|$. These are all behaviors that are absent in the classical planar filament, but which are suggested by the mathematics above in the case of a quantum planar filament.

In order to verify some of the behaviors suggested by the analytics above, we turn to numerical solutions. Since (6.65)-(6.66) are non-degenerate and are equivalent to (6.59)-(6.60), a solution pair $(\phi(x), \psi(x))$ exists (at least locally) for reasonable values of α, α' and V. We find that the standard RKF45 method is sufficient to numerically approximate the solutions of (6.59)-(6.60) to a desirable accuracy. When $\psi(x) \equiv 0$, we obtain the classical planar vortex filament solution. Therefore, the initial condition $\psi(0) = 0$ makes sense. We take $\phi(0) > 0$ to be the distance of the planar filament from the reference axis at the origin. Conditions $\phi'(0) = \psi'(0) = 0$ are not required, but they enforce a nice local symmetry at the origin.

In Fig. 6.5, we consider the planar filament in the T = 1K case in the presence of a normal fluid velocity directed along the positive x-axis, while in Fig. 6.6 we do the same for the T = 1.5K case. Amplification of waves along the line filament occur much more rapidly when temperature increases, since α increases and hence the combined effect αV increases - resulting in more exponential growth.

The numerical simulations suggest that the planar filaments do amplify due to the normal fluid flow, and that the direction of the normal fluid flow along the filament determines where this amplification takes place. This is shown nicely when comparing Figs. 6.6 and 6.7, which model the same situation only with the direction of **U** reversed. Numerical results also show that the greater the speed of the normal fluid, the greater the amplification. Both the direction and rate of amplification (as a function of temperature and normal fluid velocity) are in agreement with the qualitative analysis performed above. In particular, this

is in complete agreement with what was suggested by the analytical approximation in the small-amplitude limit, (6.63).

The rate of amplification is greater when α is larger, hence the planar filaments amplify more rapidly in warmer temperatures. In the case where $V = 0$, the amplification occurs in a symmetric way for both large negative and large positive x, as seen in Fig. 6.8. Thus, amplification can occur due to frictional effects, since the model is nonlinear. In cases where $V \approx 0$ is still physically relevant, such as the low temperature limit or for superfluid Helium 3, this implies that amplification can still occur. Such amplification in the absence of a driving normal fluid velocity agrees with what was suggested by the reduction to polar coordinates in the approximate equations (6.73)-(6.74).

Near the origin, the solutions all appear planar in form. However, for larger values of $|x|$, the solutions undergo torsion effects due to the interaction with the fluid modeled by the superfluid friction parameters, α and α'. This is best seen when we compare a true planar filament solution to the classical LIA ($\alpha, \alpha' = 0$) with one of the quantum vortex filaments. We do this in Fig 6.9, where we see that close to the origin the two filaments agree, whereas as one gets further from the origin, the effects of the superfluid friction parameters result in a bending of the rotating filament, while the influence of the normal fluid velocity causes an amplification or de-amplification. For negative x, the quantum filament eventually takes on a helical form, which contrasts with the planar form of the classical filament. For positive x, the quantum filament undergoes strong amplification.
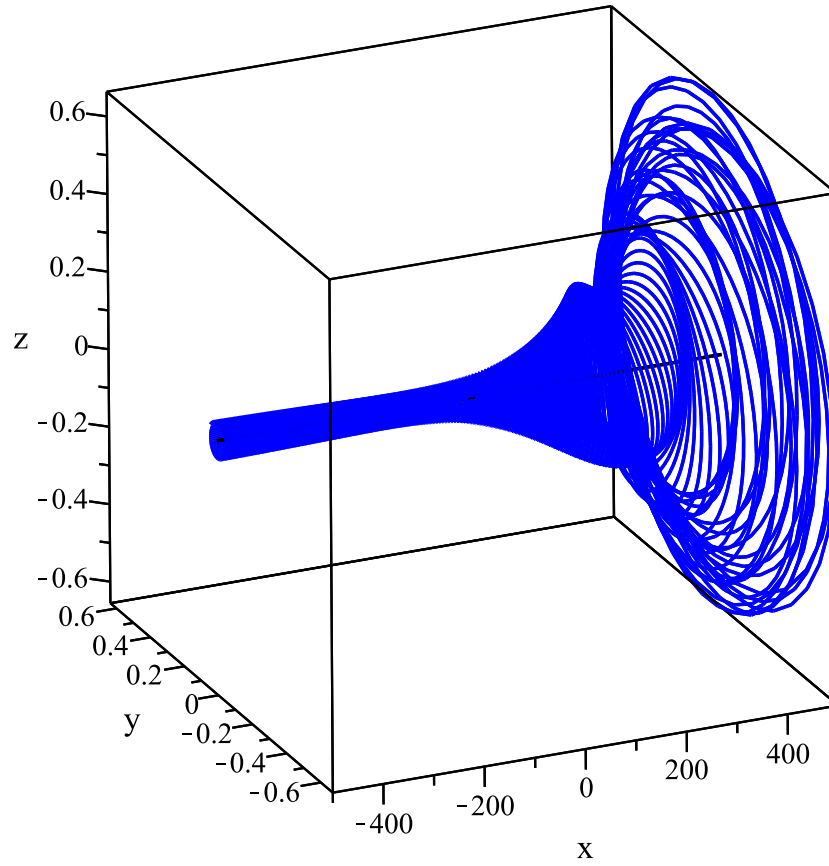
Figure 6.5: Plot of the deformed planar filament described by (6.58) when the temperature of the superfluid is T=1K ($\alpha = 0.005$, $\alpha' = 0.003$) and $V = 1$. The filament is given by numerically solving (6.59)-(6.60) subject to $\phi(0) = 0.1$, $\psi(0) = 0$, $\phi'(0) = 0$, $\psi'(0) = 0$.
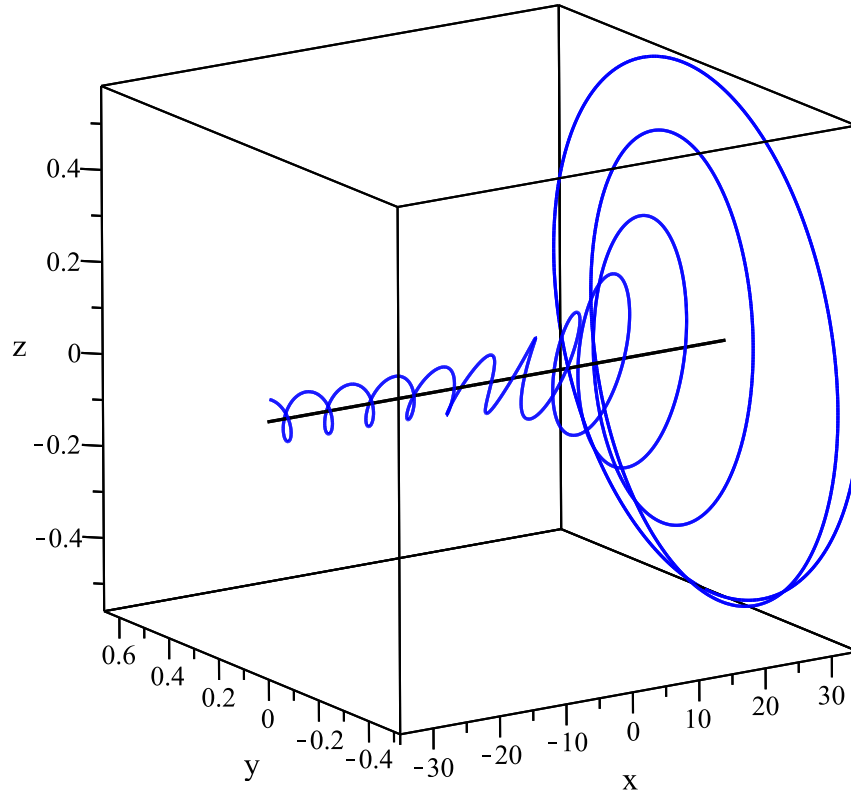
Figure 6.6: Plot of the deformed planar filament described by (6.58) when the temperature of the superfluid is T=1.5K ($\alpha = 0.073$, $\alpha' = 0.018$) and $V = 1$. The filament is given by numerically solving (6.59)-(6.60) subject to $\phi(0) = 0.1$, $\psi(0) = 0$, $\phi'(0) = 0$, $\psi'(0) = 0$.
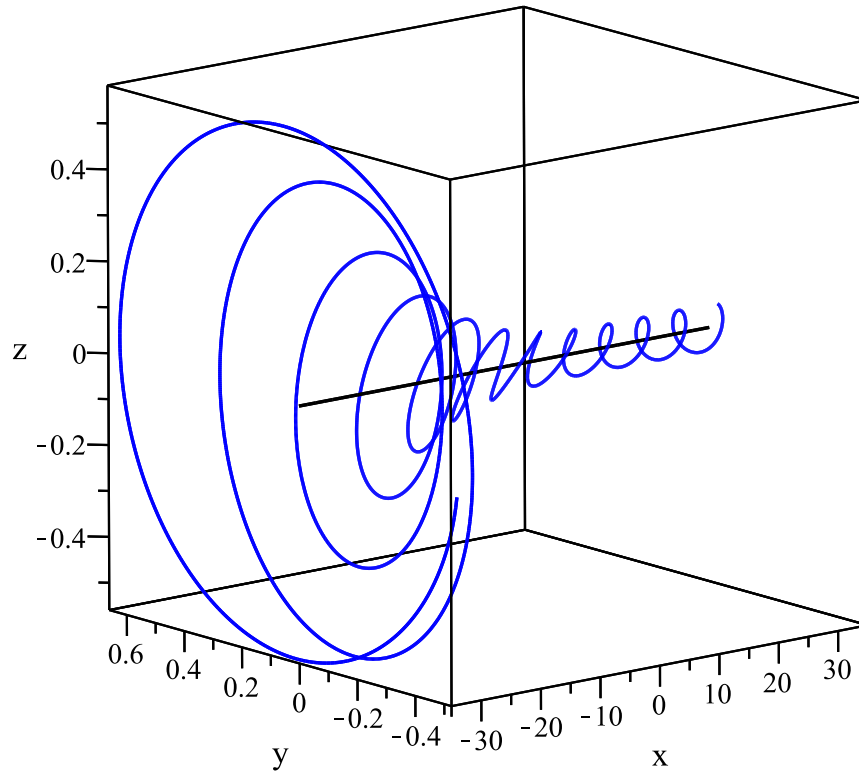
Figure 6.7: Plot of the deformed planar filament described by (6.58) when the temperature of the superfluid is T=1.5K ($\alpha = 0.073$, $\alpha' = 0.018$) and $V = -1$. The filament is given by numerically solving (6.59)-(6.60) subject to $\phi(0) = 0.1$, $\psi(0) = 0$, $\phi'(0) = 0$, $\psi'(0) = 0$.
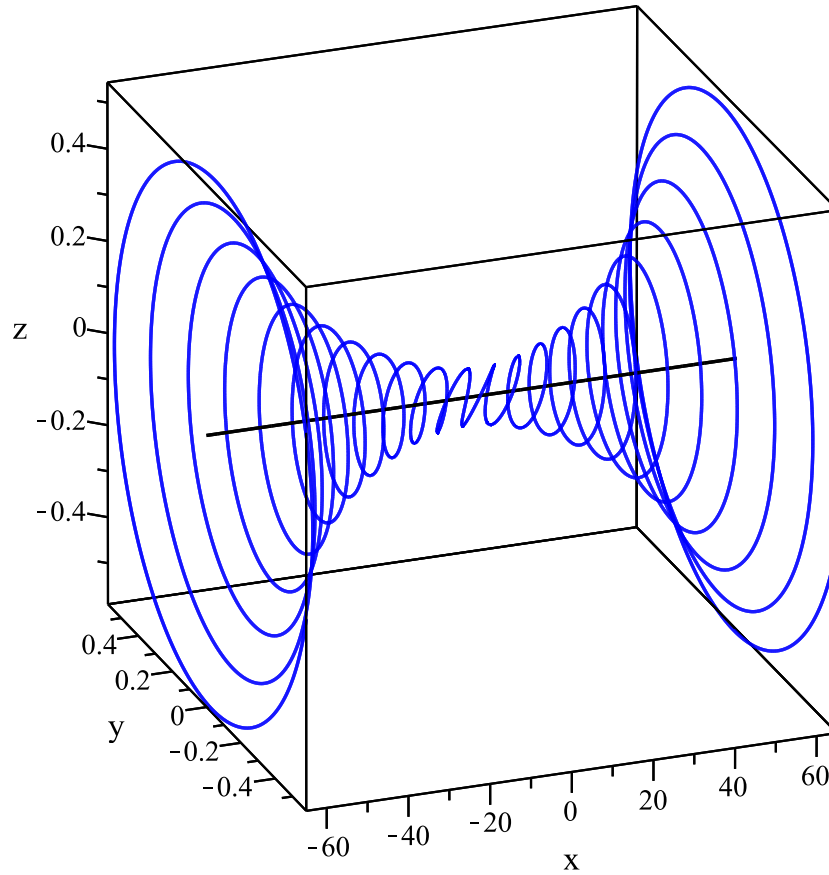
Figure 6.8: Plot of the deformed planar filament described by (6.58) when the temperature of the superfluid is T=1.5K ($\alpha = 0.073$, $\alpha' = 0.018$) and $V = 0$. The filament is given by numerically solving (6.59)-(6.60) subject to $\phi(0) = 0.1$, $\psi(0) = 0$, $\phi'(0) = 0$, $\psi'(0) = 0$.

281
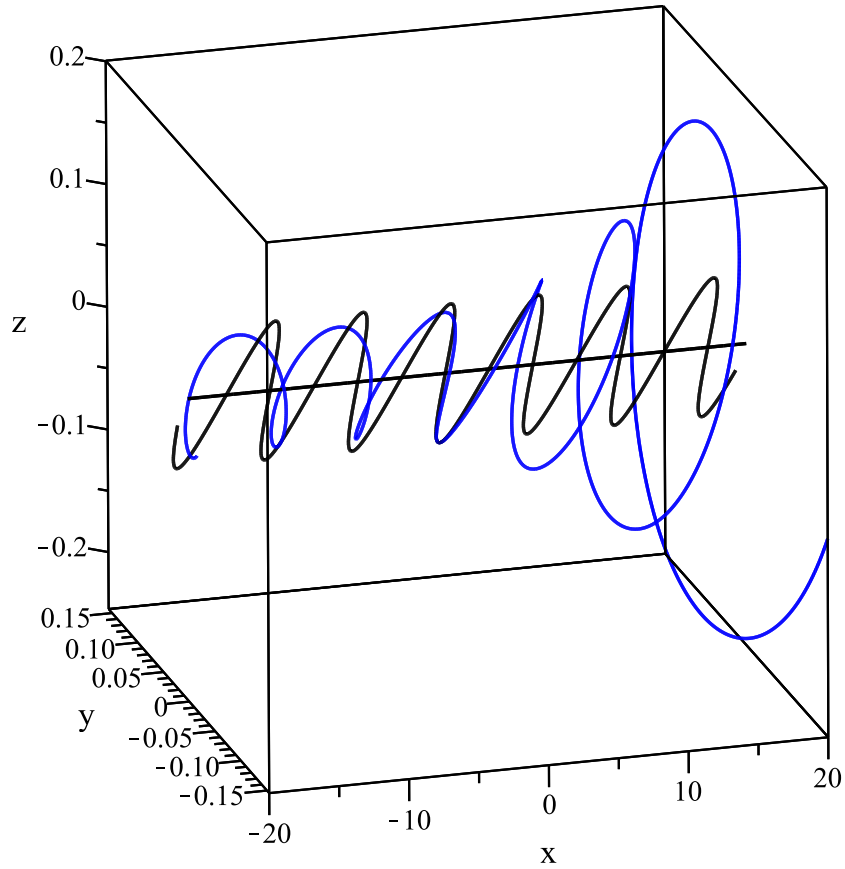
Figure 6.9: Comparison of the deformed planar filament described by (6.58) when the temperature of the superfluid is T=1.5K ($\alpha = 0.073$, $\alpha' = 0.018$) and $V = 1$, along with the classical planar filament corresponding to $\alpha = \alpha' = 0$. In both cases, the filaments are given by numerically solving (6.59)-(6.60) subject to $\phi(0) = 0.1$, $\psi(0) = 0$, $\phi'(0) = 0$, $\psi'(0) = 0$. The blue curve represents the T=1.5 deformed planar filament, while the black curve represents the classical planar filament.

6.2.4 Discussion

In summary, the quantum planar vortex filament differs from the well-known classical planar vortex filament in some important qualitative respects. First, there is an amplification of the planar perturbations of the quantum filament along the axis of orientation. This is caused by the normal fluid velocity directed along the filament. Next, while the classical planar filament maintained its form, the extension to the quantum model results in a filament that undergoes torsion effects due to the superfluid friction parameters. This causes a bending of the once planar filament the farther removed from $x = 0$ we look. On the de-amplified end of the filament, this results in an almost helical appearance for the filament. On the amplified end of the filament, an interesting pattern is formed that exhibits regularity but is not as uniform as a helical structure.

While a thermal study is beyond the scope of the results considered here, it makes sense to consider α and α' as functions of time, so that we can consider the qualitative effect of warming a superfluid which houses a planar filament, since an increase in such parameters would correspond to a warming of the superfluid. In the case where both friction parameters are zero, the classical planar filament solution is valid. If such a filament exists at temperature T$\approx$ 0K, then as the superfluid is warmed, we qualitatively expect that the filament will deform as follows. There will be a minor amplification / de-amplification of the filament along / against the direction of the normal fluid. This amplification will become more drastic as the superfluid continues to warm. While this occurs, the amplifying and de-

283

amplifying parts of the filament gradually bend as the effects of friction increase, meaning that the filament no longer exists within a plane rotating about the reference axis. As such, the filament is no longer planar.

What these results suggest is that a planar vortex filament structure in a superfluid should be a localized structure, in contrast to the classical fluid case, where such a filament maintains its form globally. Due to the effect of superfluid friction parameters and the normal fluid velocity, we see that on one side of the reference axis, the filament takes on a helical form far enough away from $x = 0$, whereas on the opposite side of the reference axis the filament undergoes strong amplification. Near $x = 0$, however, the solution maintains a planar form, even for larger values of the superfluid friction parameters or the normal fluid velocity. From this, localized planar structures can exist in a superfluid, even if such structures are no longer global like in the classical LIA.

In the case of helical Kelvin waves on a quantum vortex filament, it is known that waves of constant amplitude correspond to the critical wave number for Donnelly - Glaberson instability. If these solutions are perturbed, they will either decay to line filaments or they will amplify and blow-up. This instability is driven by the normal fluid flow along the reference axis of the vortex filament, which results in an amplification of the Kelvin waves if the amplitude is large enough at the initial time. This behavior is global, in that the decay or blow-up occurs along the entire helical filament. In the case of the deformed planar filament, a similar phenomenon to the Donnelly - Glaberson instability is seen, where the normal fluid velocity directed along the vortex filament results in amplification of the perturbations along

the line filament. However, unlike in the case of the helical perturbations, the amplification of the planar filament is local in nature, with a strong dependence on the direction of the normal fluid velocity. While the helical Kelvin waves amplify or decay uniformly for all x depending on the model parameters, the decay or amplification of the deformed planar filament is non-uniform in x.

With regards to physical experiments, the section of the filament which undergoes strong amplification may break down or dissipate, leaving a vortex filament line on half of the spatial domain. This half of the filament will be planar near $x = 0$, and helical as one moves away from the origin, in the direction of the x-axis on which the filament persists. Such a vortex filament is shown in Fig. 6.10. In this way, the planar segment of the filament may persist in time, although other sections of the filament may dissipate. This strong local behavior is in contrast to the more uniform behavior of a helical filament, which will either decay to a line filament or continue to amplify (leading to dissipation).

In the case where the amplification of the deformed planar filament is strong (i.e., the warmer superfluid case), non-local effects will likely play a considerable role in the time evolution of the vortex filament. Therefore, while the amplification under LIA is continuous in the direction of the normal fluid flow, realistically any tendency for the amplitude to grow without bound would likely be mitigated by non-local effects once the amplitude was large enough. So, while amplification is still expected along the lines shown here, any amplification is expected to be bounded for the HVBK model which includes non-local effects through the Biot-Savart integral term. This in turn implies that the results obtained here under

285

LIA would be expected to agree with experiments qualitatively, while specific quantitative details for any specific physical parameters would require these non-local effects, particularly in the case where deviations from the reference axis are large (as occurs in locations where the planar filaments amplify). The first step in studying the non-local effects would be to consider whether planar vortex filament exists under the full Biot-Savart dynamics, which is what the classical LIA approximates.
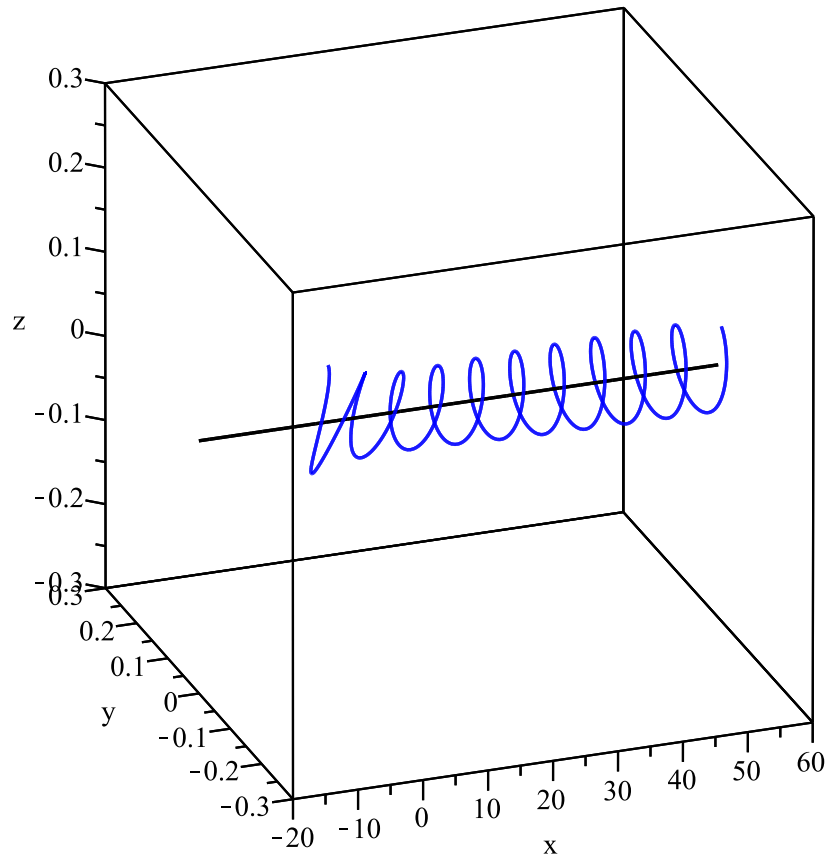
Figure 6.10: Large-time plot of the deformed planar filament described by (6.58) when the temperature of the superfluid is T=1.5K, with the same conditions given in Fig. 6.7. Segments of the filament which continue to amplify are removed, to show what might be expected experimentally after such segments dissipate or disassociate with the rest of the filament. The filament is locally planar near $x = 0$, while for large x the filament takes on a helical appearance.

6.3 Solitons and other waves on a quantum vortex filament

The quantum form of the local induction approximation (LIA, a model approximating the motion of a thin vortex filament in superfluid) including superfluid friction effects is put into correspondence with a type of cubic complex Ginsburg-Landau equation, in a manner analogous to the Hasimoto map taking the classical LIA into the cubic nonlinear Schrödinger equation. From this formulation, we determine the form and behavior of Stokes waves, 1-solitons, and other traveling wave solutions under normal and binormal friction. The most important of these solutions is the soliton on a quantum vortex filament, which is a natural generalization of the 1-soliton solution constructed mathematically by Hasimoto which motivated subsequent real-world experiments. We also conjecture on the possibility of chaos in such systems, and on the existence more complicated solitons such as breathers. The various types of solutions obtained in this section were reported in Van Gorder [114].

6.3.1 Background

A number of studies exist on the solutions to the quantum LIA. In the $\alpha, \alpha' \to 0$ limit, these solutions should collapse into solutions of the classical LIA. One highly important class of solutions to the classical LIA would be the 1-soliton solution found by Hasimoto (and mentioned in Chapter 2), by way of what is now referred to as the Hasimoto transformation, which puts the classical LIA into correspondence with the cubic NLS. While a number

of solutions to the quantum LIA have been studied either numerically or analytically, the Hasimoto 1-soliton have never been extended to the quantum LIA. The purpose of this section is to fill this important gap. Applying a method analogous to that of Hasimoto, we are able to put the quantum LIA (2.12) into correspondence with a type of complex Ginzburg-Landau equation (a natural complex-coefficient generalization of NLS). From this, we study Stokes waves, 1-solitons, and other traveling wave solutions. Each of these solutions generalizes known results for the classical LIA. We also conjecture on the possibility of chaos in such systems.

6.3.2   A map from the quantum LIA into a cubic complex Ginsburg-Landau equation

Differentiating with respect to the arclength variable s, and performing several vector manipulations, we have that the quantum LIA (2.12) becomes

$$
\begin{aligned}
\dot{\mathbf{t}} &= \frac{\partial}{\partial s} \left\{ (1 - \alpha'|\mathbf{t}|^2)\mathbf{t} \times \mathbf{t}_s - \alpha[(\mathbf{t} \cdot \mathbf{t}_s)\mathbf{t} - |\mathbf{t}|^2 \mathbf{t}_s] \right\} \\
&+ \frac{\partial}{\partial s} \left\{ \alpha \mathbf{t} \times \mathbf{U} - \alpha'\mathbf{t} \times (\mathbf{t} \times \mathbf{U}) \right\}.
\end{aligned}
\tag{6.77}
$$

Taking $\mathbf{t}$ to be a unit vector, the equation simplifies slightly to

$$
\dot{\mathbf{t}} = \frac{\partial}{\partial s} \left\{ (1 - \alpha')\mathbf{t} \times \mathbf{t}_s + \alpha \mathbf{t}_s + \alpha \mathbf{t} \times \mathbf{U} - \alpha'(\mathbf{t} \cdot \mathbf{U})\mathbf{t} \right\}.
\tag{6.78}
$$

This puts the quantum LIA (2.12) into the form of a vector conservation law.

In what follows, we shall take $\mathbf{U} = \mathbf{0}$, for brevity of the calculations. Many studies on specific structures in the quantum LIA model have taken the normal fluid velocity to zero,

as it permits one to study such structures without the influence of drift or other distorting effects on the filaments[5, 3, 117]. The physical applicability of such a scenario is limited to the very low temperature regime in superfluid Helium 4. On the other hand, in the case of superfluid Helium 3, the normal fluid velocity $\mathbf{U}$ is zero (because Helium 3 is very viscous, unlike Helium 4, so it is always at rest or in solid body rotation, but α and α' are not zero [31]). Similar results were recently attempted in the case of $\mathbf{U} \neq \mathbf{0}$ [86], however the system was not solved and only the limiting reduction to $\alpha, \alpha' = 0$ was given. Some qualitative observations were also given at lowest order.

Let $\mathbf{b}$ denote the binormal vector, and take κ and τ to be the curvature and torsion, respectively. Recall that $\mathbf{t}_s = \kappa\mathbf{n}$, $\mathbf{n}_s = -\kappa\mathbf{t} + \tau\mathbf{b}$, $\mathbf{b}_s = -\tau\mathbf{n}$. After setting $\mathbf{U} = \mathbf{0}$, we can write (6.78) as $\dot{\mathbf{t}} = (1 - \alpha')(\kappa\mathbf{b})_s + \alpha\mathbf{t}_{ss}$.

Let us define the function $\psi(s,t) = \kappa(s,t)\exp(i\int_0^s \tau(\hat{s},t)d\hat{s})$ and also a new vector-valued function by $\mathbf{m} = (\mathbf{n}+i\mathbf{b})\exp(i\int_0^s \tau(\hat{s},t)d\hat{s})$. Note that $\mathbf{m}_s = -\psi\mathbf{t}$ and $\mathbf{t}_s = \frac{1}{2}(\psi^*\mathbf{m}+\psi\mathbf{m}^*)$, where * denotes complex conjugation. Additionally, $(\kappa\mathbf{b})_s = \frac{i}{2}(\psi_s\mathbf{m}^* - \psi_s^*\mathbf{m})$. The quantum LIA (6.78) therefore takes the form

$$\dot{\mathbf{t}} = \frac{i}{2}(1 - \alpha')(\psi_s\mathbf{m}^* - \psi_s^*\mathbf{m}) + \frac{\alpha}{2}(\psi^*\mathbf{m} + \psi\mathbf{m}^*)_s. \tag{6.79}$$

We seek to derive an equation for ψ in analogy to that which was obtained by Hasimoto in the case of a standard fluid (i.e., $\alpha = \alpha' = 0$). On the one hand, note that

$$
\begin{aligned}
\dot{\mathbf{m}}_s &= -\dot{\psi}\mathbf{t} - \psi\dot{\mathbf{t}} \\
&= -(\dot{\psi} + \alpha|\psi|^2\psi)\mathbf{t} + \frac{i(1-\alpha') - \alpha}{2}\psi\psi_s^*\mathbf{m} \\
&\quad - \frac{i(1-\alpha') + \alpha}{2}\psi\psi_s\mathbf{m}^* \,.
\end{aligned}
\tag{6.80}
$$

On the other hand, assume that we have a representation for $\dot{\mathbf{m}}$ of the form

$$
\dot{\mathbf{m}} = a\mathbf{m} + b\mathbf{m}^* + c\mathbf{t} \,.
\tag{6.81}
$$

First, observe that

$$
a + a^* = \frac{1}{2}(\dot{\mathbf{m}} \cdot \mathbf{m}^* + \dot{\mathbf{m}}^* \cdot \mathbf{m}) = \frac{1}{2}\frac{\partial}{\partial t}(\mathbf{m} \cdot \mathbf{m}^*) = 0 \,,
\tag{6.82}
$$

therefore a must take the form $a = i\phi(s, t)$, for some real-valued function ϕ. By a similar process, $b \equiv 0$. We should also find that

$$
c = -\mathbf{m} \cdot \dot{\mathbf{t}} = -(i(1-\alpha') + \alpha)\psi_s \,.
\tag{6.83}
$$

Therefore, we have the representation

$$
\dot{\mathbf{m}} = i\phi(s, t)\mathbf{m} - (i(1-\alpha') + \alpha)\psi_s(s, t)\mathbf{t} \,.
\tag{6.84}
$$

Differentiation of this representation with respect to arclength gives

$$
\begin{aligned}
\dot{\mathbf{m}}_s &= i\phi_s\mathbf{m} - i\phi\psi\mathbf{t} - (i(1-\alpha') + \alpha)\psi_{ss}\mathbf{t} \\
&\quad - \frac{1}{2}(i(1-\alpha') + \alpha)\psi_s(\psi^*\mathbf{m} + \psi\mathbf{m}^*) \,.
\end{aligned}
\tag{6.85}
$$

Clearly, the coefficients of $\mathbf{t}$, $\mathbf{m}$ and $\mathbf{m}^*$ in equations (6.80) and (6.85) should match exactly. The $\mathbf{m}^*$ coefficients already match exactly. Setting the $\mathbf{m}$ coefficients equal, we obtain

$$\phi_s = \frac{1-\alpha'}{2}\frac{\partial}{\partial s}|\psi|^2 - \frac{\alpha i}{2}(\psi^*\psi_s - \psi\psi_s^*)\,, \tag{6.86}$$

hence

$$\begin{aligned}\phi(s,t) &= \frac{1-\alpha'}{2}|\psi|^2 + \alpha(\mathrm{Re}(\psi))(\mathrm{Im}(\psi)) + A(t)\\ &= \frac{1-\alpha'}{2}|\psi|^2 - \frac{i\alpha}{4}(\psi^2 - \psi^{*2}) + A(t)\,,\end{aligned} \tag{6.87}$$

where $A(t)$ is an arbitrary function of time. Despite the appearance of i, this representation is real-valued, since $\psi^2 - \psi^{*2}$ is purely imaginary. Matching the coefficients of $\mathbf{t}$, we obtain

$$\dot{\psi} + \alpha|\psi|^2\psi = i\phi\psi + (i(1-\alpha') + \alpha)\psi_{ss}\,. \tag{6.88}$$

Using (6.87), we obtain an evolution equation for the function ψ:

$$\begin{aligned}\dot{\psi} &= iA(t)\psi + (i(1-\alpha') + \alpha)\psi_{ss}\\ &+ \left(\frac{i(1-\alpha')}{2} - \alpha\right)|\psi|^2\psi + \frac{\alpha}{4}(\psi^2 - \psi^{*2})\psi\,.\end{aligned} \tag{6.89}$$

Evidently, for the solutions we take interest in, the term $\psi^2 - \psi^{*2}$ will be small (negligible), so we remove it. This term would need to be considered in the the case of higher-order perturbations to the system (at order α^2). Making this reasonable reduction, we obtain

$$\dot{\psi} = iA(t)\psi + (i(1-\alpha') + \alpha)\psi_{ss} + \left(\frac{i(1-\alpha')}{2} - \alpha\right)|\psi|^2\psi\,. \tag{6.90}$$

Under an appropriate scaling of time ($T = (1-\alpha')t$) and by defining a function Ψ such that $\psi(s,t) = \sqrt{2}\Psi(s,T)\exp(i\int_0^t A(\hat{t})d\hat{t})$, we can reduce (6.90) into

$$\Psi_T = (i + \epsilon)\Psi_{ss} + (i - 2\epsilon)|\Psi|^2\Psi\,, \tag{6.91}$$

where $\epsilon = \alpha/(1 - \alpha') << 1$. Eq. (6.91) is a type of complex Ginzburg-Landau equation. If we take $\alpha, \alpha' = 0$ (which corresponds to a standard fluid), then $\epsilon = 0$, and (6.91) reduces to the cubic NLS, and therefore these results are completely consistent with those of Hasimoto for the standard fluid LIA.

6.3.3 Stokes wave solutions for the quantum LIA

A Stokes wave solution exists for the classical LIA. To recover a Stokes wave along a quantum vortex filament, we assume a solution of the form $\Psi(s, T) = P(T)$, so that

$$iP_T + (1 + 2i\epsilon)|P|^2 P = 0. \tag{6.92}$$

Writing $P(T) = R(T) \exp(i\Theta(T))$, we find $R_T = -2\epsilon R^3$ and $\Theta_T = R^2$, which gives $R(T) = (1 + 4\epsilon T)^{-1/2}$ and $\Theta(T) = (4\epsilon)^{-1} \ln(1 + 4\epsilon T)$. $P(T)$ then takes the form

$$P(T) = \frac{\cos\left(\frac{\ln(1+4\epsilon T)}{4\epsilon}\right) + i\sin\left(\frac{\ln(1+4\epsilon T)}{4\epsilon}\right)}{\sqrt{1 + 4\epsilon T}}. \tag{6.93}$$

Taking $\psi(s, t) = P(T) \exp(i \int_0^t A(\hat{t}) d\hat{t})$ gives us the general form of a Stokes wave. In the $\epsilon = 0$ limit, we obtain the standard Stokes wave of constant modulus.

6.3.4 Soliton on a quantum vortex filament

The most interesting solution associated with the Hasimoto transformation of the LIA is likely the soliton on a vortex filament. It is natural to wonder if such a soliton solution is

possible for the quantum LIA. In order to obtain a soliton, we shall consider a stationary solution $\Psi(s, T) = \sqrt{2\omega} q(S) \exp(-i\omega t)$, with $S = \sqrt{\omega} s$. This puts (6.91) into the form

$$(1 - \epsilon i) q'' + 2(1 + 2\epsilon i)|q|^2 q + q = 0 \,, \tag{6.94}$$

or, equivalently,

$$q'' + 2 \left(\frac{1 - \epsilon^2}{1 + \epsilon^2} + \frac{3\epsilon i}{1 + \epsilon^2} \right) |q|^2 q - \left(\frac{1}{1 + \epsilon^2} + \frac{\epsilon i}{1 + \epsilon^2} \right) q = 0 \,. \tag{6.95}$$

Since $\epsilon = O(\alpha)$ and $\alpha << 1$, we may neglect terms of order ϵ^2 and higher, to obtain

$$q'' + 2 \left(1 + 3\epsilon i\right) |q|^2 q - \left(1 + \epsilon i\right) q = 0 \,. \tag{6.96}$$

When $\epsilon = 0$ (corresponding to the standard fluid case), we find $q(S) = \text{sech}(S)$, so any solution for $\epsilon > 0$ should reduce to this case in the $\epsilon \to 0$ limit. We should therefore consider a solution of the form $q(S) = \rho(S) \exp(i\epsilon\theta(S))$. This has the interpretation that curvature is determined by the $\epsilon = 0$ case, while $\epsilon > 0$ influence the torsion of the filament. Making the relevant transformation, discarding contributions of order ϵ^2 or higher, and splitting (6.96) into real and imaginary parts, we obtain

$$\rho'' + 2\rho^3 - \rho = 0 \,, \quad 2\rho'\theta' + \rho\theta'' + 6\rho^3 - \rho = 0 \,. \tag{6.97}$$

Clearly, $\rho(S) = \text{sech}(S)$, which is just the soliton from the standard fluid case. We then find that

$$\theta'(S) = (C_1 + 5\tanh(S) - 2\tanh^3(S)) \cosh^2(S) \,. \tag{6.98}$$

This derivative blows up rapidly for all values of C_1 except for $C_1 = 3$. When $C_1 = 3$, $\theta'(S) \to 1/2$ as S gets large. This in turn implies that $\theta(S)$ would grow linearly as S gets

large. Therefore, we pick $C_1 = 3$, and upon integrating (6.98) we find

$$\theta(S) = C_0 - \frac{3}{2}S + \frac{3}{4}\left(\cosh(2S) - \sinh(2S)\right) + 2\ln(\cosh(S)).$$ (6.99)

There is a far simpler, yet still rather accurate, way to represent θ by way of an asymptotic expansion. We find that

$$\theta(S) = C_0 + \frac{7}{4} - 2\ln(2) + \frac{S}{2} + \frac{11}{4}e^{-2S} + O(e^{-4S}).$$ (6.100)

Picking $C_0 = 2\ln(2) - 7/4$ to simplify the expansion,

$$\theta(S) = \frac{S}{2} + \frac{11}{4}e^{-2S} + O(e^{-4S}).$$ (6.101)

This solution gives a linear growth in S, for large enough S. We therefore have that $q(S)$ is accurately approximate by

$$q(S) = \text{sech}(S)\exp\left(i\epsilon\left\{\frac{S}{2} + \frac{11}{4}e^{-2S}\right\}\right)$$ (6.102)

up to order ϵ^2. Putting this solution back into the natural variables s and t, we obtain a soliton on a quantum vortex filament:

$$\psi(s,t) = \sqrt{2\omega}\text{sech}(\sqrt{\omega}s)\exp\left(i\mu(s,t)\right),$$ (6.103)

$$\mu(s,t) = \frac{\alpha}{1-\alpha'}\left(\frac{\sqrt{\omega}}{2}s + \frac{11}{4}e^{-2\sqrt{\omega}s}\right) - (1-\alpha')\omega t.$$ (6.104)

6.3.5 Traveling waves on a quantum vortex filament

The solution (6.103)-(6.104) constitutes a soliton along a vortex filament. The solution is stationary, with only the phase depending on time. It is, however, possible to consider a

traveling wave along a vortex filament. In the case, both the phase and the amplitude of ψ would vary in time. Let us define $\Psi(s,T) = \hat{\Psi}(\xi)$, where $\xi = s - \eta T$. Ignoring terms of order ϵ^2 and higher, we obtain

$$\hat{\Psi}'' + \eta(\epsilon - i)\hat{\Psi}' + (1 + 3\epsilon i)|\hat{\Psi}|^2\hat{\Psi} = 0. \tag{6.105}$$

Writing $\hat{\Psi}(\xi) = F(\xi)\exp(i\int_0^\xi G(\nu)d\nu)$, we obtain the system

$$F'' - FG^2 + \eta\epsilon F' + \eta FG + F^3 = 0,$$
$$2F'G + FG' - \eta F' + \eta\epsilon FG + 3\epsilon F^3 = 0, \tag{6.106}$$

which is effectively a third-order dynamical system. The system (6.106) has the interesting property that it has either one or infinitely many equilibrium points, depending on the value of the wave speed, η. If $\eta = 3/2$, there exist infinitely many equilibria of the form $(\overline{F}, \overline{G}) = (\overline{F}, -2\overline{F}^2)$, where $\overline{F} \in \mathbb{R}$. On the other hand, when $\eta \neq 3/2$, the only equilibrium is the zero equilibrium $(\overline{F}, \overline{G}) = (0, 0)$.

From numerical simulations, we find that there is an interesting bursting pattern associated with the solutions to (6.106). For large negative values of ξ, the phase and amplitude functions are reasonably well-behaved. Then, near some finite value $\xi = \xi_0$ (which in general depends on both ϵ and η), there is a bursting behavior to the phase $G(\xi)$, near where the amplitude $F(\xi)$ reaches its minimal value. Past ξ_0, the phase switches signs and gradually the dynamics become more tame. This behavior is demonstrated in Fig. 6.11. This behavior becomes more clear when we view the system in phase space. In Fig. 6.12, we plot the solution to (6.106) in the phase space (F, F', G). The solution corresponds to a

trajectory which originates infinitely far from the origin as $\xi \to -\infty$, then approaches the origin, goes through a bursting pattern, and then leaves the origin in a similar manner to which it came.
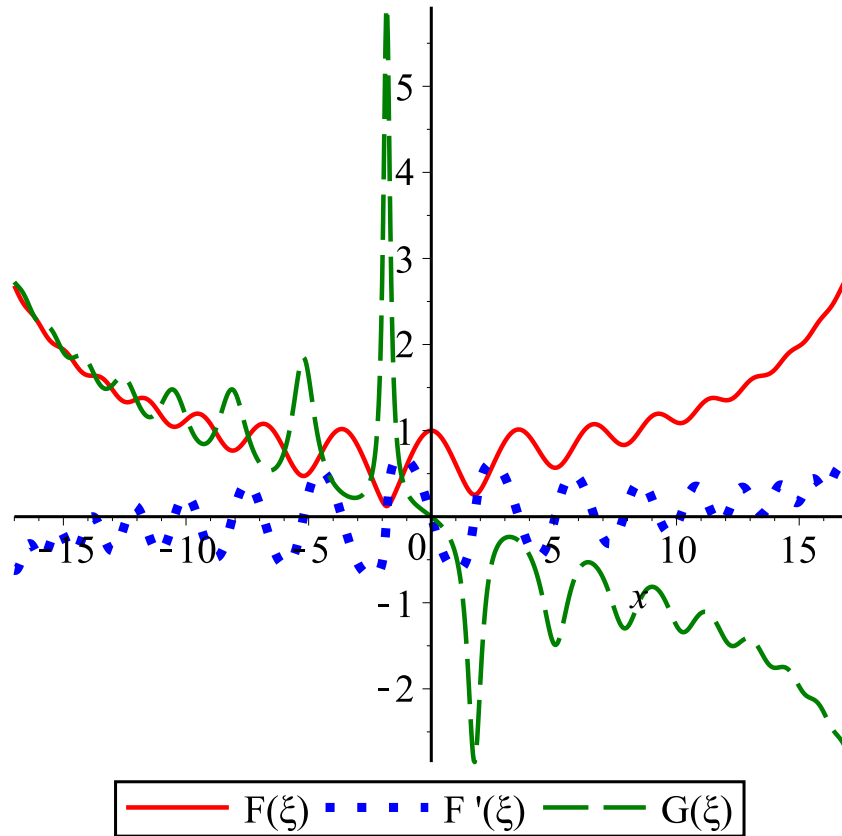
Figure 6.11: Plot of the solution to the dynamical system (6.106) when $\alpha = 0.073$, $\alpha' = 0.018$, $\eta = 0.1$. Initial conditions are $F(0) = 1$, $F'(0) = 0$ and $G(0) = 0$.
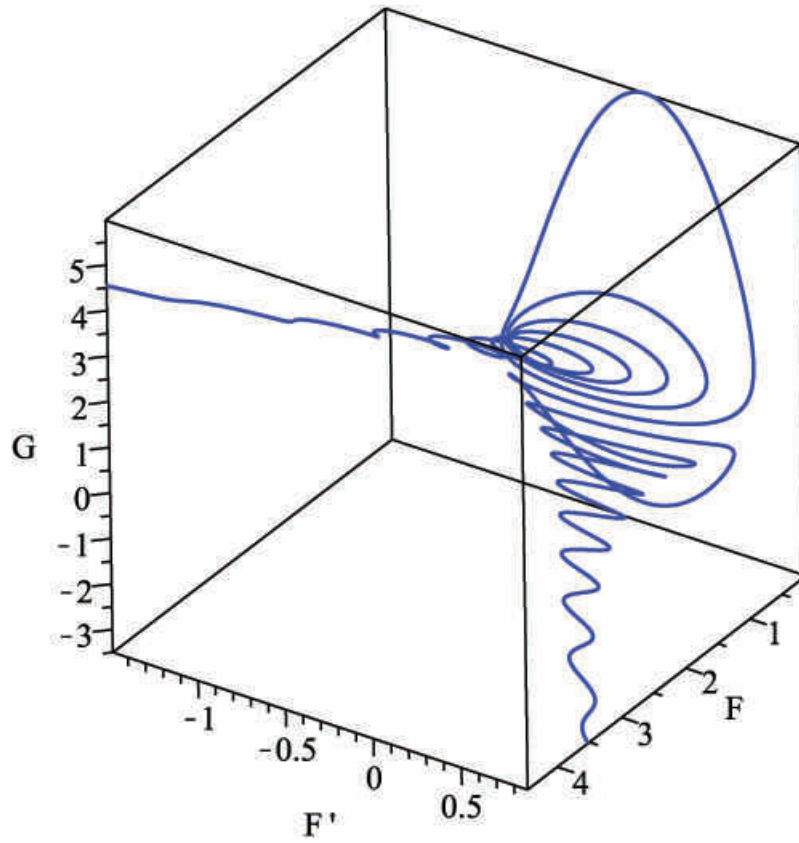
Figure 6.12: Phase space plot of the solution to the dynamical system (6.106) when $\alpha = 0.073$, $\alpha' = 0.018$, $\eta = 0.1$. Initial conditions are $F(0) = 1$, $F'(0) = 0$ and $G(0) = 0$.

6.3.6 Discussion

With this, we have successfully transformed the quantum LIA into a type of complex Ginzburg-Landau equation (6.91), by use of a method analogous to the Hasimoto transformation for a standard fluid vortex filament. Doing so, we are able to reduce the quantum LIA (6.78) (a vector conservation law) into a complex scalar PDE (6.91), which makes the system far more amenable to mathematical analysis. Such a mapping between the quantum LIA and this PDE is also desirable from a physical point of view, since it allows for greater qualitative comparison of the quantum and standard fluid LIA solutions.

Upon transforming the quantum LIA into a complex Ginzburg-Landau equation (6.91), we were able to study a number of solutions. First we obtained Stokes wave type solutions. In the case of a standard fluid, these solutions takes the form of oscillating waves with constant amplitudes. However, we were able to demonstrate that for a quantum fluid modeled under LIA, such solutions have an algebraic decay rate and therefore dissipate as time becomes large. The period of oscillation for such solutions is variable, as well, as gradually increases in time. Since the function ψ used in this section is a composite function of curvature and torsion, the physical interpretation for these solutions to the quantum LIA is that the curvature of the filament decreases in time, while the torsion increases in time, in contrast to the standard fluid solutions, where curvature is constant.

A second and rather fundamental solution is that of the soliton on a vortex filament. Hasimoto originally employed the aforementioned transform in order to demonstrate the

existence of a soliton on a vortex filament under the standard LIA. In the present section, we have been able to demonstrate analogously that such a soliton also exists under the quantum LIA. The soliton takes the form of a sech function (i.e., a bright soliton), which is what one finds for the standard fluid case as well. However, the inclusion of superfluid friction parameters results in the appearance of an additional phase factor that depends on arclength. Therefore, the curvature of the filament solution corresponding to a 1-soliton does not change when we go from the classical to the quantum LIA, while the torsion is modified - by a factor that scales as α - when we go from the classical to the quantum LIA. The Hasimoto formulation has proven useful in experiments [44], and we expect the present results should be similarly useful for experiments in superfluid vortex dynamics. Breather solitons have been found on the classical LIA [80] (with no superluid friction parameters present), and one extension of these results would be to consider breather solitons for the quantum LIA.

We considered a family of traveling waves solutions. The phase of the waves undergo a type of bursting behavior, during which they change sign (going from positive to negative). However, we did not find more complicated dynamics, such as chaos. Still, there are other possible solutions to the PDE (6.91), so more complex dynamics are certainly possible. Indeed, chaos has been shown to arise from related models [6]. Chaos in the quantum LIA was previously conjectured [57], but as of yet has not been shown. Note that our derivations exclude any strong effects from the normal fluid velocity vector, **U**. It is possible to include the effects of the normal fluid, although the derivations will be much more complicated

and lengthy. Due to the added complexity of the resulting equation, it may be possible to demonstrate chaotic behavior in the analogous equations which account for the normal fluid flow. It is also possible that the inclusion of the term $\psi^2 - \psi^{*2}$ will give more complicated dynamics in some instances.

CHAPTER 7

NON-LOCAL DISPERSIVE RELATIONS AND

CORRESPONDING VORTEX DYNAMICS

In all of the previous discussions, we have considered local models. However, the full non-local model which the LIA replaces is needed in order to study more complicated solutions. What we do in the present section is provide two types of solutions for the non-local model governing the self-induced motion of vortex filaments. For each, we are able to obtain a good analytical description of the solutions, despite the formulation is non-local, nonlinear, and singular. The results are compared to the more common results known for the LIA.

7.1   Non-local dynamics of the self-induced motion of a planar vortex filament

The local induction approximation (LIA) serves as a local approximation to the non-local Biot-Savart law governing the self-induced motion of a vortex filament. The Hasimoto planar vortex filament is a rare example of an exact solution form for the LIA. It is natural to wonder whether such a vortex filament solution would exist for the full non-local Biot-Savart law, and

if so, whether the non-local effects would drastically modify the solution properties. Noting this, we demonstrate that a planar vortex filament solution does exist for the non-local Biot-Savart formulation governing the self-induced motion of a vortex filament, provided that a non-linear integral equation (governing the spatial structure of such a filament) has a non-trivial solution. The integral equation is too complicated to solve in any exact manner, since it takes on a non-linear form and is singular. However, by using a strained parameters approach, we are able to obtain an accurate analytical approximation to the solution of this integral equation under physically reasonable assumptions. We then compare the obtained results with those known in the case of the LIA, in order to ascertain the influence of the non-locality inherent in the Biot-Savart formulation. Interestingly, we find that the LIA and Biot-Savart formulations both admit solutions with very similar spatial structures, while the non-locality primarily influences the motion of the filament, with planar filaments found in the Biot-Savart formulation rotating at nearly twice the speed of those found in the LIA for comparable parameter values. Physically these results show that planar vortex filaments exist and maintain their form under the non-local Biot-Savart formulation, with the primary influence of the non-locality being on the motion of the filaments. Mathematically, the results constitute a solution to a non-local integro-differential equation in space and time variables, since we obtain a type of solution for the non-local Biot-Savart dynamics. The results presented in this section feature in the paper Van Gorder [115].

7.1.1 Background

The self-induced motion of a thin vortex filament is commonly studied by use of the the Biot-Savart law. However, since the Biot-Savart law involves an integral term with logarithmic singularity, it is very common to apply the LIA in order to approximate the self-induced motion of such a vortex filament. This approximation takes the integral equatiion corresponding to the Biot-Savart law and reduces it into a vector partial differential equation, the solution of which gives the time evolution of the position of the vortex filament in space. Corresponding to this approximation, the classical Da Rios equations for the motion of a vortex filament in a standard fluid [8, 24] have been studied for a wide variety of vortex configurations. 1-solitons on a filament[42], torus knots [49], helical filaments [89], planar filaments [41], and self-similar structures [107] are some of the solutions found, illustrating the different physical scenarios possible. One reason that the LIA is of interest is that it is a limiting case (the zero-temperature limit) for the motion of a vortex filament in a superfluid; see Chapter 5.

While the planar filament is well-studied under the dynamics resulting from the LIA, it is natural to wonder whether such a vortex filament solution would exist for the full non-local Biot-Savart law, and if so, whether the non-local effects would drastically modify the solution properties. This issue has not been addressed before in the literature, and hence shall be the focus of this section. We first show that the question of the existence of a planar vortex filament solution for the non-local Biot-Savart formulation governing the self-induced

motion of a vortex filament can be recast into a question of whether a solution exists for a kind of singular and nonlinear integral equation involving an unknown function which shall give the spatial profile of the planar filament. Due to the nonlinearity and singularity inherent in the integral equation, an exact solution is not possible to obtain. We therefore resort to an analytical method, valid for filaments with sufficiently small deviations from the reference axis, to describe the properties of the solution. Using this method, we construct an accurate approximate solution of order A^3 (where A denotes the maximal deviation from the reference axis). This solution shares some features with the solution of [105], since the method employed is similar.

The assumption of small deviations from the reference axis is completely physically reasonable, and hence so is the solution obtained here. We compare the obtained analytical approximation with those results known in the case of the LIA. We find that the LIA and Biot-Savart formulations both admit solutions with very similar spatial structures, which makes sense in light of the fact that the spatial structure is unchanging in time. We see that the non-locality inherent in the Biot-Savart formulation primarily influences the rotational motion of the filament. Therefore, we show that planar vortex filament solutions previously discussed in the context of the LIA can actually exist for the more complicated Biot-Savart formulation, with the primary change being in the rate of the rotational motion of the filament. Meanwhile, structurally the LIA and Biot-Savart planar filaments are quite similar.

7.1.2 Biot-Savart formulation for a parameterized filament curve

Let the curve $\mathbf{r}$ represent the vortex filament. The self-induced motion of a thin vortex filament is given by the Biot-Savart law

$$\mathbf{r}_t = \frac{\kappa}{4\pi} \int_\ell \frac{(\mathbf{s} - \mathbf{r}) \times d\mathbf{s}}{|\mathbf{s} - \mathbf{r}|^3} \,. \tag{7.1}$$

Here, $\mathbf{r}$ denotes a space point in $\mathbb{R}^3$ lying on the filament, κ denotes the circulation, and ℓ is the path traced out along the filament. This representation is non-local, meaning that distant parts of the filament can effect the behavior of the filament at a specific point. Since this equation is non-local, it is difficult to solve for most vortex configurations. Often, the LIA is used to replace the integral in (7.1) with a far simpler relation, viz.,

$$\mathbf{r}_t = \mathbf{t} \times \mathbf{n}\,, \tag{7.2}$$

where $\mathbf{t}$ is the tangent vector and $\mathbf{n}$ denotes the normal vector to $\mathbf{r}$ multiplied by the curvature. The right hand side of (7.2) is the binormal vector (up to scaling).

We shall be interested in a Cartesian representation of a vortex filament, so let us write $\mathbf{r} = (x, y, z)$. Equation (7.1) gives the vector relation

$$(x_t, y_t, z_t) = \frac{\kappa}{4\pi} \int \frac{(s_1 - x, s_2 - y, s_3 - z) \times (ds_1, ds_2, ds_3)}{[(s_1 - x)^2 + (s_2 - y)^2 + (s_3 - z)^2]^{3/2}} \,. \tag{7.3}$$

This gives the time evolution for each component of $\mathbf{r}$. If we desire a solution curve $\mathbf{r}$ to the Biot-Savart law (7.1), we must be able to solve (7.3) for the position components. Depending on the type of solution sought, solving this system may vary from difficult to impossible.

Note that (7.3) is singular when $(s_1, s_2, s_3) = (x, y, z)$, which further complicates the solution of such a model. To overcome this, we shall apply the LIA to the region near (x, y, z), while we shall maintain the full Biot-Savart law outside of such a region. In other words, the time evolution of the solution curve $\mathbf{r} = (x, y, z)$ shall consist of one component giving a local effect very near each point on the curve (the LIA term) and one component giving the non-local effect (sufficiently removed from the point).

7.1.3 An integral equation for the non-local planar vortex filament

Recall that under the LIA the planar vortex filament takes the form

$$\mathbf{r}(x, t) = (x, \cos(\omega t)\psi(x), \sin(\omega t)\psi(x)) , \tag{7.4}$$

where ψ is a real-valued, twice differentiable function of x alone. The constant ω is a parameter to be determined, which has the interpretation of giving the rotational velocity of the filament. The solution (7.4) is interesting, in that it describes a filament which is aligned along a plane intersecting the x-axis. The motion consists of a rotation about the x axis. Given the complexity of the LIA, which is essentially a vector system of PDEs, such an elegant solution is rather remarkable. It is essentially a stationary state for the LIA.

Assuming a solution of the form (7.4), the time evolution due to the Biot-Savart formulation (7.1) is

$$\mathbf{r}_t(x, t) = \frac{\kappa}{4\pi} \int_{\mathbb{R}} \frac{(\mathbf{r}(x, t) - \mathbf{r}(s, t)) \times ds}{|\mathbf{r}(s, t) - \mathbf{r}(x, t)|^3} . \tag{7.5}$$

308

We calculate

$$|\mathbf{r}(s,t) - \mathbf{r}(x,t)|^3 = \left((s-x)^2 + \cos^2(\omega t)(\psi(s)-\psi(x))^2 + \sin^2(\omega t)(\psi(s)-\psi(x))^2\right)^{3/2}$$

$$= \left((s-x)^2 + (\psi(s)-\psi(x))^2\right)^{3/2} ,$$

(7.6)

$$(\mathbf{r}(x,t) - \mathbf{r}(s,t)) \times ds$$

$$= \left(0, \sin(\omega t)\left\{(\psi(s)-\psi(x)) - (s-x)\psi'(s)\right\} ds,\right.$$

(7.7)

$$\left. - \cos(\omega t)\left\{(\psi(s)-\psi(x)) - (s-x)\psi'(s)\right\} ds\right) ,$$

$$\mathbf{r}_t(x,t) = (0, -\omega\sin(\omega t)\psi(x), \omega\cos(\omega t)\psi(x)) .$$

(7.8)

Placing these expressions into (7.5), we obtain the equations

$$-\omega\sin(\omega t)\psi(x) = \sin(\omega t)\frac{\kappa}{4\pi}\int_{\mathbb{R}}\frac{(\psi(s)-\psi(x)) - (s-x)\psi'(s)}{\left((s-x)^2 + (\psi(s)-\psi(x))^2\right)^{3/2}}ds ,$$

(7.9)

and

$$\omega\cos(\omega t)\psi(x) = -\cos(\omega t)\frac{\kappa}{4\pi}\int_{\mathbb{R}}\frac{(\psi(s)-\psi(x)) - (s-x)\psi'(s)}{\left((s-x)^2 + (\psi(s)-\psi(x))^2\right)^{3/2}}ds .$$

(7.10)

Both of these equations are equivalent, so we obtain the single equation

$$\omega\psi(x) = \frac{\kappa}{4\pi}\int_{\mathbb{R}}\frac{(s-x)\psi'(s) - (\psi(s)-\psi(x))}{\left((s-x)^2 + (\psi(s)-\psi(x))^2\right)^{3/2}}ds .$$

(7.11)

Equation (7.11) constitutes a non-linear and singular integral equation for the unknown function $\psi(x)$. While superficially the integral appears to be singular with a singularity of degree three, note that the integrand actually has a first degree singularity. Indeed,

expanding the integrand about $s = x$, we find

$$\frac{(s-x)\psi'(s) - (\psi(s) - \psi(x))}{((s-x)^2 + (\psi(s)-\psi(x))^2)^{3/2}} = \frac{1}{2}\frac{\psi''(x)}{(1+\psi'^2(x))^{3/2}}\frac{1}{|s-x|}$$
$$+ \left(\frac{1}{3}\frac{\psi'''(x)}{(1+\psi'^2(x))^{3/2}} - \frac{3}{4}\frac{\psi'(x)\psi''^2(x)}{(1+\psi'^2(x))^{5/2}}\right)\text{sgn}(s-x)$$
$$+ O(|s-x|).$$
(7.12)

Therefore, the integral (7.11) itself should have a singularity of strength $\ln(|s - x|)$ for $|s - x| \ll 1$. Since (7.11) is non-linear and singular, this is little hope in obtaining an exact solution, and even numerical methods will be difficult to apply due to the form of the nonlinear dependence of the integrand on ψ. In the next section, we apply the method of multiple scales to the solution of the integral equation (7.11). In order to avoid the singularity at $s = x$, we apply the LIA for $|s - x| < \epsilon$, for some small ϵ. Then, for $|s - x| > \epsilon$, we keep the Biot-Savart integral term. This results in an extension of the LIA results which accounts for non-local effects.

7.1.4 The non-local planar vortex filament

In this section, we obtain an approximate analytical solution to the integral equation (7.11). Once a solution ψ is obtained, we will have recovered the planar vortex filament (7.4). We shall split the Biot-Savart integral into two parts, corresponding to both $|s - x| < \epsilon$ and $|s - x| > \epsilon$, where ϵ is a small length parameter. For such small ϵ, the contribution on $|s - x| < \epsilon$ is adequately approximated by the LIA. For a planar filament of the form (7.4),

the LIA gives

$$-\frac{\kappa}{4\pi}\ln(\epsilon)\frac{\psi''(x)}{(1+\psi'^2(x))^{3/2}}(0,-\sin(\omega t),\cos(\omega t)) \qquad (7.13)$$

as the approximation to the "local effects" near $s = x$ for any $x \in \mathbb{R}$. The scaling factor

of $\ln(\epsilon)$ makes sense, in light of the form of (7.12). For the region $|s - x| > \epsilon$, we keep the

integral (7.11) as it is. We therefore approximate (7.11) with the integro-differential equation

$$\omega\psi(x) = -\frac{\kappa}{4\pi}\ln(\epsilon)\frac{\psi''(x)}{(1+\psi'^2(x))^{3/2}} + \frac{\kappa}{4\pi}\int_{|s-x|>\epsilon}\frac{(s-x)\psi'(s)-(\psi(s)-\psi(x))}{((s-x)^2+(\psi(s)-\psi(x))^2)^{3/2}}ds\,. \qquad (7.14)$$

If we were to neglect the integral term (disregard non-local effects), we obtain the purely

local ODE

$$\omega\psi(x) = -\frac{\kappa}{4\pi}\ln(\epsilon)\frac{\psi''(x)}{(1+\psi'^2(x))^{3/2}}\,, \qquad (7.15)$$

and picking the scaling parameter $\omega = \frac{\kappa}{4\pi}\ln(\epsilon)$ we would have

$$\psi + \frac{\psi''}{(1+\psi'^2)^{3/2}} = 0\,, \qquad (7.16)$$

which is the ODE governing the spatial structure of the planar vortex filament.

Recall that the planar vortex filament obtained under the LIA is naturally bounded

in terms of deviation from the reference axis. In other words, for the solution ψ valid under

LIA, ψ is bounded. In particular, it may be shown that $\psi < \sqrt{2}$ (see Chapters 2-4) in order

to have a periodic solution in space. Making a similar assumption for the non-local case, let

us assume that the maximal deviation of the filament from the reference axis is $0 < A < 1$,

so that $|\psi(x) \leq A|$ for all $x \in \mathbb{R}$.

Under the assumption of a small amplitude solution ψ, it makes sense to consider

a perturbation solution in the parameter A. However, as seen in Chapter 4, secular terms

arising from regular perturbation cause blow-up of the approximations to the LIA solution. As discussed in Chapter 4, an effective way to overcome such difficulties would be to introduce a strained parameter which also depends on the parameter A. From the form of the equation (7.14), we consider an expansion

$$\psi(x) = A(\Psi_0(X) + A^2 \Psi_1(X)) + O(A^5)\,, \tag{7.17}$$

where

$$X = (1 + \eta A^2 + O(A^4))x\,. \tag{7.18}$$

Without loss of generality, we take $\Psi_0(0) = 1$, $\Psi_0'(0) = 0$ so that the maximal amplitude of ψ occurs at $x = 0$. We also take $\Psi_1(0) = \Psi_1'(0) = 0$. The parameter η will be selected in order to remove secular terms. Placing (7.17) into integro-differential equation (7.14), we find that

$$\omega\Psi_0 + \frac{\kappa}{4\pi}\ln(\epsilon)\Psi_0'' - \frac{\kappa}{4\pi}\int_{|\sigma|>\epsilon}\frac{\sigma\Psi_0'(\sigma+X) - (\Psi_0(\sigma+X) - \Psi_0(X))}{|\sigma|^3}d\sigma = 0\,. \tag{7.19}$$

Let us assume that $\Psi_0(X) = \cos(X)$. While this may seem rather arbitrary, we know that from the LIA that the order A contribution should scale like $\cos(X)$. We shall select the scale parameter ω to accommodate this selection. Under this assumption, note that

$$\int_{|\sigma|>\epsilon}\frac{\sigma\Psi_0'(\sigma+X) - (\Psi_0(\sigma+X) - \Psi_0(X))}{|\sigma|^3}d\sigma = \left(\frac{\mathrm{Ci}(\epsilon)\epsilon^2 - \epsilon\sin(\epsilon) - \cos(\epsilon) + 1}{\epsilon^2}\right)\cos(X)$$

$$= \left(\gamma - \frac{1}{2} + \ln(\epsilon) + O(\epsilon^2)\right)\cos(X)\,. \tag{7.20}$$

Here, γ denotes the Euler-Mascheroni constant, $\gamma \approx 0.57721$, while Ci denote the cosine integral function

$$\mathrm{Ci}(y) = -\int_y^\infty \frac{\cos(\theta)}{\theta} d\theta = \gamma + \ln(y) - \frac{1}{4}y^2 + O(y^4) \,. \tag{7.21}$$

Since ϵ is assumed to be small, we ignore terms of order ϵ^2 and higher. Equation (7.19) then reduces to

$$\left(\omega - \frac{\kappa}{4\pi}\left[\ln(\epsilon) + \left(\gamma - \frac{1}{2} + \ln(\epsilon)\right)\right]\right)\cos(X) = 0 \,, \tag{7.22}$$

which in turn gives us the condition

$$\omega = \frac{\kappa}{4\pi}\left(\gamma - \frac{1}{2} + 2\ln(\epsilon)\right) \,. \tag{7.23}$$

Taking this value of the scaling parameter ω, we have that $\Psi_0(X) = \cos(X)$ is the first term in the perturbation expansion (7.17).

To calculate the next term in the perturbation expansion, $\Psi_1(X)$, we collect terms of order A^3, finding

$$\omega\Psi_1 + \frac{\kappa}{4\pi}\ln(\epsilon)\Psi_1'' - \frac{\kappa}{4\pi}\int_{|\sigma|>\epsilon} \frac{\sigma\Psi_1'(\sigma+X) - (\Psi_1(\sigma+X) - \Psi_1(X))}{|\sigma|^3} d\sigma$$

$$= \frac{\kappa}{4\pi}\ln(\epsilon)\left(\frac{3}{2}\Psi_0'^2\Psi_0'' - 2\eta\Psi_0''\right) + \frac{3\eta\kappa}{4\pi}\int_{|\sigma|>\epsilon} \frac{\sigma\Psi_0'(\sigma+X) - (\Psi_0(\sigma+X) - \Psi_0(X))}{|\sigma|^3} d\sigma$$

$$- \frac{3\kappa}{8\pi}\int_{|\sigma|>\epsilon} \frac{[\sigma\Psi_0'(\sigma+X) - (\Psi_0(\sigma+X) - \Psi_0(X))][\Psi_0(\sigma+X) - \Psi_0(X)]}{|\sigma|^5} d\sigma \,.$$

$$\tag{7.24}$$

Evaluating the right-hand side at $\Psi_0(X) = \cos(X)$, we obtain

$$\omega\Psi_1 + \frac{\kappa}{4\pi}\ln(\epsilon)\Psi_1'' - \frac{\kappa}{4\pi}\int_{|\sigma|>\epsilon}\frac{\sigma\Psi_1'(\sigma+X) - (\Psi_1(\sigma+X) - \Psi_1(X))}{|\sigma|^3}d\sigma$$

$$= \frac{3\kappa}{32\pi}\ln(\epsilon)\cos(3X) - \frac{3\kappa}{8\pi}\left(\frac{133}{144} - \frac{7\gamma}{12} - \frac{2}{3}\ln(2) - \frac{7}{12}\ln(\epsilon)\right)\cos(2X)$$

$$+ \frac{\kappa}{4\pi}\left(\left(2\eta - \frac{3}{8}\right)\ln(\epsilon) + 3\eta\left(\gamma - \frac{1}{2} + \ln(\epsilon)\right)\right)\cos(X) - \frac{3\kappa}{8\pi}\left(\frac{\gamma}{12} + \frac{1}{12}\ln(\epsilon) - \frac{19}{144}\right).$$

$$(7.25)$$

Here, we have used the fact that

$$\int_{|\sigma|>\epsilon}\frac{[\sigma\Psi_0'(\sigma+X) - (\Psi_0(\sigma+X) - \Psi_0(X))][\Psi_0(\sigma+X) - \Psi_0(X)]}{|\sigma|^5}d\sigma$$

$$= \left(\frac{133}{144} - \frac{7\gamma}{12} - \frac{2}{3}\ln(2) - \frac{7}{12}\ln(\epsilon)\right)\cos(2X) \qquad (7.26)$$

$$+ \frac{\gamma}{12} + \frac{1}{12}\ln(\epsilon) - \frac{19}{144} + O(\epsilon^2),$$

and have neglected terms of order ϵ^2 and higher. A fundamental solution set for Ψ_1 in the

equation (7.24) consists of $\cos(X)$ and $\sin(X)$. Therefore, to prevent secular growth, we

must remove the term with $\cos(X)$ from the right hand side of equation (7.25). To do so,

we pick the straining parameter η so that the coefficient of $\cos(X)$ vanishes. Therefore, we

must solve

$$\left(2\eta - \frac{3}{8}\right)\ln(\epsilon) + 3\eta\left(\gamma - \frac{1}{2} + \ln(\epsilon)\right) \qquad (7.27)$$

for η, obtaining

$$\eta = \frac{3}{8}\frac{\ln(\epsilon)}{5\ln(\epsilon) + \gamma - \frac{1}{2}} = \frac{3}{40 + 4\left(\frac{2\gamma-1}{\ln(\epsilon)}\right)}. \qquad (7.28)$$

For sufficiently small ϵ, we have that $\epsilon \approx \frac{3}{40}$.

A particular solution to (7.25) will then involve the functions $\cos(3X)$, $\cos(2X)$ and

a constant. However, if we pick the conditions $\Psi_1(0) = \Psi_1'(0) = 0$, we should also have a

term involving the fundamental solution, $\cos(X)$. In order to satisfy the equation (7.25) in addition to these conditions, we should have a solution of the form

$$\Psi_1(X) = \xi_3 \cos(3X) + \xi_2 \cos(2X) - (\xi_3 + \xi_2 + \xi_0)\cos(X) + \xi_0. \tag{7.29}$$

Placing (7.29) directly into (7.25), we find that

$$\xi_3 = -\frac{1}{8}\frac{3\ln(\epsilon)}{8\gamma - 4 + 9\ln(3) + 16\ln(\epsilon)}, \tag{7.30}$$

$$\xi_2 = -\frac{1}{48}\frac{84\gamma - 133 + 96\ln(2) + 84 ln(\epsilon)}{6\gamma - 3 + 8\ln(2) + 12\ln(\epsilon)}, \tag{7.31}$$

$$\xi_0 = -\frac{1}{48}\frac{12\gamma - 19 + 12\ln(\epsilon)}{2\gamma - 1 + 4\ln(\epsilon)}. \tag{7.32}$$

We therefore have a perturbation solution of the form

$$\psi(x) = \left(A - (\xi_3 + \xi_2 + \xi_0)A^3\right)\cos\left(\left[1 + \frac{3}{40 + 4\left(\frac{2\gamma-1}{\ln(\epsilon)}\right)}A^2\right]x\right)$$

$$+ \xi_3 A^3 \cos\left(3\left[1 + \frac{3}{40 + 4\left(\frac{2\gamma-1}{\ln(\epsilon)}\right)}A^2\right]x\right) \tag{7.33}$$

$$+ \xi_2 A^3 \cos\left(2\left[1 + \frac{3}{40 + 4\left(\frac{2\gamma-1}{\ln(\epsilon)}\right)}A^2\right]x\right) + \xi_0 A^3 + O(A^5).$$

For very small ϵ, we have that $\xi_3 \approx -\frac{3}{128}$, $\xi_2 \approx -\frac{7}{48}$ and $\xi_0 \approx -\frac{1}{16}$. Therefore, the perturbation solution (7.33) is accurately approximated by

$$\psi(x) \approx \left(A - \frac{89}{384}A^3\right)\cos\left(\left[1 + \frac{3}{40}A^2\right]x\right) - \frac{3}{128}A^3\cos\left(3\left[1 + \frac{3}{40}A^2\right]x\right)$$

$$- \frac{7}{48}A^3\cos\left(2\left[1 + \frac{3}{40}A^2\right]x\right) - \frac{1}{16}A^3. \tag{7.34}$$

The solution (7.34) constitutes an accurate approximate solution to the intego-differential equation (7.14), which in turn is a good approximation to the integral equation (7.11) ob-

tained from the full non-local Biot-Savart formulation. Therefore, under the non-local Biot-Savart formulation, a planar vortex filament can still exist, and an accurate approximation is given by (7.34).

7.1.5 Comparison with known solution for the LIA

The method of strained parameters used here was applied to the standard LIA in the case of a planar vortex filament in Chapter 4. In that paper, the ϵ influence was suppressed in a parameter, so we redo the calculations here in order to preserve the parameters κ and ϵ.

Dropping the integral term from (7.14), we have that a vortex filament under LIA is determined by the solution of

$$\omega\psi + \frac{\kappa}{4\pi}\ln(\epsilon)\frac{\psi''}{(1+\psi'^2)^{3/2}} = 0. \tag{7.35}$$

Assuming a solution like that of (7.17), we find that $\Psi_0(X) = \cos(X)$ provided $\omega = \frac{\kappa}{4\pi}\ln(\epsilon)$. The next term in the perturbation expansion is then governed by

$$\Psi_1 + \Psi_1'' = \left(2\eta - \frac{3}{8}\right)\cos(X) + \frac{3}{8}\cos(3X). \tag{7.36}$$

Picking $\eta = \frac{3}{16}$ to remove the secular term, we obtain

$$\Psi_1(X) = \frac{3}{64}\cos(X) - \frac{3}{64}\cos(3X). \tag{7.37}$$

We therefore have the perturbation solution

$$\psi(x) = \left(A + \frac{3}{64}A^3\right)\cos\left(\left[1 + \frac{3}{16}A^2\right]x\right) - \frac{3}{64}A^3\cos\left(3\left[1 + \frac{3}{16}A^2\right]x\right) + O(A^5). \tag{7.38}$$

Note that ω is the rotational velocity of the filament. Let us denote by ω_{BS} and ω_{LIA} the rotational velocity for the solutions calculated by the Biot-Savart rule (7.34) and with only the LIA (7.38), respectively. With $\omega_{\mathrm{LIA}} = \frac{\kappa}{4\pi} \ln(\epsilon)$, we have

$$\omega_{\mathrm{BS}} = 2\omega_{\mathrm{LIA}} + \frac{\kappa(2\gamma - 1)}{8\pi} = 2\omega_{\mathrm{LIA}} + (6.1434 \times 10^{-3})\kappa \, . \tag{7.39}$$

We see that the direction of the rotation is the same in both cases (for small enough ϵ), while the speed of rotation is different. Indeed, $|\omega_{\mathrm{BS}}| \approx 2|\omega_{\mathrm{LIA}}|$, so the rotational speed when non-local effects are considered is approximately double that of the case where non-local effects are neglected. This suggests that non-local effects are not negligibly small in comparison to LIA effects alone, but rather that non-local effects can be on the same order of magnitude as local effects found through use of the LIA alone.

The period of the LIA filament solution over space is approximately T_{LIA}, where

$$T_{\mathrm{LIA}} = \frac{2\pi}{1 + \frac{3}{16}A^2} \approx 2\pi - \frac{3\pi}{8}A^2 + O(A^4) \, , \tag{7.40}$$

while the period of the solution approximating the full Biot-Savart model has a period of approximately T_{BS}, where

$$T_{\mathrm{BS}} = \frac{2\pi}{1 + \frac{3}{40}A^2} \approx 2\pi - \frac{3\pi}{20}A^2 + O(A^4) \, . \tag{7.41}$$

The absolute error between these periods is then

$$|T_{\mathrm{BS}} - T_{\mathrm{LIA}}| = \frac{9\pi}{40}A^2 + O(A^4) \, . \tag{7.42}$$

So, while corrections to the rotational velocity are rather large when comparing the LIA and Biot-Savart solutions, corrections to the spatial period of the planar solutions are only of

order A^2. From this, we infer that the primary influence of the non-locality is on the motion of the planar vortex filaments, rather than on the structure of such filaments.

7.1.6 Discussion

A planar solution has been constructed for the full non-local Biot-Savart dynamics governing the self-induced motion of a vortex filament. Under the assumption of a planar vortex filament solution with arbitrary (unknown) spatial structure determined by $\psi(x)$, the Biot-Savart dynamics reduce to a stationary (independent of time) integral equation for the unknown $\psi(x)$. (Actually, since the formulation also depends on a ψ' under the integral, this equation is a type of integro-differential equation.) The integral in this formulation is then approximated near a singularity of logarithmic order by the LIA, whereas away from the singularity the integral form is maintained. Therefore, there is a part of the solution due to the LIA, and another non-local part. This solution is interesting in a mathematical sense, due to the fact that it provides us with an accurate approximation to a solution of the singular and nonlinear integro-differential equation (7.11). Even numerical solution of such an integro-differential equation would be challenging. The results suggest that at the very least some of the solutions present under the LIA can also be extended to the Biot-Savart formulation.

Physically, the approximate analytical solution obtained through a strained parameter approach is quite useful. While we assume that the deviations A from the central axis are

318

sufficiently small, this is physically reasonable in light of the fact that the planar filaments only exist for the LIA when $A < \sqrt{2}$. So, the large A case is not physically interesting. For the solutions obtained in [105], the perturbation solutions were useful for $A < 0.7$. Plotting the solutions for various A, we see that the order A^3 effects are mostly negligible, so a planar filament can be approximated by

$$
\begin{aligned}
\mathbf{r}(x,t) = x\mathbf{i}_x &+ A\cos\left(\frac{\kappa}{4\pi}\left(\gamma - \frac{1}{2} + 2\ln(\epsilon)\right)t\right)\cos\left(\left[1 + \frac{3}{40}A^2\right]x\right)\mathbf{i}_y \\
&+ A\sin\left(\frac{\kappa}{4\pi}\left(\gamma - \frac{1}{2} + 2\ln(\epsilon)\right)t\right)\cos\left(\left[1 + \frac{3}{40}A^2\right]x\right)\mathbf{i}_z .
\end{aligned}
\tag{7.43}
$$

The approximate solutions suggest that the spatial structure of the planar filaments found here for the Biot-Savart dynamics is relatively unchanged from the structure of the solutions under LIA. The difference apparent when comparing the LIA and Biot-Savart solutions lies in the motion, rather than the structure, of the planar filaments. From the perturbation solutions, we have that the rotational velocity for the LIA formulation (given by ω_{LIA}) and the Biot-Savart formulation (given by ω_{BS}) relate like $\omega_{\text{BS}} \approx 2\omega_{\text{LIA}}$. Therefore, the primary effect of the non-locality is to increase the velocity of the filament.

7.2 Self-induced motion of a Cartesian helical vortex filament under the Biot-Savart model

The thin helical vortex filament is one of the fundamental exact solutions possible under the LIA. The LIA is itself an approximation to the non-local Biot-Savart dynamics governing

the self-induced motion of a vortex filament, and helical filaments have also been considered under the Biot-Savart dynamics in a variety of configurations and assumptions. In the present section, we consider the motion of such a helical filament in the Cartesian reference frame by determining the curve defining this helical filament mathematically. In order to do so, we consider a matched approximation to the Biot-Savart dynamics, with local effects approximated by the LIA in order to avoid the logrithmic singularity inherent in the Biot-Savart formulation. This, in turn, allows us to determine the rotational and translational velocity of the filament in terms of a local contribution (which is exactly that which is found under the LIA) and a non-local contribution. Performing our calculations in such a way, we can easily compare our results to those of the LIA. Both exact numerical results and approximate analytical results are given. For small wave number k, the transverse velocity scales as k^2, while for large wave numbers, the transverse velocity scales as k. On the other hand, the rotational velocity attains a maximum value at some finite k, which corresponds exactly to the wave number giving the maximal torsion.

Ricca [77] demonstrated that torsion strongly influences the structure of helical filaments. Widnall [119], Ricca [77] give numerics for helical filaments of small pitch (large wave numbers) and small amplitude regime, while Ricca [77] also gives an analytic result for the infinite-torsion case, valid when the pitch is small (wave number is large). The analytical results discussed here are complementary to those studies, since we obtain accurate analytics in the small and intermediate wave number regime (the large pitch regime). For cases we

consider, the torsion τ must be bounded like $0 < \tau < 2A^{-1}$ where A is the amplitude of the helix.

We now study helical vortex filaments under Biot-Savart dynamics in the Cartesian frame. Doing so, we quickly recover the representations for the rotational and transverse velocity of the helical filament in terms of the wave number and radius of the helix. The benefit of considering the results in Cartesian form is that we immediately can visualize the stricture of the filament, so we can use these velocities to give a closed-form position of the helical filament curve at an arbitrary time $t > 0$. As opposed to using the "cut-off" approximation in the way mentioned above, we simply replace the "local" dynamics in the Biot-Savart law directly with the LIA, while the non-local effects remain in integral form. That is, local effects are taken on a region $|x - s| < \epsilon$ (where x is a point on the filament and s denotes points within a small neighborhood of ϵ), while non-local effects are considered on $|x - s > \epsilon|$. The LIA is simpler to work with than other approaches for the inner region, since it gives an exact result (as opposed to an analytical result which must be approximated numerically). This approach has previously been employed numerically in order to study quantum turbulence [81]. Furthermore, by using the LIA for the local region, we can meaningfully compare the non-local formulation with existing results valid strictly under the LIA. The results of this section were considered in Van Gorder [116].

7.2.1   Time evolution of a helical filament

The helical filament corresponds to one possible parameterization of $\mathbf{r}$. For simplicity, we align the filament along one axis, so in Cartesian coordinates, we write

$$\mathbf{r}(x,t) = (x + \beta t, A\cos(kx - \omega t + x_0), A\sin(kx - \omega t + x_0)) \ . \tag{7.44}$$

For simplicity, we shall scale time by $\frac{\kappa}{8\pi}$ to remove the corresponding factor of the Biot-Savart integral. In this parameterization about the x-axis, we should have

$$\mathbf{t} \times \mathbf{n} = \frac{\mathbf{r}_s \times \mathbf{r}_{ss}}{|\mathbf{r}_s|^3} \ . \tag{7.45}$$

We obtain the system

$$\beta = -\frac{2\ln(\epsilon)A^2k^3}{(1 + A^2k^2)^{3/2}} + 2A^2k \int_{|s-x|>\epsilon} \frac{1 - \cos(k[s-x])}{[(s-x)^2 + 2A^2(1 - \cos(k[s-x]))]^{3/2}} ds \,, \tag{7.46}$$

$$A\omega \sin(kx - \omega t + x_0) = -\frac{2\ln(\epsilon)Ak^2}{(1 + A^2k^2)^{3/2}} \sin(kx - \omega t + x_0)$$

$$+ 2A \int_{|s-x|>\epsilon} \frac{\sin(ks - \omega t + x_0) - \sin(kx - \omega t + x_0) - k(s-x)\cos(ks - \omega t + x_0)}{[(s-x)^2 + 2A^2(1 - \cos(k[s-x]))]^{3/2}} ds \,, \tag{7.47}$$

$$-A\omega \cos(kx - \omega t + x_0) = \frac{2\ln(\epsilon)Ak^2}{(1 + A^2k^2)^{3/2}} \cos(kx - \omega t + x_0)$$

$$- 2A \int_{|s-x|>\epsilon} \frac{\cos(ks - \omega t + x_0) - \cos(kx - \omega t + x_0) + k(s-x)\sin(ks - \omega t + x_0)}{[(s-x)^2 + 2A^2(1 - \cos(k[s-x]))]^{3/2}} ds \,. \tag{7.48}$$

Equation (7.46) directly gives the translational velocity of such a helical filament, while equations (7.47) and (7.48) can be used to determine the frequency ω which provides the

rotational motion. In particular, we take i(7.47) - (7.48), from which we obtain

$$
\begin{aligned}
\omega e^{i[kx-\omega t+x_0]} = {} & -\frac{2\ln(\epsilon)k^2}{(1+A^2k^2)^{3/2}}e^{i[kx-\omega t+x_0]} \\
& + 2e^{i[kx-\omega t+x_0]}\int_{|s-x|>\epsilon}\frac{(1-ik[s-x])e^{ik[s-x]}-1}{[(s-x)^2+2A^2(1-\cos(k[s-x]))]^{3/2}}ds\,.
\end{aligned}
\tag{7.49}
$$

Simplifying this equation, and noting that the integral should have both a real and imaginary part, we obtain

$$
\begin{aligned}
\omega = {} & -\frac{2\ln(\epsilon)k^2}{(1+A^2k^2)^{3/2}} + 2\int_{|\sigma|>\epsilon}\frac{\cos(k\sigma)-1+k\sigma\sin(k\sigma)}{[\sigma^2+2A^2(1-\cos(k\sigma))]^{3/2}}d\sigma \\
& + 2i\int_{|\sigma|>\epsilon}\frac{\sin(k\sigma)-k\sigma\cos(k\sigma)}{[\sigma^2+2A^2(1-\cos(k\sigma))]^{3/2}}d\sigma\,.
\end{aligned}
\tag{7.50}
$$

Note that the integrand of the integral multiplying the i is an odd function, therefore the integral over $(-\infty,\epsilon)$ is the negative of the integral over (ϵ,∞), hence this integral is zero. This makes sense, as ω should be real-valued. On the other hand, the real part of the integral has an integrand which is an even function, so the total integral is just twice the integral over (ϵ,∞). We therefore obtain

$$
\omega = -\frac{2\ln(\epsilon)k^2}{(1+A^2k^2)^{3/2}} + 4\int_{\epsilon}^{\infty}\frac{\cos(k\sigma)-1+k\sigma\sin(k\sigma)}{[\sigma^2+2A^2(1-\cos(k\sigma))]^{3/2}}d\sigma\,.
\tag{7.51}
$$

In a similar manner, the translational velocity along the x-axis is given by

$$
\beta = -\frac{2\ln(\epsilon)A^2k^3}{(1+A^2k^2)^{3/2}} + 4A^2k\int_{\epsilon}^{\infty}\frac{1-\cos(k\sigma)}{[\sigma^2+2A^2(1-\cos(k\sigma))]^{3/2}}d\sigma\,.
\tag{7.52}
$$

With ω and β known, we can describe the motion of the helical vortex filament (7.44) exactly. In Fig. 7.1, we plot the rotational and translational velocity parameters for various values of the physical constants.

The integral term in (7.51) is equivalent to equation (19) of Widnall [119], except that integral was approximated in a different way by using the "cut-off" approximation. In this method, a function of the same singular order is added and subtracted under the integral, in order to remove the logarithmic divergence. The remaining singularity is shifted to an auxiliary integral, which can itself be evaluated in terms of a cosine integral. The quantities were Fourier transformed in Widnall [119] which helps in computation of the integrals. See equation (36) of Widnall [119]. The resulting approximations were then solved numerically.
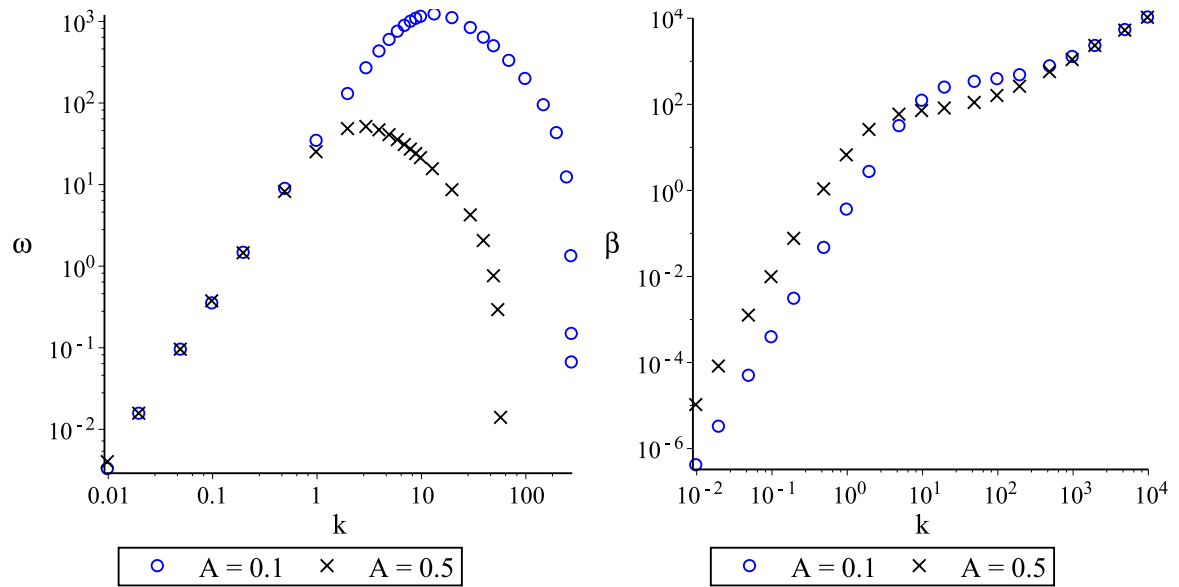
Figure 7.1: Numerical plots of the rotational velocity, ω, and transverse velocity, β, of a helical vortex filament when non-local dynamics are accounted for. The results use the LIA near the logrithmic singularlity, so these are the solutions (7.51)-(7.52). Note that we set $\epsilon = 10^{-5}$ in all plots. The precise value of ϵ is not important, since a change in the value of ϵ results in a scaling of the plots, therefore the value of ϵ does not influence the qualitative features of the solutions.

We see that there exists a particular finite value of the wave number k for which the rotational velocity of the filament is maximal. On the other hand, the behavior of the translational velocity is a bit more complicated. For small k, β scales like $\beta \sim k^2$, while for large k, the integral term dominates, giving $\beta \sim k$.

7.2.2 Approximating the relations for ω and β in the case of small and intermediate wave numbers

For s sufficiently far from $s = 0$, reasonable approximations to the integrands in (7.51) and (7.52) are

$$\frac{\cos(k\sigma) - 1 + k\sigma \sin(k\sigma)}{[\sigma^2 + 2A^2(1 - \cos(k\sigma))]^{3/2}} \approx \frac{\cos(k\sigma) - 1 + k\sigma \sin(k\sigma)}{(1 + A^2 k^2)^{3/2} \sigma^3} \tag{7.53}$$

and

$$\frac{1 - \cos(k\sigma)}{[\sigma^2 + 2A^2(1 - \cos(k\sigma))]^{3/2}} \approx \frac{1 - \cos(k\sigma)}{(1 + A^2 k^2)^{3/2} \sigma^3} , \tag{7.54}$$

respectively. The first approximation, (7.53), is of the same flavor of that used in equation (3.21) in Ricca [77]. These approximations are valid for small and intermediate values of the wave number k, since this is when the decay of the integrals dominates the oscillations sufficiently fast. We shall say more on the large-k situation later. While it is possible to obtain more accurate approximations, these approximations are accurate enough for our qualitative analysis. In Figs. 7.2 and 7.3, we give plots of the integrands (7.53) and (7.54) along with their approximations. The approximations are seen to be very accurate, provided that the helical filaments are of bounded variation (Ak and k sufficiently bounded). Even

326

for the intermediate values used in the figures, the approximations are very accurate. Only when A or k become very large would we see any breakdown in the approximations. While the large-A case is not particularly physical (since such solutions would be highly unstable, while we are considering solutions which persist in time, a priori, through the assumption (7.44)), it is possible to have large wave numbers, and we discuss this case later.
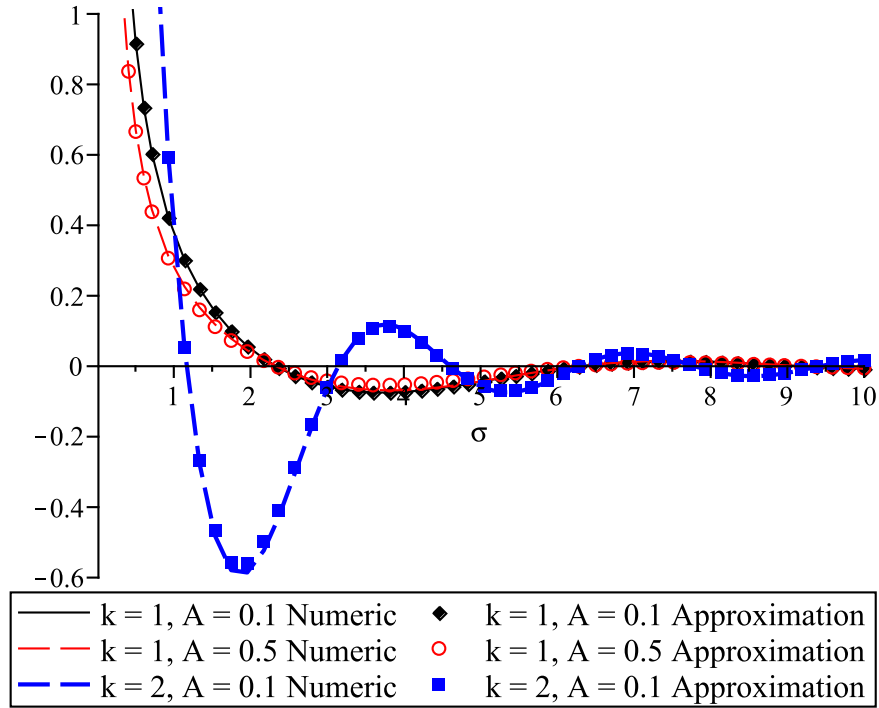
Figure 7.2: Numerical plots and approximations to the integrand given in (7.53) for various values of the physical parameters. We set $\epsilon = 10^{-5}$ in all plots. For small and intermediate values of k and A, the approximation to the integrand (7.53) is very accurate, and hence the approximating formula (7.58) for the integral term in (7.51) is accurate.
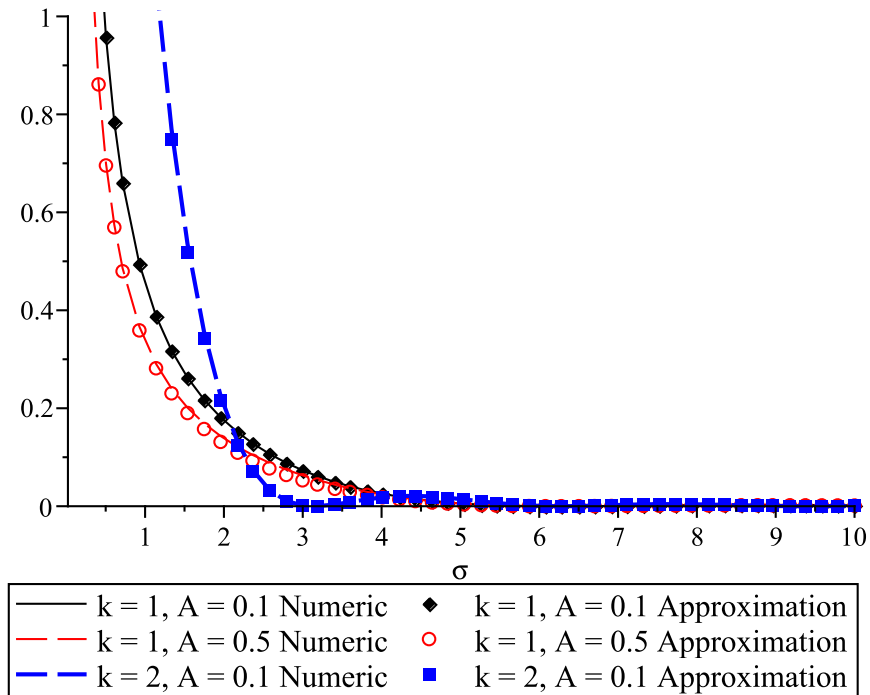
Figure 7.3: Numerical plots and approximations to the integrand given in (7.54) for various values of the physical parameters. We set $\epsilon = 10^{-5}$ in all plots. Ahain, for small and intermediate values of k and A, the approximation to the integrand (7.54) is very accurate, and hence the approximating formula (7.61) for the integral term in (7.52) is accurate.

We first have

$$\int_\epsilon^\infty \frac{\cos(k\sigma) - 1 + k\sigma\sin(k\sigma)}{[\sigma^2 + 2A^2(1 - \cos(k\sigma))]^{3/2}} d\sigma \approx \int_\epsilon^\infty \frac{\cos(k\sigma) - 1 + k\sigma\sin(k\sigma)}{(1 + A^2k^2)^{3/2}\sigma^3} d\sigma$$

$$= \frac{\cos(k\epsilon) - 1 + k\epsilon\sin(k\epsilon) - k^2\epsilon^2\text{Ci}(k\epsilon)}{2\epsilon^2(1 + A^2k^2)^{3/2}},$$

(7.55)

where Ci is the cosine integral. We find that

$$\frac{\cos(k\epsilon) - 1 + k\epsilon\sin(k\epsilon)}{\epsilon^2} = \frac{k^2}{2} + O(\epsilon^2)$$

(7.56)

and

$$\text{Ci}(k\epsilon) = \gamma + \ln(k) + \ln(\epsilon) + O(\epsilon^2),$$

(7.57)

hence

$$\int_\epsilon^\infty \frac{\cos(k\sigma) - 1 + k\sigma\sin(k\sigma)}{[\sigma^2 + 2A^2(1 - \cos(k\sigma))]^{3/2}} d\sigma \approx -\frac{k^2}{2(1 + A^2k^2)^{3/2}} \left(\gamma - \frac{1}{2} + \ln(k) + \ln(\epsilon)\right) + O(\epsilon^2).$$

(7.58)

Here, $\gamma \approx 0.5772$ is the Euler-Mascheroni constant. We neglect terms of order ϵ^2 and higher, since $\epsilon << 1$. Returning to Ricca [77], this expression is similar to his equation (3.27). The difference is the dependence on the wave number, which is scaled out in Ricca [77]. (More precisely, the results in Ricca [77] involved scaling torsion, $\tau = k/(1 + A^2k^2)$.) Keeping k present, we will be able to directly compare our results with the LIA. Ricca [77] obtained this integral in the limit $\tau \to \infty$. For this to occur, the wave number must be large and A must become small as k becomes large. We do not consider this, since for finite A the torsion will not be infinite. Rather, for finite $A > 0$, the torsion will attain a maximal value of $\tau = 2A^{-1}$ at $k = A^{-1}$. The $\tau \to \infty$ limit then corresponds to $A \to 0$, $k \to \infty$ provided $Ak \to \nu$, for $\nu < \infty$. This is a very restrictive limit, since $A \to 0$ essentially gives us a line

filament. What all of this means is that we should maintain the parameters k and A in our development, as opposed to scaling them out and taking any particular limit, in order to capture the behavior of arbitrary helical filaments.

Regarding the second integral, we have

$$\int_\epsilon^\infty \frac{1 - \cos(k\sigma)}{[\sigma^2 + 2A^2(1 - \cos(k\sigma))]^{3/2}} d\sigma \approx \int_\epsilon^\infty \frac{1 - \cos(k\sigma)}{(1 + A^2 k^2)^{3/2} \sigma^3} d\sigma$$
$$= \frac{k\epsilon \sin(k\epsilon) + 1 - \cos(k\epsilon)}{2\epsilon^2} - \frac{k^2}{2} \mathrm{Ci}(k\epsilon),$$

(7.59)

and using

$$\frac{k\epsilon \sin(k\epsilon) + 1 - \cos(k\epsilon)}{\epsilon^2} = \frac{3}{2} k^2 + O(\epsilon^2), \tag{7.60}$$

we find

$$\int_\epsilon^\infty \frac{1 - \cos(k\sigma)}{[\sigma^2 + 2A^2(1 - \cos(k\sigma))]^{3/2}} d\sigma \approx \frac{k^2}{2(1 + A^2 k^2)^{3/2}} \left(\frac{3}{2} - \gamma - \ln(k) - \ln(\epsilon) \right) + O(\epsilon^2).$$

(7.61)

Using the approximations (7.58) and (7.61) in equations (7.51) and (7.52), respectively, we have the approximations

$$\omega_{\mathrm{approx}} = -\frac{k^2(2\gamma - 1 + 2\ln(k) + 4\ln(\epsilon))}{(1 + A^2 k^2)^{3/2}} \tag{7.62}$$

and

$$\beta_{\mathrm{approx}} = \frac{A^2 k^3 (3 - 2\gamma - 2\ln(k) - 4\ln(\epsilon))}{(1 + A^2 k^2)^{3/2}}. \tag{7.63}$$

The curve describing the helical vortex filament, including non-local effects, is then given by the approximation

$$\mathbf{r}(x,t) \approx \left\{ x + \frac{A^2 k^3 (3 - 2\gamma - 2\ln(k) - 4\ln(\epsilon))}{(1 + A^2 k^2)^{3/2}} t \right\} \mathbf{i}_x$$
$$+ A\cos\left(kx + \frac{k^2(2\gamma - 1 + 2\ln(k) + 4\ln(\epsilon))}{(1 + A^2 k^2)^{3/2}} t + x_0 \right) \mathbf{i}_y \qquad (7.64)$$
$$+ A\sin\left(kx + \frac{k^2(2\gamma - 1 + 2\ln(k) + 4\ln(\epsilon))}{(1 + A^2 k^2)^{3/2}} t + x_0 \right) \mathbf{i}_z .$$

7.2.3   Comparison with the LIA and numerical approximations

If one were to strictly consider the LIA, as is often done, one would obtain (upon removing the integral terms from (7.46)-(7.48))

$$\omega_{\text{LIA}} = -\frac{2\ln(\epsilon)k^2}{(1 + A^2 k^2)^{3/2}} > 0 \quad \text{and} \quad \beta_{\text{LIA}} = A^2 k\omega_{\text{LIA}} = -\frac{2\ln(\epsilon)A^2 k^3}{(1 + A^2 k^2)^{3/2}} > 0, \qquad (7.65)$$

Under the LIA, the motion of a helical vortex filament then takes the form

$$\mathbf{r}(x,t) = \left\{ x - \frac{2\ln(\epsilon)A^2 k^3}{(1 + A^2 k^2)^{3/2}} t \right\} \mathbf{i}_x + A\cos\left(kx + \frac{2\ln(\epsilon)k^2}{(1 + A^2 k^2)^{3/2}} t + x_0 \right) \mathbf{i}_y$$
$$+ A\sin\left(kx + \frac{2\ln(\epsilon)k^2}{(1 + A^2 k^2)^{3/2}} t + x_0 \right) \mathbf{i}_z . \qquad (7.66)$$

In terms of the parameters calculated through the LIA, we have that the approximations found for small and intermediate k

$$\omega_{\text{approx}} = 2\omega_{\text{LIA}} - \frac{k^2(2\gamma - 1 + 2\ln(k))}{(1 + A^2 k^2)^{3/2}} \qquad (7.67)$$

and

$$\beta_{\text{approx}} = 2\beta_{\text{LIA}} + \frac{A^2 k^3(3 - 2\gamma - 2\ln(k))}{(1 + A^2 k^2)^{3/2}} . \qquad (7.68)$$

In Fig. 7.4, we plot these approximate solutions against both the LIA solutions and direct numerical integration of the integrals in (7.51)-(7.52). For small and intermediate k (k of order unity or smaller), these approximations are in strong agreement with the numerical integrations. For larger k, of order 10, the approximations tend to over-estimate the numerical value of β and ω slightly, whereas the LIA underestimates these values. The approximations are still more accurate than the LIA. For much larger k, say of order 10^2 and greater, both the approximation (7.62)-(7.63) as well as the LIA lose their usefulness. This is due to the fact that the integral term has an integrand which rapidly oscillates for large k.

7.2.4 Discussion

From the plots, it is clear that there exists a critical value of the wave number for which the rotational velocity is maximal. In the approximation (7.62)-(7.63), the LIA, and the numerical approximations, this value is nearly the same. Since the values are approximately the same, we use the LIA, finding that this critical wave number is give approximately by $k^* \approx \sqrt{2}A^{-1}$. Note that this corresponds to the maximal value of torsion (since torsion τ is given by $\tau = k(1 + A^2k^2)^{-1}$). So, the larger the torsion, the greater the rotational velocity. On the other hand, the plots indicate that the transverse velocity is always increasing, as mentioned when we considered the numerical results before.

In summary, the approximations (both LIA and those of (7.62)-(7.63)) are accurate for small and intermediate k (with the approximation (7.62)-(7.63) being best), while there is a sharp breakdown in the approximations for larger k. For both ω and β, the breakdown for large k is due to the fact that the integrals oscillate rapidly.

It is worth mentioning that there is a quantum form of the LIA, which is essentially the LIA applied to the HVBK model. It should be feasible to extend the resent results to that case, at least in the case of helical filaments with constant amplitude A. The exact form of a helical filament under the quantum LIA was discussed in Chapter 6. In the case of decaying filaments ($A = A(t)$ such that $A \to 0$ as $t \to \infty$), the non-local development may be possible analytically, but will be much more complicated.
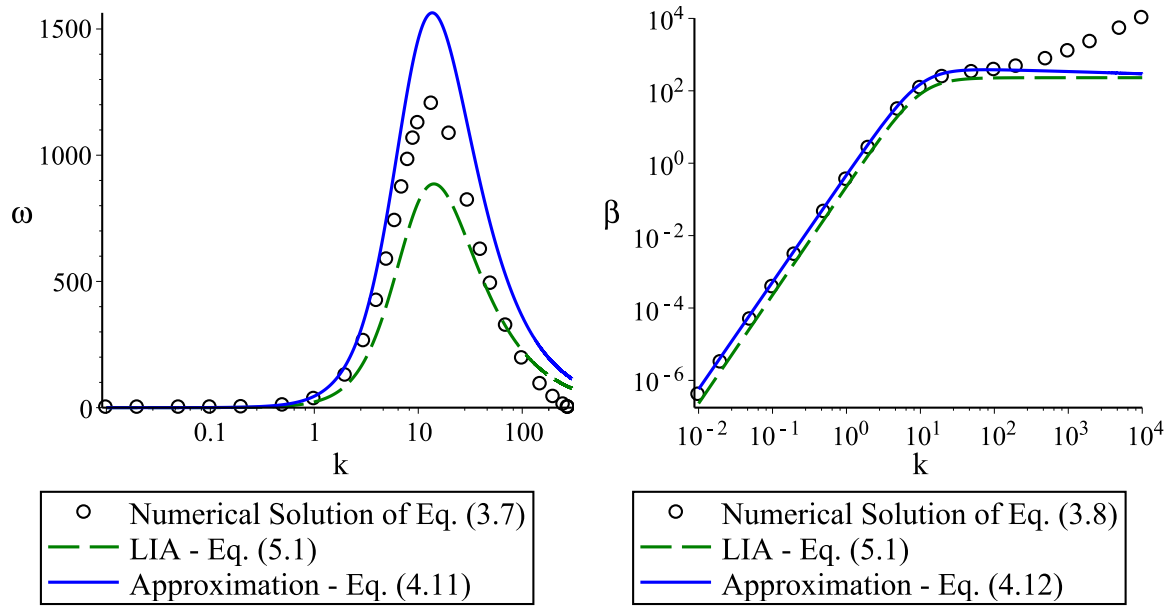
Figure 7.4: Comparison of the numerical plots and approximate solutions for the rotational velocity, ω, and transverse velocity, β, of a helical vortex filament when non-local dynamics are accounted for. The numerical results use the LIA near the logrithmic singularlity, so these are the solutions (7.51)-(7.52). Note that we set $\epsilon = 10^{-5}$ in all plots. We also take $A = 0.1$. The analytical approximations obtained in (7.62)-(7.63) are superior to the LIA (7.65) results when k is either small or in the intermediate range. Once k becomes large, both approximations lose accuracy. This is due to the fact that, for large k, the integral terms in (7.51)-(7.52) are rapidly oscillating. The approximations (7.62)-(7.63) are useful when the decay in the integrals dominates the oscillations, which is not true for large k. In the regime where the approximations are useful, note that the LIA underestimates both velocities, while the approximation (7.62)-(7.63) overestimates the velocities.

335

CHAPTER 8

CONCLUSIONS

In this report, we have studied a number of nonlinear dispersive partial differential equations of relevance to various physical scenarios. The most common application has been to vortex filament dynamics, although other applications have been mentioned and considered. The physical applicability of the results increases as the governing models become more complicates and take into account more reasonable assumptions.

Among some of the more interesting results discussed here, we were able to demonstrate the existence of space-periodic solutions for the Cartesian and arclength-tangent formulations of the LIA governing the motion of a vortex filament in Chapter 2, and we determined orbital stability properties for these solutions in Chapter 3. These solutions correspond to rotating planar filaments. Similar results were discussed for the integrable WKIS model in Chapters 2-3. We were also able to demonstrate a variety of rotating non-planar filament solutions under the 2D Cartesian LIA, in Chapter 2. Meanwhile, in Chapter 4, we were able to consider several pathological solutions which model vortex self-intersections and kinks.

Many of the vortex filament solution forms present under the LIA in Chapters 2 - 4 were generalized to the case of superfluids under various potential forms of the quantum LIA

in Chapter 5. In particular, we were able to demonstrate mathematical properties of helical, self-similar, planar, and soliton solutions under the quantum LIA. However, the potential forms of the quantum LIA are approximations to the full vector form of the LIA, and in Chapter 6 we study the exact vector form of the quantum LIA. In Chapter 6, we study planar, helical, and soliton solutions under the exact vector form of the quantum LIA, and we are able to determine the motion of such vortex filament solutions analytically. Many of the results we determine mathematically verify known experimental or numerical results from the literature.

Physically, the LIA is still not the most general model one can consider, since it ignores non-local effects. In Chapter 7, we consider the non-local equation governing the motion of a vortex filament in a classical fluid. While the non-local effects are most useful for complicated fluid flow dynamics, such as vortex mergers or the analysis of many-vortex models, we restrict our attention to two solution types which can be studied analytically. Still, these two solutions, namely the planar and helical vortex filaments, are rather fundamental, and we compare our non-local results to those discussed in earlier chapters for the LIA. We find that non-local effects result primarily in an increase in the velocity of the filament solutions (both rotational and transverse velocity is increased), while the spatial structure of the filaments is largely unchanged. Note that it is possible to extend such results to the superfluid or quantum fluid case (see below), although such results will be much more complicated.

Regarding future work, the extension of the present results to other vortex configurations, or to other nonlinear dispersive partial differential equations not studied here, seems

like an obvious avenue. Regarding the solutions considered here, it may be useful to extend other solutions to account for the effects of the the non-local formulation given in Chapter 7.

While the dispersive partial differential equations considered in Chapter 3 permit a nice and rather elegant stability analysis, for more complicated dispersion relations such stability results are expected to be far less elegant. A work-in-progress is on an orbital stability result for nonlinear dispersive partial differential equations of the form

$$iu_t = F(|u|^2, |u_x|^2)u_{xx} + G(|u|^2)u \,, \tag{8.1}$$

which is a generalization of known results for generalized NLS equation of the form

$$iu_t = au_{xx} + G(|u|^2)u \,. \tag{8.2}$$

As seen when comparing the work in Chapter 6 with that of Chapter 5, considering the full three-dimensional dynamics of quantum vortex filaments can be rather involved. The same can be said of accounting for non-locality. However, considering the quantum form of the vortex filament equation which uses the Biot-Savart dynamics instead of the LIA would be quite interesting. Such a formulation would account for both superfluid effects and the effect of non-locality on the motion of a vortex filament in a quantum fluid. Any results in the literature are numerical in nature, so analytical results in this area would be quite nice, since they may lead to qualitative observations which are ignored or not considered in the parameter regions explored numerically.

One open problem with regards to the quantum vortex filament is whether or not the quantum vortex filament equation (in any form) admits chaotic solutions. While thy has been hypothesized before due to the complicated dynamics inherent in the vortex filament equations, there has never been a specific example given. It is the author's opinion that the best chance to observe chaos in a quantum vortex filament under LIA would be in the Hasimoto-type transformation which puts the quantum LIA into correspondence with a cubic complex Ginsburg-Landau equation. In a work-in-progress, the author has already found a rich variety of bifurcations in this model.

LIST OF REFERENCES

[1] N. Akhmediev, A. Ankiewicz, J. M. Soto-Crespo, and J. M. Dudley, *Rogue wave early warning through spectral measurements?*, Physics Letters A **375** (2011) 541-544.

[2] N. Akhmediev, A. Ankiewicz, and M. Taki, *Waves that appear from nowhere and disappear without a trace*, Physics Letters A **373** (2009) 675-678.

[3] S.Z. Alamri, A. J. Youd, and C. F. Barenghi, *Reconnection of superfluid vortex bundles*, Physical Review Letters **101** (2008) 215302.

[4] A. Ankiewicz, N. Devine, and N. Akhmediev, *Are rogue waves robust against perturbations?*, Physics Letters A **373** (2009) 3997-4000.

[5] T. Araki, M. Tsubota, and S. K. Nemirovskii, *Energy Spectrum of Superfluid Turbulence with No Normal-Fluid Component*, Physical Review Letters **89** (2002) 145301.

[6] I. S. Aranson and L. Kramer, *The world of the complex Ginzburg-Landau equation*, Reviews of Modern Physics **74** (2002) 99-143.

[7] H. Aref and E.P. Flinchem, *Dynamics of a vortex filament in a shear flow*, Journal of Fluid Mechanics **148** (1984) 477-497.

[8] R. J. Arms and F. R. Hama, *Localized-induction concept on a curved vortex and motion of an elliptic vortex ring*, Physics of Fluids **8** (1965) 553-559 .

[9] H. Bailung, S. K. Sharma, and Y. Nakamura, *Observation of Peregrine solitons in a multi-component plasma with negative ions*, Physical Review Letters **107** (2011) 255005.

[10] U. Bandelow and N. Akhmediev, *Persistence of rogue waves in extended nonlinear Schrdinger equations: Integrable SasaSatsuma case*, Physics Letters A **376** (2012) 1558-1561.

[11] V. Banica and L. Vega, *On the stability of a singular vortex dynamics*, Communications in Mathematical Physics **286** (2009) 593-627.

[12] F. Baronio, A. Degasperis, M. Conforti, and S. Wabnitz, *Solutions of the vector nonlinear Schrdinger equations: evidence for deterministic rogue waves*, Physical Review Letters **109** (2012) 044102.

[13] I.L. Bekarevich and I.M. Khalatnikov, *Phenomenological derivation of the equations of vortex motion in He II*, Sov. Phys. JETP **13** (1961) 643-646.

[14] T.B. Benjamin and J.E. Feir, *The disintegration of wave trains on deep water Part 1. Theory*, Journal of Fluid Mechanics **27** (1967) 417-430.

[15] Yu. V. Bludov, R. Driben, V. V. Konotop, and B. A. Malomed, *Instabilities, solitons and rogue waves in $\mathcal{PT}$-coupled nonlinear waveguides*, Journal of Optics **15** (2013) 064010.

[16] Y.V. Bludov, V.V. Konotop, and N. Akhmediev, *Matter rogue waves*, Physical Review A **80** (2009) 033610.

[17] G. Boffetta, A. Celani, D. Dezzani, J. Laurie, and S. Nazarenko, *Modeling Kelvin Wave Cascades in Superfluid Helium*, Journal of Low Temperature Physics **156** (2009) 193-214.

[18] M. Blaauboer, B.A. Malomed, and G. Kurizki, *Spatiotemporally Localized Multidimensional Solitons in Self-Induced Transparency Media*, Physical Review Letters 84 (2000) 1906-1909.

[19] M. Boiti, V. S. Gerdjikov and F. Pempinelli, *The WKIS system: Bäcklund transformations, generalized Fourier transforms and all that*, Progress of Theoretical Physics **75** (1986) 1111-1141.

[20] F. Calogero and A. Degasperis, *Spectral Transform and Solitons: Tools to Solve and Investigate Nonlinear Evolution Equations, Volume 1. Volume 13 of Studies in Mathematics and Its Applications* (Elsevier Amsterdam, 1982).

[21] A. Chabchoub, N. P. Hoffmann, and N. Akhmediev, *Rogue wave observation in a water wave tank*, Physical Review Letters **106** (2011) 204502.

[22] S.M. Chang, S. Gustafson, K. Nakanishi, and T.P. Tsai, *Spectra of linearized operators for NLS solitary waves*, SIAM J. Math. Analysis **39(4)** (2007) 1070-1111.

[23] D.K. Cheng, W.M. Cromar, and R.J. Donnelly, *Influence of an Axial Heat Current on Negative-Ion Trapping in Rotating Helium II*, Physical Review Letters **31** (1973) 433-436.

[24] L.S. Da Rios, *Sul moto d'un liquido indefinite con un filetto vorticoso di forma qualunque*, Rendiconti del Circolo Matematico di Palermo **22** (1906) 117.

[25] S.I Davis, P.C Hendry, and P.V.E McClintock, *Decay of quantized vorticity in superfluid ^4He at mK temperatures*, Physica B **280** (2000) 43-44.

[26] V.P. Dmitriyev, *Helical waves on a vortex filament*, American Journal of Physics **73** (2005) 563-565.

[27] J. M. Dudley, G. Genty, F. Dias, B. Kibler, and N. Akhmediev, *Modulation instability, Akhmediev Breathers and continuous wave supercontinuum generation*, Optics Express **17** (2009) 21497-21508.

[28] K. Dysthe, H. E. Krogstad, and P. Muller, *Oceanic rogue waves*, Annual Review of Fluid Mechanics **40** (2008) 287-310.

341

[29] E. Fehlberg, Low-order classical Runge-Kutta formulas with step size control and their application to some heat transfer problems, NASA Technical Report 315 (1965).

[30] F. Fenton and A. Karma, *Vortex dynamics in three-dimensional continuous myocardium with fiber rotation: filament instability and fibrillation*, Chaos **8** (1998) 20-47.

[31] S. N. Fisher and G. R. Pickett, *Quantum Turbulence in Superfluid ^3He at Very Low Temperatures*, Progress in Low Temperature Physics **16** (2009) 147-194.

[32] E. Fonda, D. P. Meichle, N. T. Ouellette, S. Hormoz, K. R. Sreenivasan, and D. P. Lathrop, *Visualization of Kelvin waves on quantum* vortices, arXiv:1210.5194 (2012)

[33] Y. Fukumoto, *Stationary configurations of a vortex filament in background flows*, Proceedings of the Royal Society of London A **453** (1997) 1205-1232.

[34] Y. Fukumoto and M. Miyajima, *The localized induction hierarchy and the Lund-Regge equation*, Journal of Physics A: Mathematical and General **29** (1996) 8025-8034.

[35] V. Gerdjikov, G. Vilasi, and A. B. Yanovski, *Integrable Hamiltonian Hierarchies: Spectral and Geometric Methods. Volume 748 of Lecture Notes in Physics* (Springer Berlin Heidelberg, 2008).

[36] W.I. Glaberson, W.W. Johnson, and R.M. Ostermeier, *Instability of a Vortex Array in He II*, Physical Review Letters **33** (1974) 1197-1200.

[37] E.E. Goldstein and D.M. Petrich, *Solitons, Euler's equation, and vortex patch dynamics*, Physical Review Letters **69** (1992) 555-558.

[38] S. Gutiérrez, J. Rivas, and L. Vega, *Formation of Singularities and Self-Similar Vortex Motion Under the Localized Induction Approximation*, Communications in Partial Differential Equations **28** (2003) 927-968.

[39] H.E. Hall and W.F. Vinen, *The rotation of liquid helium II. I. Experiments on the propagation of second sound in uniformly rotating helium II*, Proceedings of the Royal Society of London A **238** (1956) 204-214.

[40] H.E. Hall and W.F. Vinen, *The rotation of liquid helium II. II. The theory of mutual friction in uniformly rotating helium II*, Proceedings of the Royal Society of London A **238** (1956) 215-234.

[41] H. Hasimoto, *Motion of a Vortex Filament and its relation to Elastica*, Journal of the Physical Society of Japan **31** (1971) 293-294.

[42] H. Hasimoto, *A soliton on a vortex filament*, Journal of Fluid Mechanics **51** (1972) 477-485.

[43] J.S. He, H.R. Zhang, L.H. Wang, K. Porsezian, and A.S. Fokas, *Generating mechanism for higher-order rogue waves*, Physical Review E **87** (2013) 052914.

[44] E. J. Hopfinger and F.K. Browand, *Vortex solitary waves in a rotating, turbulent flow*, Nature **295** (1982) 393-395.

[45] B. Ilan, Y. Sivan, and G. Fibich, *A quantitative approach to soliton instability*, Optics Letters **36** (2011) 397-399.

[46] Y.V. Kartashov, V.A. Vysloukh, and L. Torner, *Rotary solitons in Bessel optical lattices*, Physical Review Letters **93** (2004) 093904.

[47] C. Kharif and E. Pelinovsky, *Physical mechanisms of the rogue wave phenomenon*, European Journal of Fluid Mechanics B - Fluids **22** (2003) 603-634.

[48] B. Kibler, J. Fatome, C. Finot, G. Millot, F. Dias, G. Genty, N. Akhmediev, and J. M. Dudley, *The Peregrine soliton in nonlinear fibre optics*, Nature Physics **6** (2010) 790-795.

[49] S. Kida, *A vortex filament moving without change of form*, Journal of Fluid Mechanics **112** (1981) 397-409.

[50] S. Kida, *Stability of a steady vortex filament*, Journal of the Physical Society of Japan **51** (1982) 1655-1662.

[51] L. D. Landau and E. M. Lifshitz, Fluid Mechanics, Addison and Wesley (1959).

[52] J. Langer and D.A. Singer, *Lagrangian aspects of the Kirchhoff elastic rod*, SIAM Review **38** (1996) 605-618.

[53] M. Lakshmanan and S. Ganesan, *Equivalent forms of a generalized Hirota's equation with linear inhomogeneities*, Journal of the Physical Society of Japan **52** (1983) 4031-4033.

[54] M. Lakshmanan and S. Ganesan, *Geometrical and gauge equivalence of the generalized Hirota, Heisenberg and Wkis equations with linear inhomogeneities*, Physica A **132** (1985) 117-142.

[55] J. Laurie, V.S. L'vov, S. Nazarenko, and O. Rudenko, *Interaction of Kelvin Waves and Non-Locality of the Energy Transfer in Superfluids*, Physical Review B **81** (2010) 104526.

[56] T. Lipniacki, *Quasi-static solutions for quantum vortex motion under the localized induction approximation*, Journal of Fluid Mechanics **477** (2003) 321-337.

[57] T. Lipniacki, *Shape-preserving solutions for quantum vortex motion under localized induction approximation*, Physics of Fluids **15** (2003) 1381-1395.

[58] P. Lundquist, D. R. Andersen, and Yu. S. Kivshar, *Multicolor solitons due to four-wave mixing*, Physical Review E **57** (1998) 3551-3555.

[59] F. Maggioni, S.Z. Alamri, C.F. Barenghi, and R.L. Ricca, *Kinetic energy of vortex knots and unknots*, Il Nuovo Cimento C **32** (2009) 133-142.

[60] F. Maggioni, S.Z. Alamri, C.F. Barenghi, and R.L. Ricca, *Velocity, energy, and helicity of vortex knots and unknots*, Physical Review E **82** (2010) 026309.

[61] V.G. Makhankov, Y.P. Rybakov, and V.I. Sanyuk, *Localised nontopological structures: construction of solutions and stability problems*, Physics-Uspekhi **37** (1994) 113-137.

[62] B. A. Malomed, P. Drummond, H. He, A. Berntson, D. Anderson, M. Lisak, *Spatiotemporal solitons in multidimensional optical media with a quadratic nonlinearity*, Physical Review E **56** (1997) 4725-4735.

[63] B.A. Malomed, D.J. Kaup, and R.A. Van Gorder, *Unstaggered-staggered solitons in two-component discrete nonlinear Schrdinger lattices*, Physical Review E **85** (2012) 026604.

[64] A. Melikyan and G. Weber, *Integrable theories and generalized graded Maillet algebras*, Journal of Physics A: mathematical and Theoretical **47** (2014) 065401.

[65] F.G. Mertens, N.R. Quintero, and A.R. Bishop, *Nonlinear Schrödinger equation with spatiotemporal perturbations*, Physical Review E **81** (2010) 016608.

[66] D. Mihalache, D. Mazilu, and L. Torner, *Stability of walking vector solitons*, Physical Review Letters **81** (1998) 4353-4356.

[67] D.W. Moore and P.G. Saffman, *The instability of a straight vortex filament in a strain field*, Proceedings of the Royal Society of London A **346** (1975) 413-425.

[68] V. L. Okulov, *On the stability of multiple helical vortices*, Journal of Fluid Mechanics **521** (2004) 319-342.

[69] M. Onorato, D. Proment, A. Toffoli, *Triggering rogue waves in opposing currents*, Physical Review Letters **107** (2011) 184502.

[70] M. Onorato, S. Residori, U. Bortolozzo, A. Montina, and F. T. Arecchi, *Rogue waves and their generating mechanisms in different physical contexts*, Physics Reports **528** (2013) 47-89.

[71] R.M. Ostermeier and W.I. Glaberson, *Instability of vortex lines in the presence of axial normal fluid flow*, Journal of Low Temperature Physics **21** (1975) 191-196.

[72] E.A. Ostrovskaya, Y.S. Kivshar, D.V. Skryabin, and W.J. Firth, *Stability of Multihump Optical Solitons*, Physical Review Letters **83** (1999) 296-299.

[73] D. H. Peregrine, *Water waves, nonlinear Schrödinger equations and their solutions*, Journal of the Australian Mathematical Society, Series B: Applied Mathematics **25** (1983) 16-43.

[74] R.L. Ricca, *Rediscovery of da Rios equations*, Nature **352** (1991) 561-562.

[75] R.L. Ricca, *Physical interpretation of certain invariants for vortex filament motion under LIA*, Physics of Fluids A **4** (1992) 938-944.

[76] R.L. Ricca, *Torus knots and polynomial invariants for a class of soliton equations*, Chaos **3** (1993) 83-91.

[77] R. L. Ricca, *The effect of torsion on the motion of a helical vortex filament*, Journal of Fluid Mechanics **273** (1994) 241-259.

[78] R.L. Ricca, D.C. Samuels, and C.F. Barenghi, *Evolution of vortex knots*, Journal of Fluid Mechanics **391** (1999) 29-44.

[79] N.N. Rosanov, A.G. Vladimirov, D.V. Skryabin, and W.J. Firth, *Internal oscillations of solitons in two-dimensional NLS equation with nonlocal nonlinearity*, Physics Letters A **293** (2002) 45-49.

[80] H. Salman, *Breathers on quantized superfluid vortices*, Physical Review Letters **111** (2013) 165301.

[81] K.W. Schwarz, *Three-dimensional vortex dynamics in superfluid ^4He: Line-line and line-boundary interactions*, Physical Review B **31** (1985) 5782-5804.

[82] T. Shimizu and M. Wadati, *A New Integrable Nonlinear Evolution Equation*, Progress of Theoretical Physics **63** (1980) 808-820.

[83] H. J. Shin, *Deformation of a Peregrine soliton by fluctuating backgrounds*, Physical Review E **88** (2013) 032919.

[84] B.K. Shivamoggi and G.J.F. van Heijst, *Motion of a vortex filament in the local induction approximation: Reformulation of the Da Rios-Betchov equations in the extrinsic filament coordinate space*, Physics Letters A **374** (2010) 1742-1744.

[85] B.K. Shivamoggi, *Vortex motion in superfluid^4 He: Reformulation in the extrinsic vortex-filament coordinate space*, Physical Review B **84** (2011) 012506.

[86] B. K. Shivamoggi, *Vortex motion in superfluid ^4He: effects of normal fluid flow*, European Physical Journal B **86** (2013) 275.

[87] D.V. Skryabin and W.J. Firth, *Instabilities of higher-order parametric solitons: Filamentation versus coalescence*, Physical Review E **58** (1998) R1252-R1255 .

[88] D. R. Solli, C. Ropers, P. Koonath, and B. Jalali, *Optical rogue waves*, Nature **450** (2007) 1054-1057.

[89] E.B. Sonin, *Dynamics of helical vortices and helical-vortex rings*, EPL **97** (2012) 46002.

[90] E.B. Sonin, *Symmetry of Kelvin-wave dynamics and the Kelvin-wave cascade in the T=0 superfluid turbulence*, Physical Review B 85 (2012) 104516.

[91] V. I. Shrira and V. V. Geogjaev, *What makes the Peregrine soliton so special as a prototype of freak waves?*, Journal of Engineering Mathematics **67** (2010) 11-22.

[92] B. Svistunov, *Superfluid turbulence in the low-temperature limit*, Physical Review B **52** (1995) 3647-3653.

[93] C.Y. Tsai and S.E. Widnall, *The stability of short waves on a straight vortex filament in a weak externally imposed strain field*, Journal of Fluid Mechanics **73** (1976) 721-733.

[94] M. Tsubota, T. Araki and S.K. Nemirowskii, *Dynamics of vortex tangle without mutual friction in superfluid ^4He*, Physical Review B **62** (2000) 11751-11762.

[95] M. Umeki, *A locally induced homoclinic motion of a vortex filament*, Theoretical and Computational Fluid Dynamics **24** (2010) 383-387.

[96] M. Umeki, *A real-space representation of a locally induced vortex filament*, Theoretical and Applied Mechanics Japan **61** (2013) 195.

[97] M.G. Vakhitov and A.A. Kolokolov, *Stationary solutions of the wave equation in a medium with nonlinearity saturation*, Soviet Radiophysics **16** (1973) 783-789.

[98] R. A. Van Gorder, *Motion of a vortex filament in the local induction approximation: a perturbative approach*, Theoretical and Computational Fluid Dynamics 26 (2012) 161-171.

[99] R. A. Van Gorder, *Integrable stationary solution for the fully nonlinear local induction equation describing the motion of a vortex filament*, Theoretical and Computational Fluid Dynamics **26** (2012) 591-594.

[100] R. A. Van Gorder, *Exact solution for the self-induced motion of a vortex filament in the arclength representation of the local induction approximation*, Physical Review E **86** (2012) 057301.

[101] R. A. Van Gorder, *Exact stationary solution method for the Wadati-Konno-Ichikawa-Schimizu (WKIS) equation*, Progress of Theoretical Physics **128** (2012) 993-999.

[102] R. A. Van Gorder, *Fully nonlinear local induction equation describing the motion of a vortex filament in superfluid ^4He*, Journal of Fluid Mechanics **707** (2012) 585-594.

[103] R. A. Van Gorder, *Orbital Stability for Rotating Planar Vortex Filaments in the Cartesian and Arclength Forms of the Local Induction Approximation*, Journal of the Physical Society of Japan **82** (2013) 094005.

[104] R. A. Van Gorder, *Orbital stability for stationary solutions of the Wadati-Konno-Ichikawa-Schimizu (WKIS) equation*, Journal of the Physical Society of Japan **82** (2013) 064005.

[105] R. A. Van Gorder, *Scaling laws and accurate small-amplitude stationary solution for the motion of a planar vortex filament in the Cartesian form of the local induction approximation*, Physical Review E **87** (2013) 043203.

[106] R. A. Van Gorder, *Motion of a helical vortex filament in superfluid ^4He under the extrinsic form of the local induction approximation*, Physics of Fluids **25** (2013) 085101

[107] R. A. Van Gorder, *Self-similar vortex dynamics in superfluid ^4He under the Cartesian representation of the Hall-Vinen model including superfluid friction*, Physics of Fluids **25** (2013) 095105.

[108] R. A. Van Gorder, *Quantum vortex dynamics under the tangent representation of the local induction approximation*, Journal of Fluid Mechanics **740** (2014) 5-16.

[109] R. A. Van Gorder, *General rotating quantum vortex filaments in the low-temperature Svistunov model of the LIA*, submitted (2014).

[110] R. A. Van Gorder, *Orbital instability of the Peregrine soliton*, submitted (2014).

[111] R. A. Van Gorder, *Scaling laws and unsteady solutions of the integrable 2D local induction approximation*, submitted (2014).

[112] R. A. Van Gorder, *Decay of helical Kelvin waves on a vortex filament under the quantum LIA*, submitted (2014).

[113] R. A. Van Gorder, *Dynamics of a planar vortex filament under the quantum local induction approximation*, submitted (2014).

[114] R. A. Van Gorder, *Solitons and other waves on a quantum vortex filament*, submitted (2014).

[115] R. A. Van Gorder, *Non-local dynamics of the self-induced motion of a planar vortex filament*, submitted (2014).

[116] R. A. Van Gorder, *Self-induced motion of a Cartesian helical vortex filament under the Biot-Savart model*, submitted (2014).

[117] W.F. Vinen, *Decay of superfluid turbulence at a very low temperature: The radiation of sound from a Kelvin wave on a quantized vortex*, Physical Review B **64** (2001) 134520.

[118] M. Wadati, K. Konno, and Y.-H. Ichikawa, *A Generalization of Inverse Scattering Method*, Journal of the Physical Society of Japan **46** (1979) 1965-1966.

[119] S.E. Widnall, *The stability of a helical vortex filament*, Journal of Fluid Mechanics **54** (1972) 641-663.

[120] S.E. Widnall, *The structure and dynamics of vortex filaments*, Annual Review of Fluid Mechanics **7** (1975) 141-165.

[121] J. Yang, Nonlinear Waves in Integrable and Nonintegrable Systems, SIAM Mathematical Modelling and Computation. Philadelphia, PA, USA (2010).

[122] X. Ying, Z. Ruguang, and W. Jianwen, *An integrable decomposition of the WKIS equation*, Journal of Xuzhou Normal University (Natural Science Edition) **29(4)** (2011) 27-32.

[123] V. E. Zakharov and A. A. Gelash, *Nonlinear stage of modulation instability*, Physical Review Letters **111** (2013) 054101.